School of Earth and Planetary Sciences

Gold Source and Deportment in the Daqiao Epizonal Orogenic Gold Deposit, China

Yafei Wu

This thesis is presented for the Degree of

Doctor of Philosophy

of

Curtin University

May 2019

Declaration

To the best of my knowledge and belief this thesis contains no material previously published by any other person except where due acknowledgement has been made.

This thesis contains no material which has been accepted for the award of any other degree of diploma in any university.

Yafei Wu

Date 08/05/2019

Abstract

Gold (Au) is the most noble of all metals and has served as the foundation of solid monetary systems for centuries. Orogenic Au deposits are the second important global Au supplier after Witwatersrand placer Au and are thus a perennial exploration target. Extensive previous studies have recognized that Au is often sourced from underlying and/or host sediments during regional metamorphism and deformation, is transported mainly as bisulfide complexes, and coprecipitates with hydrothermal sulfides and quartz as a consequence of changing ore fluid conditions. However, certain aspects, such as the Au source, transport, precipitation, and remobilization mechanisms have long been debated. Such aspects include the role of magmatism, the role of silica in hydrothermal fluids, and the relative importance of fluid-crystal kinetics and changes in bulk fluid conditions for the incorporation of Au into sulfides. Further, the redistribution of Au during sulfide replacement has been noted, but the detailed micron-scale processes and mechanisms are poorly understood.

The West Qinling Orogen (WQO) formed during the Late Triassic closure of Paleo-Tethys and subsequent collision between North China Craton and South China Block. Numerous Au deposits of Late Jurassic to Early Cretaceous age, with and without evidence of contemporary magmatic activity, are widely distributed in the eastern and western parts of this orogen (EQO and WQO), respectively. The Daqiao epizonal orogenic Au deposit, hosted by weakly metamorphosed Triassic turbidites in the WQO, has a reserve of more than 105 tonnes of Au. Gold ores are characterized by intensely silicified tectonic breccias and hydraulic breccias. Invisible Au occurs in irregularly zoned pyrite and marcasite that are closely associated with chalcedony as hydrothermal cements of breccia ores. Replacement of auriferous pyrite by texturally-complex pyrite and marcasite is commonly observed in this deposit. However, the source of Au and fluid at the Daqiao deposit remain unknown. The role of silica in Au transport, controls on Au precipitation in sulfide, and Au remobilization during pyrite replacement have not been documented. These questions are explored via a combination of petrographic observations, cutting-edge elemental and isotopic analytical techniques, and laboratory experiments.

Trace element and sulfur isotope compositions of pyrite collected from hydrothermally altered Late Triassic granodiorite dykes within the Late Jurassic to Early Cretaceous Daqiao deposit analysed by laser ablation multi-collector inductively coupled plasma mass spectrometry (LA–MC–ICP–MS) are used to characterize the source of Au and fluid. Results show that dyke-hosted auriferous pyrite was sourced from underlying Paleozoic Ni- and Se-rich carbonaceous sedimentary rocks. In contrast, Au deposits in the EQO are genetically related to magmatism. We propose that Au mineralization of Late Jurassic to Early Cretaceous ages in the Qinling orogen was driven to some extent by the far-field effects of contemporary subduction of Paleo-Pacific plate. Differences in Au source and mineralization styles in the WQO and EQO are likely related to differences in their respective distances from the subduction front.

To investigate the role of silica in Au transport, experiments on Au solubility in amorphous SiO_2-bearing liquids including silica gel solution and colloidal silica suspension were performed in the laboratory. It is the first time that Au solubility experiments have been carried out in such two silica-bearing liquids. Preliminary results show that dissolved Au concentrations in the colloidal silica solutions are comparable to Au concentrations reported from other silica and ligand-rich geothermal fluids. Such concentrations are also similar to those proposed for the mineralizing fluids that formed giant Au deposits. We suggest that silica-bearing fluids are capable of stabilizing and transporting dissolved Au by some complexation in various hydrothermal Au systems in Earth’s crust.

The mechanisms that control Au incorporation into in zoned pyrite were investigated using a novel combination of nanoscale secondary ion mass spectrometry (NanoSIMS) and atom probe tomography (APT) on an Au-rich arsenian pyrite crystal from the Daqiao deposit. Results show that sharp transitions between the micro-scale compositionally distinct core-mantle-rim zones in pyrite formed as a consequence of episodic fluctuations in external fluid composition. However, micron- to atomic-scale distribution and zoning patterns of Au, As, and Cu were controlled by a combination of kinetic effects during pyrite crystallization, including crystal surface structure effects, heteroepitaxial Stranski-Krastanov growth, and diffusion-limited self-organization. Nano-scale heterogeneities in Au, As, and Cu

present as solid solution in pyrite suggest that interpretation of spikes on microbeam-derived depth-concentration profiles as metallic particles should be treated with caution.

Gold remobilization during replacement of pyrite was explored using a combination of LA–ICP–MS, NanoSIMS, and secondary ion mass spectrometry (SIMS). Results show that replacement of auriferous pyrite mainly proceeds via a two-step replacement via a dissolution and reprecipitation mechanism. During the replacement, Au, Te, Se, Zn, Co, Tl, Ni, W, and As were released from crystal lattice of parent pyrite. In subsequent replacement, marcasite enriched in Au, W, Tl, As, Sb, Ag, Se, and Zn relative to porous pyrite is thought to have formed via precipitation triggered by further oxidation and/or immediate reduction in threshold supersaturation. Dissolution of the impurity-rich pyrite and precipitation of new pyrite and marcasite could have occurred at low pH and at high concentrations of dissolved Fe^{2+} condition caused by partial oxidation of fluids. This oxidation is demonstrated by a general trend of decreasing $\delta^{34}S$ values caused by pressure fluctuations during hydraulic fracturing. This study emphasizes that the pressure-driven hydrothermal process plays a key role in the micron- to nano-scale redistribution of Au and other trace metals during episodic replacement of pyrite in brittle rheological zones from epizonal orogenic gold systems.

To summarize, this PhD project has explored different aspects of Au source, transport, precipitation, and remobilization from an orogenic gold deposit at Daqiao, China. These results show that orogenic Au deposits could be sourced from either metamorphic devolatilization or magmatism. Preliminary experiments suggest that silica has an important role in Au transport. The formation of Au zoning in pyrite was addressed via a combination of micron- to atomic-scale characterization. The complex Au zoning records both the changing external fluid composition and local fluid-crystal kinetic effects. Fluid-mediated mineral-scale Au remobilization formed as a consequence of pressure-driven hydrothermal process. The knowledge gained has increased our understanding of the formation of orogenic Au deposits and identified aspects for further study.

Acknowledgements

First of all, I would like to express my sincere gratitude and appreciation to my primary supervisor Assoc. Prof. Katy Evans. Thank you for hosting me as a joint PhD student and believing in me like nobody else. I will never forget your endless support and encouragement when I was experiencing challenges and difficulties at the beginning of my study at Curtin. Thank you for indefatigably passing you wisdom, logical and critical thinking to me, for always providing valuable perspectives on diverse aspects of my PhD project including sample preparation, analytical strategy development, experimental work, paper revision and publishing, and even job-seeking, and for your kindness and tolerance when I haven't performed well at work. Your guidance and support in my continuous improvement has been amazing – I can't thank you enough for leading me into such a wonderful science world!

I sincerely think my co-supervisors, Dr. Kirsten Rempel and Dr. Denis Fougerouse. Thank you, Kirsten, for your great dedication and patience while you taught me solution experimentation which I had never performed before. This interesting and valuable experimental experience has incented me to widen my research from a variety of perspectives. And thank you, Denis, not only because of your irreplaceable contribution to my PhD project, but also for your always insightful comments, hardworking, positive and passionate attitude that have helped and deeply affected me. Working with you, I have got a more clear understanding about how to critically define an important scientific problem, find a solution to it, and finally publish the high-quality results.

My sincere gratitude goes to Prof. Jianwei Li at China University of Geosciences (Wuhan), who is such a tremendous and influential supervisor for me. It is my great honor to have been a valuable member of this innovative and collaborative research group led by you. I would like to thank you because you continuously support my PhD study and research, because you always encourage and guide me when I have encountered difficulties, and because of your patience and immense knowledge. Your supervision of both my research career as well as on cultivating my personality have been invaluable. Your great enthusiasm and selfless dedication to the subject

research of *Mineral Deposits* have deeply influenced and inspired me to continuously improve myself to grow as a real and competent economic geologist.

I am really indebted to so many researchers who have helped me during my PhD project. These include Dr. Xiao-Ye Jin and Prof. Ross Large for LA–ICP–MS trace element analysis; Drs. Hugh O'Brien (GSF), Yann Lahaye (GSF), and A/Prof. Zhan-Ke Li for LA-MC-ICP-MS sulfur isotopic analysis; Drs. Louise A. Fisher (CSIRO) and Siyu Hu (CSIRO) for SXRF analysis; Drs. Christopher G. Ryan (CSIRO) and Mark A. Pearce (CSIRO) for SXRF data processing; Dr. Paul Guagliardo (UWA) for NanoSIMS analysis. I also thank Profs. Steven M. Reddy (Curtin) and David W. Saxey (Curtin) for their expertise during atom probe analysis; Drs. Lars Crede (Curtin) and Prok Vasilyev (Curtin) for their help during laboratory work; Dr. Ji-Xiang Sui (CUG), master Shi-Da Lu (CUG), and local geologists for the help during field investigation.

I would like to express my deepest gratitude to my family. Thank you for always reminding me to be a good man with honesty, kindness, diligence, and generosity, for tolerating me when I make mistakes, and for encouraging me when I'm stuck in unpleasant situations. Special thanks go to my girlfriend, a very kind-hearted girl always being there to back-up me and share all the ups and downs with me, even when we have been thousands of kilometers apart for two years.

Thanks are also due to funding agencies, including the National Natural Science Foundation of China (41772081, 41072057, and 41325007), the GPMR State Key Laboratory (grant MSFGPMR03), the Fundamental Research Funds for the Central Universities, China University of Geosciences in Wuhan (CUGCJ1711), the China Geological Survey (grant 1212011120570), and National Demonstration Center for Experimental Mineral Exploration Education at China University of Geosciences (Wuhan), Australian Science and Industry Endowment Fund (SIEF) and Australian Synchrotron, Chinese Scholarship Council/Curtin International Postgraduate Research Scholarship.

Finally, I want to reiterate that this PhD project could not have been performed well without enormous support from so many people, whether named above or not, thank you all!

List of publications included as a part of this thesis

This PhD thesis consists of one unpublished chapter describing the solution experimental work, and three research papers, which are published in international peer-reviewed journals at the time of submission of this thesis. The relationships between each chapter are clarified in the Introduction chapter, and further summarized in the synthesis chapter.

The formatting of each chapter within this thesis may appear to vary, and may differ to the published form based on the requirement and formatting guidelines of each individual journal and this thesis. Due to the nature of this thesis as a composite of peer-reviewed manuscripts there is some degree of repetition throughout.

The three research papers are listed below:

Chapter 2

Wu Y.F., Li J.W., Evans K., Fougerouse D., and Rempel K., 2019, Source and possible tectonic driver for Jurassic–Cretaceous gold deposits in the West Qinling Orogen, China. *Geoscience Frontiers*, 10 (1): 107–117 (Impact factor 4.256).

Chapter 4

Wu Y.F., Fougerouse D., Evans K., Reddy S.M., David W.S., Paul G., and Li J.W., 2019, Gold, arsenic, and copper zoning in pyrite: a record of fluid chemistry and growth kinetics. *Geology*, 47 (7): 641–644 (Impact factor 5.451).

Chapter 5

Wu Y.F., Evans K., Li J.W., Fougerouse D., Large R.R., and Guagliardo P., 2019, Metal remobilization and ore-fluid perturbation during episodic replacement of auriferous pyrite from an epizonal orogenic gold deposit. *Geochimica et Cosmochimica Acta*, 245 (15): 98–117 (Impact factor 4.609).

Table of contents

List of figures

List of tables

Chapter 1

Introduction

1.1 Ore-forming processes of orogenic gold deposits

Orogenic gold deposits, arguably the predominant gold mineralization type in accretionary and collisional orogenic belts from Archean to Tertiary times, are the source of >75% of gold recovered through history (Phillips, 2013). Two genetic models, including the crustal continuum model (e.g., Groves, 1993, 2003) and metamorphic devolatilization model (Phillips and Powell, 2009, 2010), have been proposed to explain the occurrence of orogenic gold deposits in metamorphic rocks ranging from granulite to sub-greenschist facies. The continuum model suggests that orogenic gold deposits can form throughout a 20–25 km vertical crustal profile at a wide temperature range from 750 ºC to 180 ºC (e.g., Groves et al., 1995). The metamorphic model notes that large metal-rich fluid volumes cannot migrate effectively through rocks hotter than ~650 ºC to deposit gold (Tomkins and Grundy, 2009). It is therefore proposed that gold mineralization hosted in high-grade (amphibolite to granulite) metamorphic rocks formed at greenschist facies conditions before metamorphism at the higher metamorphic grade (metamorphic model; Phillips and Powell, 2009, 2010).

On the basis of formation depth and metamorphic grade of host rock, the orogenic gold mineralization is commonly classified into three types: epizonal type hosted by prehnite-pumpellyite (< 6 km), mesozonal type hosted by greenschist (6–12 km), and hypozonal type hosted by amphibolite-granulite (> 12 km; Groves, 1993; Gebre-Mariam et al., 1995; Groves et al., 1998, 2003). Epizonal orogenic gold deposits differ from their deeper counterparts in host rocks, brittle structures with multiple brecciation, open-space filling vein textures, low-temperature minerals, influx of surface water, and much lower CO_2 concentration in ore fluids (Gebre-Mariam et al., 1995). These features are consistent with epithermal gold mineralization (Hedenquist et al., 2000), however, other aspects that include the metallogenic setting, genetic relationship with magmatism, alteration style, and

source of metals and ore fluids can be used for the identification of the two types of shallow-level gold mineralization (e.g., Gebre-Mariam et al., 1995; Hedenquist et al., 2000).In spite of the wealth of previous synthetic studies on orogenic gold mineralization (e.g., Groves, 1987, 1993, 1998, 2000, 2003, 2016, 2019; Groves and Santosh, 2015; Goldfarb et al., 1991, 2001, 2015; Kerrich and Cassidy, 1994; Phillips and Evans, 2004; Phillips and Powell, 2009, 2010; Tomkins, 2010, 2013a, b; Goldfarb and Santosh, 2014; Goldfarb and Groves, 2015), certain aspects of ore-forming processes, such as the gold source, gold transport in silica-rich metamorphic hydrothermal fluids, micron- to nano-scale processes responsible for gold deposition and incorporation into host sulfides, and for gold remobilization and re-enrichment during multiple fluid infiltration episodes, have been little explored and continue to be controversial. Previous studies on the aforementioned aspects and the main scientific problems remain to be resolved are briefly summarized as follows:

1.1.1 Source of fluid and gold

It has been suggested that orogenic gold deposits are the products of aqueous-carbonic fluids, which are typically characterized by 5–20 mol% CO_2, significant concentrations of CH_4 and/or N_2, common estimates of 0.01–0.36 mol% H_2S, a near neutral pH of 5.5, and salinities of 3–7 wt.% NaCl equiv., with Na>K>>Ca, Mg (e.g., Ridley and Diamond, 2000; Goldfarb and Groves, 2015). The source of ore fluids responsible for orogenic gold mineralization has been extensively studied. Most of the studies favor a metamorphic source, either from fluids released during metamorphism of deeper gold-hosting basinal and oceanic rock sequences (Goldfarb and Groves, 2015), or from devolatilization of the sediment wedge above a subducting slab (Groves and Santosh, 2015). Metamorphic desulfidation reactions can occur at a wide range of temperatures depending on the country rock assemblage (Goldfarb and Groves, 2015). For example, the pyrite to pyrrhotite conversion with consequent effective liberation of diverse trace metals from metamorphic schists can proceed in the temperature range of 400–575 °C (Ferry, 1981). Tomkins (2010) has further argued that release of sulfur during metamorphic reactions is accompanied by the breakdown of chlorite under lower-amphibolite facies metamorphic conditions.

It is commonly believed that gold is sourced from metamorphic sedimentary rocks at depths (e.g., Goldfarb et al., 2005). Such sediments contain elevated Au, As, and other ore-related trace elements accumulated via biogenic activities (Large et al., 2009, 2011, 2014, 2015; Tomkins, 2013b). Previous studies have shown that depletion of Au, As, and a suite of other trace metals in mid- to high-grade schists relative to unmetamorphosed protolith sediments in Otago and Alpine, New Zealand, was caused by the release of metals from sedimentary and/or diagenetic sulfides during regional metamorphism (Pitcairn et al., 2006). In a later case, the existence of ethane (C_2H_6) in fluid inclusions from Canadian and Ghanaian orogenic gold deposits has been used to support the proposal that gold and hydrothermal ore fluids were derived from deeply buried, carbonaceous pyritic sediments (Gaboury, 2013). Sediment-derived gold is particularly significant for the formation of Phanerozoic orogenic gold deposits that are commonly hosted in basins dominated by sedimentary turbidite sequences (Tomkins, 2013b).

In addition, it has been suggested that metamorphic devolatilization reactions within hydrated and carbonated mafic and ultramafic sequences during upper greenschist to lower amphibolite facies metamorphism can also provide significant gold and fluids for the formation of orogenic gold deposits (e.g., Powell et al., 1991). Thermodynamic modelling has shown that the large volumes of low salinity and H_2O–CO_2–H_2S-bearing hydrothermal fluids generated via metamorphic conversion of mafic and ultramafic successions on a cubic kilometer-scale can be effective in dissolving and transporting large amounts of gold (Phillips and Powell, 2010). Gold-hosting mafic and ultramafic sequences are the predominant gold source for the orogenic gold deposits hosted in Precambrian terranes that are dominated by ultramafic to felsic volcanic rocks underlying the gold mineralization (Groves and Santosh, 2015).

The orogenic gold deposits in Jiaodong gold province, eastern China are somewhat atypical in that formation is not consistent with the metamorphic model for orogenic gold deposits formed during greenschist- to amphibolite-facies metamorphism (Groves and Santosh, 2015). Gold deposits of ca. 120 Ma in age in this area are hosted by Late Jurassic granitoids formed by partial melting of thickened lower crust, so gold deposition cannot be attributed to regional greenschist- to amphibolite-facies metamorphism within the Precambrian wall rocks (e.g., Goldfarb and Santosh, 2014).

The formation of the Jiaodong orogenic gold deposits coincided with the subduction of the Palaeo-Pacific plate underneath the Eurasian plate, leading to the suggestion that the gold was derived from late-orogenic metamorphic devolatilization of stalled subduction slabs and oceanic sediments (Goldfarb and Santosh, 2014; Groves and Santosh, 2015).

Other studies have suggested that gold sourced from contemporaneous igneous rocks may contribute to the formation of orogenic gold deposits (e.g., Tan et al., 2012). However, Goldfarb and Groves (2015) demonstrated that there is no consistent temporal association between orogenic gold and magmatic activity, no specific type of magmatism consistently associated with orogenic gold mineralization, and no consistent zonation of trace metals around plutons. That orogenic mineralization is often gold-only also supports the idea that gold is of metamorphic origin because magmatic-hydrothermal fluids generally contain a wide range of other trace metals (Tomkins, 2010). The role of early-formed intrusions may instead be to serve as competent physical traps for later gold vein deposition (Kerrich, 1991).

In spite of these results, which show that the gold and fluids for orogenic gold deposits are mostly produced by metamorphism, relationships between orogenic gold mineralization and coeval magmatism in some metamorphic belts still remain ambiguous. For example, orogenic gold deposits in the Jiaodong gold province, China, are spatially and temporally associated with mafic dykes, which contain numerous magmatic sulfides with the same trace element association as the gold ores (Tan et al., 2012). These results, when combined with Pb isotopes, imply a genetic link between orogenic gold mineralization and mafic magmatism. Systematic dating and isotopic studies show that orogenic lode gold deposits at the margins of North China Craton formed coevally with extensive felsic to mafic magmatic activity, indicating a magmatic source of gold and ore fluids triggered by the thinning and destruction of the lithosphere beneath the craton (Li et al., 2012).

In the Phanerozoic Qinling Orogen, China, some of the numerous orogenic gold deposits that are widely distributed in the eastern and western part of the orogen are spatially and genetically associated with coeval magmatism (Mao et al., 2002, 2008, 2010). In Chapter 2 of this thesis, we investigate the source of gold and fluids for the world-class Daqiao orogenic gold deposit and then briefly explore how geotectonic

setting is linked to the style of orogenic gold mineralization in different parts within the Qinling orogen.

1.1.2 Gold transport in orogenic hydrothermal fluids

Given the elevated concentrations of CO_2 (5–20 mol%) and H_2S (0.01–0.36 mol%), neutral pH and low salinity (3–7 wt.% NaCl equiv.) in metamorphic fluids (Goldfarb and Groves, 2015), and the close assocaition of gold and sulfide minerals (e.g., pyrite, marcasite, and arsenopyrite), it is commonly believed that gold is predominantly transported in the form of sulfide complexes such as $AuHS^0$, $Au(HS)^{2-}$, and $Au_2(HS)_2S^{2-}$ (Seward, 1973; Phillips and Groves, 1983; Mikucki, 1998; Loucks and Mavrogenes, 1999), rather than as chloride complexes (e.g., $AuCl^{2-}$ and $AuCl_2H$; Gammons and Williams-Jones, 1995; Frank et al., 2002) in orogenic ore fluids. The consistently CO_2-rich composition of orogenic hydrothermal fluids has been suggested to be a critical factor that provides the near-neutral pH buffering required for high gold solubility as the gold-hydrosulfide complexes in fluids (Phillips and Evans, 2004).

However, it is also notable that gold occurs in intimate association with hydrothermal silica minerals such as quartz and chalcedony at all stages of orogenic gold deposition, indicating a potential relationship between dissolved silica and gold transported in orogenic ore fluids. A positive correlation between the intensity of silicification and gold depoition is common in other types of hydrothermal gold systems. For example, alternating colloform bands of fine-grained quartz and amorphous opal bands have been reported to contain abundant electrum in epithermal bonanza ores (100–1000 g/t Au; Saunders, 1990). Millimeter-scale gold dendrites in amorphous opal from hot-spring gold deposit have been suggested to form from a silica and gold-rich colloidal precursor (Sherlock and Lehrman, 1995). In Carlin-type deposits, hydrothermal silica commonly occurs as intense, multistage silicification that co-precipitates with disseminated fine-grained auriferous arsenian sulfides and sulfarsenides (Cline and Hofstra, 2000).

In spite of the long recognized intimate association of hydrothermal silica and gold, few previous studies have focused on the role of silica in complexation and transport of gold in hydrothermal fluids, with an exception of the experimental study by Fan et

al. (2001). These workers suggested that $AuH_3SiO_4^0$ is the dominant gold complex in both acidic Au-SiO_2-HCl-H_2O and alkaline Au-SiO_2-Na_2SiO_3-H_2O systems at 25–300°C and water-saturated vapor pressure. However, it is also notable that gold concentrations are much higher in the Cl-enriched runs than in those with low Cl concentrations (i.e., mean 81.6 ppb Au with 0.55 m Cl vs. 11.4 ppb Au with 0.003 m Cl; Fan et al., 2001). Due to the correlation between Cl and Au concentrations, the presence of AuCl2- and/or AuCl2H complexes cannot be ruled out (cf. Gammons and Williams-Jones, 1995; Frank et al., 2002). Thus it is impossible to precisely evaluate the role of silica in the solubility of gold from the Cl-bearing system studied by Fan et al. (2001).

In Chapter 3, I describe a preliminary experimental study that investigates gold solubility (i.e., total dissolved gold) in amorphous SiO_2-bearing liquids including silica gel solution and colloidal silica suspension. These results shed light on the complementary role of silica in the transport and stabilization of dissolved gold in silica-rich hydrothermal fluids during the formation of orogenic and other types of hydrothermal gold systems in the upper crust.

1.1.3 Gold incorporation into arsenian pyrite

It has been suggested that destabilization of gold-sulfide complexes and consequent deposition of gold are promoted by a decreasing activity of HS^- and fO_2 and/or a decreasing pH (e.g., see a review in Williams-Jones et al., 2009). These changes in external fluid conditions and the resultant decreasing gold solubility could be accomplished by a variety of fluid-rock processes such as fluid boiling, oxidation, cooling, and sulfidation of wall-rocks (Williams-Jones et al., 2009). Orogenic gold mineralization is characterized by intense hydrothermal pyritization and a close association between gold and arsenian sulfides (e.g., Hodkiewicz, 2009).

Previous trace element mapping techniques have shown that gold and other related trace metals are commonly heterogeneously distributed in arsenian pyrite and show complex zoning patterns. For example, elevated concentration of gold in pyrite occurs as oscillatory-zoned bands where arsenic is rich and iron is depleted relative to proximal gold-poor pyrite regions (e.g., Fleet et al., 1989; Fleet and Mumin, 1997). A study using LA–ICP–MS trace elemental mapping revealed that composite pyrite

from Australian Bendigo orogenic gold deposit has gold-rich zoning that consists of three closely associated and parallel micron-scale rims at the outermost margin of euhedral pyrite (Large et al., 2009). More recently, high spatial resolution nanoscale secondary ion mass spectrometry (NanoSIMS) elemental mapping analysis has revealed that gold together with arsenic and copper could occur as tens to hundreds of rhythmic zonations across a 20-micron pyrite rim from Carlin-type deposits, China (e.g., Yan et al., 2018).

However, the mechanism for the incorporation of complex-zoned gold into arsenian pyrite remains a subject of debate. It has been suggested that micron-scale irregular or cyclic gold zoning in pyrite records fluctuations in hydrothermal fluid composition (e.g., Barker et al., 2009; Deditius et al., 2009; Tardani et al., 2017). However, the results of recent atom probe studies highlight the importance of crystal growth kinetics and crystal-plastic deformation for sub-micron gold distribution in arsenopyrite and pyrite (Fougerouse et al., 2016, 2019).

In Chapter 4, I describe the application of NanoSIMS and atom probe tomography (APT) to characterize complex gold zoning in auriferous pyrite from the Daqiao orogenic gold deposit, China. These results provide new insights into the complementary roles of fluid and crystallization processes in the compositional zoning of arsenian pyrite that can be also applied to other mineral–fluid systems.

1.1.4 Gold remobilization during sulfide replacement

Hydrothermal dissolution of auriferous sulfides and subsequent reprecipitation and re-enrichment of gold and other trace metals in the replaced regions are ubiquitous in orogenic gold systems worldwide. For example, detailed textural observations and LA–ICP–MS trace element analysis show that visible gold in hydrothermally altered rims of pyrite and arsenopyrite from orogenic gold deposits in the Eastern Goldfields Province, Western Australia, formed via the remobilization of gold from the sulfide lattices during hydrothermal replacement processes (Morey et al., 2008). In another case, Cook et al. (2013) noted that gold liberated from sulfide lattice during the hydrothermal alteration of auriferous arsenopyrite grains from a Proterozoic Australian orogenic gold deposit at Tanami was re-precipitated and re-enriched either around the margins of the replaced arsenopyrite or within swarms of

crosscutting microfractures. In a recent study, Rottier et al. (2016) proposed that changing fluids conditions from epithermal systems in Peru, drove hydrothermal replacement of pyrrhotite and arsenopyrite by marcasite and pyrite via a dissolution-reprecipitation mechanism associated with systematic redistribution of a number of trace elements.

However, the details of the replacement behavior of marcasite, a polymorph of pyrite and a significant gold-hosting iron sulfide in many hydrothermal gold deposits (e.g., Arehart et al., 1993; Fleet and Mumin, 1997; Pals et al., 2003; Franchini et al., 2015; Rottier et al., 2016), and related metal redistribution process have not been documented. Marcasite formation is kinetically favored over pyrite, but it is metastable in many geological environments and thus tends to be highly reactive. Formation and preservation conditions for marcasite have been documented experimentally, with stability favored at low pH and low temperature (Murowchick and Barnes 1986; Murowchick, 1992; Qian et al., 2011).

In Chapter 5, I document details of textural relationships for auriferous pyrite replaced by pyrite and marcasite in gold ores from the Daqiao orogenic gold deposit, China. *In-situ* LA–ICP–MS trace element analysis and NanoSIMS element mapping combined with SIMS sulfur isotope analysis are used to reveal the redistribution of gold and other trace elements and related variations in sulfur isotopic composition.

1.2 Research area

1.2.1 Geological setting of Qinling Gold Province, China

The Phanerozoic WNW-ESE-striking Qinling Orogen extends for 2,500 km across the eastern margin of the Asian continent and formed during the continental collision between the North China Craton (NCC) and the South China Block (SCB) (Figure 1.1; Mattauer et al., 1985). This orogen records a multistage orogenic history from Middle Paleozoic to Early Mesozoic mainly involving prolonged subduction and closure of the Shangdan and Mianlue oceans (Meng and Zhang, 1999; Dong et al., 2011, 2013). Paleozoic orogenesis along the Shangdan suture was associated with Early Devonian northward subduction and closure of the Shangdan Ocean, and subsequent continental subduction beneath the North Qinling Terrain from Middle

Devonian to Early Triassic (Dong et al., 2013). Continued orogenesis in the Triassic, which completed formation of the Qinling Orogen, mainly resulted from northward subduction of the Mianlue Ocean and subsequent continental collision between the NCC and SCB (Zhang et al., 1995, 1996, 2001; Dong et al., 2011). The Qinling Orogen underwent post-orogenic intracontinental tectonism from the Middle Jurassic (Dong et al., 2011). The tectonic overprinting by large-scale southward overthrusting along regional faults occurred from the Late Jurassic to Cretaceous (Zhang et al., 2001; Dong et al., 2011, 2013).

The Qinling Orogen is divided into the East and West Qinling Orogens (EQO and WQO) by the northeast-trending Chengxian-Huixian-Fengxian Fault. The Qinling Orogen is dominated by Cambrian to Triassic marine sediments in the south, which are separated by the Shangdan suture from mélanges consisting of Neoproterozoic to early Paleozoic ophiolites and metasediments in the north (Dong et al. 2011). Granitoids in the WQO have progressively older emplacement ages from east (200–220 Ma) to west (240–250 Ma; e.g., Sun et al. 2002; Zeng et al. 2014; Dong and Santosh 2016). Late Jurassic to Early Cretaceous intrusions (150–125 Ma) are widely distributed in the EQO, but are rare in the WQO (Li et al. 2012a, b).

Numerous gold deposits have been discovered in the Qinling Orogen, making it the second largest gold province in China (Wu et al., 2018a). However, gold deposits in the EQO and WQO of different ages show different mineralization styles and relationships with magmatism. In the EQO, gold deposits of Late Jurassic to Early Cretaceous ages are best developed in the Neoarchean to early Paleoproterozoic metamorphic rocks in the Xiaoqinling district (Mao et al. 2008, 2010; Li et al. 2012a, b), with a small number of deposits in the southern marine sequences (Liu et al. 2015). Geochemical and isotopic dating results have shown that gold deposits in the EQO are genetically associated with the widespread contemporaneous magmatism (ca. 150–125 Ma; Mao et al. 2008, 2010; Li et al. 2012a, b).

In contrast, gold deposits in the WQO formed during two main pulses (i.e., Late Triassic to Early Jurassic, and Late Jurassic to Early Cretaceous; Wu et al., 2018b). The WQO is divided into northern and southern belts by the regional Hezuo-Lintan-Liangdang Fault. Gold deposits in the northern belt are mainly hosted by Devonian greenschist facies flysch rocks, and predominantly occur as quartz stockworks and veinlets along major ductile-brittle shear zones or their secondary

structures. Typical features are visible gold, carbonic ore fluids, and a lack of low temperature sulfide mineral assemblage. These deposits are commonly considered to be orogenic (Mao et al., 2002; Chen et al., 2004; Goldfarb et al., 2014).

Gold mineralization in the southern belt is mostly hosted by low-grade or unmetamorphosed Triassic turbidite sequences, with a minor proportion of gold in Early Cambrian and Devonian carbonaceous clastic rocks (Li and Peters, 1998). Gold mineralization in this belt is structurally controlled and associated with a suite of elements typical of lower temperature gold systems (Au–Hg–Sb–As–Tl–W±U) with invisible gold present in arsenic sulfides (Mao et al., 2002). Although some gold deposits are partly hosted by dikes or in the contact metamorphic zones, most gold deposits are not spatially associated with plutons (Chen et al., 2004). These deposits have been described and mined for decades, but there is no consensus on the sources of ore fluids and metals, or on the ore-forming processes (e.g. Mao et al., 2002; Zhou et al., 2002; Chen et al., 2004; Chen and Santosh, 2014).

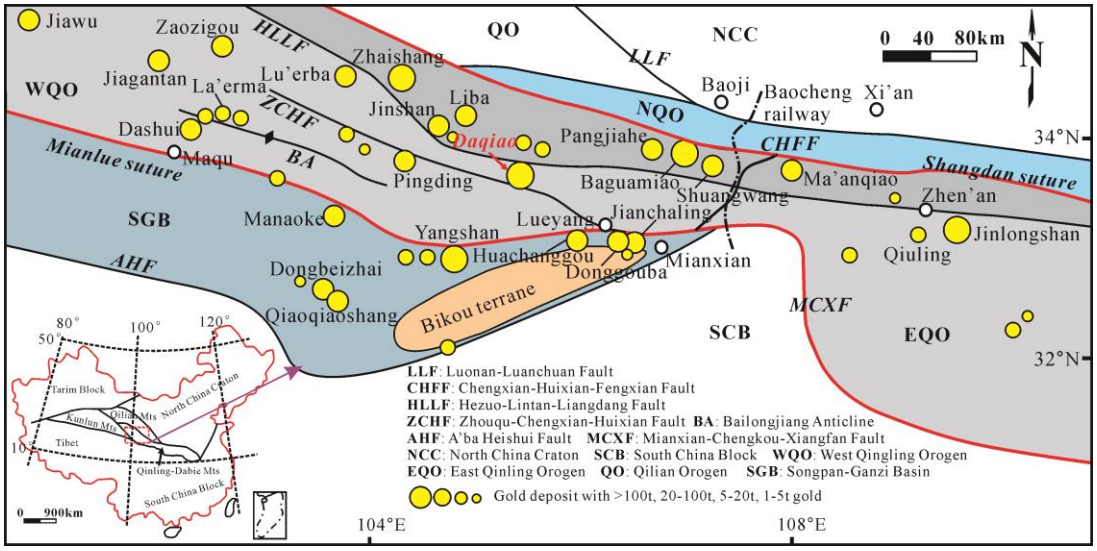

Figure 1.1 A simplified map showing tectonic division of the Qinling Orogen. Major faults, gold deposits and the location of Daqiao are also shown (modified from Liu et al., 2015).

1.2.2 Previous studies on Daqiao gold deposit

The Daqiao gold deposit was discovered in 2006, and is one of the largest gold deposits in the WQO with a total proven reserve of over 105 t Au (averaging 3–4 g/t; Wu et al., 2018a). It is located on the southern part of the regional deep fault (HLLF) that separates the northern and southern gold deposits (Figure 1.1). The Daqiao gold

mineralization is hosted in middle Triassic weakly-metamorphosed carbonaceous turbidites and controlled by NE-trending folds and a series of higher order thrust faults (Figure 1.2; You and Zhang, 2009). The turbidite sequences consist of siltstone, siliceous, calcareous and pelitic slates, with lesser pyritic carbonaceous slates and thin to thick-bedded limestone. In the mine, a number of granodiorite and minor diorite porphyry dikes are altered by variable degrees of hydrothermal alteration and occasionally weak gold mineralization. These dykes are spatially associated with the gold orebodies. The orebodies are dominated by a suite of intensely silicified auriferous tectonic breccias and overprinting hydraulic breccias (Wu et al., 2018a). Hydrothermal alteration at Daqiao deposit mainly consists of multistage silicification, sulfidation, sericitization, and carbonatization.

Preliminary studies of fluid inclusions suggest that ore fluids were low salinity (<10 wt% NaCl equiv) and temperature (100 to 240 °C), and the gold was deposited at less than 1 km depth (Xu et al., 2015). Based on the bulk silica and lead isotope results of silicified breccia and pyrite separates, Liu et al. (2017) have suggested that gold and other metals were derived from a mixtures of magma and strata, and that the Daqiao deposit was classified as a hot-spring type. Zhang et al. (2018) described the deposit and ore geology, in particular, the features of distinct auriferous breccias, and proposed that auriferous breccias formed by the overprinting of early-formed tectonic breccias by hydraulic breccias. Based on a detailed characterization of the ore-forming stages, paragenesis of sulfides, and trace elemental and sulfur isotopic compositions of sulfides, Wu et al. (2018a) proposed that gold mainly occurs as invisible gold, held as solid solution in rapidly crystallized pyrite and marcasite showing framboidal, colloform, and zoned textures. Therefore, their favored interpretation is that the Daqiao gold deposit should be classified as an epizonal orogenic deposit type. Recent sericite $^{40}Ar/^{39}Ar$ dating and LA–ICP–MS zircon U–Pb dating results show that the Daqiao gold deposit formed between 151–127 Ma, much later than the emplacement (215–188 Ma) of intermediate to silicic dykes in the mine (Wu et al., 2018b).

In spite of these new results, certain aspects such as the intimate association of intense silicification and gold deposition, the incorporation of invisible gold into fine-grained sulfides with distinctive and complex textures, and gold redistribution during the multistage hydrothermal fluid infiltration episodes, have not been

documented.

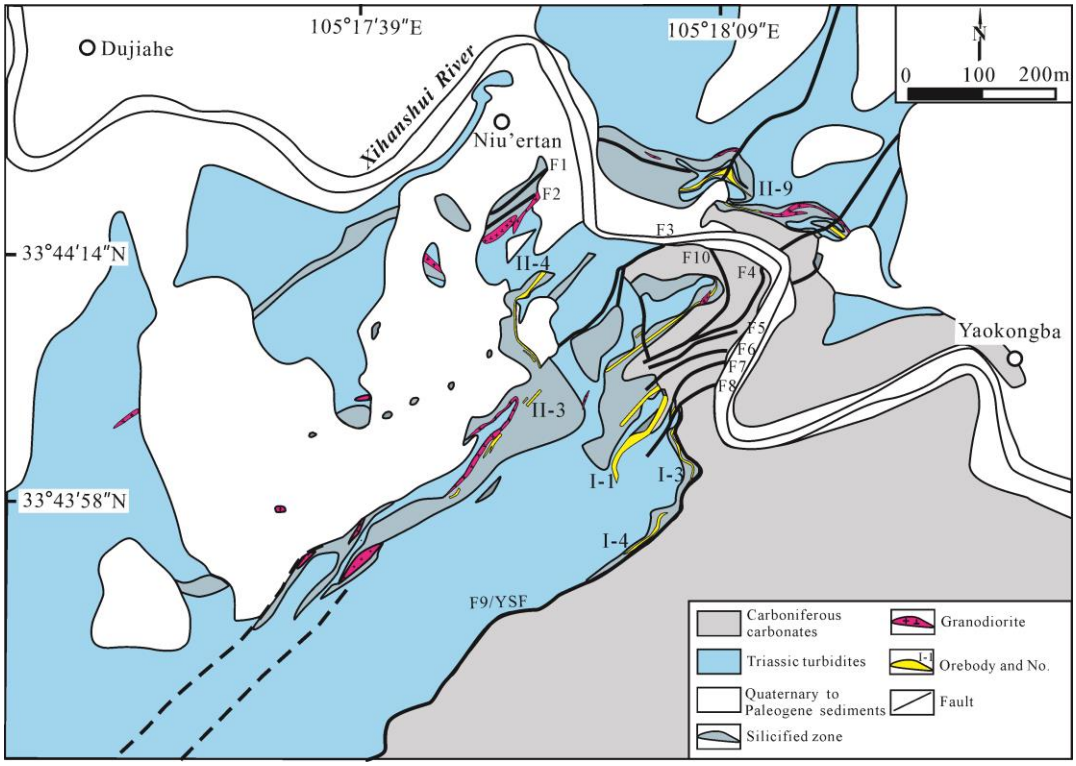

Figure 1.2 Geological map of Daqiao orogenic gold deposit (Modified after You and Zhang, 2009)

1.3 Objectives of this thesis

This PhD project focuses on the gold source and explores new perspectives relating to gold deportment in orogenic hydrothermal fluids, such as gold transport in silica-rich fluids, micon- to nano-scale processes responsible for gold deposition in arsenian pyrite, and fluid-mediated gold remobilization and re-enrichment, during the formation of the word-class Daqiao orogenic gold deposit, China. These aims are achieved via a combination of detailed petrographic observation, solution experimentation, and use of a variety of cutting-edge analytical instrumentation.

The four specific objectives are to:

(1) Identify the gold source of the Daqiao orogenic gold deposit, with a particular emphasis on the comparison of gold source for gold mineralization within the eastern and western parts of the Qinling Orogen.

(2) Experimentally evaluate the gold solubility in silica-bearing liquids and the possibility that gold can be stablized and transported by dissolved silica in fluids.

(3) Characterize the micron- to nano-scale complex gold zoning patterns in arsenian pyrite, and understand the mechanisms of gold deposition and incorporation into pyrite.

(4) Characterize the complex micron-scale processes of hydrothermal replacement of auriferous pyrite, and gold remobolization and re-enrichment during the development of the replacement.

1.4 Research methods

1.4.1 Field work

A total of four-months was spent in the field at the Daqiao mine and surrouding areas in the Longnan city, Gansu province, China. This work took place in 2014 and 2015. The main task was to record regional-scale geological observations, document deposit-scale hydrothermal alteration and mineralization features, and collect samples. A total of 300 samples were collected from outcrops, open pits, boreholes, and underground tunnels, including different types of gold ores, wall rocks of various degrees of hydrothermal alteration and mineralization, and granodiorite dykes.

1.4.2 Laboratory analysis

Preliminary laboratory processing including rock cutting, polishing, and crushing, and preparation of sections of various thicknesses (20–200 μm) were conducted in the sample preparation laboratory, School of Earth Resources, China University of Geosciences (Wuhan). Textural observations of thin and thick sections were undertaken using a Nikon optical transmitted and reflected light microscopy.

Scanning electron microscopy (SEM) and energy-dispersive X-ray spectroscopy (EDS) observations were made using a Quanta 450 field emission SEM equipped with a SDD Inca X-Max 50 at the State Key Laboratory of Geological Processes and Mineral Resources (GPMR), China University of Geosciences (Wuhan).

Laser ablation inductively coupled plasma mass spectrometry (LA–ICP–MS) analysis of pyrite and marcasite was conducted using a Photon Machines Analyte G2 LA system (193 nm, 4 ns excimer laser) attached to a PerkinElmer DRC-e ICP-MS, at the U.S. Geological Survey, Denver Federal Center, and using a New Wave

213-nm solid-state laser microprobe coupled to an Agilent 4500 quadrupole ICP–MS, at CODES, University of Tasmania.

LA-MC-ICP-MS sulfur isotope analysis of pyrite and marcasite was conducted using a Nu Plasma HR multicollector ICP-MS together with a Photon Machine Analyte G2 laser system, at the Geological Survey of Finland (GSF), Espoo, Finland.

Secondary ion mass spectrometry (SIMS) sulfur isotope analysis of pyrite and marcasite was performed using the Cameca IMS-1280 at the Institute of Geology and Geophysics (Beijing), Chinese Academy of Sciences.

Nanoscale secondary ion mass spectrometry (NanoSIMS) analysis was performed at the Centre for Microscopy, Characterisation and Analysis (CMCA) at the University of Western Australia (UWA), using a CAMECA NanoSIMS 50L.

Atom probe tomography (APT) analysis of pyrite was conducted at the Advanced Resource Characterization Facility at Curtin University. The specimens were prepared using a Tescan Lyra3 Focused Ion Beam Scanning Electron Microscope (FIB–SEM) with a Ga^+ ion source, employing standard lift-out techniques. A Cameca LEAP 4000X HR in laser assisted mode was employed for analysis.

Experiments on gold solubility in silica-bearing fluids were conducted at the Curtin Experimental Geochemistry (CEG) facility at the School of Earth and Planetary Sciences, Curtin University. The concentrations of gold and silica were conducted at the LabWest Minerals Analysis Pty Ltd in Perth using a Perkin Elmer Nexion 300 inductively coupled plasma mass spectrometer (ICP–MS).

1.5 Thesis structure

This PhD thesis begins with this introduction (**Chapter 1**) that reviews the ore-forming processes of orogenic gold deposits, and focusing on, the gold source, transport, gold incorporation into sulfides, gold remobilization and re-enrichment processes, the geological setting for mineralization in the Qinling Orogen, the deposit geology of the Daqiao gold deposit in the West Qinling Orogen, and the scientific questions that this PhD project aims to address.

In **Chapter 2**, I discuss the source of the gold and fluids that formed the Daqiao gold

deposit, and the possible tectonic drivers that led to the differences in gold source and mineralization styles in the western and eastern parts of the Qinling Orogen.

In **Chapter 3**, preliminary solution experiments on gold solubility in silica-bearing liquids and the possibility of stabilization of dissolved gold by silica species are described.

In **Chapter 4**, complex gold zoning patterns in arsenian pyrite are documented, and new hypotheses to account for gold incorporation into pyrite are proposed.

In **Chapter 5**, I describe multiple phases of hydrothermal replacement of auriferous pyrite and consequent gold redistribution and re-enrichment. These processes were triggered by pressure-driven fluid fluactuations.

Chapter 6 presents a summary and synthesis of the thesis.

1.6 References

Arehart, G. B., Chryssoulis, S. L., Kesler, S. E., 1993. Gold and arsenic in iron sulfides from sediment-hosted disseminated gold deposits; implications for depositional processes. Economic geology 88, 171–185.

Barker, S., Hickey, K., Cline, J., Dipple, G., Kilburn, M., Vaughan, J., Longo, A., 2009. Uncloaking invisible Au: use of nanoSIMS to evaluate Au, trace elements and sulfur isotopes in pyrite from Carlin-type Au deposits. Economic Geology 104, 897–904.

Chen, Y.J., Zhang, J., Zhang, F.X., Franco, P., and Li, C., 2004. Carlin and Carlin-like gold deposits in the Western Qinling Mountains and their metallogenic time, tectonic setting and model. Geological Review 50, 134–152.

Chen, Y.J., Santosh, M., 2014. Triassic tectonics and mineral systems in the Qinling Orogen, central China: Geological Journal 49, 338–358.

Cline, J.S., Hofstra, A.A., 2000. Ore-fluid evolution at the Getchell Carlin-type gold deposit, Nevada, USA. European Journal of Mineralogy 12, 195–212.

Cook, N. J., Ciobanu, C. L., Meria, D., Silcock, D., Wade, B., 2013. Arsenopyrite-pyrite association in an orogenic gold ore: Tracing mineralization history from textures and trace elements. Economic Geology 108, 1273–1283.

Deditius, A.P., Utsunomiya, S., Ewing, R.C., Chryssoulis, S.L., Venter, D., Kesler, S.E., 2009. Decoupled geochemical behavior of As and Cu in hydrothermal systems. Geology 37, 707–710.

Dong, Y.P., Zhang, G.W., Neubauer, F., Liu, X.M., Genser, J., Hauzenberger, C., 2011. Tectonic evolution of the Qinling orogen, China: Review and synthesis. Journal of Asian Earth Sciences 41, 213–237.

Dong, Y.P., Liu, X.M., Neubauer, F., Zhang, G.W., Tao, N., Zhang, Y.G., Zhang, X.N., Li, W., 2013. Timing of Paleozoic amalgamation between the North China and South China Blocks: Evidence from detrital zircon U-Pb ages. Tectonophysics 586, 173–191.

Dong, Y.P., Santosh, M., 2016, Tectonic architecture and multiple orogeny of the Qinling orogenic belt, central China. Gondwana Research 29, 1–40.

Fan, W., Wang, S., Tian, Y., Chen, Z.X., 2001. Complexation of Si in hydrothermal systems. Chinese Journal of Geochemistry 20, 201-209.

Ferry J. M., 1981. Petrology of graphitic sulfide-rich schists from south-central Maine: an example of desulfidation during regional prograde metamorphism. American Mineralogist 66, 908–931.

Fleet M. E., MacLean P. J., and Barbier J., 1989. Oscillatory-zoned As-bearing pyrite from strata-bound and stratiform gold deposits; an indicator of ore fluid evolution. Econ. Geol. Monog 6, 356–362.

Fleet, M. E., Mumin, A. H., 1997. Gold-bearing arsenian pyrite and marcasite and arsenopyrite from Carlin Trend gold deposits and laboratory synthesis. American Mineralogist 82, 182-193.

Fougerouse, D., Reddy, S.M., Saxey, D.W., Rickard, W.D., Van, Riessen. A., and Micklethwaite, S., 2016. Nanoscale Au clusters in arsenopyrite controlled by growth rate not concentration: Evidence from atom probe microscopy. American Mineralogist 101, 1916–1919.

Fougerouse, D., Reddy, S.M., Kirkland, C.L., Saxey, D.W., Rickard, W.D., Hough, R.M., 2019. Time-resolved, defect-hosted, trace element mobility in deformed Witwatersrand pyrite. Geoscience Frontiers 10, 55–63.

Franchini, M., McFarlane, C., Maydagán, L., Reich, M., Lentz, D. R., Meinert, L., Bouhier, V., 2015. Trace metals in pyrite and marcasite from the Agua Rica porphyry-high sulfidation epithermal deposit, Catamarca, Argentina: Textural features and metal zoning at the porphyry to epithermal transition. Ore Geology Reviews, 66, 366–387.

Frank M.R., Candela P.A., Piccoli P.M., Glascock M.D., 2002. Gold solubility, speciation and partitioning as a function of HCl in the brine-silicate, melt-metallic gold system at 800°C and 100 MPa. Geochimica et Cosmochimica Acta 66, 3719-3732.

Gaboury, D., 2013. Does gold in orogenic deposits come from pyrite in deeply buried carbon-rich sediments?: Insight from volatiles in fluid inclusions. Geology 41, 1207-1210.

Gammons C. H. Williams-Jones A. E., 1995. The solubility of Au-Ag alloy AgCl in HCl/NaCl solutions at 300°C: New data on the stability of Au (I) chloride complexes in hydrothermal solutions. Geochimica et Cosmochimica Acta 59, 3453-3468.

Goldfarb, R.J., Snee, L.W., Miller, L.D., Newberry, R.J., 1991. Rapid dewatering of the crust deduced from ages of mesothermal gold deposits. Nature 354, 296-298.

Goldfarb, R.J., Phillips, G.N., Nokleberg,W.J., 1998. Tectonic setting of synorogenic gold deposits of the Pacific Rim. Ore Geology Reviews 13, 185-218.

Goldfarb, R.J., Groves, D.I., Gardoll, S., 2001. Orogenic gold and geologic time: a global synthesis. Ore Geology Reviews 18, 1-75.

Goldfarb, R.J., Baker, T., Dubé, B., Groves, D.I., Hart, C.J.R., Gosselin, P., 2005. Distribution, character, and genesis of gold deposits in metamorphic terranes. Economic Geology 100th Anniversary, 407-450.

Goldfarb, R.J., Taylor, R.D., Collins, G.S., Goryachev, N.A., Orlandini, O.F., 2014. Phanerozoic continental growth and gold metallogeny of Asia. Gondwana Research 25, 48-102.

Goldfarb, R.J., Santosh, M., 2014. The dilemma of the Jiaodong gold deposits: are they unique? Geoscience Frontiers 5, 139-153.

Goldfarb, R.J., Groves, D.I., 2015. Orogenic gold: common or evolving fluid and metal sources through time. Lithos 233, 2-26.

Groves, D.I., Phillips, G.N., Ho, S.E., Houstoun, S.M., Standing, C.A., 1987. Craton-scale distribution of Archaean greenstone gold deposits: predictive capacity of the metamorphic model. Economic Geology 82, 2045-2058.

Groves, D.I., 1993. The crustal continuum model for late-Archaean lode-gold deposits of the Yilgarn Block, Western Australia. Mineralium Deposita 28, 366-374.

Groves, D. I., Ridley, J. R., Bloem, E. M. J., Gebre-Mariam, M., Hagemann, S. G., Hronsky, J. M. A., McCuaig, T. C., 1995. Lode-gold deposits of the Yilgarn block: products of Late Archaean crustal-scale overpressured hydrothermal systems. Geological Society, London, Special Publications 95, 155-172.

Groves, D.I., Goldfarb, R.J., Gebre-Mariam, M., Hagemann, S.G., Robert, F., 1998. Orogenic gold deposits: a proposed classifi cation in the context of their crustal distribution and relationship to other gold deposit types. Ore Geology Reviews 13, 7-27.

Groves, D.I., Goldfarb, R.J., Knox-Robinson, C.M., Ojala, J., Gardoll, S., Yun, G.Y., Holyland, P., 2000. Late-kinematic timing of orogenic gold deposits and significance for computer- based exploration techniques with emphasis on the

Yilgarn Block, Western Australia. Ore Geology Reviews 17, 1-38.

Groves, D. I., Goldfarb, R. J., Robert, F., Hart, C. J., 2003. Gold deposits in metamorphic belts: overview of current understanding, outstanding problems, future research, and exploration significance. Economic geology 98, 1-29.

Groves, D.I., Santosh, M., 2015. The giant Jiaodong gold province: the key to a unified model for orogenic gold deposits. Geoscience Frontiers 7, 409-2417.

Groves, D. I., Goldfarb, R. J., Santosh, M., 2016. The conjunction of factors that lead to formation of giant gold provinces and deposits in non-arc settings. Geoscience Frontiers 7, 303-314.

Groves, D. I., Santosh, M., Goldfarb, R. J., Zhang, L., 2019. Structural geometry of orogenic gold deposits: Implications for exploration of world-class and giant deposits. Geoscience Frontiers 9, 1163-1177.

Hodkiewicz, P.F., Groves, D.I., Davidson, G.J., Weinberg, R.F., Hagemann, S.G., 2009. Influence of structural setting on sulphur isotopes in Archean orogenic gold deposits, Eastern Goldfields Province, Yilgarn, Western Australia. Mineralium Deposita 44, 129-150.

Kerrich, R., 1991. Mesothermal gold deposits: a critique of genetic hypotheses. In: Robert, F., Sheahan, P.A., Green, S.B. (Eds.), Greenstone Gold and Crustal Evolution: Geological Association of Canada, NUNA Conference Volume, pp. 13-31.

Kerrich, R., Cassidy, K. F., 1994. Temporal relationships of lode gold mineralization to accretion, magmatism, metamorphism and deformation—Archean to present: A review. Ore Geology Reviews 9, 263-310.

Large, R.R., Danyushevsky, L., Hollit, C., Maslennikov, V., Meffre, S., Gilbert, S., Bull, S., Scott, R., Emsbo, P., Thomas, H., Singh, B., Foster, J., 2009. Gold and trace element zonation in pyrite using a laser imaging technique: Implications for the timing of gold in orogenic and carlin-style sedimenthosted deposits: Economic Geology and the Bulletin of the Society of Economic Geologists 104, 635-668.

Large, R.R., Bull, S.W., and Maslennikov, V., 2011. A carbonaceous sedimentary source-rock model for Carlin-type and orogenic gold deposits: Economic Geology and the Bulletin of the Society of Economic Geologists 106, 331-358.

Large, R.R., Halpin, J.A., Danyushevsky, L.V., Maslennikov, V.V., Bull, S.W., Long,

J.A., Gregory, D.D., Lounejeva, E., Lyons, T.W., Sack, P.J., McGoldrick, P.J., Calver, C.R., 2014. Trace element content of sedimentary pyrite as a new proxy for deep-time ocean-atmosphere evolution. Earth and Planetary Science Letters 389, 209-220.

Large, R.R., Gregory, D.D., Steadman, J.A., Tomkins, A.G., Lounejeva, E., Danyushevsky, L.V., Halpin, J.A., Maslennikov, V.V., Sack, P.J., Mukherjee, I., Berry, R., Hickman, A., 2015. Gold in the oceans through time. Earth and Planetary Science Letters 428, 139-150.

Li, J. W., Li, Z. K., Zhou, M. F., Chen, L., Bi, S. J., Deng, X. D., Qiu, H.N., Cohen, B., Zhao, X. F., 2012a. The Early Cretaceous Yangzhaiyu lode gold deposit, North China Craton: a link between craton reactivation and gold veining. Economic Geology 107, 43-79.

Li, J.W., Bi, S.J., Selby, D., Chen, L., Vasconcelos, P., Thiede, D., Zhou, M.F., Zhao, X.F., Li, Z.K., Qiu, H.N., 2012b. Giant Mesozoic gold provinces related to the destruction of the North China craton. Earth and Planetary Science Letters 349, 26-37.

Liu, J.J., Dai, H.Z., Zhai, D.G., Wang, J.P., Wang, Y.H., Yang, L.B., Mao, G.J., Liu, X.H., Liao, Y.F., Yu, C., Li, Q.Z., 2015. Geological and geochemical characteristics and formation mechanisms of the Zhaishang Carlin-like type gold deposit, western Qinling Mountains, China. Ore Geology Reviews 64, 273-298.

Liu, Y. H., Li, Z., Zhou, S., Han, Y. X., Li, H., Li, X., Zhou, S. F., 2015. Geological characteristics, ore-forming ages and geological significance of Donggou-Jinlongshan gold deposit, South Qinling belt. Earth Science Frontiers, 22, 1-13.

Liu, Y., Han, Y., Wei, J., Teng, F., Tian, R., Gao, Z., 2018. Geological and geochemical characteristics and prospecting potential of the Daqiao hot spring-type gold deposit in the west Qinling Orogen. Geological Journal 53, 136-146.

Loucks, R. R., Mavrogenes, J. A., 1999. Gold solubility in supercritical hydrothermal brines measured in synthetic fluid inclusions. Science 284, 2159-2163.

Mao, J.W., Qiu, Y.M., Goldfarb, R.J., Zhang, Z.C., Garwin, S., and Fengshou, R., 2002. Geology, distribution, and classification of gold deposits in the western Qinling belt, central China: Mineralium Deposita 37, 352-377.

Mao, J. W., Xie, G. Q., Bierlein, F., Qü, W. J., Du, A. D., Ye, H. S., Pirajno, F., Li, H.M., Guo, B.J., Li, Y.F., Yang, Z. Q., 2008. Tectonic implications from Re-Os dating of Mesozoic molybdenum deposits in the East Qinling-Dabie orogenic belt. Geochimica et Cosmochimica Acta 72, 4607-4626.

Mao, J. W., Xie, G. Q., Pirajno, F., Ye, H. S., Wang, Y. B., Li, Y. F., Xiang, J.F., Zhao, H. J., 2010. Late Jurassic-Early Cretaceous granitoid magmatism in Eastern Qinling, central-eastern China: SHRIMP zircon U-Pb ages and tectonic implications. Australian Journal of Earth Sciences 57, 51-78.

Mattauer, M., Matte, P., Malavieille, J., Tapponnier, P., Maluski, H., Qin, X.Z., Lun, L.Y., Qin, T. Y., 1985. Tectonics of Qinling Belt: Build-up and evolution of Eastern Asia. Nature 317, 496-500.

Meng, Q.R., Zhang, G.W., 1999. Timing of collision of the North and South China blocks: Controversy and reconciliation. Geology 27, 123-126.

Mikucki, E. J., 1998. Hydrothermal transport and depositional processes in Archean lode-gold systems: A review. Ore geology reviews 13, 307-321.

Morey, A. A., Tomkins, A. G., Bierlein, F. P., Weinberg, R. F., Davidson, G. J., 2008. Bimodal distribution of gold in pyrite and arsenopyrite: Examples from the Archean Boorara and Bardoc shear systems, Yilgarn craton, Western Australia. Economic Geology 103, 599-614.

Murowchick, J. B., Barnes, H. L., 1986. Marcasite precipitation from hydrothermal solutions. Geochimica et Cosmochimica Acta 50, 2615-2629.

Murowchick, J. B., 1992. Marcasite inversion and the petrographic determination of pyrite ancestry. Economic Geology 87, 1141-1152.

Pals, D. W., Spry, P. G., Chryssoulis, S., 2003. Invisible gold and tellurium in arsenic-rich pyrite from the Emperor gold deposit, Fiji: implications for gold distribution and deposition. Economic Geology 98, 479-493.

Phillips, G. N., Groves, D. I., 1983. The nature of Archaean gold-bearing fluids as deduced from gold deposits of Western Australia. Journal of the Geological Society of Australia 30, 25-39.

Phillips, G.N., Australian and global setting for gold in 2013, in Proceedings World Gold 2013, Brisbane, Australia, 26-29 September, 2013. The Australian Institute of Mining and Metallurgy, 15-21.

Phillips, G.N., Evans, K.A., 2004. Role of CO_2 in the formation of gold deposits. Nature 429, 860-863.

Phillips, G.N., Powell, R., 2009. Formation of gold deposits: Review and evaluation of the continuum model. Earth-Science Reviews 94, 1-21.

Phillips, G.N., Powell, R., 2010. Formation of gold deposits: A metamorphic devolatilization model: Journal of Metamorphic Geology 28, 689-718.

Pitcairn, I.K., Teagle, D.A.H., Craw, D., Olivo, G.R., Kerrich, R., Brewer, T.S., 2006. Sources of metals and fluids in orogenic gold deposits: Insights from the Otago and Alpine Schists, New Zealand. Economic Geology and the Bulletin of the Society of Economic Geologists 101, 1525-1546.

Powell, R., Will, T.M., Phillips, G.N., 1991. Metamorphism in Archaean greenstone belts: Calculated fluid compositions and implications for gold mineralization. Journal of Metamorphic Geology 9, 141-150.

Qian, G., Xia, F., Brugger, J., Skinner, W. M., Bei, J., Chen, G., Pring, A., 2011. Replacement of pyrrhotite by pyrite and marcasite under hydrothermal conditions up to 220 C: An experimental study of reaction textures and mechanisms. American Mineralogist 96, 1878-1893.

Ridley, J.R., Diamond, L.W., 2000. Fluid chemistry of orogenic lode gold deposits and implications for genetic models. Reviews in Economic Geology 13, 146-162.

Rottier, B., Kouzmanov, K., Wälle, M., Bendezú, R., Fontboté, L., 2016. Sulfide replacement processes revealed by textural and LA–ICP–MS trace element analyses: example from the early mineralization stages at Cerro de Pasco, Peru. Economic Geology 111, 1347-1367.

Saunders, J.A., 1990. Colloidal transport of gold and silica in epithermal precious-metal systems: Evidence from the Sleeper deposit, Nevada. Geology 18, 757-760.

Seward, T. M., 1973. Thio complexes of gold and the transport of gold in hydrothermal ore solutions. Geochimica et Cosmochimica Acta 37, 379-399.

Sherlock, R.L., Lehrman, N.J., 1995. Occurrences of dendritic gold at the McLaughlin Mine hot-spring gold deposit. Mineralium Deposita 30, 323-327.

Simmons, S.F., Brown, K.L., 2006. Gold in magmatic hydrothermal solutions and the rapid formation of a giant ore deposit. Science 314, 288-291.

Simmons, S.F., Brown, K.L., 2007. The flux of gold and related metals through a volcanic arc, Taupo Volcanic Zone, New Zealand. Geology 35, 1099-1102.

Sun, W.D., Li, S.G., Chen, Y.D., Li, Y.J., 2002, Timing of synorogenic granitoids in

the South Qinling, central China: Constraints on the evolution of the Qinling-Dabie orogenic belt. Journal of Geology 110, 457-468.

Tan, J., Wei, J., Audétat, A., Pettke, T., 2012. Source of metals in the Guocheng gold deposit, Jiaodong Peninsula, North China Craton: link to early Cretaceous mafic magmatism originating from Paleoproterozoic metasomatized lithospheric mantle. Ore Geology Reviews 48, 70-87.

Tardani, D., Reich, M., Deditius, A.P., Chryssoulis, S., Sánchez-Alfaro, P., Wrage, J., Roberts, M.P., 2017. Copper-arsenic decoupling in an active geothermal system: A link between pyrite and fluid composition. Geochimica et Cosmochimica Acta 204, 179-204.

Tomkins, A.G. Grundy, C., 2009. Upper temperature limits of orogenic gold deposit formation: constraints from the granulite-hosted Griffin's Find Deposit, Yilgarn Craton. Economic Geology 104, 669-685.

Tomkins, A.G., 2010. Windows of metamorphic sulfur liberation in the crust: Implications for gold deposit genesis. Geochimica et Cosmochimica Acta 74, 3246-3259.

Tomkins, A. G., 2013. On the source of orogenic gold. Geology 41, 1255-1256.

Tomkins, A.G., 2013b. A biogeochemical influence on the secular distribution of orogenic gold. Economic Geology and the Bulletin of the Society of Economic Geologists 108, 193-197.

Tomkins, A.G., Grundy, C., 2009. Upper Temperature Limits of Orogenic Gold Deposit Formation: Constraints from the Granulite-Hosted Griffin's Find Deposit, Yilgarn Craton: Economic Geology and the Bulletin of the Society of Economic Geologists 104, 669-685.

Williams-Jones, A.E., Bowell, R.J., Migdisov, A.A., 2009. Gold in solution: Elements 5, 281-287.

Wu Y.F., Li J.W., Evans K., Koenig A.E., Li Z.K., O'Brien H., Lahaye Y., Rempel K., Hu S.Y., Zhang Z.P., and Yu J.P., 2018a. Ore-Forming Processes of the Daqiao Epizonal Orogenic Gold Deposit, West Qinling Orogen, China: Constraints from Textures, Trace Elements, and Sulfur Isotopes of Pyrite and Marcasite, and Raman Spectroscopy of Carbonaceous Material. Economic Geology 113, 1093-1132.

Wu Y.F., Li J.W., Evans K., Vasconcelos P.M., Thiede D.S., Fougerouse D., and Rempel K., 2018b. Late Jurassic to Early Cretaceous age of the Daqiao gold

deposit, West Qinling Orogen, China: implications for regional metallogeny. Mineralium Deposita, doi: 10.1007/s00126-018-0835-z.

Xu, L., Wu, B.X., Wang, Y.L., Wang, Z.X., Wang, G., and Sun, Z.P., 2015. Fluid inclusion characteristics and geological significance at Daqiao gold deposit. Journal of Jinlin University 45, 568-569.

Yan, J., Hu, R., Liu, S., Lin, Y., Zhang, J., Fu, S., 2018. NanoSIMS element mapping and sulfur isotope analysis of Au-bearing pyrite from Lannigou Carlin-type Au deposit in SW China: New insights into the origin and evolution of Au-bearing fluids. Ore Geology Reviews 92, 29-41.

You, G.J., Zhang, Z.P., 2009. Geological characteristics of Daqiao gold deposit in Gansu province and its significance in prospecting for gold deposit. Gansu Geology 18, 1-8.

Zeng, Q.T., Mccuaig, T.C., Tohver, E., Bagas, L., Lu, Y.J., 2014. Episodic Triassic magmatism in the western South Qinling Orogen, central China, and its implications. Geological Journal 49, 402-423.

Zhang, G.W., Zhang, Z.Q., Dong, Y.P., 1995. Nature of main tectono-lithostratigraphic units of the Qinling Orogen: implications for the tectonic evolution. Acta Petrologica Sinica 11, 101-114 (in Chinese with English abs.).

Zhang, G.W., Meng, Q.G., Yu, Z.P., Sun, Y., Zhou, D.W., Guo, A.L., 1996. Orogenesis and dynamics of the Qinling orogen. Science in China Series D: Earth Sciences (English Edition) 39, 225-234.

Zhang, G.W., Zhang, B.R., Yuan, X.C., Xiao, Q.H., 2001. Qinling orogenic belt and continental dynamics. Beijing, Science Press, 855p (in Chinese).

Zhang, Z.P, Wu, Y.F, Li, J.W., 2018. Characteristics and Genesis of the silicified breccias in the Daqiao gold deposit, West Qinling Orogen: Geological Science and Technology Information 37, 79-88.

Zhou, T.H., Goldfarb, R.J., and Phillips, N.G., 2002. Tectonics and distribution of gold deposits in China - an overview. Mineralium Deposita 37, 249-282.

Chapter 2

Source and possible tectonic driver for Jurassic-Cretaceous gold deposits in the West Qinling Orogen, China

This chapter is a published paper in *Geoscience Frontiers*:

Wu Y.F., Li J.W., Evans K., Fougerouse D., and Rempel K., 2019, Source and possible tectonic driver for Jurassic–Cretaceous gold deposits in the West Qinling Orogen, China. *Geoscience Frontiers*, 10 (1): 107–117 (Impact factor 4.256).

Contributions by co-authors

Ya-Fei Wu and Jian-Wei Li collected samples. Ya-Fei Wu performed sample preparation for petrographic observations, *in situ* trace element and sulfur isotope analyses. Ya-Fei Wu is the primary author of the manuscript with the helpful discussions, suggestions and guidance, from all-coauthors.

Abstract

The West Qinling Orogen (WQO) in Central China Orogenic Belt contains numerous metasedimentary rock-hosted gold deposits (>2,000 t Au), which mainly formed during two pulses: one previously recognized in the Late Triassic to Early Jurassic (T3-J1) and one only recently identified in the Late Jurassic to Early Cretaceous (J3-K1). Few studies have focused on the origin and geotectonic setting of the J3-K1 gold deposits.

Textural relationships, LA–ICP–MS trace element and sulfur isotope compositions of pyrites in hydrothermally altered T3 dykes within the J3-K1 Daqiao deposit were used to constrain relative timing relationships between mineralization and pyrite growth in the dykes, and to characterize the source of ore fluid. These results are integrated with an overview of the regional geodynamic setting, to advance understanding of the tectonic driver for J3-K1 hydrothermal systems.

Pyrite in breccia- and dyke-hosted gold ore at Daqiao have similar chemical and isotopic compositions and are considered to be representative of J3-K1 gold deposits in WQO. Co/Ni and sulfur isotope ratios suggest that ore fluids were derived from underlying Paleozoic Ni- and Se-rich carbonaceous sedimentary rocks. The geochemical data do not support the involvement of magmatic fluids. However, in the EQO (East Qinling Orogen), J3-K1 deposits are genetically related to magmatism.

Gold mineralization in WQO is contemporaneous with magmatic deposits in the EQO and both are controlled by NE- and EW-trending structures produced by changes in plate motion of the Paleo-Pacific plate as it was subducted beneath the Eurasian continent. We therefore infer that the J3-K1 structural regime facilitated the ascent of magma in the EQO and metamorphic fluids in the WQO with consequent differences in the character of contemporaneous ore deposits. If this is correct, then the far-field effects of subduction along the eastern margin of NE Asia extended 1000’s of km into the continental interior.

2.1 Introduction

The far-field effects of changes in plate motion during Mesozoic subduction of the Paleo-Pacific plate have been invoked to explain changes in stress regime and widespread gold mineralization in NE Asia (Figure 2.1; e.g., Zhai and Deng, 1996; Goldfarb et al., 1998, 2007; Qiu et al., 2002; Ratschbacher et al., 2003; Mao et al., 2005, 2006, 2008, 2010; Lan et al., 2011; Sun et al., 2007, 2010, 2013). However, the timing and reach of these far-field effects and their relation to gold mineralization at different distances from the plate boundary remain poorly understood. A better understanding of the geotectonic evolution of NE Asian response to such changes and their control on gold endowment is needed to design effective mineral exploration strategies.

The 2,500 km long Qinling Orogenic Belt (QOB) in central China is an ideal place to determine how changes in plate motion affected the geodynamics and gold mineralization in the continental interior (Figs. 2.1, 2.2). In the East Qinling Orogen (EQO), magmatism and genetically related Au, Cu-Mo and Pb-Zn deposits of Late Jurassic to Early Cretaceous age (J3–K1, ca. 150–125 Ma) are widely distributed (Figure 2.2; e.g., Shanzha and Xiaoqinling; Mao et al., 2008, 2010; Li et al., 2012a, b; Xie et al., 2017). It has been suggested that tectonism during this period was affected by subduction of the Paleo-Pacific plate (Mao et al., 2008, 2010). In the West Qinling Orogen (WQO), most gold deposits are Late Triassic to Early Jurassic in age (T3–J1; ca. 216–203 Ma; Zeng et al., 2012; Liu et al., 2014; Wang et al., 2014; Hu, 2015; Zhang, 2016; Lin et al., 2017), and are spatially associated with intrusions and dykes (ca. 220–200; Dong et al. 2011; Dong and Santosh 2016). However, a small number of Late Jurassic to Early Cretaceous (J3-K1) gold deposits in the WQO are not associated with magmatic activity (ca. 151–125 Ma; Huang et al., 1996; Lu et al., 2006; Qi et al., 2006; Liu et al., 2015; Wu et al., 2018a, b). The formation of J3-K1 gold deposits without magmatism in the WQO, while Au, Cu-Mo, Pb-Zn deposits formed in response to magmatism in the EQO requires explanation.

The large Daqiao gold deposit (>105 t Au at 3-4 g/t) was studied to advance understanding of ore-formation in the WQO (Figure 2.2). High-precision sericite $^{40}Ar/^{39}Ar$ dates show that this J3-K1 deposit was produced by multiple episodes of hydrothermal activity between 151–127 Ma (Wu et al., 2018b). Gold ore is hosted in

Triassic turbidites and in granodiorite and diorite porphyry dykes dated at ca. 215 and 188 Ma, respectively (Wu et al., 2018b). In this paper, the textures, chemical, and sulfur isotope composition of the dyke-hosted pyrites are used to constrain the source of sulfur and ore fluids in the WQO. The J3-K1 deposits and setting in the WQO are then compared to those in the EQO.

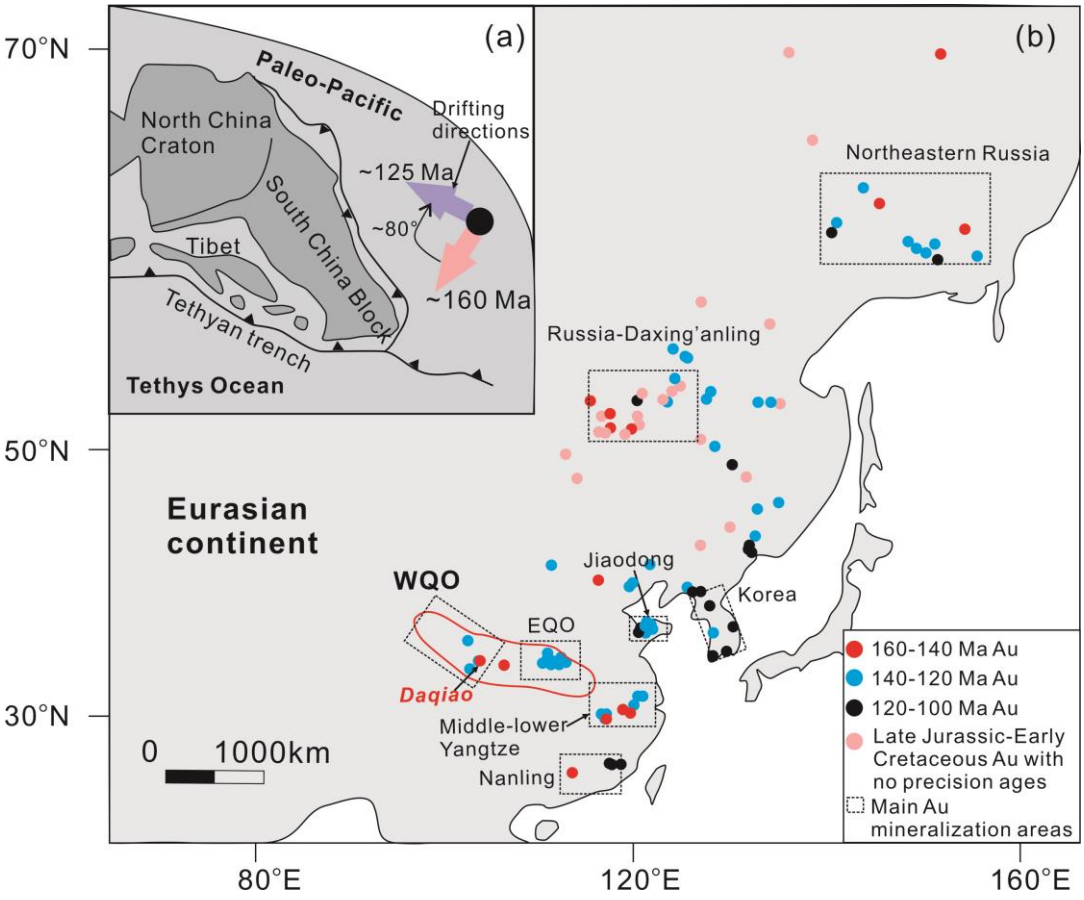

Figure 2.1 a) Subduction and drifting history of the Paleo-Pacific plate since the Late Jurassic. b) Main areas with intensive Late Jurassic to Early Cretaceous magmatism and related gold mineralization in the NE Asia. Modified after Sun et al. (2007), Mao et al. (2005) and Goldfarb et al. (2014).

2.2 Regional geological setting

Mesozoic oblique subduction of the Paleo-Pacific ocean plate beneath the Eurasian continent is thought to have started at ca. 160 Ma (Figure 2.1a; Ren et al., 1992; Niu et al., 2003). The drifting direction of the Paleo-Pacific plate changed from roughly SW at ca. 160 Ma to NW at ca. 125–122 Ma (Koppers et al., 2003; Sun et al., 2007).

At ca. 160 Ma, the principal stress direction in the QOB was NS and gradually shifted to EW by ca. 140 Ma (Mao et al., 2005, 2006). Polymetallic deposits genetically associated with the subduction-related magmatic centers occur across the whole NE Asia with peaks at ca. 150–140 Ma and 130–119 Ma (Figure 2.1b; Mao et al., 2005, 2008; Li et al., 2003, 2006, 2012a, b; Goldfarb et al., 2014).

The QOB is separated from the North China Craton (NCC) by the Luonan-Luanchuan Fault and from the South China Block (SCB) by the Triassic Mianlue suture zone (Figure 2.2; Zhang et al., 2001; Dong et al., 2011, 2013). This orogen records subduction of proto-Tethyan oceanic crust collision between the NCC and Qinling micro-plate along the Shangdan suture in the Middle Paleozoic, and subduction of the paleo-Tethyan oceanic crust and collision between the Qinling terrain and the SCB along Mianlue suture in the Early Mesozoic (Meng and Zhang, 1999; Dong et al., 2011). The QOB can be divided into four suture zone or thrust fault bounded terranes from north to south (Figure 2.2): the Southern North China Craton (S-NCC), North Qinling Belt (NQB), South Qinling Belt (SQB) and Northern South China Block (N-SCB) (Zhang et al., 1995). The QOB has also been divided into the eastern and western parts (EQO and WQO). Both are dominated by the Cambrian to Triassic marine sedimentary rocks, with some Archean metamorphosed supracrustal rocks in the EQO (Li et al. 2012a; Liu et al., 2015).

Mesozoic granitoid intrusions are widespread in the QOB (Figure 2.2; Dong and Santosh, 2016). The majority of intrusions in the WQO (ca. 230–200 Ma) contain mafic enclaves and are enriched in LILE with negative εNd(t) and εHf(t) values. J3-K1 (164–100 Ma) intrusions are rare in the WQO but are widespread in the EQO (Figure 2.2). J3-K1 granitoids commonly contain biotite and hornblende, have high Mg# and higher εHf(t) values than Late Triassic granitoids, which indicate they assimilated less continental crust (Wu et al., 2014).

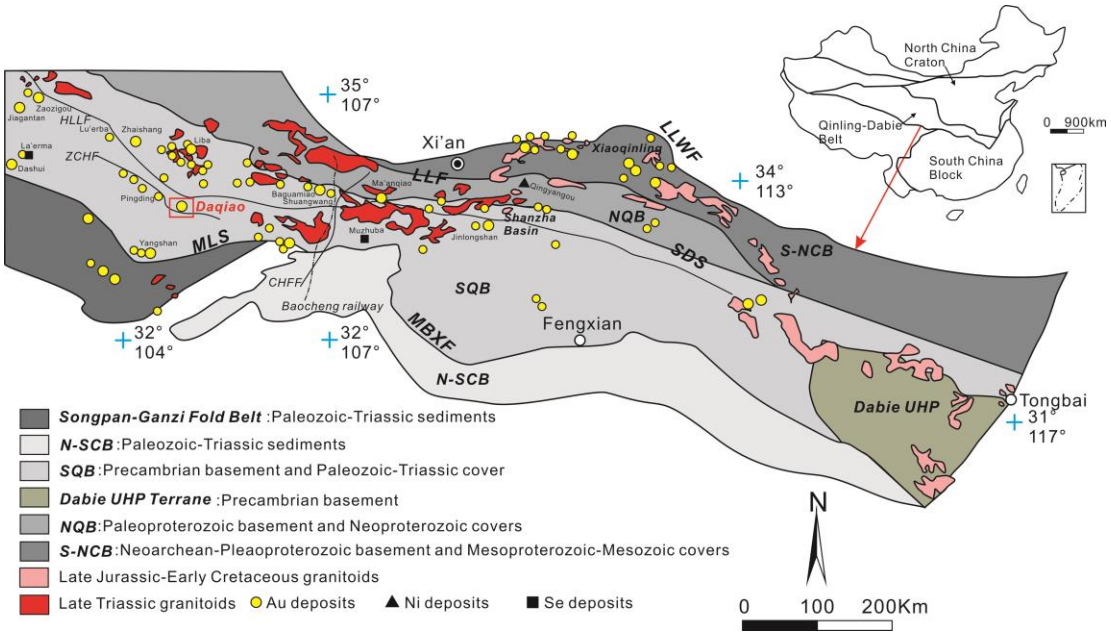

Figure 2.2 A simplified map of geotectonic terranes in the Qinling-Dabie orogenic belt (modified from Dong and Santosh 2016). Major faults, plutons, gold deposits, and the location of Daqiao gold mine study area (red box) are also shown. The inset shows the location of the Qinling orogen in China. Abbreviations: LLWF = Lingbao-Lushan-Wushan Fault; LLF = Luonan-Luanchuan Fault; SDS = Shangdan Suture; HLLF = Hezuo-Lintan-Liangdang Fault; ZCHF = Zhouqu-Chengxian-Huixian Fault; CHFF = Chengxian-Huixian-Fengxian Fault; MLS = Mianlue Suture; MBXF = Mianlue-Bashan-Xiangguang Fault; S-NCC = Southern North China Craton; NQB = North Qinling Belt; SQB = South Qinling Belt; N-SCB = Northern South China Block; Dabie UHP = Dabie ultrahigh pressure terrane; WQO = West Qinling Orogen; EQO = East Qinling Orogen

2.3 Deposit geology

The Daqiao gold deposit is located between the northern Hezuo-Lintan-Liangdang Fault (HLLF) and the southern Zhouqu-Chengxian-Huixian Fault (ZCHF; Figure 2.2; Zhang et al., 2018). Gold mineralization is mainly hosted in Middle Triassic Huashiguan Formation turbidites that are in fault contact with Carboniferous limestone (Figure 2.3; Wu et al., 2018a; Zhang et al., 2018). There are a number of reverse faults in the mine, which mostly strike NE. Ore bodies at Daqiao are characterized by auriferous breccias (Figure 2.4a) and are spatially related to the NE-striking reverse faults. The breecias can be classified into three types: tectonic breecia A, hydraulic breecias B and C. A complex paragenesis is determined by four sulfide stages: diagenetic pre-ore pyrite, hydrothermal early-ore disseminated pyrite

and marcasite, main-ore pyrite and marcasite aggregates, and late-ore coarse-grained marcasite with minor pyrite and stibnite. Hydrothermal alteration consists of multistage silicification, sulfidation, sericitization and carbonatization (Figure 2.4b). Arsenian pyrite and marcasite are the predominant ore minerals that contain varied amounts of invisible gold (Wu et al., 2018a).

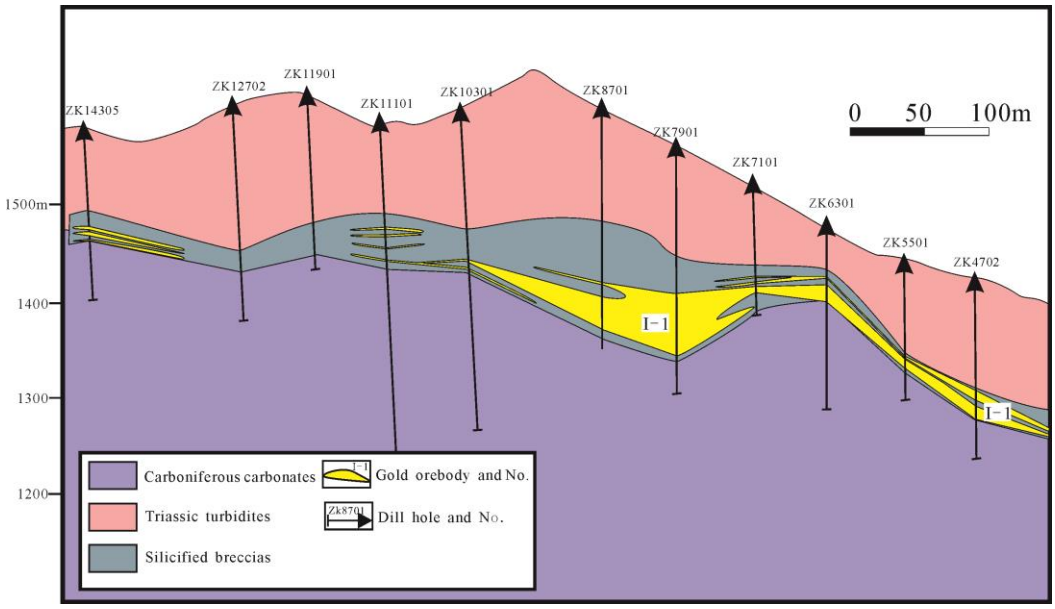

Figure 2.3 Representative cross section showing the occurrence and morphology of the major ore bodies at the Daqiao gold deposit.

A number of granodiorite dykes and a few diorite porphyry dykes intrude the Carboniferous and Triassic sediments at Daqiao (Figure 2.4c, d). Individual dykes extend for several tens to a few hundred meters along northeast or northwest strike and are 2 to 10 m in thickness. In gold ore bodies, these dykes exhibit variable degrees of silicification, sericitization, sulfidation, carbonatization, and gold mineralization (Figure 2.4c-f). Recent LA–ICP–MS zircon U-Pb dating of the granodiorite and diorite porphyry dykes suggests they were emplaced at ca. 215–212 Ma and 188 Ma, respectively (Wu et al., 2018b).

Two kinds of pyrite have been identified in granodiorite dykes with different degrees of hydrothermal alteration (Figure 2.4c-f). In the less intensely altered dykes (Figure 2.4c, e), pyrite occurs as fine-grained anhedra to subhedra (20–100 μm across), or in deformed and cataclastic aggregates (150–600 μm across). Pyrite commonly contains inclusions of, or occurs as veinlets with, chalcopyrite, galena, and sphalerite. Irregular and deformed pyrite aggregates replace silicate minerals (Figure 2.4e). In dykes with intense alteration, pyrite is subhedral, between 200 and 300 μm in

diameter (Figure 2.4d, f), has a characteristic porous texture, and contains fine-grained inclusions of mica and feldspar (2–20 μm across).

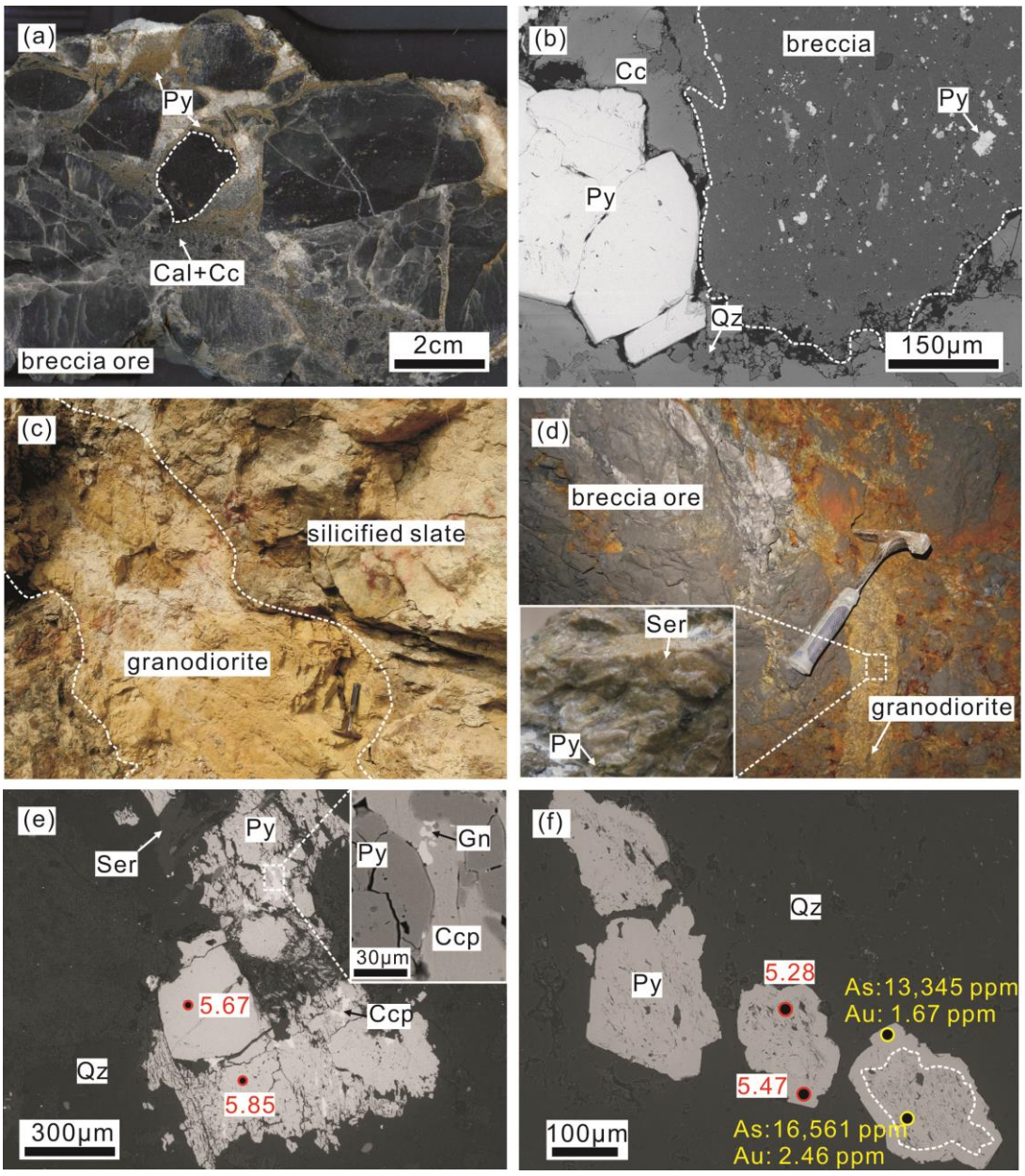

Figure 2.4 Photographs (a, c, d) and back-scattered electron (BSE) images (b, e, f) showing the features of gold mineralization, altered dykes and disseminated pyrite at Daqiao. a) Black silicified siltstone cemented by calcite-chalcedony-pyrite matrix forming high-grade breccia ore. b) Silicified breccia with disseminated sulfides is surrounded by late calcite-quartz-pyrite. c) Granodiorite dyke intruding slate of the Triassic Huashiguan Formation. d) Contact between breccia ore and intensely altered granodiorite dykes with aggregates of sericite and pyrite. e) Deformed and cataclastic pyrite subhedra and pyrite aggregates intergrown with chalcopyrite, sphalerite, galena, and sericite. Smooth and porous pyrites have similar sulfur isotope compositions. f) Subhedral pyrite grains with porous cores containing fine-grained silicate inclusions. The rim and core have high Au-As concentrations and similar sulfur isotope compositions. Cal = Chalcedony, Cc = calcite, Ccp chalcopyrite, Gn galena,

Ser sericite, Py pyrite, Qz quartz, Sp sphalerite.

2.4 Samples and methods

2.4.1 Sample description

Polished thin sections and section blocks of dykes containing pyrite were characterized initially by optical microscopy and scanning electron microscopy (SEM). Two samples of altered and mineralized granodiorite dykes (DQ123 with 0.4g/t Au, and DQ477 with 2.5g/t Au) were collected from borehole ZK6802 (depth of 316m) and underground workings, respectively, which are 2.5 kilometres apart. Sample DQ123 is silicified and contains disseminated pyrite, but it is less intensely altered than DQ477, which contains coarse-grained sericite and pyrite aggregates that formed during intense hydrothermal alteration (Figure 2.4d).

2.4.2 LA–ICP–MS multi-element analysis of sulfides

The trace element concentrations of pyrite in each granodiorite dyke samples were determined by laser ablation inductively coupled plasma mass spectrometry (LA–ICP–MS). The analytical instrumentation employed in this study was a Photon Machines Analyte G2 LA system (193 nm, 4 ns excimer laser) attached to a PerkinElmer DRC-e ICP-MS, at the U.S. Geological Survey, Denver Federal Center. Laser ablation was carried out using a 30 micrometer spot size, a fluence of 5 J/cm2 at 7 Hz with a 35 s baseline and 40–50 s of ablation. Ablated materials were transported in He carrier gas to a modified glass mixing bulb where the He and sample aerosol were mixed coaxially with Ar prior to the ICP torch. Concentration and detection limit calculations were conducted using the protocol of Longerich et al. (1996). Signals were calibrated using USGS MASS-1 sulfide reference material and iron (^{57}Fe) was used as the internal standard (Wilson et al., 2002). The reference material (MASS-1) was analyzed 5–10 times at the beginning of the analytical session and monitored throughout the session for drift. Signals were screened visually for heterogeneities such as micro-inclusions or zoning. The results are given in Table 2.1, and the reported mean concentrations for trace elements were calculated assuming that concentrations are zero for spot analyses below detection limit (b.d.l.).

2.4.3 LA-MC-ICP-MS sulfur isotope analysis

Polished thin sections and section blocks analyzed using LA–ICP–MS trace element spot analysis were re-polished and used for in-situ sulfur isotope analysis. In situ S isotope analyses of pyrite were performed using a Nu Plasma HR multicollector ICP–MS together with a Photon Machine Analyte G2 laser system, at the Geological Survey of Finland (GSF), Espoo, Finland. Samples were ablated in He gas (gas flows = 0.4 and 0.1 l/min) within a HelEx ablation cell (Müller et al., 2009). During ablation, the data were collected in static mode (^{32}S, ^{34}S). Pyrite was ablated using a spot size of 30 micrometers and a fluence of 0.83 J/cm^2 at 5 Hz. The total S signal obtained for pyrite was typically 1.0–1.2 V. Under these conditions, after a 20 s baseline, 50–60 s of ablation is needed to obtain an internal precision of $^{34}S/^{32}S \leq \pm$ 0.000005 (1 SE). Three pyrite standards were used for external standard bracketing (PPP-1) (Gilbert et al., 2014) and quality control (Pyrite1 and Pyrite2 from GSF) of analyses (Wong et al., 2017). The results are given in Table 2.2.

2.5 Results

Pyrite from the altered dykes at Daqiao contains many trace elements (Figure 2.5; Co, Ni, Cu, Zn, As, Se, Ag, Sb, Te, Au, Tl, and Pb). The gold content of DQ123 pyrite grains varies from b.d.l to 3.28 ppm (mean = 1.36 ppm, standard deviation (s.d.) = 1.36, n = 5), while arsenic varies from 484 to 14,378 ppm (mean = 6,967 ppm, s.d. = 4,798, n = 5). In DQ477, the gold concentration ranges from 1.67 to 2.99 ppm (mean = 2.37, s.d. = 0.54, n = 3) and arsenic ranges from 13,346 to 22,624 ppm (mean = 17,510, s.d. = 3,847, n = 3). Although pyrite spot analyses from the two dyke samples demonstrate similar trace element patterns, a number of trace elements are more enriched in sample DQ477 than DQ123 (Figure 2.5e), for instance, Ni (mean 265.5 ppm vs. 149.2 ppm), Se (453.4 ppm vs. 55.9 ppm), Cu (95.2 ppm vs. 1.1 ppm), Ag (5.8 ppm vs. 0.1 ppm), Sb (82.6 ppm vs. 2.0 ppm), Te (6.6 ppm vs. 1.3 ppm), and Pb (102.1 ppm vs. 2.0 ppm).

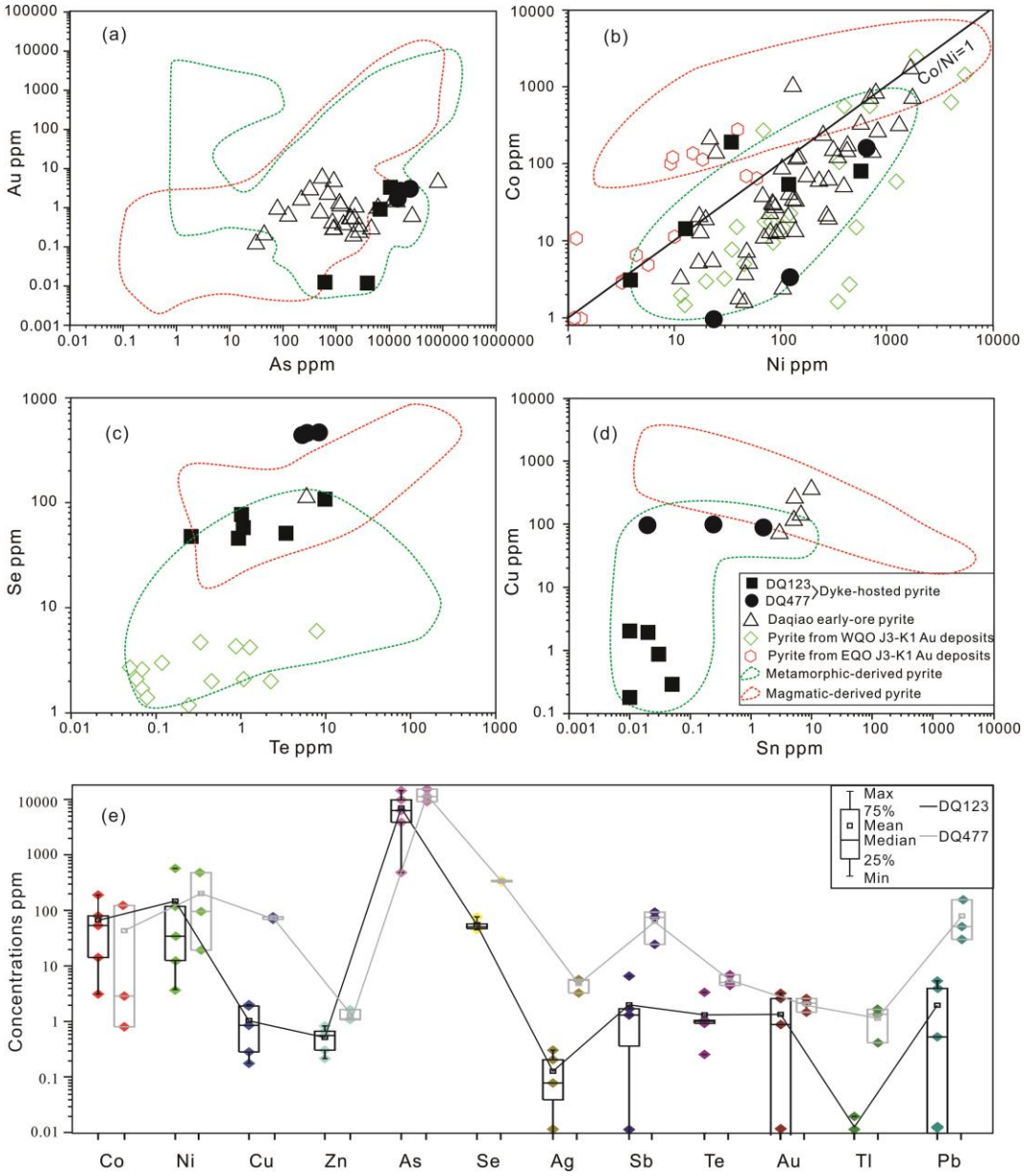

Figure 2.5 Plots of element concentrations derived from LA–ICP–MS spot analyses on pyrite compared with the compositional ranges of magmatic- and metamorphic-derived pyrite, using data from Belousov et al. (2016) and Keith et al. (2018), trace element contents of pyrite in Daqiao early ore stage breccia-hosted ores (Wu et al., 2018b), and pyrite from other Au deposits of J3-K1 ages in WQO and EQO (Zhang et al., 2014; Bi et al., 2016). a) As vs. Au: Most pyrites show high Au and As, falling into the metamorphic region. b) Ni vs. Co: Pyrite from Daqiao and gold deposits in WQO have Co/Ni in the metamorphic/sedimentary region. c) Te vs. Se: Pyrite from DQ477 has higher Se content than pyrite from DQ123 and other Au deposit in WQO. d) Sn vs. Cu: Pyrite from DQ477 and Daqiao early ore stage have higher Cu contents than pyrite from DQ123, and most spot analyses plot in the metamorphic-derived pyrite region. e) Comparisons of pyrite trace element patterns between DQ123 and DQ477.

The $\delta^{34}S$ signatures of fourteen spot analyses of pyrite from these two dyke samples range from +4.9 to +7.1 ‰ (Figure 2.6; mean +5.6 ‰, s.d. = 0.5). In DQ123, with the exception of one analysis at +7.1 ‰, all the pyrite grains show a relatively homogenous $\delta^{34}S$ values from +4.9 to +6.0 ‰ (mean = +5.8 ‰, s.d. = 0.6, n = 8). In DQ477, $\delta^{34}S$ values of all the pyrite grains have narrow range of $\delta^{34}S$ values from +5.3 to +6.0 ‰ (mean = +5.5 ‰ , s.d. = 0.2, n = 6).

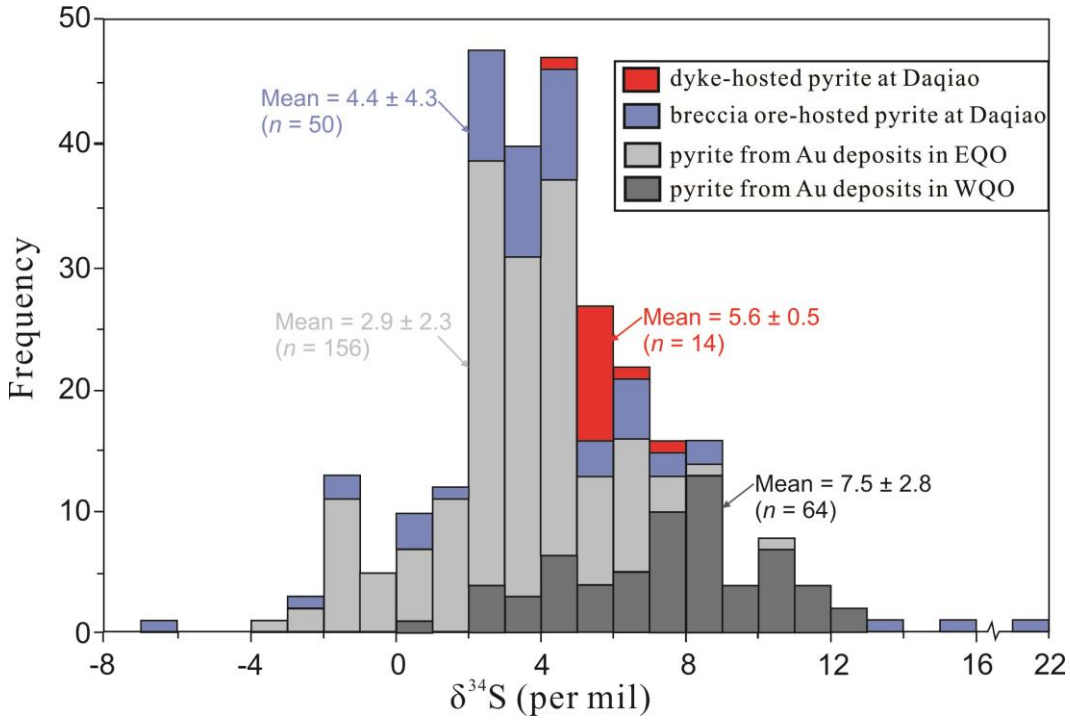

Figure 2.6 Sulfur isotope composition of pyrites from Daqiao, and other representative gold deposits in the EQO and WQO of J3-K1 and T3-J1 ages, respectively (Shi et al., 1989; Chen et al., 1994; Li et al., 2001; Gong, 2014; Li et al., 2012b; Wu et al., 2018a).

Table 2.1 LA–ICP–MS trace element analysis of pyrite hosted by altered granodiorite dykes at the Daqiao gold deposit

Analysis no.	Co	Ni	Cu	Zn	As	Se	Ag	Sn	Sb	Te	Au	Tl	Pb
DQ123-1	53.92	120	0.18	0.68	483.6	77.13	0.01	0.01	0.01	1.02	0	0	0.01
DQ123-2	80.19	574.94	0.29	0.85	3875.84	47.61	0.31	0.05	6.67	0.26	0	0.02	0.01
DQ123-3	191.3	34.56	2.04	0.57	14377.83	57.9	0.04	0.01	1.33	1.07	2.63	0	5.45
DQ123-4	14.36	12.78	0.87	0.31	6279.39	45.75	0.21	0.03	1.73	0.94	0.9	0	4.01
DQ123-5	3.16	3.84	1.93	0.22	9816.91	51.09	0.08	0.02	0.37	3.41	3.28	0	0.54
Mean	68.58	149.22	1.06	0.53	6966.71	55.90	0.13	0.02	2.02	1.34	1.36	0.00	2.00
S.D.	67.27	216.79	0.79	0.23	4798.02	11.40	0.11	0.01	2.41	1.08	1.36	0.01	2.28
DQ477-1	0.91	23.86	98.45	1.27	22624.49	458.31	3.84	0.02	30.53	6.03	2.99	1.93	37.65
DQ477-2	160.5	649.19	98.77	1.23	13345.52	464.46	6.61	0.24	120.69	8.34	1.67	0.46	203.38
DQ477-3	3.37	123.42	88.52	1.9	16560.87	437.39	6.84	1.61	96.55	5.31	2.46	1.55	65.31
Mean	54.92	265.49	95.25	1.47	17510.29	453.39	5.76	0.62	82.59	6.56	2.37	1.31	102.11
S.D.	74.65	274.34	4.76	0.31	3847.15	11.59	1.36	0.70	38.11	1.29	0.54	0.62	72.49

S.D. = Standard deviation

Table 2.2 LA-MC-ICP-MS in situ sulfur isotope composition of pyrite hosted by altered granodiorite dykes at the Daqiao gold deposit

Analysis no.	Sulfide type	$\delta^{34}S$‰ VCDT	2σ
DQ123-1	Pyrite	7.1	0.2
DQ123-2		5.7	0.2
DQ123-3		6.0	0.2
DQ123-4		5.9	0.3
DQ123-5		5.2	0.2
DQ123-6		5.7	0.3
DQ123-7		5.7	0.2
DQ123-8		4.9	0.2
Mean		5.8	0.2
S.D.		0.6	0.0
DQ477-1	Pyrite	5.3	0.2
DQ477-2		5.5	0.2
DQ477-3		5.3	0.2
DQ477-4		5.3	0.3
DQ477-5		6.0	0.2
DQ477-6		5.5	0.2
Mean		5.5	0.23
S.D.		0.2	0.0

S.D. = Standard deviation

2.6 Discussion

Previous geochronological studies using zircon LA–ICP–MS, SHRIMP (sensitive high-resolution ion microprobe), and TIMS (thermal ionization mass spectrometry) dating suggest that the majority of gold deposits and igneous intrusions in the WQO have T3-J1 ages (ca. 225–180 Ma) and formed in a syn- to post- collisional setting (Figure 2.7; Dong et al., 2011). Only a few gold deposits of J3-K1 age have been reported (Wu et al., 2018b), and these show no association with magmatic activity (Figure 2.7). The substantial time gap between the youngest records of extensional deformation in the Qinling Orogen (e.g., the ca. 188 Ma dykes at Daqiao), the lack of J3-K1 magmatism, and the small number of J3-K1 gold deposits in the WQO suggests that the J3-K1 gold deposits are related to a poorly characterized geotectonic event.

If pyrite hosted in post T3-J1 dykes records fluid flow associated with the J3-K1

events, then the trace element contents and sulfur isotope ratios of the pyrite can be used to characterize the fluid source, and, in conjunction with the regional geodynamic context, to draw conclusions on the timescales and nature of the causes of the fluid flow.

2.6.1 Relationship of dyke-hosted pyrite to J3-K1 mineralization at Daqiao

Petrogenesis and zircon Lu-Hf isotope studies suggest that pyrite-bearing granodiorite dykes at Daqiao are mainly produced by partial melting of thickened lower crust in a compressional setting (Shan et al., 2016). This is consistent with evidence from contemporaneous intrusions in the WQO (ca. 220–210 Ma), such as Al-saturation, LILE enrichment, negative εNd(t) and εHf(t) values (Sun et al., 2002; Zeng et al., 2014). Texturally, pyrite in the most altered dykes is similar to early-ore stage subhedral pyrite disseminations in the breccia-hosted ores at Daqiao (Wu et al., 2018a). However, the deformed and cataclastic pyrite aggregates in less intensely altered dykes are typically intergrown with other sulfide phases and are texturally dissimilar to pyrite in breccia-hosted ores.

The As and Au composition of pyrite from the two dykes (DQ123 and DQ477) are comparable (mean 6,967 vs. 17,510 ppm As; 1.36 vs. 2.37 ppm Au), and mostly plot within the range of Daqiao early-ore stage pyrite with up to 87,444 ppm As and 5.7 ppm Au (Figure 2.5a). The lower abundance of trace elements (Figure 2.5; Au, As, Se, Co, Te, Cu, and Sn) and less intense alteration in DQ123 (Figure 2.4c) relative to DQ477 may be indicative of lower temperatures or fluid-rock ratios than DQ477. However, the lower abundance of trace elements in DQ123 pyrite could also be due to sequestration of these elements in other sulfides (Figure 2.4e; e.g., Co and Se into sphalerite, Se into chalcopyrite; Large et al., 2009; Genna and Gaboury, 2015). The $\delta^{34}S$ values of dyke-hosted pyrite, which range from +4.9 to +7.1‰ (mean +5.6‰) is similar to that of the early-ore stage pyrite (mean +4.4‰; Wu et al., 2018a). Together, the trace element, and sulfur isotopic characteristics of early ore-stage breccia-hosted and dyke-hosted pyrite are representative of the episodic J3-K1 fluids that formed Daqiao gold mineralization.

2.6.2 Characteristics of J3-K1 fluid flow in the dykes at Daqiao

Pyrite trace elements compositions (e.g., Co, Ni, and Se) have commonly been used to assess origin (e.g., Price, 1972; Huston et al., 1995; Belousov et al., 2016). For example, pyrite from volcanic exhalative and felsic intrusion-related sulfide ores generally has hundreds of ppm Co, tens of ppm of Ni with Co/Ni = 5–50 (Price, 1972). Elevated Co/Ni is caused by the more rapid extraction of Ni than Co from the fluid to the solid phase during magmatic differentiation (Loftus-Hills and Solomon, 1967). Conversely, low Co/Ni ratios (<1) are thought to be typical of sedimentary pyrite (Loftus-Hills and Solomon, 1967; Large et al., 2014).

Breccia- and dyke-hosted pyrite at Daqiao have Co/Ni mean ratios of 0.36 (Wu et al., 2018a) and 0.29 (six of eight spots) and are within the range of those reported for global sedimentary pyrite (Figure 2.5b; Large et al., 2014). This similarity argues against a magmatic-hydrothermal origin, such as that inferred for pyrite from Au deposits in the EQO (Figure 2.5b), for the dyke-hosted pyrite and instead supports derivation of sulfur and trace metals from a sedimentary source rock. Possible candidates for such a source are the underlying Paleozoic shales and carbonaceous pelites in the WQO. These Paleozoic sediments, particularly those from the Cambrian to Silurian, have a low mean Co/Ni ratio of 0.07 (Wang, 2009).

Although Se content in dyke-hosted pyrite from DQ123 is within the range of pyrite from orogenic Au and porphyry Cu (-Au) deposits, pyrite from DQ477 has higher Se contents of ca. 500 ppm (Figure 2.5c; Keith et al., 2018). In marine environments, Se accumulates in organic matter due to biological uptake and substitutes for S in sedimentary pyrite (Diener and Neumann, 2011; Mitchell et al., 2012). For example, at the Bendigo orogenic gold deposit the reported means are 67 ppm and 32 ppm Se for diagenetic and hydrothermal pyrite, respectively (Thomas et al., 2011). In the case of Se-rich hydrothermal pyrite at the Cornish, Scottish, Australian (CSA) orogenic Cu-Pb-Zn deposit, Australia, Brill (1989) proposed that Se (mean = 319 ppm) was mainly leached from the underlying sediments and transported by the metamorphic fluids. A deep-seated sedimentary Se source at Daqiao is possible, given that high Se concentrations (up to 232 ppm) are present in Paleozoic carbonaceous sediments across the QOB, such as the La’erma and Muzhuba deposits in the WQO and EQO (Figure 2.2; Liu and Zheng, 1993; Liu et al., 2000; Tu, 2008).

The $\delta^{34}S$ values from dyke-hosted pyrite at Daqiao exhibit a narrow range from +4.9 to +7.1 ‰ (mean +5.6 ‰), suggestive of a very uniform, or well mixed, sulfur reservoir (Faure, 1986). These $\delta^{34}S$ values are similar to that of breccia ore-hosted pyrite at Daqiao (mean +4.4 ‰) and of pyrite from other orogenic gold deposits of T3-J1 ages in WQO (mean +7.5 ‰), which all indicate that the source of sulfur and fluids have been produced by metamorphic devolatilization of underlying Paleozoic sedimentary rocks (Figure 2.6; Shi et al., 1989; Chen et al., 1994; Li et al., 2001; Gong, 2014; Wu et al., 2018a). In contrast, uniform and low $\delta^{34}S$ values (mean +2.9 ‰) of ore stage pyrite from six gold deposits of J3-K1 ages in EQO are similar to that of magmatic pyrite from nearby pluton (2.1–4.3‰; Nie et al., 2001) and likely indicate a magmatic sulfur source (Li et al., 2012b).

Other similarities between the regional sediments and breccia ores at Daqiao also support sediment-derived fluids. Devonian carbonaceous phyllites and schists in the WQO are characterized by well-developed laminated diagenetic pyrite framboids that contain 0.1–1.7 ppm Au and 0.2–1.6 wt% As (Zhang et al., 2000; Qi et al., 2003). Such Au and As enriched rocks are a possible Au and As source for the Au and As in the Daqiao ores (Wu et al., 2018a). Silurian and Cambrian siliceous rocks and carbonaceous shales that underlie Daqiao are also associated with enrichment of PGE, U, and Se (Tan, 1992; Liu and Zheng., 1993). The Daqiao breccia ores contain distinct, fine-grained hydrothermal PGE-, U- and Se- rich minerals closely associated with the ore-stage sulfides (Wu et al., 2018a).

2.6.3 Comparison to the EQO

The J3-K1 Daqiao gold mineralization is contemporaneous with widespread J3-K1 (ca. 150–125 Ma) magmatism and polymetallic mineralization in the EQO (Fan et al., 2011; Li et al. 2012a, b; Xie et al., 2017) and elsewhere in NE Asia (Figures. 2.2, 2.6; Goldfarb et al., 1998, 2007; Sun et al., 2007, 2013). It has been proposed that magmatism and mineralization in the EQO is related to oblique subduction of the Paleo-Pacific ocean plate beneath the Eurasian continent (e.g., Mao et al., 2008, 2010). The plate subduction led to a regional tectonic regime transition with changes in the principal stress vectors from NS-trending at ca. 160 Ma to near EW-trending at ca. 140 Ma (Mao et al., 2005, 2006).

Structural studies of gold mines across the QOB show that T3-J1 ages deposits, such as Baguamiao, Shuangwang, Liba and Simaoling, are consistently controlled by WNW-trending faults and folds, whereas later NE-trending structures are barren (e.g., Gong, 2014; Wang et al., 2014; Zhang, 2016). These WNW-trending structures are thought to be a consequence of regional southward overthrusting after the T3 collision between the SCB and NCC (Chen et al., 2004). In gold deposits of J3-K1 age (e.g., Daqiao and Jinlongshan), the NE- or EW-trending brittle structures control the distribution of ore (Liu et al., 2015; Zhang et al., 2018). In eastern China, such as the Jiaodong and Middle-Lower Yangtze belt, NE-trending faults or intersections of NE and EW-trending faults are also the dominant ore controlling structures (Fan et al., 2003; Mao et al., 2006).

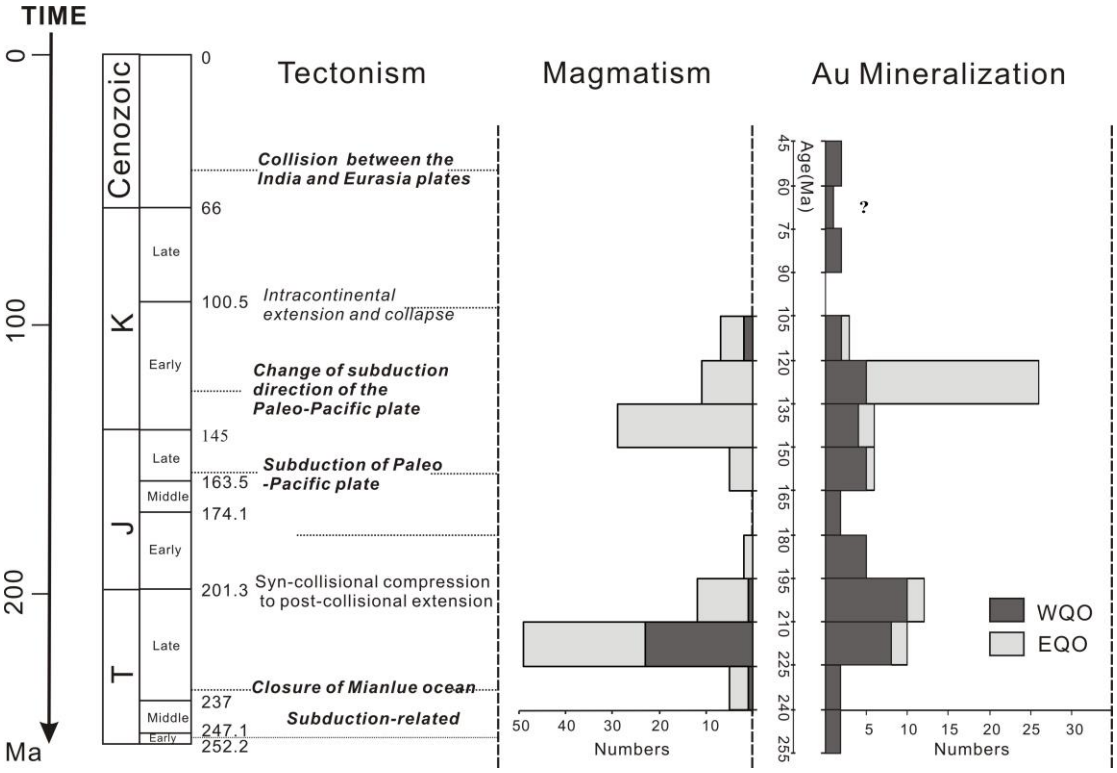

Figure 2.7 Summary diagram illustrating the timescale of tectonic events (Ren 1992; Niu et al., 2003; Dong et al., 2011, 2013; Dong and Santosh, 2016), magmatism (Sun et al., 2002; Zeng et al., 2014; Xie et al., 2017), and gold mineralization (Mao et al., 2002, 2005, 2008; Chen et al., 2004; Lu et al., 2006; Qi et al., 2006; Li et al., 2012a, b; Liu et al., 2015) in WQO and EQO.

In NE Asia, polymetallic mineralization peaked at ca. 150–140 Ma and 130–119 Ma and gradually decreased in intensity from east to west (Figure 2.1; Mao et al., 2005, 2008; Li et al., 2003, 2006, 2012a, b). Intense mineralization mostly occurs in the

circum-Pacific regions, such as Korea (granite-related Au-Ag; Choi et al., 2005), Northeast Russia (granite-related Au-Ag; Goldfarb et al., 2014), Jiaodong in east China (granite-related or orogenic Au; Qiu et al., 2002; Fan et al., 2003; Li et al., 2003, 2006), Daxing'anling in North China (granite-related Sn-Cu-Pb-Zn; Mao et al., 2005), Middle-Lower Yangtze belt in Central China (porphyry-skarn Cu-Au-Fe; Mao et al., 2006), and Nanling in South China (granite-related W-Sn-Mo-Au; Hua et al., 2005).

It is therefore interesting to consider whether subduction of the Paleo-Pacific plate influenced mineralization in the WQO, which lies about 2,000 km from the current trench. On the basis of seismic data, Molar and Tapponnier (1975) and Tapponnier and Molar (1979) suggest that plate collision-related continental lithosphere deformation can extend as far as 3,000 km, as seen in the Eocene collision between India and Eurasia plates. If such deformation could drive sufficient heating and fluid release, then J3-K1 gold mineralization, including the Daqiao deposit, in the WQO may be, to some extent, a consequence of the tectonic regime in NE Asia, via processes related to the subduction and drifting of Paleo-Pacific plate. While it is difficult to conceptualise mechanisms that would transfer stress over such small timescales and long distances, such transfer might be facilitated by weak, young, sediments in the Qinling Orogen, that are sandwiched between the rigid, ancient, NCC and SCB.

2.6.4 Synthesis and implications

Most of the gold deposits, particularly in the northern belt of the WQO (e.g., Ma'anqiao, Baguamiao, Shuangwang, and Liba) were thought to form during the T3–J1 (ca. 216–203 Ma; e.g., Zeng et al., 2012; Liu et al., 2014; Wang et al., 2014; Hu, 2015; Zhang, 2016; Lin et al., 2017). Although these deposits are spatially associated with contemporaneous intrusions or dykes (ca. 220–200 Ma; Dong et al., 2011, 2013), they are thought to be related to metamorphic devolatilization of underlying Paleozoic sediments during regional deformation associated with the NCC-SCB collision and subsequent orogenic deformation (ca. 227–195 Ma; Li et al., 1996, 1999; Yang et al., 1999; Zhang et al., 2002). The entire QOB then evolved towards an intra-continental orogenic stage (Dong et al. 2011).

At ca. 140 Ma, the regional tectonic regime in the QOB changed in response to a change in plate motion (Mao et al., 2005, 2006). In the EQO, relatively intensive far-field effects triggered widespread J3-K1 magmatism and polymetallic mineralization (Mao et al., 2008, 2010; Li et al., 2012a, b; Xie et al., 2017). This intensive magmatism, which introduced fluids, sulfur and other ore components into the upper crust, was probably caused by lithospheric thinning induced by the change in Paleo-Pacific plate motion, which was accompanied by delamination and thermal erosion (Mao et al., 2010; Li et al., 2012b; Xie et al., 2017). In the WQO, no J3-K1 magmatism has been reported, which indicates a relatively low heat flow and fluid flux compared to that in EQO resulted from the lithospheric thinning (Li et al., 2012b). Geochemical evidence suggests that gold mineralization is genetically related to fluids produced by metamorphic devolatilization of underlying Paleozoic sediments. We propose that differences in the fluid sources and mineralization style of J3-K1 ages in the WQO and EQO are likely related to differences in their respective distances from the subduction front of the Paleo-Pacific plate.

To conclude, we propose that gold mineralization of J3-K1 ages in the WQO is mostly controlled by the NE or EW-trending brittle structures and was driven to some extent by the far-effects of subduction of Paleo-Pacific plate. Better recognition and models for these structures are critical to successful exploration of J3-K1 gold deposits in the WQO.

2.7 Conclusion

Integration of the regional tectonics with geochronology suggests that J3-K1 gold deposits in the WQO are a consequence of far-field effects of Mesozoic subduction of the Paleo-Pacific plate beneath the Eurasian continent. J3-K1 changes in plate motion resulted in N-S trending extension and formation of NE and EW-trending brittle structures that controlled fluid flow and gold deposition. The sources of sulfur and ore fluids in the J3-K1 age Daqiao deposit were produced by metamorphic devolatilization of the underlying Paleozoic trace element-rich sediments, which is unlike the intrusion-related deposits in the EQO. It may be that the differences in fluid source and mineralization style of J3-K1 gold deposits in the WQO and EQO

are related to differences in their respective distances from the subduction front of the Paleo-Pacific plate, with important implications for the timescales and lateral extent of subduction-related effects on gold mineralization.

2.8 Acknowledgments

We acknowledge the valuable support from Daqiao Mining Ltd. and the Geological Survey of Gansu Province for access to samples and information about the Daqiao deposit. Research work was financially supported by the National Natural Science Foundation of China (grant 41325007), the GPMR State Key Laboratory (grant MSFGPMR03), the China Geological Survey (grant 1212011120570), and National Demonstration Center for Experimental Mineral Exploration Education at China University of Geosciences (Wuhan). The senior author acknowledges the receipt of a Chinese Scholarship Council/Curtin International Postgraduate Research Scholarship. This paper benefited from constructive reviews from Albert H Hofstra and other three anonymous reviewers. Ours thanks go to editorial suggestions from editor Christopher Spencer.

2.9 References

Belousov, I., Large, R.R., Meffre, S., Danyushevsky, L.V., Steadman, J., Beardsmore, T., 2016. Pyrite compositions from VHMS and orogenic Au deposits in the Yilgarn Craton, Western Australia: Implications for gold and copper exploration. Ore Geology Reviews 79, 474-499.

Bi, S.H., Li, Z.K., Tang, K.F., Gao, K., 2016. LA–ICP–MS in situ trace element analysis of pyrite from Dongtongyu gold deposit and its metallogenic significance. Earth Science 41, 1121-1140.

Brill, B.A., 1989. Trace-element contents and partitioning of elements in ore minerals from the CSA Cu-Pb-Zn deposit, Australia, and implications for ore genesis. The Canadian Mineralogist 27, 263-274.

Chen, Y., 1994. Sources of ore-forming materials in the Liba gold deposit, west Qinling orogen. Northwestern Geology 15, 5-9.

Chen, Y.J., Zhang, J., Zhang, F.X., Franco, P., Li, C., 2004. Carlin and Carlin-like gold deposits in the Western Qinling Mountains and their metallogenic time, tectonic setting and model. Geological Review 50, 134-152.

Choi, S.G., Kwon, S.T., Ree, J.H., So, C.S., Pak, S.J., 2005. Origin of Mesozoic gold mineralization in South Korea. The Island Arc 14, 102-114.

Diener, A., Neumann, T., 2010. Synthesis and incorporation of selenide in pyrite and mackinawite. Radiochimica Acta 99, 791-798.

Dong, Y.P., Zhang, G.W., Neubauer, F., Liu, X.M., Genser, J., Hauzenberger, C., 2011. Tectonic evolution of the Qinling orogen, China: Review and synthesis. Journal of Asian Earth Sciences 41, 213-237.

Dong, Y.P., Liu, X.M., Neubauer, F., Zhang, G.W., Tao, N., Zhang, Y.G., Zhang, X.N., Li, W., 2013. Timing of Paleozoic amalgamation between the North China and South China Blocks: Evidence from detrital zircon U-Pb ages. Tectonophysics 586, 173-191.

Dong, Y.P., Santosh, M., 2016. Tectonic architecture and multiple orogeny of the Qinling orogenic belt, central China. Gondwana Research 29, 1-40.

Fan, H.R., Zhai, M.G., Xie, Y.H., Yang, J.H., 2003. Ore-forming fluids associated with granite-hosted gold mineralization at the Sanshandao deposit, Jiaodong gold province, China. Mineralium Deposita 38, 739-50.

Fan, H.R., Hu, F.F., Wilde, S.A., Yang, K.F., Jin, C.W., 2011. The Qiyugou gold-bearing breccia pipes, Xiong'ershan region, central China: fluid inclusion and stable-isotope evidence for an origin from magmatic fluids. International Geology Review 53, 25-45.

Faure, G., 1986. Principles of Isotope Geology, 2nd edition. John Wiley and Sons, New York, 1779 pp.

Gansu Geological Survey, 2011. Verification report of reserve resource at Daqiao gold deposit, Xihe County, Gansu Province, unpublished report (in Chinese).

Genna, D., Gaboury, D., 2015. Deciphering the hydrothermal evolution of a VMS system by LA–ICP–MS using trace elements in pyrite: An example from the Bracemac-McLeod deposits, Abitibi, Canada, and implications for exploration. Economic Geology 110, 2087-2108.

Gilbert, S.E., Danyushevsky, L.V., Rodemann, T., Shimizu, N., Gurenko, A., Meffre, S., Thomas, H., Large, R.R., Death, D., 2014. Optimisation of laser parameters for the analysis of sulphur isotopes in sulphide minerals by laser ablation ICP-MS.

Journal of Analytical Atomic Spectrometry 29, 1042-1051.

Goldfarb, R.J., Phillips, G.N., Nokleberg, W.J., 1998. Tectonic setting of synorogenic gold deposits of the Pacific Rim. Ore Geology Reviews 13, 185-218.

Goldfarb, R.J., Hart, C., Davis, G., Groves, D., 2007. East Asian gold: Deciphering the anomaly of Phanerozoic gold in precambrian cratons. Economic Geology 102, 341-345.

Goldfarb, R.J., Taylor, R.D., Collins, G.S., Goryachev, N.A., Orlandini, O.F., 2014. Phanerozoic continental growth and gold metallogeny of Asia. Gondwana Research 25, 48-102.

Gong, Y.J., 2014. The study on the tectonic-fluid system and metallogeni mechanism of Shuangwang gold deposit in Shaanxi Province. Ph.D. thesis, China University of Geosciences (Wuhan), 101p.

Hu, Q.Q., 2015. The mineralization features, mechanism and metallogenic regularity of the Fengtai Pb-Zn polymetallic ore cluster in West Qinling, China (in Chinese). Ph.D. thesis, Chinese Academy of Geological Sciences, 150 pp.

Hua, R.M., Chen, P.R., Zhang, W.L., Yao, J.M., Lin, J.F., Zhang, Z.S., Gu, S.Y., Liu, X.D., Qi, H.W., 2005. Metallogenesis related to Mesozoic granitoids in the Nanling Range, South China and their geodynamic settings. Acta Geologica Sinica 79, 810-820.

Huang, W.K., Gan, X.P., Shan, Z.X., Chen, L.X., Liu, Y., 1996. A study of petrology and metallognetic epoch of gold in Jianchaling deposit, Shaanxi Province. Geochimica 25, 150-156.

Huston, D.L., Sie, S.H., Suter, G.F., Cooke, D.R., Both, R.A., 1995. Trace elements in sulfide minerals from eastern Australian volcanic-hosted massive sulfide deposits; Part I, Proton microprobe analyses of pyrite, chalcopyrite, and sphalerite, and Part II, Selenium levels in pyrite; comparison with delta ^{34}S values and implications for the source of sulfur in volcanogenic hydrothermal systems. Economic Geology 90, 1167-1196.

Keith, M., Smith, D.J., Jenkin, G.R., Holwell, D.A., Dye, M.D., 2018. A review of Te and Se systematics in hydrothermal pyrite from precious metal deposits: insights into ore-forming processes. Ore Geology Reviews 96, 269-282.

Koppers, A.A.P., Staudigel, H., Duncan, R.A., 2003. High-resolution $^{40}Ar/^{39}Ar$ dating of the oldest oceanic basement basalts in the western Pacific basin. Geochemistry, Geophysics, Geosystems 4, 8914.

Lan, T.G., Fan, H.R., Santosh, M., Hu, F.F., Yang, K.F., Yang, Y.H., Liu, Y., 2011. Geochemistry and Sr-Nd-Pb-Hf isotopes of the Mesozoic Dadian alkaline intrusive complex in the Sulu orogenic belt, eastern China: Implications for crust–mantle interaction. Chemical Geology 285, 97-114.

Large, R.R., Danyushevsky, L., Hollit, C., Maslennikov, V., Meffre, S., Gilbert, S., Bull, S., Scott, R., Embsbo, P., Thomas, H., Singh, B., Foster, J., 2009. Gold and trace element zonation in pyrite using a laser imaging technique: Implications for the timing of gold in orogenic and Carlin style sediment-hosted deposits. Economic Geology 104, 635-668.

Large, R.R., Halpin, J.A., Danyushevsky, L.V., Maslennikov, V.V., Bull, S.W., Long, J.A., Gregory, D.D., Lounejeva, E., Lyons, T.W., Sack, P.J., McGoldrick, P.J., Calve, C.R., 2014. Trace element content of sedimentary pyrite as a new proxy for deep-time ocean-atmosphere evolution. Earth and Planetary Science Letters 389, 209-220.

Li, F.D., Zou, X.H., Gao, J.P., Lu, Y., Zhang, H.Y., 2001. On the rapid-positioning and prediction for micro dissemination type (sedimentary rock host) gold deposit (ore bodies), Ma'anqiao. Northwestern Geology 34, 27-63.

Li, J.W., Vasconcelos, P.M., Zhang, J., Zhou, M.F., Zhang, X.J., Yang, F.H., 2003. $^{40}Ar/^{39}Ar$ constraints on a temporal link between gold mineralization, magmatism, and continental margin transtension in the Jiaodong gold province, eastern China. The Journal of geology 111, 741-751.

Li, J.W., Vasconcelos, P.M., Zhou, M.F., Zhao, X.F., Ma, C.Q., 2006. Geochronology of the Pengjiakuang and Rushan gold deposits, eastern Jiaodong gold province, northeastern China: implications for regional mineralization and geodynamic setting. Economic Geology 101, 1023-1038

Li, J.W., Li, Z.K., Zhou, M.F., Chen, L., Bi, S.J., Deng, X.D., Qiu, H.N., Cohen, B., Zhao, X.F., 2012a. The Early Cretaceous Yangzhaiyu lode gold deposit, North China Craton: a link between craton reactivation and gold veining. Economic Geology 107, 43-79.

Li, J.W., Bi, S.J., Selby, D., Chen, L., Vasconcelos, P., Thiede, D., Zhou, M.F., Zhao, X.F., Li, Z.K., Qiu, H.N., 2012b. Giant Mesozoic gold provinces related to the destruction of the North China craton. Earth and Planetary Science Letters 349, 26-37.

Li, J.Y., Wang, Z.Q., Zhao, M., 1999. $^{40}Ar/^{39}Ar$ thermochronological constraints on the

timing of collisional orogeny in the Mian-Lue collision belt, southern Qinling Mountains. Acta Geologica Sinica 73, 208-215.

Li, S.G., Sun, W.D., Zhang, G.W., 1996. Chronology and geochemistry of metavolcanic rocks from Heigouxia valley in Mian-Lue tectonic belt, South Qinling: evidence for a Paleozoic oceanic basin and its close time. Science in China (Series D) 39, 300-310.

Lin, Z.W., Zhou, Y.Z., Qin, Y., Yue, S.W., 2017. Fuchsite $^{40}Ar/^{39}Ar$ geochronology of the Huachanggou gold Deposit and its tectonic implications. Geotectonica et Metallogenia 41, 315-327 (in Chinese with English abs.)

Liu, J.J., Zheng, M.H., 1993. La'erma Se-Cu-U-Ni-Mo-PGE-Au deposit of submarine exhalative genesis in La'erma. Journal of Precious Metallic Geology 2, 100-103.

Liu, J.J., Zheng, M.H, Liu, J.M., Su, W.C., 2000. Geochemistry of the La'erma and Qiongmo Au-Se deposits in the western Qinling Mountains, China. Ore Geology Reviews 17, 91-111.

Liu, J.J., Dai, H.Z., Zhai, D.G., Wang, J.P., Wang, Y.H., Yang, L.B., Mao, G.J., Liu, X.H., Liao, Y.F., Yu, C., Li, Q.Z., 2015. Geological and geochemical characteristics and formation mechanisms of the Zhaishang Carlin-like type gold deposit, western Qinling Mountains, China. Ore Geology Reviews 64, 273-98.

Liu, X.L., Wang, Y.T., Hu, Q.Q., Wei, R., Wang, R.T., Wen, S.W., Chen, M.S., Yang, G.H., 2014. Sm-Nd isotopic dating of carbonate minerals from the Chaima gold deposit in the Fengxian-Taibai ore concentration area, Shaanxi Province and its implications. Acta Petrologica Sinica 30: 271-280 (in Chinese with English abs.)

Liu, Y.H., Li, Z., Zhou, S., Han, Y.X., Li, H., Li, X., Zhou, S.F., 2015. Geological characteristics, ore-forming ages and geological significance of Donggou-Jinlongshan gold deposit, South Qinling belt. Earth Science Frontiers 22, 1-13.

Loftus-Hills, G., Solomon, M., 1967. Cobalt, nickel and selenium in sulphides as indicators of ore genesis. Mineralium Deposita 2, 228-242.

Longerich, H.P., Jackson, S.E., Günther, D., 1996. Laser ablation inductively coupled plasma mass spectrometric transient signal data acqusition and analyte concentration calculation. Journal of Analytical Atomic Spectroscopy 11, 899-904.

Lu, Y.M., Li, H.G., Chen, Y.G., Zhang, G.L., 2006. $^{40}Ar/^{39}Ar$ dating of alteration minerals from Zhaishang gold deposit in Minxian County, Gansu Province, and

its geologic significance. Mineral Deposits 25, 590-597.

Meng, Q.R., Zhang, G.W., 1999. Timing of collision of the North and South China blocks: Controversy and reconciliation. Geology 27, 123-126.

Mao, J.W., Qiu, Y.M., Goldfarb, R.J., Zhang, Z.C, Garwin, S., Fengshou, R., 2002. Geology, distribution, and classification of gold deposits in the western Qinling belt, central China. Mineralium Deposita 37, 352-377.

Mao, J.W., Xie, G.Q., Zhang, Z.H., Li, X.F., Wang, Y.T., Zhang, C.Q., Li, Y.F., 2005. Mesozoic large-scale metallogenic pulses in North China and corresponding geodynamic settings. Acta Petrologica Sinca 21, 169-188.

Mao, J.W., Wang, Y.T., Lehmann, B., Yu, J.J., Du, A.D., Mei, Y.X., Li, Y.F., Zang, W.S., Stein, H.J., Zhou, T.F., 2006. Molybdenite Re-Os and albite $^{40}Ar/^{39}Ar$ dating of Cu-Au-Mo and magnetite porphyry systems in the Yangtze River valley and metallogenic implications. Ore Geology Review 29, 307-324.

Mao, J.W., Xie, G.Q., Bierlein, F., Qu, W.J., Du, A.D., Ye, H.S., Pirajno, F., Li, H.M., Guo, B.J., Li, Y.F., Yang, Z.Q., 2008. Tectonic implications from Re-Os dating of Mesozoic molybdenum deposits in the East Qinling-Dabie orogenic belt. Geochimica et Cosmochimica Acta 72, 4607-4626.

Mao, J.W., Xie, G.Q., Pirajno, F., Ye, H.S., Wang, Y.B., Li, Y.F., Xiang, J.F., Zhao, H.J., 2010. Late Jurassic-Early Cretaceous granitoid magmatism in Eastern Qinling, central-eastern China: SHRIMP zircon U-Pb ages and tectonic implications. Australian Journal of Earth Sciences 57, 51-78.

Mitchell, K., Mason, P.R., Van Cappellen, P., Johnson, T.M., Gill, B.C., Owens, J.D., Diaz, J., Ingall, E.D., Reichart, G.J., Lyons, T.W., 2012. Selenium as paleo-oceanographic proxy: A first assessment. Geochimica et Cosmochimica Acta 89, 302-317.

Molnar, P., Tapponnier, P., 1975. Cenozoic tectonics of Asia: effects of a continental collision. Science 189, 419-426.

Müller, W., Shelley, M., Miller, P., Broudec, S., 2009. Initial performance metrics of a new custom-designed ArF excimer LA-ICPMS system coupled to a two-volume laser-ablation cell. Journal of Analytical Atomic Spectrometry 24, 209-214.

Nie, F.J., Jiang, S.H., Zhao,Y.M., 2001. Lead and sulfur isotope study of the Wenyu and Dongchuang quartz vein-type gold deposits in the Xiaoqinling area, Henan and Shaanxi Province, central China. Mineral.Deposita 20, 163-173.

Niu, B.G., He, Z.J., Song, B., Ren, J.S., 2003. SHRIMP dating of the Zhangjiakou

volcanic series and its significance. Geological Bulletin of China 22, 140-141.

Price, B.J., 1972. Minor elements in pyrites from the Smithers map area, British Columbia and exploration applications of minor element studies: M.S. thesis, The University of British Columbia, 270 pp.

Qi, J.Z., Yuan, S.S., Li, L., Sun, B., Guo, J.H., Li, Z.H., Fan, Y.X., Liu, W., Gao, Q.B., 2003. Geological features and ore-controlling factors of the Yangshan superlarge gold deposit, Gansu province, China. Geological Review 49, 85-92.

Qi, J.Z., Yang, G.C., Li, L., Fan, Y.X., Liu, W., 2006. Isotope geochemistry, chronology and genesis of the Yangshan gold deposit, Gansu. Geology in China 33, 1345-1353.

Qiu, Y.M., Groves, D.I., McNaughton, N.J., Wang, L.G., Zhou, T.H., 2002. Nature, age, and tectonic setting of granitoid-hosted, orogenic gold deposits of the Jiaodong Peninsula, eastern North China craton, China. Mineralium Deposita 37, 283-305.

Ratschbacher, L., Hacker, B.R., Calvert, A., Webb, L.E., Grimmer, J.C., McWilliams, M.O., Hu, J., 2003. Tectonics of the Qinling (Central China): tectonostratigraphy, geochronology, and deformation history. Tectonophysics 366, 1-53.

Ren, J.S., Chen, T.Y., Niu, B.G., 1992. Tectonic evolution of the continental lithosphere of the East China and adjacent area and relevant mineralization. Science Press, Beijing, 230 pp.

Shan, L., Zhang, D.M., Pang, Y.C., Liu, J.J., Zhang, W.Y., Zhao, M.M., Zhang, Z.P., 2016. Late Triassic magmatic activity in the Daqiao gold deposit of West Qinling belt: Zircon U-Pb chronology and Lu-Hf isotope evidence. Geological Bulletin of China 35, 2045-2057.

Shi, Z.L., Liu, J.X., Fan, S.C., 1989. Geological characteristics and genesis of Shuangwang gold deposit, Shaanxi province. Science and Technology Publishing House of Shaanxi, Xi'an, 98pp.

Sun, W.D., Li, S.G., Chen, Y.D., Li, Y.J., 2002. Timing of synorogenic granitoids in the South Qinling, central China: Constraints on the evolution of the Qinling-Dabie orogenic belt. Journal of Geology 110, 457-468.

Sun, W.D., Ding, X., Hu, Y.H., Li, X.H., 2007. The golden transformation of the Cretaceous plate subduction in the west Pacific. Earth and Planetary Science Letters 262, 533-542.

Sun, W.D., Ling, M.X., Yang, X.Y., Fan, W.M., Ding, X., Liang, H.Y., 2010. Ridge subduction and porphyry copper-gold mineralization: An overview. Science

China Earth Sciences 53, 475-84.

Sun, W.D., Li, S., Yang, X.Y., Ling, M.X., Ding, X., Duan, L.A., Zhan, M.Z., Zhang, H., Fan, W.M., 2013. Large-scale gold mineralization in eastern China induced by an Early Cretaceous clockwise change in Pacific plate motions. International Geology Review 55, 311-21.

Tan, G.Y., 1992. Geological character of Pingding As-Au deposit and its metallogenic mechanism. Acta Geologica Gansu 1, 48-54.

Tapponnier, P., Molnar, P., 1979. Active faulting and Cenozoic tectonics of the Tien Shan, Mongolia, and Baykal regions. Journal of Geophysical Research: Solid Earth 84, 3425-3459.

Thomas, H.V., Large, R.E., Bull, S.W., Maslennikov, V., Berry, R.F., Fraser, R., Froud, S., Moye, R., 2011. Pyrite and pyrrhotite textures and composition in sediments, laminated quartz veins, and reefs at Bendigo gold mine, Australia: Insights for ore genesis. Economic Geology 106, 1-31.

Tu, H.K., 2008. Discovery and application of the Qinling Se deposit with its forming mechanism research. Mineral Resources and Geology 22, 27-32.

Wang, L.S., 2009. Study on the metallogenic regularity and geological-geochemistry for black rock series and related typical deposits in Qinling Mountains, Shaanxi. Ph.D. thesis, Northwest University, 165 pp.

Wang, Y.T., Li, X., Wang, R.T., Liu, X.L., Hu, Q.Q., Li, J.H., 2014. Evidence of Ar-Ar age for the metallogenic epoch of Simaoling gold deposit in Fengxian-Taibai ore cluster of Shaanxi. Journal of Earth Science and Environment 36, 61-72.

Wilson, S.A., Ridley, W.I. Koenig, A.E., 2002. Development of sulfide calibration standards for the laser ablation inductively coupled plasma mass spectrometry technique. Journal of Analytical Atomic Spectroscopy 17, 406-409.

Wong, K.H., Zhou, M.F., Chen, W.T., O'Brien, H., Lahaye, Y., Chan, S.L.J., 2017. Constraints of fluid inclusions and in-situ S-Pb isotopic compositions on the origin of the North Kostobe sediment-hosted gold deposit, eastern Kazakhstan. Ore Geology Reviews 81, 256-269.

Wu, F.F., Wang, Z.Q., Yan, Z., Chen, L., Xia, C.L., Guo, Y.H., Peng, Y.M., 2014. Geochemical characteristics, zircons U-Pb ages and Lu-Hf isotopic composition of the Yanshanian intermediate-acidic plutons in the Shanyang-Zhashui areas, Qinling Orogenic Belt. Acta Petrologica Sinica 30, 451-471.

Wu, Y.F., Li, J.W., Evans, K., Koenig, A.E., Li, Z.K., O'Brien, H., Lahaye, Y., Rempel,

K., Hu, S.Y., Zhang, Z.P., Yu, J.P., 2018a. Ore-Forming Processes of the Daqiao Epizonal Orogenic Gold Deposit, West Qinling Orogen, China: Constraints from Textures, Trace Elements, and Sulfur Isotopes of Pyrite and Marcasite, and Raman Spectroscopy of Carbonaceous Material. Economic Geology 113, 1093-1132.

Wu, Y.F., Li, J.W., Evans, K., Vasconcelos, P.M., Thiede, D.S., Fougerouse, D., Rempel, K., 2018b. Late Jurassic to Early Cretaceous age of the Daqiao gold deposit, West Qinling Orogen, China: Implications for regional metallogeny. Mineralium Deposita. https://doi.org/10.1007/s00126-018-0835-z

Xie, G.Q., Mao, J.W., Wang, R.T., Meng, D.M., Sun, J., Dai, J.Z., Ren, T., Li, J.B., Zhao, H.J., 2017. Origin of the Lengshuigou porphyry-skarn Cu deposit in the Zha-Shan district, South Qinling, central China, and implications for differences between porphyry Cu and Mo deposits. Mineralium Deposita 52, 621-639.

Yang, C.H., Wei, C.J., Zhang, S.G., Li, H.M., Wan, Y.S., Li, R.S., 1999. U-Pb zircon dating of granulite facies rocks from the Foping area in the southern Qinling mountains. Geological Review 45, 173-179.

Zeng, Q.T., McCuaig, T.C., Hart, C.J.R., Jourdan, F., Muhling, J., Bagas, L., 2012. Structural and geochronological studies on the Liba goldfield of the West Qinling Orogen, Central China. Mineralium Deposita 47, 799-819.

Zeng, Q.T, Mccuaig, T.C., Tohver, E., Bagas, L., Lu, Y.J., 2014. Episodic Triassic magmatism in the western South Qinling Orogen, central China, and its implications. Geological Journal 49, 402-423.

Zhai, Y., Deng, J., 1996. Outline of the mineral resources of China and their tectonic setting. Australian Journal of Earth Sciences 43, 673-685.

Zhang, F.X., Chen, Y.J., Li, C., Zhang, J., Ma, J.Q., Li, X., 2000. Features of geologic-geochemistry of Jinlongshan-Qiuling gold deposit and its genesis in Qinling belt: Dynamics on mineralizing process of Carlin type gold deposits of Qinling type. Science in China Series D: Earth Sciences 30 (Suppl.), 73-81.

Zhang, G.W., Zhang, Z.Q., Dong, Y.P., 1995. Nature of main tectono-lithostratigraphic units of the Qinling Orogen: implications for the tectonic evolution. Acta Petrologica Sinica 11, 101-114.

Zhang, G.W., Zhang, B.R., Yuan, X.C., Xiao, Q.H., 2001. Qinling orogenic belt and continental dynamics. Science Press, Beijing, 855 pp (in Chinese).

Zhang, J., 2016. Study of mineralization process and mechanism in Baguamiao super

large gold deposit, Fengtai ore region, Shaanxi, China. Ph.D. thesis, Chinese Academy of Geological Sciences, 200 pp.

Zhang, J., Li, L., Gilbert, S., Liu, J.J., Shi, W.S., 2014. LA–ICP–MS and EPMA studies on the Fe-S-As minerals from the Jinlongshan gold deposit, Qinling Orogen, China: implications for ore-forming processes. Geological Journal. 49, 482-500.

Zhang, Z.P, Wu, Y.F, Li, J.W., 2018. Characteristics and Genesis of the silicified breccias in the Daqiao gold deposit, West Qinling Orogen: Geological Science and Technology Information 37, 79-88.

Zhang, Z.Q., Zhang, G.W., Tang, S.H., Wang, J.H., Xu, J.F., Yang, Y.C., 2002. Age of Anzishan granulites in the Mianxian-Lueyang suture zone of Qinling orogen: with a discussion of the timing of final assembly of Yangtze and north China craton blocks. Chinese Science Bulletin 47, 1925-1929.

Chapter 3

A preliminary experimental investigation of gold solubility in silica-bearing liquids

This chapter describes laboratory work to investigate gold (Au) solubility (i.e., total dissolved Au) in amorphous SiO_2-bearing liquids including silica (Si) gel solution and colloidal Si suspension. It is the first time that Au solubility experiments have been carried out in such two silica-bearing liquids, though two previous studies have been done on Au solubility in SiO_2-NaCl-H_2O and Na_2SiO_3-H_2O solutions (Zeng et al., 1997; Fan et al., 2001). Preliminary results show dissolved Au concentrations in the colloidal Si solutions are comparable to the Au concentrations reported from different Si and other ligands-rich geothermal fluids, analogous to the mineralizing fluids for giant Au deposits (Simmons and Brown, 2006, 2007). We suggest that silica-bearing fluids are capable of stabilizing and transporting dissolved Au in various hydrothermal Au systems in Earth's crust.

3.1 Introduction

The deposition of silica (Si) is abundant throughout the lifetimes of hydrothermal vein and disseminated mineralization in the upper crust, and is present in various forms including amorphous opal, chalcedony, and crystalline quartz (e.g., Fournier, 1985; Saunders, 1990, 1994; Dong et al., 1995; Saunders and Schoenly, 1995; Sherlock and Lehrman, 1995; Bowell et al., 1999; Cline and Hofstra, 2000; Lubben et al., 2012). It has been suggested that the co-occurrence of hydrothermal Si and ore minerals is an indicator that Si plays a role in ore-forming fluids in transporting and concentrating metals to economic grades (Herrington and Wilkinson, 1993; Wilkinson et al., 1996; Hough et al., 2011; Prokofiev et al., 2017). A clear understanding of the chemistry and stability of metal complexes in aqueous silica-bearing systems is critical for quantitative interpretations of metal transport

and deposition mechanisms during hydrothermal mineralization, however, few experimental studies have focused on the ore-forming media of Si.

Silicification is the primary hydrothermal alteration in hydrothermal Au deposits and multiple generations of hydrothermal Si are spatially associated with native gold, auriferous sulfides and sulfarsenides (e.g., Saunders, 1990, 1994; Cline and Hofstra, 2000). The positive correlation between the intensity of silicification and Au grade in ores can be used as an ore exploration vector (Wu et al., 2018). It has been suggested that colloidal Au is shielded by colloidal Si and the combined colloids are stable up to 350°C (Frondel, 1938), and undergo mechanical transport during upwards-directed migration of hydrothermal fluids in the formation of epithermal to mesothermal and hot-spring-type bonanza-grade Au veins (e.g., 100–1000 g/t; Saunders, 1990, 1994; Herrington and Wilkinson, 1993; Sherlock and Lehrman, 1995). However, the colloidal Si-Au transport mechanism does not explain the intimate co-occurrence of dispersed hydrothermal silicification and invisible Au (i.e., submicron or lattice-bound Au)-rich sulfides in the low-grade but large-tonnage Carlin and other sediment-hosted disseminated Au deposits (e.g., 1–10 g/t; Bowell et al., 1999; Cline and Hofstra, 2000; Lubben et al., 2012).

Previous experimental studies have suggested that the dissolved Au in hydrothermal fluids is transported predominantly as chloride complexes (e.g., $AuCl_2^-$ and $AuCl_2H$; Gammons and Williams-Jones, 1995; Frank et al., 2002; Stefánsson and Seward, 2003b; see review by Williams-Jones et al., 2009), sulfide complexes such as $AuHS^0$, $Au(HS)_2^-$, and $Au_2(HS)_2S^{2-}$ (Seward, 1973; Shenberger and Barnes, 1989; Benning and Seward, 1996; Stefánsson and Seward, 2004), and aqueous hydroxide complexes (i.e., $AuOH^-$; Stefánsson and Seward, 2003a). Alternatively, two sets of experiments by Zeng et al. (1997) and Fan et al. (2001) suggested that the dissolved Au can be complexed as $AuOH^0$, $AuOHCl^-$, and/or $AuH_3SiO_4^0$ in SiO_2-NaCl-H_2O and Na_2SiO_3-H_2O systems. However, the involvement of different ligands in these two systems makes it hard to evaluate the possible contribution of Si to the Au solubility.

Here, we summarize representative petrological evidence for the intimate association of amorphous Si and auriferous spherular pyrite in an epizonal orogenic gold deposit (Daqiao, China; Wu et al., 2018), and present the results of a preliminary experimental study to characterize the Au solubility in silica-bearing liquids including Si gel solution and colloidal Si suspension at 200 °C and water-saturated

vapor pressure (Psat). The data are discussed in the context of Au solubility in natural Si-rich geothermal fluids, and the role of Si in stabilizing and transporting Au is assessed.

3.2 Intimate association of amorphous Si and Au-rich pyrite in nature

Here we present a typical textural observation of the close association of amorphous hydrothermal Si and invisible Au-rich pyrite at the Daqiao orogenic Au deposit, China. Three stages of silicification have been distinguished in the mine and are described in detail by Wu et al. (2018). In particular, in the hydrothermal cements of hydraulic breccia ores, two stages of silicification occur as chalcedony (Chc) together with minor calcite (Cc) precipitating coevally with the aggregates of pyrite (Figure 3.1a). Framboidal aggregates of numerous fine-grained (~1 μm) pyrite grains in the chalcedony veinlets (Figure 3.1b and c) are enriched in invisible Au (mean 27 ppm Au; LA–ICP–MS analysis; Wu et al., 2018). Chalcedony displays distinct colloform bands and hosts concentrically zoned or irregularly distributed fine-grained (~5 μm) spherical pyrite grains (Figure 3.1d-f). Aggregates of chalcedony spherules enclosing fine-gained pyrite euhedra (Figure 3.1 g and h) are analogous to the described turbid chalcedonic spherules in the Voltri mesothermal Au-quartz veins, Italy (Figure 3.1i), which have been suggested to crystallize from a Si gel (Herrington and Wilkinson, 1993). The association of amorphous Si and auriferous pyrite at Daqiao and other Au deposits thus indicates that the invisible Au deposition is closely associated with a Si-rich mineralizing fluid.

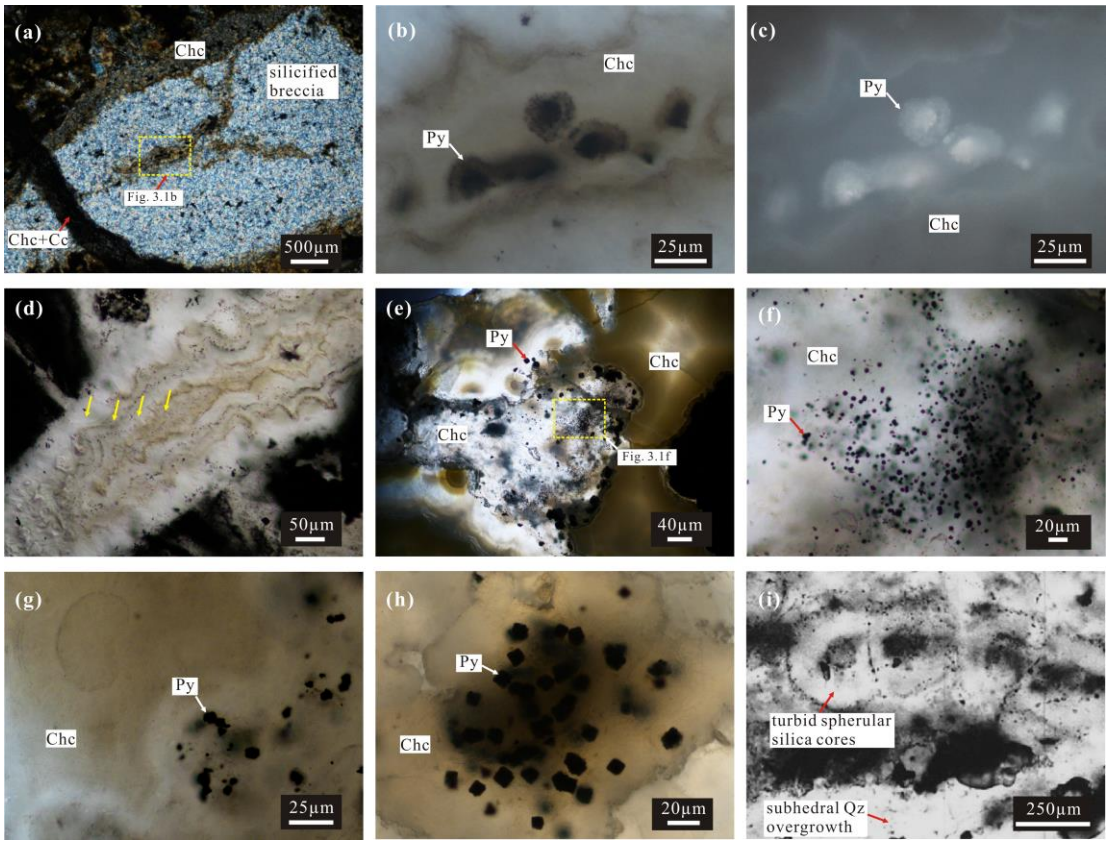

Figure 3.1 Transmitted- (a, b, and d-i) and reflected-light (c) photomicrographs showing the close association of hydrothermal chalcedony (Chc) and invisible Au-rich pyrite (Py) grains at the Daqiao Au deposit. a) Chalcedony occurs as overgrowth on the margins of silicified breccias as well as veinlets in the fractures of breccias; Chc is in turn crosscut by later Chc-calcite (Cc) veinlets. b–c) Close-up of the area marked in Figure 3.1a containing framboidal aggregates of fine-grained Py (~1 μm) in Chc veinlets. d) Fine-grained Py in the colloform bands (marked with yellow arrows) of Chc. e) Turbid Chc containing opaque Py overgrown by zoned Py-free Chc. f) Close-up of the turbid Chc, which contains numerous fine-grained spherical Py grains. g) Spherical Chc containing Py grains. h) Aggregates of Chc spherules enclosing Py euhedras. i) Turbid spherical silica cores overgrown by quartz (Qz) from the Voltri Au deposit, Italy (Herrington and Wilkinson, 1993).

3.3 Experiments of Au solubility in silica-bearing liquids

3.3.1 Starting Si materials

Two silica-bearing starting materials, silica gel granules and colloidal silica suspension normally used as a desiccant and a polishing solution, respectively, were chosen to produce the different silica-bearing liquids used in the experiments. Silica gel granules with particle size of 4 mm and pH of 2.5 (~20 °C) were provided by *Sorbsil-Chameleon*. The Si gel contains ≥ 93 wt. % amorphous $SiO_2.xH_2O$ and ≤ 5

wt. % ammonium iron sulfate dodecahydrate [$NH_4Fe\ (SO_4)_2 \cdot 12\ H_2O$]. Colloidal Si suspension provided by *Struers* contains 10–30 vol. % amorphous SiO_2, 50–70 vol. % H_2O, and 5–20 vol. % 1, 3-Butandiol ($C_4H_{10}O_2$), with the pH of 9–10 at 20 °C to prevent the colloidal Si sol from spontaneous coagulation.

3.3.2 Apparatus

Gold solubility experiments in Si gel solution were conducted in 45 mL Teflon-lined stainless steel autoclaves, *Parr Instrument Co*. This apparatus is useful for experiments at temperatures to 250 °C and pressures to 124 bar. Detailed components of the steel autoclaves and reactants are shown in Figure 3.2. Another set of experiments using colloidal Si suspension was conducted in machined 45 ml screw-top titanium autoclaves, which are also suitable for the temperature and pressure of interest in this study that is 200°C, with Psat of 15.5 bar calculated using *SteamTab, ChemicaLogic Co.*

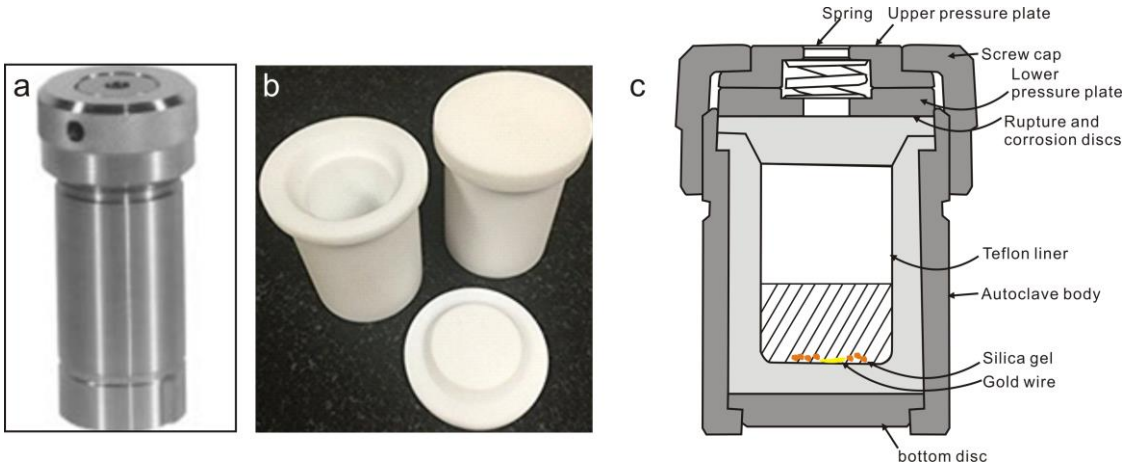

Figure 3.2 Stainless steel autoclave (a), Teflon-liners (b), and a schematic of an assembled autoclave filled with Si gel granules, Au wire, and Milli-Q water (c) used in the Si gel experiments.

3.3.3 Experimental strategy

All equipment was cleaned with aqua regia for 24 hours at room temperature to remove any Au contamination, and then with ultra-pure Milli-Q water to clean the residual aqua regia (HNO_3 and HCl in a 1:3 molar ratio) before each experiment. Both the Teflon-lined and titanium autoclaves were pre-tested with pure water at 200 °C in furnace for 24 hours to ensure that they sealed properly. To avoid potential metal contamination from titanium autoclaves, the inner walls of the titanium vessels

were passivated to produce a protective coating of TiO_2 by adding 10 mL ultra-pure HNO_3 (nitric acid, 67 vol. %) and heating at 100 °C for 24 hours.

Details of reactants in the two series of experiment are summarized in Table 3.1 and Table 3.2. In series I, 6 runs in Teflon-lined autoclaves were loaded with an average of 0.011 g Au wire (standard deviation s.d. = 0.002 g), 0.021 g of Si gel (s.d. = 0.0004 g), and 9.97 g of Milli-Q H_2O (s.d. = 0.01 g; Figure 3.2c). Another 2 runs with 0.013 g Au wire plus 9.98 g Milli-Q H_2O, and 0.021 g Si gel plus 9.98 g Milli-Q H_2O, respectively, were conducted as blanks. In series II, 7 runs in titanium autoclaves were loaded with a mean of 10.76 g colloidal Si suspension (s.d. = 0.08 g) and 0.006 g Au wire (s.d. = 0.001 g). Two runs loaded only with colloidal Si suspension were used as blanks. All of these 15 runs were conducted at 200 °C and Psat of 15.5 bar in a furnace.

3.3.4 Sampling and Au–Si analysis

Solutions (~2–8 mL) in the autoclaves were sampled every 2 to 7 days. During sampling, each autoclave was removed from furnace and then placed in the water bath to quickly quench to room temperature, and then the remaining Au wire was removed from the solution and weighted. 3 mL aqua regia was added to wash the inner walls of the Teflon-liners and titanium vessels to dissolve any Au precipitates and to stabilize dissolved Au before analysis.

All solutions in series I were analyzed for Au and Si, while solutions and some Si solids in runs that leaked runs (see below) in series II plus two samples of pure colloidal Si suspension used as blanks were analyzed only for Au. The Au and Si analyses were conducted at the *LabWest Minerals Analysis Pty Ltd* in Perth using a Perkin Elmer Nexion 300 inductively coupled plasma mass spectrometer (ICP-MS), with a plasma power of 1300 W and flow rate of 0.9 L/min. The detection limits for analyses of Au and Si are 0.05 ppb and 0.05 ppm, respectively.

3.4 Results

3.4.1 Experiment series I

Analyses of the recovered solutions from a series of 4 Si gel experiments conducted at 200 °C over 7–28 days show that the total dissolved Au increases from 0.44 ppb (7 days) to 7.6 ppb (12 days), then decreases to 4.2 ppb (28 days), with an unrealistically high value of 9,100 ppb Au at 21 days (Table 3.1; Figure 3.3). The total dissolved Si displays a continuous increase from 1.02 ppm (7 days) through 88.4 ppm (14 days) to 192 ppm (21 days) before a decrease to 79.3 ppm (28 days). The two Au–Si concentrations in solutions at 12 days and 28 days show a mean value of 5.9 ppb Au and 83.9 ppm Si.

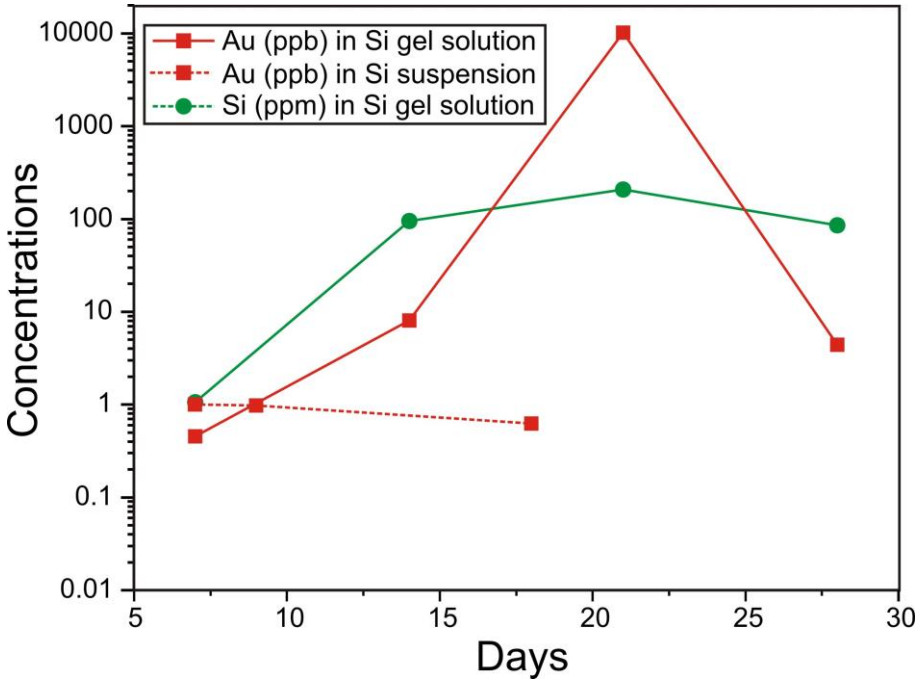

Figure 3.3 Concentrations of Au and Si in the two different colloidal silica-bearing liquids heated at 200°C and Psat as a function of time.

3.4.1 Experiment series II

Three analyses of the recovered colloidal Si suspensions heated at 200 °C show a slight decrease in Au concentration from 0.97 ppb (7 days) through 0.89 ppb (9 days) to 0.57 ppb (21 days) with a mean of 0.81 ppb Au (Table 3.2; Figure 3.3). Although all the autoclaves were pre-tested for sealing, silica-bearing solutions in 4 of 8 Teflon-lined autoclaves and 5 of 9 titanium autoclaves leaked after heating at 200 °C after 14 to 35 days (Tables 3.1 and 3.2). In titanium autoclaves that had undergone leakage, residual Si solids were sampled for Au analysis. For the 5 leaked titanium autoclaves, Au concentration in the residual Si solids was mostly below the detection

limit, with an exception of one sample with 0.09 ppb Au. Two pure colloidal Si suspension samples taken to measure as blanks contain no detectable Au (Table 3.2).

Table 3.1 Experimental data and concentrations of Au and Si in Si gel solutions (experiment series I) at 200°C and Psat.

Run No.	Auto No.	Days	H_2O (g)	Au wire (g)	Silica gel (g)	Au (ppb)	Si (ppm)	Note
Run-1	I	35	9.98	0.013	0.000	N.A.	N.A.	Leaked
Run-2	II	35	9.98	0.000	0.021	N.A.	N.A.	Leaked
Run-3	III	7	9.97	0.011	0.021	0.44	1.02	
Run-4	IV	14	9.98	0.009	0.020	7.6	88.4	
Run-5	V	21	9.95	0.014	0.021	9100	192	
Run-6	VI	21	9.95	0.008	0.020	N.A.	N.A.	Leaked
Run-7	VII	28	9.97	0.012	0.021	4.2	79.3	
Run-8	VIII	35	9.99	0.011	0.021	N.A.	N.A.	Leaked
Mean			9.97	0.011	0.021	4.08	56.24	
S.D.			0.01	0.002	0.0004	2.92	39.22	

Note: S.D. = standard deviation; N.A. = not analysed, due to the leaking of autoclaves; mean calculation of Au and Si excludes the Run-5.

Table 3.2 Experimental data and concentrations of Au in colloidal Si suspensions (experiment series II) at 200°C and Psat.

Run No.	Auto No.	Days	Silica suspension (g)	Au wire (g)	Au (ppb)	Note
Run-1	I’	7	10.73	0.0050	0.97	
Run-2	II’	9	10.73	0.0052	0.89	
Run-3	III‘	11	10.85	0.0084	< 0.05	
Run-4	II	14	10.74	0.0050	< 0.05	Leaked*
Run-5	III	17	10.65	0.0067	0.09	Leaked*
Run-6	IV	21	10.73	0.0055	0.57	
Run-7	VI'	25	10.71	0.0055	< 0.05	Leaked*
Run-8	VII'	25	10.91	0.0000	< 0.05	Leaked*
Run-9	Blank	25	10.83	0	N.A.	Leaked
SI	Blank	25	10.00	0.0000	< 0.05	Si suspension
SII	Blank	25	10.00	0.0000	< 0.05	Si suspension
Mean			10.76	0.006	0.63	
S.D.			0.08	0.001	0.35	

Note: S.D. = standard deviation; Leaked* = Autoclave leakage but Au was analysed in residual Si solids

3.5 Discussion

3.5.1 Gold solubility in two silica-bearing liquids at 200°C and Psat

Equilibrium concentrations of Au and Si

In series I of the experiments using Si gel solution, in spite of the limited runs, the Au and Si concentrations are correlated, and reach a generally stable concentration after 7–14 days (Figure 3.3). An unrealistic Au spike of 9100 ppb at 21 days is likely due to Au contamination either during the sampling process or ICP-MS analysis. The mean values of 5.9 ppb Au and 83.9 ppm Si from the two stable and analogous concentrations at 14 and 28 days possibly represent the equilibrium concentrations of Au and Si in the Si gel solutions at 200°C and Psat.

In series II of the experiments, using colloidal Si suspension, Au concentration fluctuates slightly between 0.57 and 0.97 ppb. These values are different to the blank value of <0.05 ppb. The mean value of 0.81 ppb Au might record the Au equilibrium concentration in the colloidal Si suspensions at 200°C and Psat (Figure 3.3).

Silica speciation

It has been suggested that the solubility of amorphous Si in water at temperatures of 0–250°C and Psat can be calculated using Eq. (1) (Fournier, 1977):

$$\text{Log } S_T = [-731/ (T+273.15)] + 4.52 \qquad (1)$$

Where S_T is the solubility of Si in mg/kg and T is the temperature in Celsius. The calculated solubility of amorphous Si at 200°C is 623 ppm, which is ~7 times the mean concentration of 83.9 ppm Si measured in the Si gel solutions. It might be that dissolved SiO_2 in Si gel solutions mainly occurs as silicic acid (H_4SiO_4) and $H_3SiO_4^-$ that form via Eqs. 2 and 3 (Zeng et al., 1997). In contrast, the 10–30 vol. % amorphous SiO_2 in the colloidal Si suspensions occurs as nanoscale colloidal particles (Si sol).

$$SiO_2 + 2H_2O = H_4SiO_4 \qquad (2)$$

$$H_4SiO_4 = H_3SiO_4^- + H^+ \qquad (3)$$

Gold complexation

In the Au-H_4SiO_4-H_2O system, it has been suggested that dissolved Au may occur in two forms: $AuOH^0$ via hydrolysis (Eq. 4; Stefánsson and Seward, 2003a), and $AuH_3SiO_4^0$ via complexation with H_4SiO_4 (Eq. 5; Fan et al., 2001):

$$Au + H_2O = AuOH^0 + 0.5H_2 \quad (4)$$

$$Au + H_4SiO_4 = AuH_3SiO_4^0 + 0.5H_2 \quad (5)$$

Zeng et al. (1997) argued that the $AuH_3SiO_4^0$ is absent in Au-H_4SiO_4-H_2O system due to the stable bonds of H^+ and O^{2-} in $H_4SiO_4^0$ so that H^+ is not readily substituted by Au^+ ions. Nevertheless, several lines of evidence in this study probably support the Si–Au complexation. Firstly, the measured dissolved Au concentrations are notably higher in the Si gel solutions compared to that in the colloidal Si suspensions (0.44–7.6 ppb vs. 0.57–0.97 ppb Au) at 200°C and Psat, with an exception at 7 days (Figure 3.3). The low dissolved Au concentration at 7 days in Si gel solution may be due to the low Si concentration (1.02 ppm Si; Table 3.1) at the beginning of the experiment. Secondly, the positive Si–Au correlation in Si gel solutions (Figure 3.3) indicates that Si may have played a role in the dissolution and/or complexation of Au. However, it's also possible that the two elements were dissolving in water independently.

In contrast, in the colloidal Si system, it has been suggested that Si colloids can shield and thus protect Au colloids both against electrolyte and against spontaneous coagulation to 350°C (Frondel, 1938). However, the Au concentration (mean 0.81 ppb) measured in colloidal Si suspensions suggests that the presence of colloidal Au particles is unlikely. Alternatively, Au could be complexed as $AuOH^0$ via hydrolysis in the colloidal Si suspensions.

Role of Au hydrolysis

Previous experiments by Stefánsson and Seward (2003a) have suggested that Au solubility in aqueous solution ranges from 2–400 ppb (300–600°C and 500–1500 bar), and increases with increasing temperature and/or decreasing pressure and hydrogen molality. In particular, at intermediate to alkaline pH and high temperature

(e.g., 300–600°C) in dilute solution, the decreased dielectric constant of H_2O can promote stable bonds between Au^+ and OH^- (Williams-Jones et al., 2009).

It is difficult to precisely estimate the concentration of dissolved Au complexed with hydroxyl at 200°C and Psat, but this concentration is expected to be reasonably lower than that measured at 300°C (2 ppb Au; Stefánsson and Seward, 2003a). Given the alkaline environment (*pH* of 9–10 at 20°C) in the colloidal Si suspensions, it is interesting to speculate if Au hydrolysis has played a major role in the Au dissolution and complexation. If this is the case, dissolved Au (mean 0.81 ppb) was dominantly complexed with hydroxyl in the form of $AuOH^0$ in Si suspensions at 200°C. In comparison, the formation of $AuOH^0$ complex would not have been favored in the Si gel solutions because of the acidic environment (pH of 2.5 at 20°C); OH^- concentrations are higher in higher *pH* solutions. If only the two Au complexes (i.e., $AuOH^0$ and $AuH_3SiO_4^0$) are taken into account, more than 5.1 ppb Au of the total 5.9 ppb dissolved Au in the Si gel solutions may be complexed with dissolved Si (Table 3.3). However, more experimental work is needed to further explore this hypothesis.

Influence of other impurities

It is also necessary to consider the potential influence of the impurities in the two silica-bearing liquids: the ≤ 5 wt. % ammonium iron sulfate dodecahydrate [$NH_4Fe(SO_4)_2 \cdot 12\ H_2O$] and 5–20 vol. % 1, 3-Butandiol ($C_4H_{10}O_2$) in the Si gel and colloidal Si suspensions, respectively. It has been suggested that Au-NH_3 complex [$Au(NH_3)_2^+$] could contribute to Au solubility in solutions at 300 °C, with a maximum in solubility at the N_2-NH_3-NH_4^+ triple point (Wood et al., 1992). However, $NH_{3\ (aq)}$ has been proved to be absent in acidic solution at 300 °C (Liu et al., 2014). Thus the ammonia contained in the iron sulfate dodecahydrate is unlikely to be an important ligand of dissolved Au in the acidic Si gel solutions.

A recent experimental study by Crede et al. (2018) has demonstrated that organic components such as sulfur-bearing 1-dodecanethiol play a role in the Au^{3+} reduction and formation of Au^+ complexation as $Au(RS)_2^-$ (RS is the 1-dodecanethiol with deprotonated thiol group) in organic solutions below 125 °C. Despite a lack of study of Au complexation with 1,3-Butanediol, its sulfur-free structure makes it unlikely to be involved in stabilizing dissolve Au. Nonetheless, as a reductant, 1,3-Butanediol

may have contributed to keeping Au species reduced and inhibiting dissolution as Au^+ complexes in the colloidal Si suspensions.

Table 3.3 A summary of the possible speciation and complexation of Si and Au in the two silica-bearing liquids and the influences of pH and impurities at 200°C and Psat.

	Si gel solution	**Colloidal Si suspension**
Si speciation	H_4SiO_4, $H_3SiO_4^-$	Colloidal SiO_2 particles (sol)
Si equilibrium concentration	83.9 ppm	–
Au speciation	$AuOH^0$, $AuH_3SiO_4^0$	$AuOH^0$
Mean Au equilibrium concentration	5.9 ppb	0.81 ppb
pH influence on Au hydrolysis	Weak Au hydrolysis	Strong Au hydrolysis
Influence of other components	No influence (no Au-NH_3 complex)	No 1,3-Butanediol-Au complexation, but Au dissolution as Au^+ may be inhibited

3.5.2 Comparison with previous Au–Si experiments

A series of experiments in the Au–SiO_2–NaCl–H_2O system at 300°C and 50 MPa by Zeng et al. (1997) suggested that the dissolved Au (2.3–18.6 ppb) was complexed as $AuOH^0$ and $AuOHCl^-$, in spite of the fact of 576–808 ppm dissolved Si. In contrast, Fan et al. (2001) suggested that the $AuH_3SiO_4^0$ is the dominant Au complex in both the acidic Au–SiO_2–HCl–H_2O and alkaline Au–SiO_2–Na_2SiO_3–H_2O systems at 25–300°C and Psat.

However, the Au concentrations of 7.23–150 ppb in silica-bearing solutions measured by Fan et al. (2001) are much lower than those in aqueous solutions (2–400 ppb Au; Stefánsson and Seward, 2003a), chloride-bearing (2–6420 ppb Au; Stefánsson and Seward, 2003b), and sulfide-bearing aqueous solutions (7–131000 ppb Au; Stefánsson and Seward, 2004) measured over a wide range of temperatures and pressures (100–600°C and 500–1800 bar; Table 3.4).

Notably, in the Au–SiO_2–HCl–H_2O system at 250°C studied by Fan et al. (2001), Au concentrations are much higher in the Cl-enriched runs than in those with low Cl concentrations (i.e., mean 81.6 ppb Au with 0.55 m Cl vs. 11.4 ppb Au with 0.003 m Cl). The dependence of Au concentration on Cl^- suggests that the dissolved Au was at least partly complexed with Cl in the forms of $AuCl_2^-$ and/or $AuCl_2H$ (cf. Gammons and Williams-Jones, 1995; Frank et al., 2002; Stefánsson and Seward, 2003b). A

contribution of Cl to Au complexation is also consistent with the much higher Au concentrations in the Au–SiO_2–HCl–H_2O system of Fan et al. (2001) compared to that in the Au–SiO_2–H_2O system investigated in this study.

3.5.3 Comparison with natural Si-bearing systems

The Au concentrations of 0.44–7.6 ppb in the Si gel solutions falls in the range of dissolved Au in Si-bearing (hundreds of ppm), deep (>1 km) geothermal fluids (Table 3.4), in Papua New Guinea (~15 ppb Au; Simmons and Brown, 2006), New Zealand (<0.1–23 ppb Au; Simmons and Brown, 2007), and Iceland (mean 14 ppb Au; Hannington et al., 2016). It has been suggested that sustained Au-rich fluid fluxes in these geothermal systems produce giant hydrothermal Au deposits in a short period (e.g., ~1300 t Au within ~55000 years; Simmons and Brown, 2006).

Table 3.4 A summary of Au solubility in various natural Si, S, Cl-bearing solutions

Au solubility (ppb)	T (°C)	P (bar)	pH	Solutions	References
In Si solutions					
7~108	250	Psat	-	Cl	Fan et al., 2001
18~150	250	Psat	-	$Na_2Si_2O_3$	Fan et al., 2001
In S and Cl-bearing solutions					
7~131000	100~500	500	neutral to alkaline	reduced S and Cl	Stefánssona and Seward, 2004
2~400	300~600	500~1500	acidic to alkaline	aqueous solution	Stefánssona and Seward, 2003a
2~6420	300~600	500~1800	acidic	with Cl	Stefánssona and Seward, 2003b
2~1000	150~500	500~1500	acid	low total sulfur	Benning and Seward, 1996
2000~108000	150~500	500~1500	neutral	high total sulfur	Benning and Seward, 1996
10000	650		-	magmatic fluids	Heinrich, 2005
1~16	> 275		neutral	with Cl and SO_4	Simmons and Brown, 2006
1.4~21	270~315	40	neutral	with Si, Cl, S	Hannington et al., 2016
1~6	284~295		-	black smoker fluids	Brown et al., 2009

However, it is also notable that other Au ligands such as Cl and H_2S are abundant in the geothermal fluids. For instance, the mean concentrations of Cl and H_2S in the Reykjanes geothermal fluids are 18,377 ppm and 37.2 ppm, respectively (n = 6; Hannington et al., 2016). Thus higher Au concentrations in the silica-bearing

geothermal fluids than in the Si gel solutions at 200°C can be attributed to complexation of Au with aqueous Cl and H_2S.

3.5.4 Implications for the role of Si in invisible Au mineralization

Previous studies of the role of Si in hydrothermal Au mineralization focused on epithermal to mesothermal and hot-spring bonanza ores (e.g., Saunders, 1990, 1994; Herrington and Wilkinson, 1993; Sherlock and Lehrman, 1995). In these Au systems, it has been suggested that both Si and Au occur as colloids, and that the transport of Au as Si–Au colloids explains the distinct texture of colloform amorphous Si and co-existing millimeter-scale native Au dendrites (Saunders, 1990; Sherlock and Lehrman, 1995). In low-grade disseminated Au deposits, however, the absence or near-absence of visible Au grains implies that dissolved Au is generally unsaturated in the mineralizing fluids, which precludes a colloidal Au transport mechanism. However, it remains possible that in some cases Au was transported as Si–Au colloids in hydrothermal fluids but didn't deposit because of the changing fluid conditions did not effectively destabilize the colloids.

The results of the preliminary experiments presented here show that in the acidic Au–SiO_2–H_2O solutions at 200°C, dissolved Au, analogous to that in natural geothermal fluids, could be stabilized by dissolved Si, partly by Si–Au complexation as $AuH_3SiO_4^0$. The Si–Au correlation in silica-bearing solution is a new insight that aids interpretation of the spatial relationship between dispersed hydrothermal silicification and auriferous sulfide disseminations commonly-observed in the low-grade but large-tonnage Au systems, such as Carlin and other sediment-host deposits.

3.6 Summary

The new experimental data show that the Au concentrations are higher in acidic Si gel solutions than in alkaline colloidal Si suspensions at 200°C and Psat. In the acidic Si gel solutions, dissolved Au may be complexed and stabilized in the both forms of $AuOH^0$ and $AuH_3SiO_4^0$, while Au may dominantly occur as $AuOH^0$ in the alkaline Si gel suspensions. Gold concentrations in the Si gel solutions are comparable to those

in Si-rich geothermal fluids that have been linked with formation of giant Au deposits. The preliminary results suggest that dissolved Au can be stabilized and thus transported in the generic silica-bearing solutions, with broad implications for the formation of intensely silicified low-grade refractory sulfide Au ores in the upper crust.

3.7 References

Benning, L.G., Seward, T.M., 1996. Hydrosulphide complexing of Au (I) in hydrothermal solutions from 150–400°C and 500–1500 bar. Geochimica et Cosmochimica Acta 60, 1849-1871.

Bowell, R.J., Baumann, M., Gingrich, M., Tretbar, D., Perkins, W.F., Fisher, P. C., 1999. The occurrence of gold at the Getchell mine, Nevada. Journal of Geochemical Exploration 67, 127-143.

Chouinard, A., Paquette, J., Williams-Jones, A.E., 2005. Crystallographic controls on trace-element incorporation in auriferous pyrite from the Pascua epithermal high-sulfidation deposit, Chile-Argentina. The Canadian Mineralogist 43, 951-963.

Cline, J.S., Hofstra, A.A., 2000. Ore-fluid evolution at the Getchell Carlin-type gold deposit, Nevada, USA. European Journal of Mineralogy 12, 195-212.

Crede, L.S., Liu, W., Evans, K.A., Rempel, K.U., Testemale, D., Brugger, J., 2019, Crude oils as ore fluids: An experimental in-situ XAS study of gold partitioning between brine and organic fluid from 25 to 250° C. Geochimica et Cosmochimica Acta 244, 352-365.

Dong, G., Morrison, G., Jaireth, S., 1995. Quartz textures in epithermal veins, Queensland: classification, origin and implication. Economic Geology 90, 1841-1856.

Fan, W., Wang, S., Tian, Y., Chen, Z.X., 2001. Complexation of Si in hydrothermal systems. Chinese Journal of Geochemistry 20, 201-209.

Fournier, R.O., Rowe, J. J., 1977, The solubility of amorphous silica in water at high temperatures and pressures. American. Mineralogist 62, 1052-1056.

Fournier, R.O., 1985, The behavior of silica in hydrothermal solutions, in Berger,

B.R., and Bethke, P.M., eds., Geology and Geochemistry of Epithermal Systems: Reviews in Economic Geology 2, 45-62.

Frank M.R., Candela P.A., Piccoli P.M., Glascock M.D., 2002. Gold solubility, speciation and partitioning as a function of HCl in the brine-silicate, melt-metallic gold system at 800°C and 100 MPa. Geochimica et Cosmochimica Acta 66, 3719-3732.

Frondel, C., 1938. Stability of colloidal gold under hydrothermal conditions. Economic Geology 33, 1-20.

Gammons C. H. Williams-Jones A. E., 1995. The solubility of Au-Ag alloy AgCl in HCl/NaCl solutions at 300°C: New data on the stability of Au (I) chloride complexes in hydrothermal solutions. Geochimica et Cosmochimica Acta 59, 3453-3468.

Hannington, M., Hardardóttir, V., Garbe-Schönberg, D., Brown, K.L., 2016. Gold enrichment in active geothermal systems by accumulating colloidal suspensions. Nature Geoscience 9, 299-302

Herrington, R.J., Wilkinson, J.J., 1993. Colloidal gold and silica in mesothermal vein systems. Geology 21, 539-542.

Hough, R.M., Noble, R.R.P., Reich, M., 2011. Natural gold nanoparticles. Ore Geology Reviews, 42, 55-61.

Iler, R.K., 1979, The chemistry of silica: New York, John Wiley & Sons, 866 p.

Kooi, E., 1966, The surface charge in oxidized silicon. The Surface Properties of Oxidized Silicon. Springer, Berlin, Heidelberg, 114-132.

Liu, W., Etschmann, B., Testemale, D., Hazemann, J. L., Rempel, K., Müller, H., Brugger, J., 2014, Gold transport in hydrothermal fluids: Competition among the Cl^-, Br^-, HS^- and $NH_{3\ (aq)}$ ligands. Chemical Geology, 376, 11-19.

Lubben, J.D., Cline, J.S., Barker, S.L., 2012. Ore fluid properties and sources from quartz-associated gold at the Betze-Post Carlin-type gold deposit, Nevada, United States. Economic Geology 107, 1351-1385.

Prokofiev V. Y., Kamenetsky V. S., Selektor S. L., Rodemann T., Kovalenker V. A., Vatsadze S. Z., 2017. First direct evidence for natural occurrence of colloidal silica in chalcedony-hosted vacuoles and implications for ore-forming processes. Geology 45, 71-74.

Saunders, J.A., 1990. Colloidal transport of gold and silica in epithermal precious-metal systems: Evidence from the Sleeper deposit, Nevada. Geology

18, 757-760.

Saunders, J.A., 1994. Silica and gold textures in bonanza ores of the Sleeper Deposit, Humboldt County, Nevada; evidence for colloids and implications for epithermal ore-forming processes. Economic Geology 89, 628-638.

Saunders, J.A., Schoenly, P.A., 1995. Boiling, colloid nucleation and aggregation, and the genesis of bonanza Au-Ag ores of the Sleeper deposit, Nevada. Mineralium Deposita 30, 199-210.

Seward, T.M., 1973. Thio complexes of gold and the transport of gold in hydrothermal ore solutions. Geochimica et Cosmochimica Acta 37, 379-399.

Sherlock, R.L., Lehrman, N.J., 1995. Occurrences of dendritic gold at the McLaughlin Mine hot-spring gold deposit. Mineralium Deposita 30, 323-327.

Shenberger, D.M., Barnes, H.L., 1989. Solubility of gold in aqueous sulphide solutions from 150 to 350 °C. Geochimica et Cosmochimica Acta 53, 269-278.

Simmons, S.F., Brown, K.L., 2006. Gold in magmatic hydrothermal solutions and the rapid formation of a giant ore deposit. Science 314, 288-291.

Simmons, S.F., Brown, K.L., 2007. The flux of gold and related metals through a volcanic arc, Taupo Volcanic Zone, New Zealand. Geology 35, 1099-1102.

Stefánsson, A., Seward T. M., 2003a. The hydrolysis of gold (I) in aqueous solutions to 600°C and 1500 bar. Geochimica et Cosmochimica Acta 67, 1677-1688.

Stefánsson, A., Seward T.M., 2003b. The stability of chloridogold (I) complexes in aqueous solutions from 300 to 600°C and from 500 to 1800 bar. Geochimica et Cosmochimica Acta 67, 4459-4576.

Stefánsson, A., Seward T M., 2004. Gold (I) complexing in aqueous sulphide solutions to 500°C at 500 bar. Geochimica et Cosmochimica Acta 68, 4121-4143.

Wilkinson, J.J. Nolan, J. Rankin, A.H., 1996. Silicothermal fluid: A novel medium for mass transport in the lithosphere: Geology, v. 24, p. 1059-1062.

Williams-Jones, A.E., Bowell, R.J., Migdisov, A.A., 2009. Gold in solution. Elements 5, 281-287.

Wood, S.A., Mountain, B.W., Pan, P., 1992, The aqueous geochemistry of platinum, palladium and gold: recent experimental constraints and a re-evaluation of theoretical predictions. The Canadian Mineralogist, 30, 955-982.

Wu, Y.F., Li, J.W., Evans, K., Koeing, A.E., Li, Z.K., O'Brien, H., Lahaye, Y.,

Rempel, K., Hu, S.Y., Zhang, Z.P. Yu, J.P., 2018. Ore-Forming Processes of the Daqiao Epizonal Orogenic Gold Deposit, West Qinling Orogen, China: Constraints from Textures, Trace Elements and Sulfur Isotopes of Pyrite and Marcasite, and Raman Spectroscopy of Carbonaceous Material. Economic Geology 113, 1093-1132.

Zeng, Y.S. Wang, F.Z., Ai, R.Y., 1997. Solubility of gold in the SiO_2-NaCl-H_2O system at 300°C and50 MPa. Science in China Series D: Earth Sciences 40, 485-490.

Chapter 4

Gold, arsenic, and copper zoning in pyrite: a record of fluid chemistry and growth kinetics

This chapter is a published paper in *Geology*:

Wu Y.F., Fougerouse D., Evans K., Reddy S.M., David W.S., Paul G., and Li J.W. Gold, arsenic, and copper zoning in pyrite: a record of fluid chemistry and growth kinetics. *Geology*, 47 (7): 641–644 (Impact factor 5.451).

Contributions by co-authors

Samples were collected and prepared by Ya-Fei Wu and Jian-Wei Li; Denis Fougerouse performed the APT analysis with the help of Steven M. Reddy and David W. Saxey; Paul Guagliardo and Ya-Fei Wu performed the NanoSIMS analysis; Manuscript was prepared by Ya-Fei Wu with insightful discussions with Denis Fougerouse, Katy Evans, Jian-Wei Li, and contributions from other co-authors.

Abstract

Chemical zoning in minerals records fluid-rock interaction and crystal growth kinetics via texturally complex features, the genesis of which remains a subject of debate. Here, we combine, for the first time, observations of micrometer (μm) to atomic-scale textural evidence to recognize multiple processes and mechanisms that controlled trace element zoning in a gold (Au)-rich arsenian pyrite crystal from the Daqiao epizonal orogenic Au deposit, China, using a novel combination of nanoscale secondary ion mass spectrometry (NanoSIMS) and atom probe tomography (APT). Chemically distinct μm-scale concentric zones of pyrite formed in response to changing fluid composition in a dynamic hydraulic fracturing environment. At a smaller scale, within an Au-rich zone, sector zones of Au, As, and Cu at the μm- to sub-μm-scale were controlled by the structure of the crystal surface. Micron-scale patchy distribution of Au, As, and Cu and atomic-scale transitions from homogenous to heterogeneous “island” arsenian pyrite formed as a consequence of heteroepitaxial Stranski-Krastanov growth. Nanometer (nm)-scale Au oscillatory zoning is interpreted as a consequence of diffusion-limited self-organization processes at the crystal-fluid interface. The recognition of kinetically-driven intrinsic processes enables us to see how these interact with extrinsic factors (e.g., pressure decreases) to produce the complexity in mineral zoning. Nano-scale heterogeneities in Au, As, and Cu present as solid solution in pyrite suggest that interpretation of spikes on microbeam-derived depth-concentration profiles as metallic particles should be treated with caution.

4.1 Introduction

Circulation of fluids in Earth’s crust is responsible for transport of mass and heat associated with formation of ore and hydrocarbon deposits and metamorphic reactions that influence lithospheric rheology (e.g., Plümper et al., 2017). To establish the processes that occur at the evolving mineral-fluid interface, a correct interpretation of compositional information stored in the minerals that grow in these environments is required. Compositional zoning of trace elements in minerals has

long fascinated petrologists because it is a time-resolved record of the complex physicochemical processes taking place at the mineral-fluid interface during crystallization (e.g., Allègre et al., 1981; Shore and Fowler, 1996; Wang et al., 2009). Mechanisms invoked to explain the diverse zoning patterns in minerals can be split, broadly, into extrinsic mechanisms that invoke changing conditions in external bulk fluids (e.g., Barker et al., 2009; Deditius et al., 2009), and intrinsic mechanisms driven by local crystal-fluid kinetic effects such as crystal surface structure effects (e.g., Dowty, 1976; Chouinard et al., 2005), and the effects of self-organization (e.g., Putnis et al., 1992). Relationships between these mechanisms remain ambiguous. It has been suggested that large μm- to millimeter-scale zones record changing fluid chemistry (e.g., Fowler et al., 2002), though numerical modeling suggests that centimeter (cm)-scale oscillatory zones could also be controlled by local kinetic effects (Wang et al., 2009). Distinction between, and recognition of combinations of, these end-member processes is challenging, partly because of the fine scale of analysis needed for discrimination.

Pyrite (FeS_2) is found in many different crustal environments and is one of the most common hosts for Au. Gold incorporated in pyrite as sub-μm nanoparticles and/or as solid solution is referred to as refractory Au or invisible Au (Palenik et al., 2004). Gold distribution in pyrite is commonly zoned, and the diverse zoning patterns, including cyclic, sector, oscillation and irregular patches, can constrain the nature of mineralizing fluids and the Au incorporation kinetic processes (Chouinard et al., 2005). Micron-scale irregular or cyclic Au zoning in pyrite has been interpreted to record fluctuations in hydrothermal fluid composition (e.g., Barker et al., 2009; Deditius et al., 2009; Tardani et al., 2017), though the results of recent atom probe studies highlight the importance of crystal growth kinetics and crystal-plastic deformation for sub-μm Au distribution in arsenopyrite and pyrite (Fougerouse et al., 2016, 2019). In spite of these promising preliminary results, direct evidence that relates kinetic growth controls to zoning of invisible Au in pyrite has not been documented.

Here, we utilize nanoscale secondary ion mass spectrometry (NanoSIMS) and atom probe tomography (APT) to characterize μm- to atomic-scale compositional variations in a complex-zoned Au-rich arsenian pyrite crystal from an epizonal orogenic gold deposit at Daqiao, China (Figure 4.1A), and use the results to constrain

the nature and mechanisms responsible for trace element zoning in pyrite. Our results provide new insights into the complementary roles of fluid and crystallization processes in the compositional zoning of minerals that can be applied to other mineral-fluid systems. The results are also used to evaluate previous interpretations of microbeam-derived trace element concentrations in finely zoned minerals.

4.2 SAMPLE CONTEXT AND METHODOLOGY

The Daqiao epizonal orogenic Au deposit in the West Qinling Orogen, China, is hosted in Triassic turbidites mineralized in the latest Jurassic to earliest Cretaceous (Figure 4.1A; Wu et al., 2018). Two types of hypogene sulfide breccia ores (tectonic and hydraulic breccias; Figure 4.1B) with an average Au grade of 3–4 g/t account for 90% of the total proven Au reserves (105 t; Wu et al., 2018). Invisible Au is present in main-ore stage fine-grained pyrite framboids, colloform, and zoned pyrite, and marcasite (Figure 4.DR1), all of which occur mainly in the hydrothermal cements of hydraulic breccia ores. A representative zoned pyrite grain from the cements of a hydraulic breccia ore (sample DQ198; 5.0 g/t Au), which is intergrown with chalcedony, calcite, and marcasite, was selected to investigate the details of Au zoning (Figure 4.2A).

Ion mapping of ($^{63}Cu^{32}S^-$, $^{75}As^{32}S^-$, and $^{197}Au^-$) was undertaken using a Cameca NanoSIMS 50L. Three atom probe specimens, taken across a 1–5 μm Au-As-rich zone (insert of Figure 4.2A), were manufactured using a Tescan Lyra3 focused-ion beam SEM with a Ga^+ ion source. A Cameca LEAP 4000X HR in laser-assisted mode was employed for APT analysis. More detailed analytical procedures are given in Appendix A (GSA Data Repository; Table 4.DR1; Figure 4.DR2).

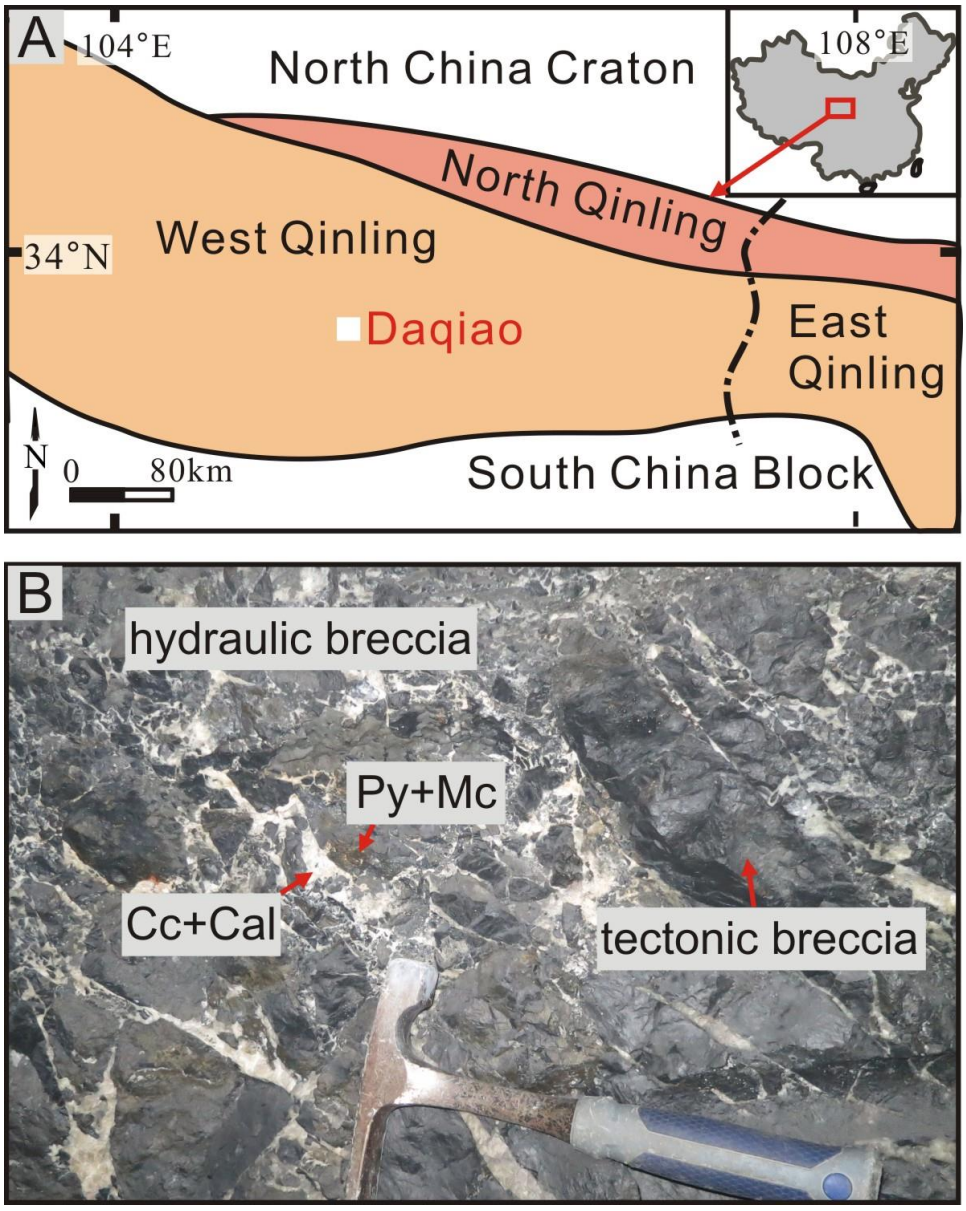

Figure 4.1 A: A simplified geological map of geotectonic terranes in the Qinling Orogen and the location of Daqiao gold deposit (white box). B: Representative photograph showing tectonic and hydraulic breccias at Daqiao deposit. Cal–Chalcedony; Cc–Calcite; Mc–Marcasite; Py–Pyrite.

4.3 RESULTS

4.3.1 Micro-scale textures

The analyzed pyrite crystal is composed of a homogenous core, a bright and irregular, 1 to 5 μm wide arsenian pyrite mantle and a finely zoned rim (Figure 4.2A). In three regions mapped by NanoSIMS (R1–R3), trace elements (Au, As and Cu) are

enriched and correlated in the BSE-bright domain, whereas the core and the external rim do not display enrichment in these elements (Figures. 4.2 and 4.DR3). Within the arsenian pyrite zones, Au, As, and Cu exhibit different distribution patterns: patches (1–2 μm across; Figure 4.2C-E); and 1 to 5 μm wide irregular sector zoning (Figure 4.2B, E, G and I).

4.3.2 Atomic-scale textures

Atom probe analyses from the inner zone of the arsenian pyrite (specimen 1; inset of Figure 4.2A), reveal a homogeneous distribution of As (4.30 at.% or atomic percent), Au (131 appm or atomic parts per million), and Cu (1028 appm) (Figure 4.3A; Table 4.DR2). In specimen 2 from the central domain, the distribution of As, Au, and Cu is heterogeneous (Figure 4.3B). Irregular shaped domains ~20 nm across, are characterized by high trace element abundances (As = 4.28 at.%; Au = 164 appm; Cu = 1189 appm), whereas the matrix hosts lower concentrations of the same trace elements (As = 2.11 at.%; Au = 71 appm; Cu = 640 appm). Co-located As, Au, and Cu within the outer domain (specimen 3) exhibit oscillatory zones with composition bands less than 5 nm wide (Figure 4.3C). The high-As zones comprise 4.35 at.% As, 118 appm Au and 1087 appm Cu, whereas the low-As zones contain 2.22 at.% As, 54 appm Au and 713 appm Cu.

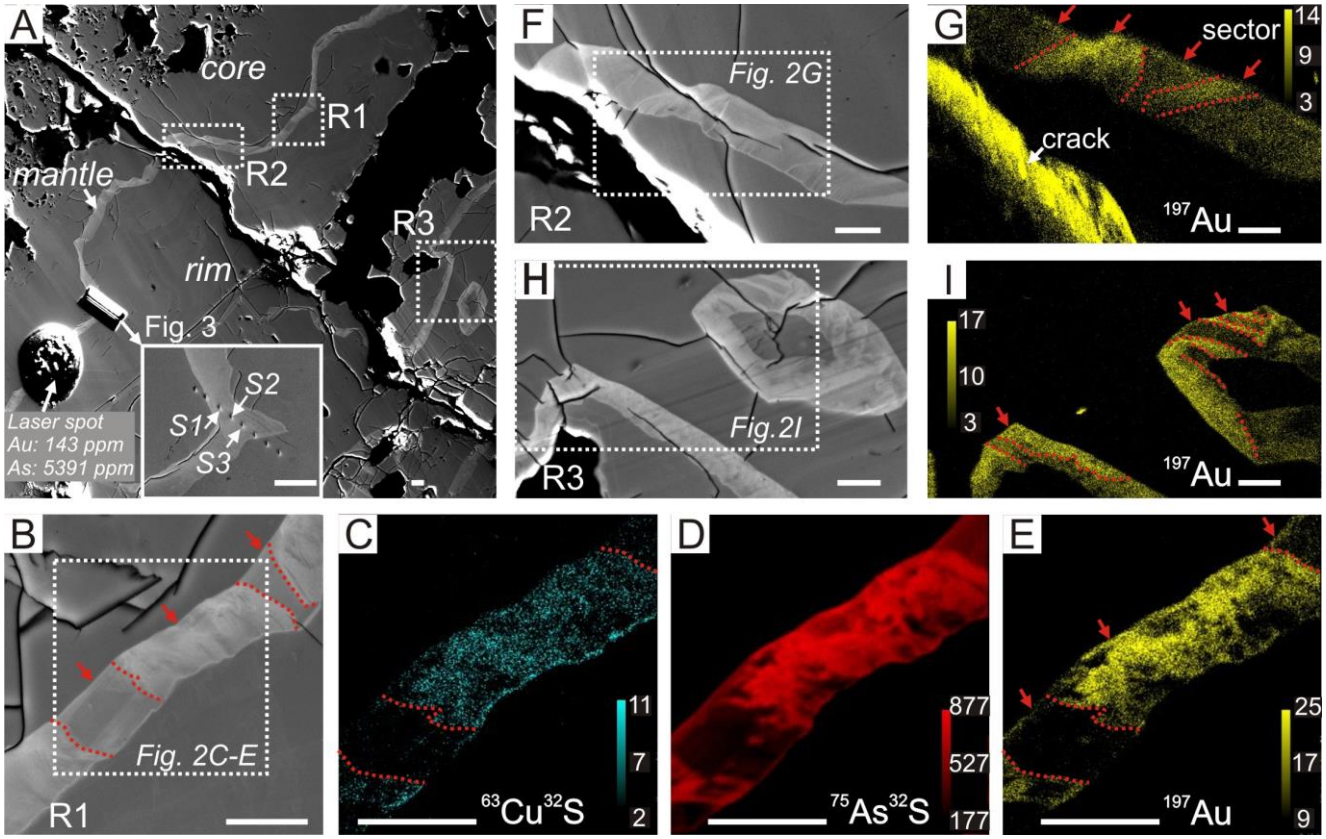

Figure 4.2 BSE images (A, B, F and H), and NanoSIMS elemental mapping (C-E, G and I; in counts) of Daqiao pyrite. In Figure 4. 2A, the bright mantle zone contains high Au and As concentrations (143 ppm and 5391 ppm, respectively; LA–ICP–MS; Wu et al., 2018) relative to the pyrite core and rim; 3 regions analyzed by NanoSIMS (R1–R3) are indicated with white dashed boxes; locations of 3 APT specimens (S1–S3) are shown in the insert. Sector zoning is marked with red arrows. Scale bar is 5 μm

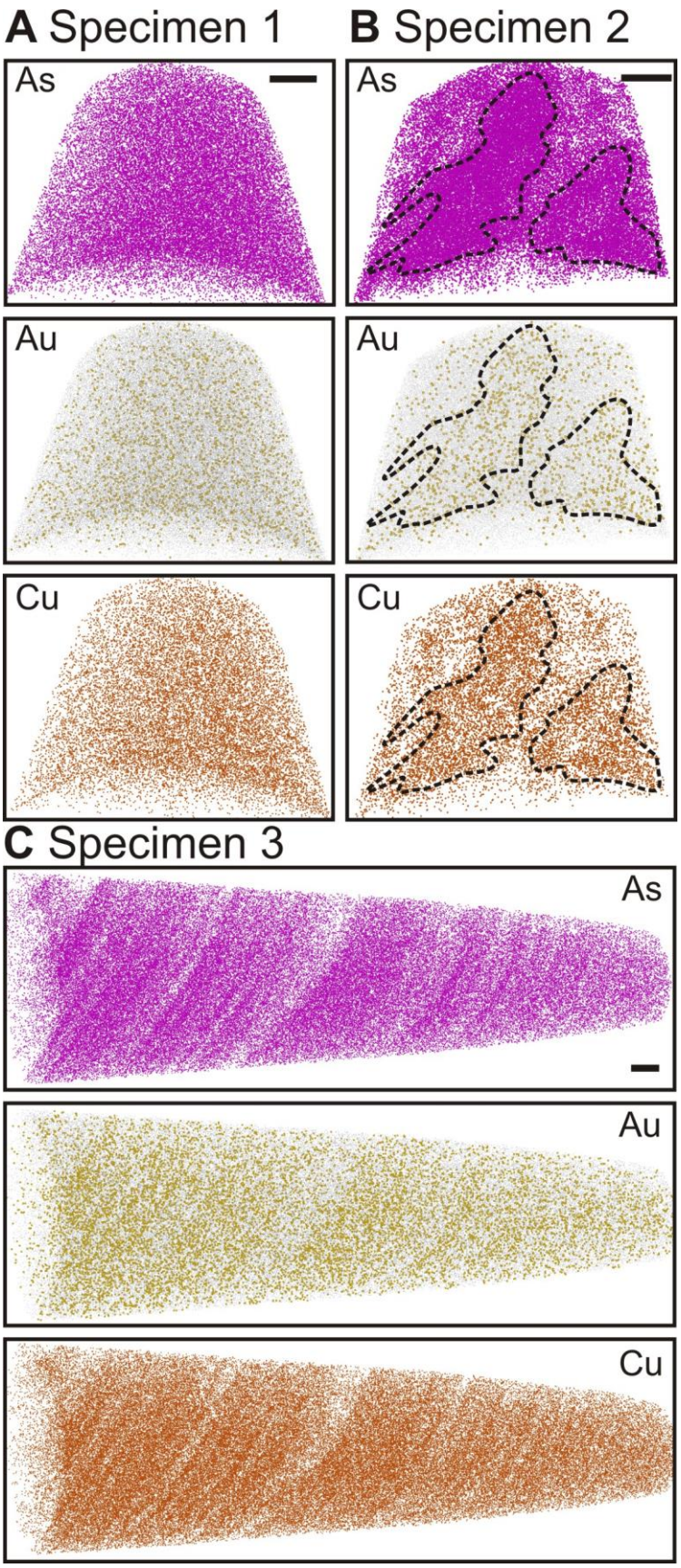

Figure 4.3 Arsenic, Au, and Cu maps of APT specimen 1 (A), specimen 2 (B), and specimen 3 (C). Each sphere represents one atom. Scale bar is 20 nm.

4.4 RESULTS

4.4.1 The combined extrinsic and intrinsic processes for zoning complexity

Episodic fluctuations in pressure, temperature, and composition in bulk fluids have been invoked to explain chemical zonations in minerals (Shore and Fowler, 1996). In the Daqiao pyrite, the sharp transition between the μm-scale compositionally different core-mantle-rim zones (Figure 4.2A) is consistent with fluctuations in bulk fluid conditions, and indeed such processes have been suggested to be the cause for chemical zoning in pyrite in other Au deposits (e.g., Barker et al., 2009; Deditius et al., 2009; Tardani et al., 2017).

At the Daqiao deposit, the narrow Au-rich arsenian pyrite mantle zone is thought to have formed in response to a short-lived FeS_2 supersaturation event (Wu et al., 2018). This supersaturation event, inferred from textural evidence provided by framboidal and colloform Au-rich pyrite in the cements of hydraulic breccias, was likely induced by fluctuations in fluid pressure in a dynamic hydraulic fracturing environment (Wu et al., 2018). However, extrinsic changes in fluid chemistry can explain only a subset of the observations. Micron-scale features such as the patches and sector zones of Au, As, and Cu (Figure 4.2) in pyrite are inconsistent with fluid-pressure induced cycles in metal precipitation, which would produce zones parallel to the boundary of growing pyrite.

Differences in chemical partitioning at crystal faces in response to differences in free energy associated with spatial variations in geometry and growth rate can produce sector chemical zoning (Dowty, 1976). For example, trace element zones are preferentially partitioned in the {111} and {110} faces in pyrite (Chouinard et al., 2005). Sector zoning is preserved when crystal growth rate exceeds near-surface- and lattice-diffusion rates during crystal growth (Watson, 2004). The μm-scale growth sectors in Au, As, and Cu (Figure 4.2) are consistent with crystal-controlled sector zones. Ion diffusion rate is inferred to have been slow relative to pyrite crystallization rate at Daqiao because the fluids were relatively low temperature (100–240 °C; Wu et al., 2018).

The Au, As, and Cu patches in arsenian pyrite (Figure 4.2C-E) are morphologically

similar to irregular “islands” on growing crystal interfaces that formed by heteroepitaxial Stranski-Krastanov (SK) growth (e.g., Mo et al., 1990; Kaiser, 2002). In SK growth mode, lattice mismatch, such as this induced by As incorporation into pyrite lattice, could have led to the precipitation of a strained but homogenous arsenian pyrite layer influenced by high surface energy and wetting effects on the surface of As-poor pyrite core (Figure 4. 4A; Mo et al., 1990). The SK model predicts that formation of this layer would have been followed by the growth of irregular islands to reduce strain energy in crystal (Figure 4.4B). Subsequent growth would result in the coalescence of these islands until a continuous crystal layer forms (Figure 4.4C; Kaiser, 2002). The SK growth mode is consistent with the irregular Au patches (Figure 4.2C-E) and the atomic-scale distribution transition from homogenous arsenian pyrite close to the border with the core (i.e., specimen 1) to the heterogeneous patchy distribution in specimen 2 (Figure 4.3A and B).

During the growth of continuous pyrite layer, incompatible trace elements such as Au, As, and Cu would become enriched at crystal-fluid interface when growth rate is faster than near-surface diffusion (Watson, 2004). New-formed pyrite in contact with the incompatible-enriched fluid layer incorporates these elements to produce an Au-As-Cu-rich composition. Continued pyrite growth depletes essential constituents (Fe, S) in the near-surface fluid with a consequent decrease in growth rate. Replenishment of bulk fluid into the crystal-fluid interface restarts the cycle to produce alternating zones of trace-element depletion and enrichment. Slow near-surface diffusion relative to the pyrite growth rate, as discussed above, is consistent with the production and preservation of nm-scale oscillations in Au, As, and Cu in APT specimen 3 (Figure 4.3C) by diffusion-limited self-organization (Figure 4.4C). Numerical modeling suggests that different self-organized nonlinear feedback processes can produce cm to sub-μm-scale chemical oscillations (Putnis et al., 1992; Wang et al., 2009).

Our results do not invalidate previous conclusions of extrinsic, fluid-driven mineral zoning. The sharp transition between the μm-scale compositionally distinct core-mantle-rim zones in Daqiao pyrite have formed as a consequence of episodic fluctuations in external fluid composition, consistent with suggestions from previous work on pyrite chemical zoning in Carlin-type and epithermal Au deposits (e.g., Barker et al., 2009; Deditius et al., 2009). However, μm- to atomic-scale distribution

and zoning patterns of Au, As, and Cu were controlled by a combination of kinetic effects during pyrite crystallization, including crystal surface structure effects, heteroepitaxial Stranski-Krastanov growth, and diffusion-limited self-organization.

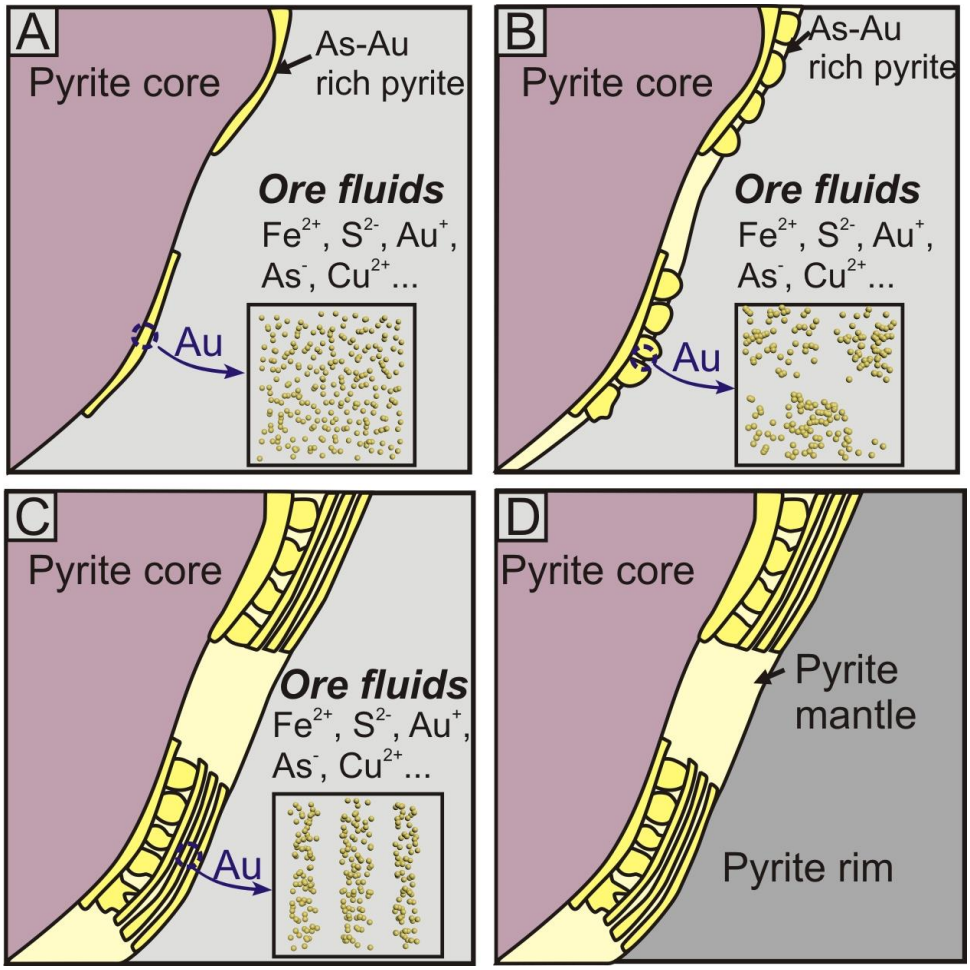

Figure 4.4 Schematic illustration showing the formation process of Au distribution in Daqiao pyrite. A: As-Au-rich pyrite "wetting" the surface of As-Au-poor pyrite core. B: Stranski-Krastanov growth of pyrite "islands". C: Self-organized pyrite oscillation. D: Growth of Au-poor pyrite rim from metal-depleted fluids.

To summarize, the simultaneous, or close to simultaneous, occurrence of multiple processes involving a combination of extrinsic and intrinsic controls has broad implications for interpretation of the crystallization history of commonly-observed compositionally zoned crystals in evolving mineral-fluid systems in the crust; it is not sufficient to infer that either one or the other produced any given zoning pattern without consideration of the possibility that multiple processes may have operated. The ability to make small scale observations enables us not only to see the effects of kinetically-driven intrinsic processes, but to begin to understand how these interact with extrinsic factors such as fluid chemistry variation or pressure decreases to

produce the observed zoning complexity. It is essential that observations and interpretations are at scales from cm to nm if we are to make any progress in recognition and interpretation of the interactions between those processes.

4.4.2 Implications for interpretation of Au occurrence in sulfides during microbeam analyses

A clear understanding of the Au occurrence in sulfides is prerequisite for optimal processing of the refractory ores that are an increasingly important, economically, as a host for Au. The presence of Au nanoparticles in sulfides has been recognized by HTEM (high-resolution transmission electron microscopy; e.g., Palenik et al., 2004) and APT (Fougerouse et al., 2016). More commonly, however, the occurrence of metallic Au particles is suggested on the basis of time-resolved depth-concentration profiles obtained by *in situ* quantitative microbeam techniques, such as LA–ICP–MS (laser ablation–inductively coupled plasma–mass spectrometry) and SIMS (secondary ion mass spectrometry). Gold spikes in the profiles are interpreted to indicate the presence of Au micron- or nano-particles, while more homogeneous profiles are suggested as a record of Au held in solid solution in sulfide lattices (e.g., Reich et al., 2005; Cook et al., 2009; Large et al., 2011; Gregory et al., 2014, 2015). However, care must be taken with such interpretations, because variations in lattice-bounded Au concentrations on the sub-μm scale, such as those revealed in this work, would produce a spike in LA–ICP–MS and SIMS profiles that could be confused with Au particles, given the relatively coarse spatial resolution of the LA–ICP–MS and SIMS techniques (10–10s μm). Consideration of this ambiguity is essential during interpretation of microbeam-derived profiles of trace metals in zoned sulfides and other minerals.

4.5 ACKNOWLEDGMENTS

This research work was financially supported by National Natural Science Foundation of China (41772081, 41072057, and 41325007), Fundamental Research Funds for the Central Universities (CUGCJ1711), and GPMR State Key Laboratory (MSFGPMR03). The senior author acknowledges the receipt of CSC/CIPRS

scholarship. This is contribution 19 from CUG Center for Research in Economic Geology and Exploration Targeting (CREGET). The Australian Resource Characterisation Facility (ARCF), under the auspices of the National Resource Sciences Precinct (NRSP), is supported by the Science and Industry Endowment Fund (SIEF RI13-01). This paper greatly benefited from constructive and thorough reviews from three anonymous reviewers. Our thanks go to editorial suggestions from Dennis Brown.

4.6 REFERCENCES CITED

Allègre, C.J., Provost, A., Jaupart, C., 1981. Oscillatory zoning. a pathological case of crystal growth. Nature, v. 294, p. 223-228.

Barker, S., Hickey, K., Cline, J., Dipple, G., Kilburn, M., Vaughan, J., Longo, A., 2009. Uncloaking invisible Au: use of nanoSIMS to evaluate Au, trace elements and sulfur isotopes in pyrite from Carlin-type Au deposits. Economic Geology 104, 897-904.

Chouinard, A., Paquette, J., Williams-Jones, A.E., 2005. Crystallographic controls on trace-element incorporation in auriferous pyrite from the Pascua epithermal high-sulfidation deposit, Chile–Argentina. The Canadian Mineralogist 43, 951-963.

Cook, N.J., Ciobanu, C.L., Mao, J., 2009. Textural control on gold distribution in As-free pyrite from the Dongping, Huangtuliang and Hougou gold deposits, North China Craton (Hebei Province, China). Chemical Geology 264, 101-121.

Deditius, A.P., Utsunomiya, S., Ewing, R.C., Chryssoulis, S.L., Venter, D., Kesler, S.E., 2009. Decoupled geochemical behavior of As and Cu in hydrothermal systems. Geology 37, 707-710.

Dowty, E., 1976. Crystal structure and crystal growth: II. Sector zoning in minerals. American Mineralogist 61, 460-469.

Fougerouse, D., Reddy, S.M., Saxey, D.W., Rickard, W.D., Van, Riessen. A., Micklethwaite, S., 2016. Nanoscale Au clusters in arsenopyrite controlled by growth rate not concentration: Evidence from atom probe microscopy. American Mineralogist 101, 1916-1919.

Fougerouse, D., Reddy, S.M., Kirkland, C.L., Saxey, D.W., Rickard, W.D., Hough, R.M.,

2019. Time-resolved, defect-hosted, trace element mobility in deformed Witwatersrand pyrite. Geoscience Frontiers 10, 55-63.

Fowler, A., Prokoph, A., Stern, R., Dupuis, C., 2002. Organization of oscillatory zoning in zircon: analysis, scaling, geochemistry, model of a zircon from Kipawa, Quebec, Canada. Geochimica et Cosmochimica Acta 66, 311-328.

Gregory, D., Meffre, S., Large, R., 2014. Comparison of metal enrichment in pyrite framboids from a metal-enriched and metal-poor estuary. American Mineralogist 99, 633-644.

Gregory, D.D., Large, R.R., Halpin, J.A., Baturina, E.L., Lyons, T.W., Wu, S., Danyushevsky, L., Sack, P., Chappaz, A., Maslennikov, V.V., Bull, S.W., 2015. Trace element content of sedimentary pyrite in black shales. Economic Geology 110, 1389-1410.

Kaiser, N., 2002. Review of the fundamentals of thin-film growth. Applied optics 41, 3053-3060.

Large, R.R., Bull, S.W., Maslennikov, V.V., 2011. A carbonaceous sedimentary source-rock model for Carlin-type and orogenic gold deposits. Economic Geology 106, 331-358.

Mo, Y.W., Savage, D.E., Swartzentruber, B.S., Lagally, M.G., 1990. Kinetic pathway in Stranski-Krastanov growth of Ge on Si (001). Physical Review Letters 65, 1020-1023.

Palenik, C.S., Utsunomiya, S., Reich, M., Kesler, S.E., Wang, L., Ewing, R.C., 2004. “Invisible” Au revealed: Direct imaging of Au nanoparticles in a Carlin-type deposit. American Mineralogist 89, 1359-1366.

Plümper, O., Botan, A., Los, C., Liu, Y., Malthe-Sørenssen, A., Jamtveit, B., 2017. Fluid-driven metamorphism of the continental crust governed by nanoscale fluid flow. Nature geoscience 10, 685-690.

Putnis, A., Fernandez-Diaz, L., Prieto M., 1992. Experimentally produced oscillatory zoning in the (Ba, Sr) SO_4 solid solution. Nature 358, 743-745.

Reich, M., Kesler, S.E., Utsunomiya, S., Palenik, C.S., Chryssoulis, S.L., Ewing, R.C., 2005, Solubility of Au in arsenian pyrite. Geochimica et Cosmochimica Acta 69, 2781-2796.

Shore, M., Fowler, A.D., 1996. Oscillatory zoning in minerals: a common phenomenon. The Canadian Mineralogist 34, 1111-1126.

Tardani, D., Reich, M., Deditius, A.P., Chryssoulis, S., Sánchez-Alfaro, P., Wrage, J., Roberts, M.P., 2017. Copper-arsenic decoupling in an active geothermal system: A

link between pyrite and fluid composition. Geochimica et Cosmochimica Acta 204, 179-204.

Wang, Y., Xu, H., Merino, E., Konishi, H., 2009. Generation of banded iron formations by internal dynamics and leaching of oceanic crust. Nature Geoscience 2, 781-784.

Watson, E.B., 2004. A conceptual model for near–surface kinetic controls on the trace-element and stable isotope composition of abiogenic calcite crystals1. Geochimica et Cosmochimica Acta 68, 1473-1488.

Wu, Y.F., Li, J.W., Evans, K., Koenig, A.E., Li, Z.K., O'Brien, H., Lahaye, Y., Rempel, K., Hu, S.Y., Zhang, Z.P., Yu, J.P., 2018. Ore-forming processes of the Daqiao epizonal orogenic gold deposit, West Qinling Orogen, China: constraints from textures, trace elements, and sulfur isotopes of pyrite and marcasite, and Raman spectroscopy of carbonaceous material. Economic Geology 113, 1093-1132.

Chapter 5

Metal remobilization and ore-fluid perturbation during episodic replacement of auriferous pyrite from an epizonal orogenic gold deposit

This chapter is a published paper in *Geochimica et Cosmochimica Acta*:

Wu Y.F., Evans K., Li J.W., Fougerouse D., Large R.R., and Guagliardo P., 2019, Metal remobilization and ore-fluid perturbation during episodic replacement of auriferous pyrite from an epizonal orogenic gold deposit. *Geochimica et Cosmochimica Acta*, 245 (15): 98–117 (Impact factor 4.609).

Contributions by co-authors

Ya-Fei Wu and Jian-Wei Li collected samples. Ya-Fei Wu performed sample preparation for petrographic observations, *in situ* trace element and sulfur isotope analyses. Ya-Fei Wu and Paul Guagliardo conducted NanoSIMS analysis. Ya-Fei Wu is the primary author of the manuscript with the helpful discussions, suggestions and guidance, from Katy Evans and other coauthors.

Abstract

Mineral-scale episodic replacement of auriferous pyrite by texturally-complex pyrite, marcasite and minor arsenopyrite occurred in breccia ores from the Daqiao epizonal orogenic gold deposit, West Qinling Orogen, China. This study uses a novel combination of laser ablation-inductively coupled plasma-mass spectrometry (LA–ICP–MS), Nanoscale secondary ion mass spectrometry (NanoSIMS), and secondary ion mass spectrometry (SIMS) to investigate the remobilization and re-concentration of gold and other trace elements during this complex replacement process and the probable mechanism. Several lines of evidence including some degree of preservation of external morphology, sharp contacts and compositional differences between the parent pyrite and product pyrite and marcasite, and reaction-induced porosity suggest that the replacement of parent pyrite proceeds via a two-step replacement via a dissolution and reprecipitation mechanism, plus an additional marcasite overgrowth. During the replacement of euhedral pyrite, depletion of gold and other trace elements (Te, Se, Zn, Co, Tl, Ni, W, and As) in porous product pyrite relative to its precursor indicate exsolution and remobilization of these metals from crystal lattice of the original pyrite. In the subsequent replacement of porous pyrite by two types of marcasite and minor arsenopyrite, euhedral product marcasite contains low contents of trace elements, possibly due to high metal solubility in the acidic fluids favorable for marcasite precipitation. The complex-zoned marcasite significantly enriched in gold and other metals relative to porous pyrite (W, Tl, As, Sb, Ag, Se, and Zn) is thought to have formed via precipitation triggered by further oxidation and/or immediate reduction in threshold supersaturation. Dissolution of the impurity-rich pyrite and precipitation of new pyrite and marcasite generations could have occurred at low pH plus high concentrations of dissolved Fe^{2+} condition caused by partial oxidation of aqueous H_2S and/or S^{2-} in ore fluids. The fluid oxidation is evidenced by a general decreasing trend of $\delta^{34}S$ values from the parent euhedral pyrite, to product porous pyrite, euhedral marcasite, and complex-zoned marcasite. The isotopic results are consistent with ore fluid oxidation controlled by pressure fluctuations during multistage hydraulic fracturing in a fault-valve regime at Daqiao deposit. This quantitative study emphasizes that the pressure-driven hydrothermal process plays a key role in the

micron- to nano-scale redistribution and re-enrichment of gold and other trace metals during episodic replacement of auriferous pyrite in brittle rheological zones from epizonal orogenic gold systems.

5.1 INTRODUCTION

Dissolution and reprecipitation replacement of auriferous iron sulfides and sulfarsenides, typically pyrite (FeS_2, cubic), marcasite (FeS_2, orthorhombic), pyrrhotite ($Fe_{1-x}S$, x=0–0.125) and arsenopyrite (FeAsS), is ubiquitous in hypogene gold mineralization systems worldwide (e.g., Morey et al., 2008; Sung et al., 2009; Cook et al., 2013; Rottier et al., 2016; Fougerouse et al., 2016). Such replacement occurs when an externally-derived hydrothermal fluid comes into contact with pre-existing auriferous sulfide and sulfarsenide minerals with which they are under-saturated. These minerals begin to dissolve and form an interfacial layer of fluids at the mineral surfaces that is supersaturated with respect to a more stable product phase (Putnis, 2002, 2009; Brugger et al., 2010; Qian et al., 2010, 2011; Harlov et al., 2011; Altree-Williams et al., 2015). Comprehensive studies of replacement of auriferous iron sulfides and sulfarsenides are therefore crucial to decipher redistribution and re-enrichment of gold (e.g., visible gold) plus other trace metals, and to monitor fluctuations in ore fluid fluxes and compositions, especially in the formation of giant and high-grade ore shoots (e.g., Tomkins and Mavrogenes, 2001; Tomkins et al., 2007; Morey et al., 2008; Cook et al., 2009, 2013; Sung et al., 2009; Thomas et al., 2011; Rottier et al., 2016; Fougerouse et al., 2016, 2017). However, the micron- to nano-scale textural diversity and complexity that arise from replacement may significantly obscure the original characteristics of auriferous mineral precipitation (Putnis, 2009; Altree-William et al., 2015), hampering a process-based interpretation for high grade gold ores evolution.

Previous studies of replacement of auriferous minerals in hydrothermal gold deposits mostly focus on pyrite-arsenopyrite and associated metal redistribution and reprecipitation (e.g., Dubé et al., 2004; Large et al., 2007; Morey et al., 2008; Cook et al., 2009, 2013; Sung et al., 2009; Fougerouse et al., 2016; Selvaraja et al., 2017; LaFlamme et al., 2018). However, the details of replacement behavior of marcasite, a

polymorph of pyrite and a significant gold-hosting iron sulfide in many hydrothermal gold deposits (e.g., Arehart et al., 1993; Fleet and Mumin, 1997; Cline, 2001; Pals et al., 2003; Franchini et al., 2015; Rottier et al., 2016), and related metal redistribution process has not been documented. Marcasite formation is kinetically favored over pyrite, but it is metastable in many geological environments and thus tends to be highly reactive. Formation and preservation conditions for marcasite have been experimentally documented, with stability favored at low pH and low temperature (Murowchick and Barnes 1986; Murowchick, 1992; Qian et al., 2011). Natural marcasite overgrowths on pre-existing pyrite have been described in a small number of low-temperature hydrothermal uranium deposits and sedimentary rocks (Goldhaber et al, 1978, 1979; Schieber and Riciputi, 2005; Schieber, 2007, 2011). In these cases, however, no specific formation mechanism was identified for the aggregates of pyrite and marcasite other than a "general replacement". Moreover, metal transfer related to these processes has not been quantitatively documented.

Despite the potential contribution of dissolution and reprecipitation reactions to the replacement of auriferous iron sulfides and sulfarsenides, the details of these processes and associated redistribution of gold are poorly understood, partly due to the very fine-grained size (less than a few tens of microns) of replacement minerals and ambiguous replacement textures. Previous studies of trace element redistribution during replacement processes have mostly relied on scanning electron microscopy-energy dispersive X-ray spectroscopy (SEM-EDS), electron microprobe (EMP) and laser ablation-inductively coupled plasma-mass spectrometry (LA‐ICP‐MS) (Fleet and Mumin, 1997; Morey et al., 2008; Cook et al., 2009, 2013; Sung et al., 2009). However, the utility of the SEM-EDS and EMP is limited because of the low concentrations of trace elements relative to detection limits. Although LA‐ICP‐MS can provide quantitative results for trace elements present at very low concentrations (>0.01 ppm; Large et al., 2009), the spot size of laser beam is quite large (30–75 μm) relative to the details of micron- to nano-scale chemical variation. Ion probe mapping using NanoSIMS (Nanoscale secondary ion mass spectrometry) has the advantage of combined sub-50 nm lateral resolution and low detection limits and provides an attractive option for qualitative mapping of low concentrations of trace elements at high spatial resolution (McLoughlin et al., 2011). Furthermore, SIMS, with a spot size as small as 10 μm, provides an opportunity to study sulfur

isotopic variation between the different generations of sulfides and their replacements (Chen et al., 2015).

In this study, we document details of textures and overprinting relationships for auriferous pyrite replaced by pyrite and marcasite in breccia gold ores from the Mesozoic Daqiao epizonal orogenic gold deposit, West Qinling Orogen, China. In-situ LA–ICP–MS trace element spot and line analyses and NanoSIMS element mapping combined with SIMS sulfur isotope analysis are used to reveal the redistribution of gold and other trace elements and related variations in sulfur isotopic composition. A mechanism to explain the observations is proposed, and implications for fluid-mediated pyrite replacement and related metal transfer in hydrothermal gold systems are discussed.

5.2 GEOLOGICAL BACKGROUND AND SAMPLING

The Qinling Orogen formed as a result of the prolonged subduction of the proto-Tethyan ocean and subsequent collision between the North China Craton (NCC) and Qinling micro-plate along the Shangdan suture in the middle Paleozoic, and subduction of the paleo-Tethyan ocean and subsequent collision between the Qinling terrain and the South China Block (SCB) along the Mianlue suture in the Early Mesozoic (Figure 5.1a; Meng and Zhang 1999; Dong et al. 2011). This orogen extends along a NW-strike for 2,500 km from the Dabie Mountains in the east to the Qilian Mountains and Kunlun Mountains in the west (insert of Figure 5.1a). The West Qinling Orogen (WQO), separated from the East Qinling Orogen (EQO) broadly by the Baocheng Railway, can be further divided into the northern, central and southern domains by the Shangdan suture and Hezuo-Lintan-Liangdang Fault (HLLF), respectively (Wu et al., 2018a). The northern domain is an early Paleozoic oceanic arc, while the central and southern domains are characterized by greenschist-facies Devonian flysch metasedimentary rocks and unmetamorphosed to low-grade Triassic turbidites, respectively (Mao et al., 2002). The Triassic syn- to post-collisional granitoids (250–200 Ma) widely distribute in the WQO (Zeng et al., 2014).

The central and southern domains of the WQO host numerous orogenic gold deposits,

which are thought to have formed during Late Triassic to Early Cretaceous peaking at ca. 216–200 Ma and 144–125 Ma (Wu et al., 2018b). Gold deposits are mostly localized along several crustal-scale, first-order southward thrust faults, such the HLLF and ZCHF (Zhouqu-Chengxian-Huixian-Fengxian Fault), which strike northwest to nearly east-west in excess of 400 km (Figure 5.1a). These faults are thought to have formed during the Late Jurassic to Early Cretaceous north-south compression in the Qinling orogenic belt (Dong et al., 2016). Seismic reflection profiling indicates that the overthrust belt is characterized by complex stacking thrust sheets, duplexes and opposed folds and faults (Liu et al., 2006). It is proposed that these crustal-scale thrust faults are channels for large-scale upwards-directed migration of fluids generated at depth (Robert et al., 1995).

The Daqiao orogenic gold deposit of latest Jurassic and Early Jurassic age in the southern domain has more than 105 t of gold resources at an average grade of 3–4 g/t (Wu et al., 2018a). The comprehensive deposit geology has been described in Wu et al. (2018a) and briefly summarized here. Orebodies are structurally controlled by a number of second-order reverse faults steeply dipping 55 to 80° north or southwest and mostly localized in fracture zones at the contact between Triassic turbidites and Carboniferous limestone (Figure 5.1b). High-angle reverse faults are suggested to be fluid-activated valves that controlled flow from geopressured reservoirs, drove cyclic fluctuations in fluid pressure that caused mineral precipitation (e.g., Sibson et al., 1988; Cox, 1995; Robert et al., 1995).

Two economic styles of breccia, tectonic and hydraulic breccias, have been identified in the mine (Figure 5.2). The strongly silicified tectonic breccia A contains disseminated auriferous pyrite and marcasite (up to 4 g/t; Figure 5.2a and b). Tectonic breccias with high competence were hydraulically brecciated (Figure 5.2c) and the resultant hydraulic breccia B is filled with chalcedony and irregular fine-grained cement-hosted pyrite, minor marcasite and arsenopyrite (Figure 5.2d and e). Breccia B was further hydraulically brecciated to form more complex high-grade (up to 12 g/t) breccia C cemented by calcite, pyrite, marcasite, and minor chalcedony (Figure 5.2d and e).

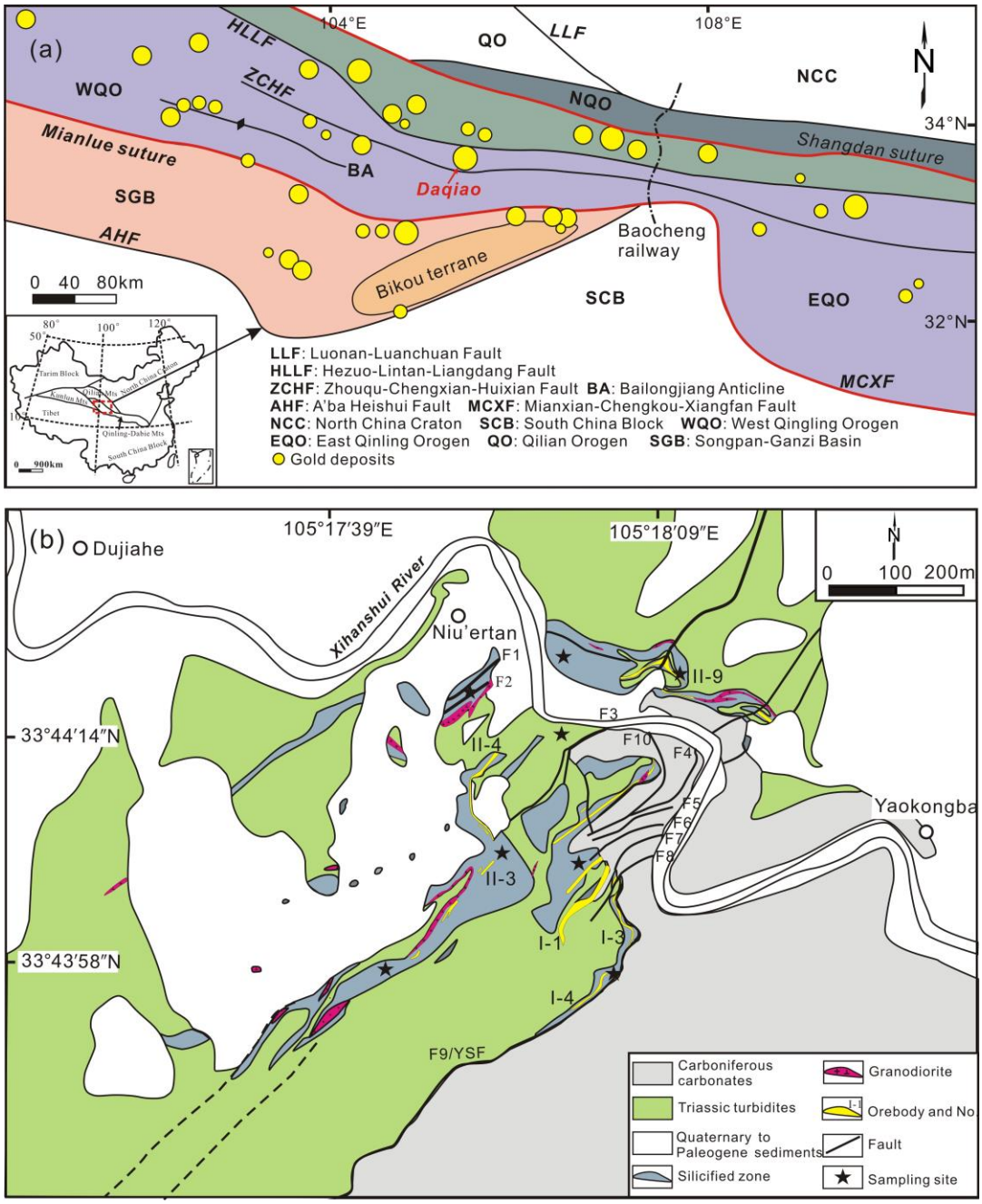

Figure 5.1 (a) A simplified map showing tectonic division of the Qinling Orogen. Also shown are the major faults, gold deposits and the location of Daqiao (modified from Wu et al., 2018a). The insert indicates the location of the West Qinling Orogen in China. (b) Geology of the Daqiao gold deposit.

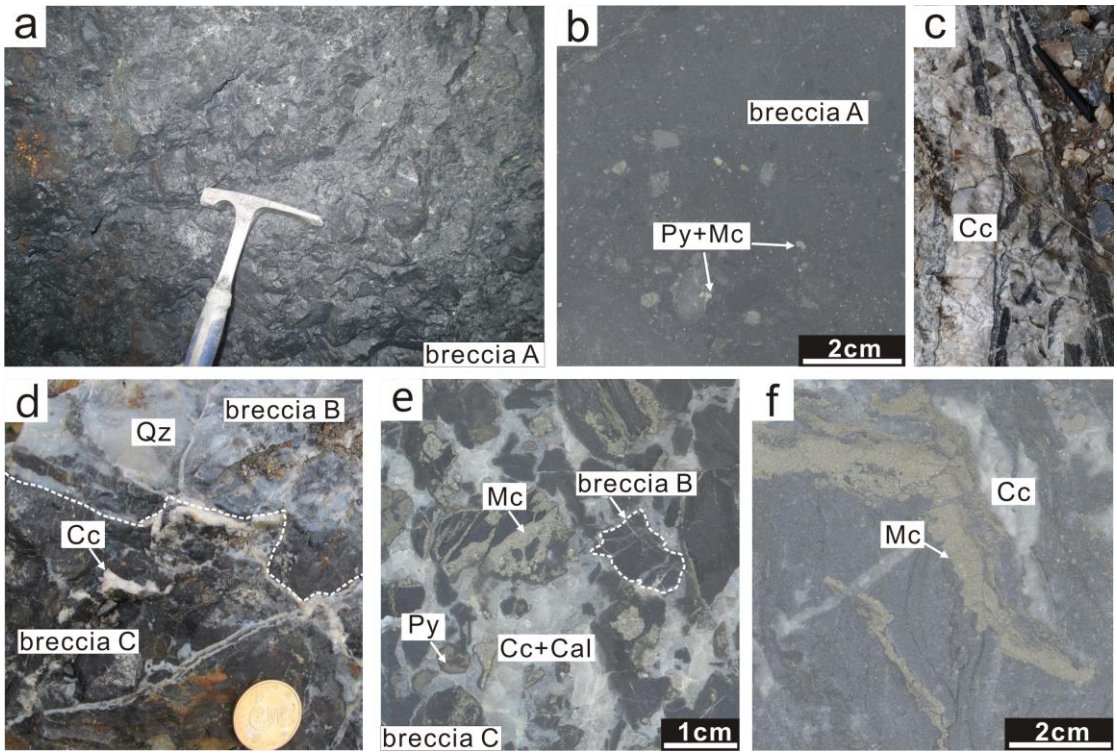

Figure 5.2 Photographs illustrating textures of breccia ores of the Daqiao gold deposit. (a) Typical auriferous silicified tectonic breccia A. (b) Fine-grained pyrite (Py) and marcasite (Mc) disseminations in silicified tectonic breccias A. (c) Hydraulic limestone breccias cemented by coarse calcite (Cc) veins. (d) Multistage hydraulic brecciation first cemented by quartz (Qz) and then by calcite. (e) Black silicified breccia A cemented by quartz and sulfides forming breccia B and then filled with calcite-chalcedony (Cal)-marcasite matrix (breccia C). (f) Late-ore stage marcasite-calcite veinlets in altered slate.

A detailed interpretation of hydrothermal stages and different generations of sulfides is provided by Wu et al. (2018a). The early-ore stage sulfide euhedras and aggregates (Py_2, Py_3, Py_4, Mc_1, and Mc_2) are dominantly hosted by tectonic breccia A (Figure 5.2a and b), whereas the main-ore stage sulfides (Py_5 and Mc_3) mainly occur in hydraulic breccias B and C (Figure 5.2d and e). In the late-ore stage, non- or sub-economic coarse-grained marcasite and minor pyrite-pyrrhotite-calcite veins (Py_6 and Mc_4) developed in altered slates (Figure 5.2f).

Complex early- to main-ore stage aggregates of various generations of pyrite and marcasite occur in the breccias in both the tectonic and hydraulic breccia ores at Daqiao deposit. Approximately fifty unweathered breccia (A, B, and C) samples were collected from outcrops, open pits, boreholes, and underground tunnels in order to provide a representative suite of samples for petrographical and geochemical

analyses (Figure 5.1b).

5.3 METHODS

Samples containing iron sulfides, and typical host rocks, were prepared as polished thick and thin sections. The thick sections were examined under optical microscopy to characterize the multiple generations of sulfides, and areas of interest (3–5 mm in diameter) were drilled out and mounted in 25-mm diameter epoxy discs together with pyrite standards for SIMS sulfur isotope analysis (Chen et al., 2015). The samples were carefully polished, sonicated, and mount-scale photomicrographed under an optical microscope using reflected light. The images were used to navigate to regions of interest to perform the microanalyses. Prior to in-situ compositional and sulfur isotopic analyses, the polished discs were carbon coated and imaged with the scanning electron microscope (SEM) in backscattered electron (BSE) and secondary electron (SE) modes to determine the detailed mineralogy, qualitative mineral compositional zoning, textural relationships and paragenesis. We used a diverse combination of micro-analytical techniques to investigate the elemental and isotopic characteristics of various generations of pyrite and marcasite. The methodology is summarized below and more standard and specific details for each are given in Appendix B.

5.3.1 LA–ICP–MS multi-element analysis of sulfides

Concentrations of trace elements in pyrite and marcasite were determined using laser-ablation inductively coupled plasma-mass spectrometry (LA–ICP–MS) at CODES, University of Tasmania. This instrumentation employs a New Wave 213-nm solid-state laser microprobe coupled to an Agilent 4500 quadrupole ICP-MS. The method is described in detail in Large et al. (2009) and Thomas et al. (2011). Spot ablation was carried out using a 25 to 40 micrometer spot size at 5 J/cm^2 and using 5 Hz, with a 30 s baseline and 30–45 s of ablation. Two laser profiles with profile lengths of 500 to 600 μm across pyrite and marcasite aggregates were also measured. Thirty-nine LA–ICP–MS spot analyses on pyrite and thirty-three on marcasite were measured (Table B5.1).

5.3.2 NanoSIMS multi-element imaging of sulfides

After trace element analysis, the epoxy mounts were polished with a series of diamond polishing powders (down to 1 μm) to minimize surface topography and coated with 10 nm of platinum to provide conductivity at high voltage. NanoSIMS analysis was performed at the Centre for Microscopy, Characterisation and Analysis (CMCA) at the University of Western Australia (UWA), using a CAMECA NanoSIMS 50L. The method is described in McLoughlin et al. (2011). A Cs^+ ion source with a spot size of approximately 50 nm was employed. Negative secondary ions ($^{34}S^-$, $^{63}Cu^{32}S^-$, $^{60}Ni^{32}S^-$, $^{75}As^{32}S^-$, $^{123}Sb^-$, and $^{197}Au^-$) were then sputtered from the sample surface using a beam current of ~2.5 pA.

5.3.3 SIMS sulfur isotope analysis

High-precision secondary ion mass spectrometry (SIMS) S-isotope analysis was carried out using the Cameca IMS-1280 at the Institute of Geology and Geophysics (Beijing), Chinese Academy of Sciences. Analytical conditions and procedures for high-precision S-isotope analyses with this IMS-1280 are described in detail elsewhere (Chen et al., 2015). We used the same parameters as Chen et al. (2015) and applied a Cs^+ primary ion beam, with a spot size of approximately ~10×15 μm, impact energy of 10 kV, and an intensity of ~2.5 nA.

Analyses of matrix-matched reference material should be used to correct the mass fractionation during SIMS analysis (e.g., LaFlamme et al., 2016, 2018). However, due to a lack of suitable marcasite standard, two pyrite standards: Sonora pyrite ($\delta^{34}S_{VCDT}$ = +1.61‰; Farquhar et al., 2013) and Balmat pyrite ($\delta^{34}S_{VCDT}$ = +16.12 ± 0.68‰, 2 σ; Whitehouse, 2013) were used during both the pyrite and marcasite analysis sessions. Pyrite standard has been utilized for SIMS and LA-MC-ICP-MS sulfur isotope analysis for marcasite in other studies (e.g., Rouxel et al., 2008; Wong et al., 2017). Here, we use a comparison of results from the two techniques to assess potential matrix effects. Eighteen SIMS spot analyses on pyrite and twenty-nine on marcasite were measured (Table B5.2).

5.4 RESULTS

5.4.1. Petrographic features

Detailed optical and SEM petrographic observations revealed that inclusion-free pyrite is surrounded by porous pyrite, that is, in turn, bordered by marcasite together with minor arsenopyrite in the Daqiao breccias (Figure 5.3, Table 5.1). Sulfide generations and replacement/overgrowth reactions are described with notation of the form $X_{i\text{-}j}$, which means that sulfide X of generation i is inferred to have replaced and/or overgrown sulfide j of a previous generation. The generations of interest here are Py_3, $Py_{4\text{-}py}$, $Mc_{2\text{-}py}$ in the early-ore stage, and $Mc_{3\text{-}py}$ and Apy in the main-ore stage.

Py_3 aggregates (0.01–2 mm across) are generally nonporous and free or almost free of mineral inclusions (Figure 5.3a-g). Py3 commonly contains narrow internal cyclic elemental zones in the SEM images (Figure 5.3c and d).

$Py_{4\text{-}py}$ (0.01–1 mm across) borders Py_3 (Figure 5.3a-d) and is also present in Py_3 microfractures and interstitial spaces between Py_3 grains (Figure 5.3e-g and i). $Py_{4\text{-}py}$ commonly contains mineral inclusions (5–100 μm in diameter), such as chalcopyrite, galena, and arsenopyrite (Figure 5.3a-c, and e). $Py_{4\text{-}py}$ aggregates are characterized by abundant pores varying in size (1–50 μm in diameter), which exhibit no perceptible preferred orientation. Porosity in most of $Py_{4\text{-}py}$ occupies approximately 1–10 %, or in some cases 10–25 % of the volume, although we note that the petrographical techniques used are not quantitative and cannot identify sub-micron pores. The contact between Py_3 and $Py_{4\text{-}py}$ is sharp and curvilinear (contact marked with yellow lines in Figure 5.3a-g, i and k).

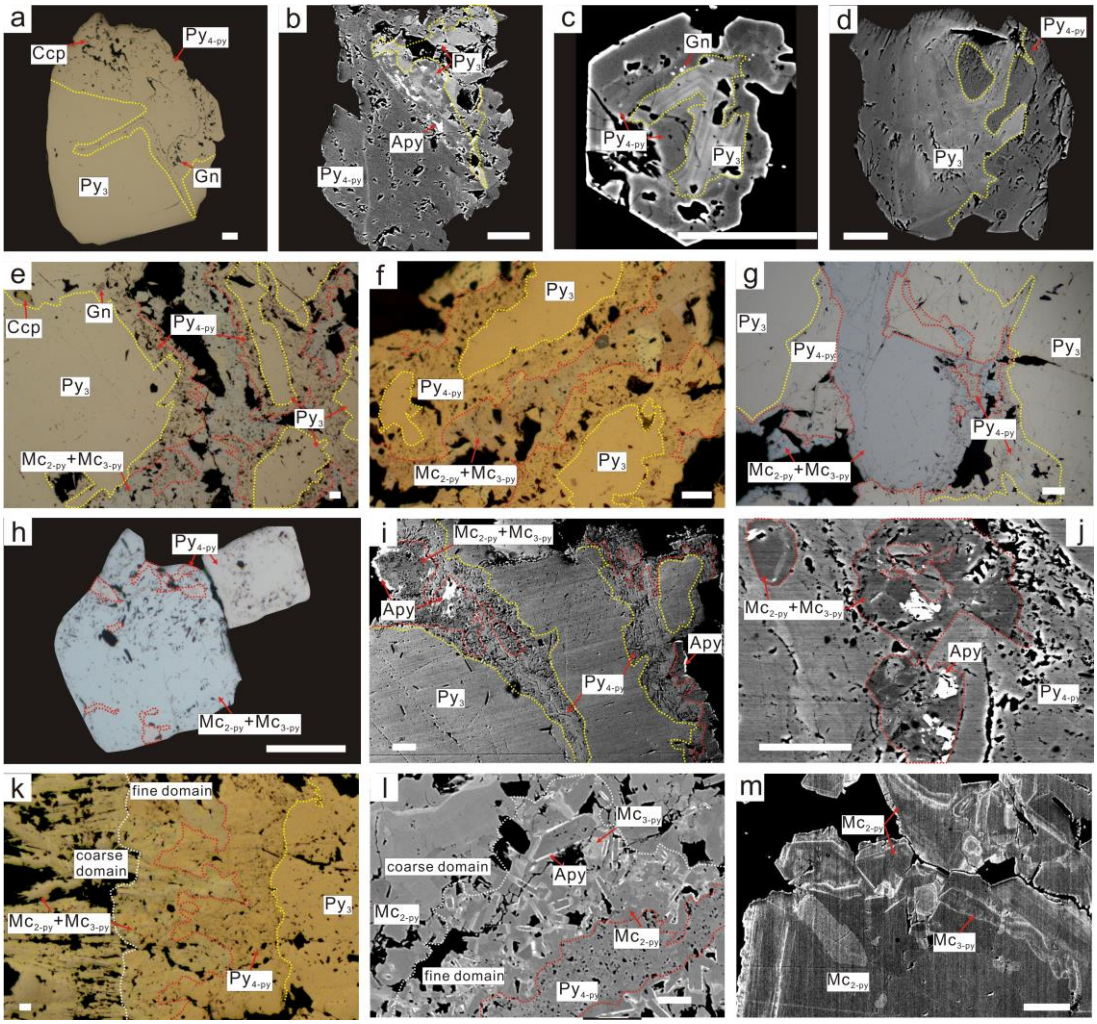

Figure 5.3 Typical textures and overprinting relationships of different generations of pyrite and marcasite at Daqiao deposit. (a-d) Inclusion-free, zoned pyrite (Py_3) is surrounded by porous pyrite ($Py_{4\text{-}py}$) plus minor chalcopyrite (Ccp), galena (Gn), and arsenopyrite (Apy) inclusions. Note the sharp and curvilinear interfaces among them (contacts marked with yellow lines). (e and f) $Py_{4\text{-}py}$ borders Py_3 and is also present in Py_3 microfractures and interstitial spaces between Py_3 grains; $Py_{4\text{-}py}$ is in turn bordered by aggregates of marcasite ($Mc_{2\text{-}py}$ and $Mc_{3\text{-}py}$; contact marked by red lines). (g and h) Marcasite ($Mc_{2\text{-}py}$ and $Mc_{3\text{-}py}$) containing irregular $Py_{4\text{-}py}$ inclusions shows similar external morphology with euhedral $Py_{4\text{-}py}$ grains. (i) Marcasite ($Mc_{2\text{-}py}$ and $Mc_{3\text{-}py}$) and arsenopyrite (Apy) veinlets and inclusions in porous $Py_{4\text{-}py}$ that presents in the microfractures and margins of Py_3. (j) Close-up of intergrowth of marcasite and Apy inclusions. (k) $Mc_{2\text{-}py}$ and $Mc_{3\text{-}py}$ are characterized by a bimodal grain size distribution with a fine and a coarse grained domain (contact marked by white lines) bordering porous $Py_{4\text{-}py}$. (l) Bright zoned $Mc_{3\text{-}py}$, Apy and $Mc_{2\text{-}py}$ euhedras occurs as aggregates surrounding $Py_{4\text{-}py}$ in the fine-grained domain. (m) Bright, sub-micron sector and cyclic bands of $Mc_{3\text{-}py}$ in $Mc_{2\text{-}py}$. Scale bar is 30 μm.

Marcasite consisting of $Mc_{2\text{-}py}$ and $Mc_{3\text{-}py}$ is anisotropic with yellowish-brown to

grayish-blue polarization colors (Figure 5.3e-h and k). $Mc_{2\text{-}py}$ and $Mc_{3\text{-}py}$ are commonly intergrown and are characterized by a bimodal grain size distribution with a fine (1–100 μm) and a coarse (up to 300 μm) grained domain (Figure 5.3k and l). In the fine-grained domains, $Mc_{2\text{-}py}$ microcrystals occurs as aggregates surrounding $Py_{4\text{-}py}$, with sharp, planar to curvilinear interfaces between $Py_{4\text{-}py}$ and $Mc_{2\text{-}py}$ (contact marked with red lines in Figure 5.3e-l). Porous $Mc_{2\text{-}py}$ and $Mc_{3\text{-}py}$ also contains irregular $Py_{4\text{-}py}$ inclusions and shows similar external morphology with euhedral $Py_{4\text{-}py}$ grains (Figure 5.3g and h). $Mc_{2\text{-}py}$ commonly displays some fine pores and a lower average atomic mass than $Py_{4\text{-}py}$ shown as a darker color in BSE images (Figure 5.3i and j). Zoned $Mc_{3\text{-}py}$, in some cases, surrounds $Mc_{2\text{-}py}$ crystals and varies in size (1–10 μm; Figure 5.3l). In BSE image of the fine-grained domains, marcasite aggregates are zoned with irregular bright, sector and sub-micrometer cyclic bands of $Mc_{3\text{-}py}$ in $Mc_{2\text{-}py}$ crystals (Figure 5.3m), suggesting a precipitation cyclicity between $Mc_{2\text{-}py}$ and $Mc_{3\text{-}py}$. There are minor fine-grained Apy veinlets or inclusions (1–10 μm), closely intergrown with $Mc_{2\text{-}py}$ and zoned $Mc_{3\text{-}py}$ (Figure 5.3i, j and l).

The coarse-grained domains generally border the fine-grained $Mc_{2\text{-}py}$ and $Mc_{3\text{-}py}$ domains (contact marked by white lines in Figure 5.3k and l). In this domain, tabular $Mc_{2\text{-}py}$ contains little porosity. Infrequent sub-micron $Mc_{3\text{-}py}$ bands are present in $Mc_{2\text{-}py}$, and Apy inclusions are notably absent (Figure 5.3l).

5.4.2. Sulfide trace element compositions

Wu et al. (2018a) report LA–ICP–MS spot analyses of all the different generations of pyrite and marcasite from the Daqiao deposit, and interpret these data in the context of sulfide evolution and deposition mechanisms during hydrothermal fluid flow and gold mineralization. In this study, we present additional LA–ICP–MS data that enable a better understanding in the complex textures of pyrite and marcasite aggregates in the breccias. Seventy-two previously unreported analyses of pyrite and marcasite given in Table B5.1 are summarized in Table 5.2. The results (Figure 5.4) are based on combination of the 72 spot analyses and the data reported in Wu et al. (2018a). Data from two previously unreported LA–ICP–MS transects across complex sulfide aggregates are also presented in Figure 5.5. Because of the large compositional variations, median values are used for comparison (Figure 5.6).

Py_3

Gold contents in the euhedral inclusion-free Py_3 interpreted as early-ore stage vary from b.d.l. (below detection limit) to 107 ppm with a median of 0.5 ppm, while arsenic ranges from b.d.l. to 87444 ppm (median = 3115 ppm, *n* = 49; Figure 4a). A range of other trace elements occurred at concentrations above the detection limits in Py_3, mainly including Co, Ni, Cu, Zn, Se, Ag, Sb, Tl, and Pb (Table 5.2, Figure 5.4b-f). Spikes in As, Co, Ni, Sb, Cu, and Tl were revealed by the LA–ICP–MS line analyses (Figure 5.5c and d).

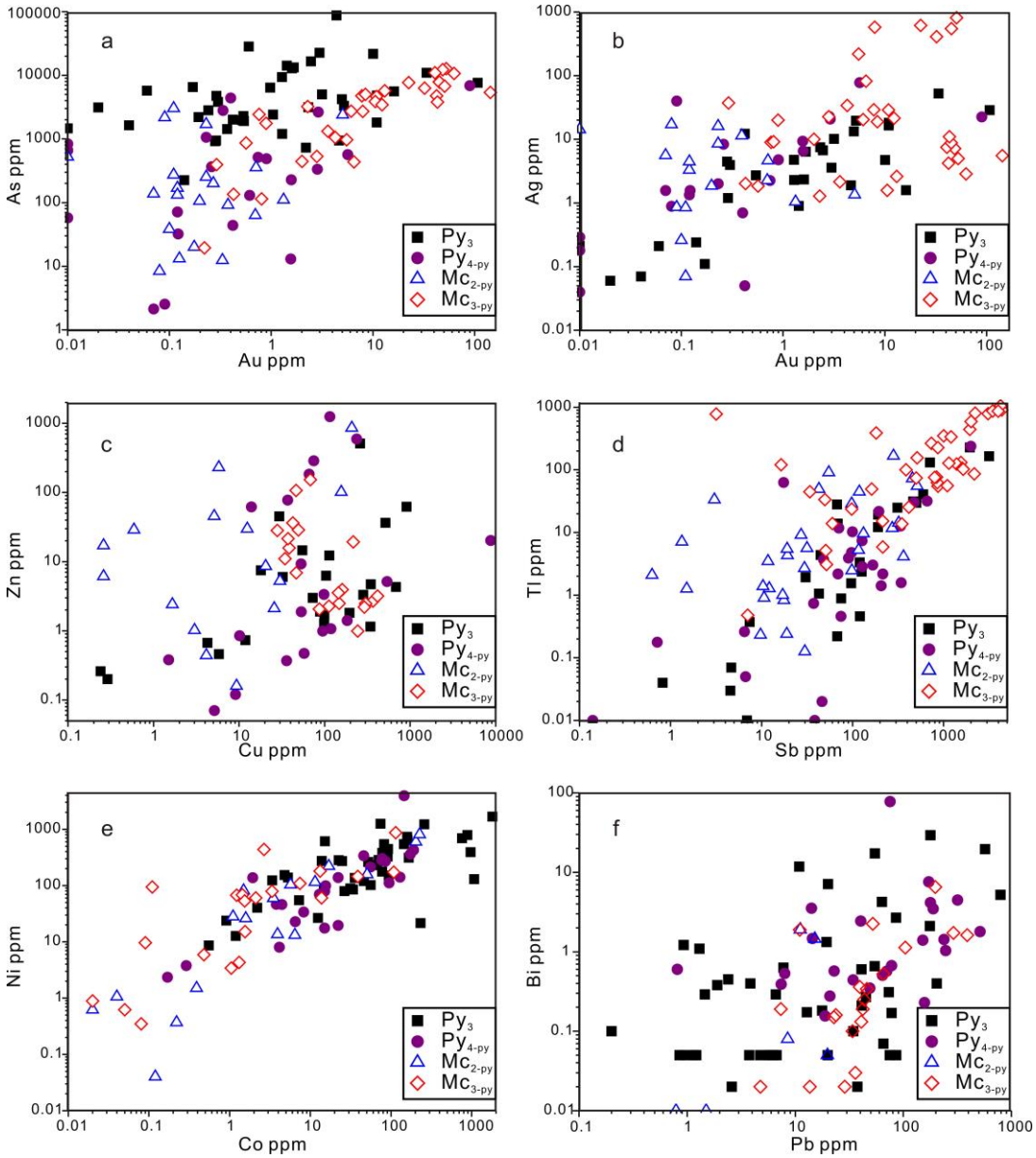

Figure 5.4 Diagrams showing results of LA–ICP–MS spot analysis on the different generations of pyrite and marcasite. (a) Au-As. (b) Au-Ag. (c) Cu-Zn. (d) Sb-Tl. (e) Co-Ni. (f) Pb-B

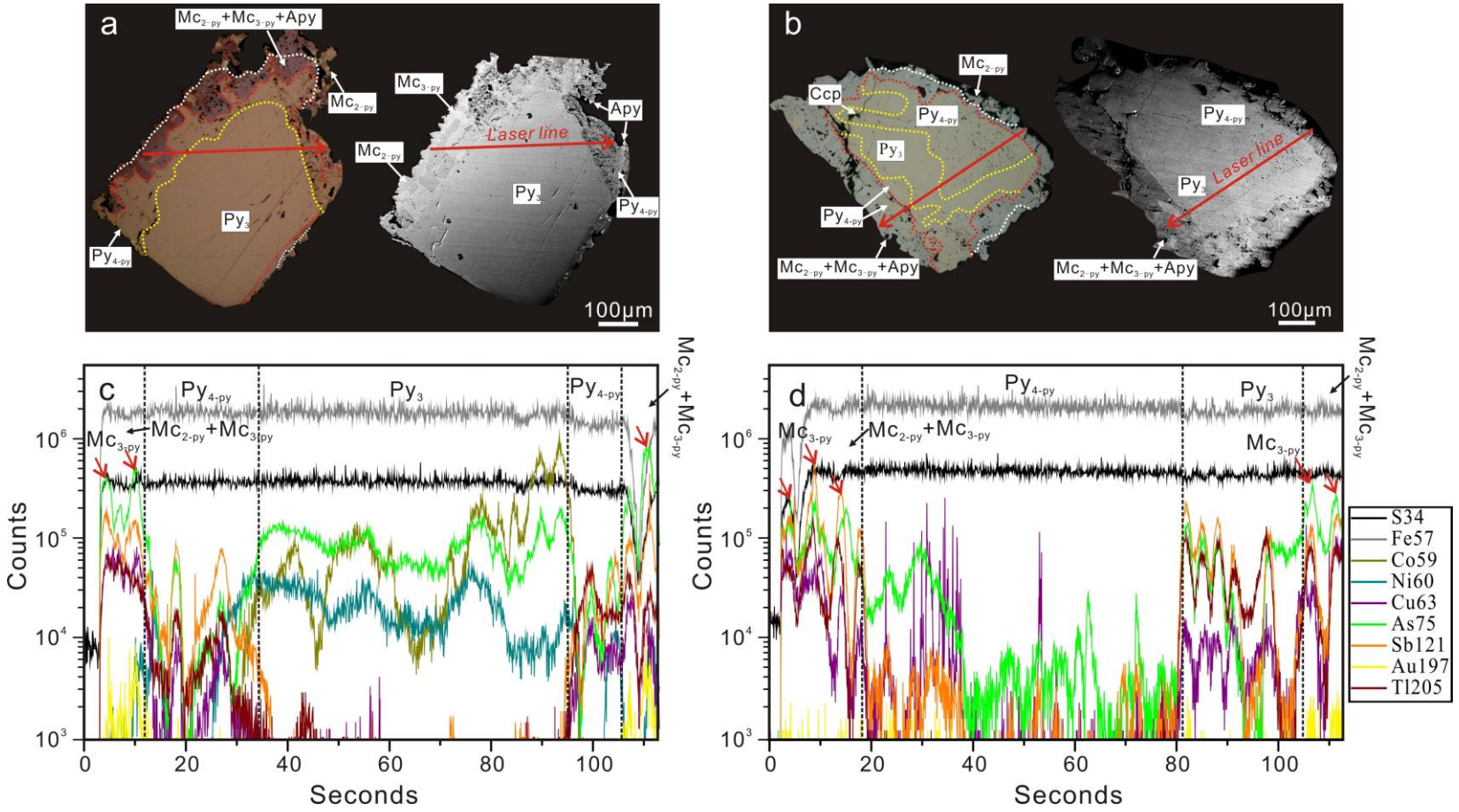

Figure 5.5 (a and b) Comparisons of typical sulfide textures involving co-existing Py_3, $Py_{4\text{-}py}$ and marcasite ($Mc_{2\text{-}py}$ and $Mc_{3\text{-}py}$) under reflected microscopy and SEM. (c and d) LA–ICP–MS profiles showing the trace element variations across different sulfides as shown on (a) and (c), respectively

Table 5.1 Comparison between diagnostic features of dissolution and reprecipitation, overgrowth, solid-state diffusion, and sulfide textures from the Daqiao gold deposit

Main features	Dissolution and reprecipitation	Overgrowth	Solid-state diffusion	Sulfide textures at Daqiao gold deposit
Preservation of external morphology	tight (dissolution-limiting) or rough (reprecipitation-limiting) preservation of external morphology of parent phase	overgrowth phase coarsens the external morphology of pre-existing phase	preservation of external morphology of parent phase	some aspects of preservation of external morphology of Py_3 and $Py_{4\text{-}py}$
Phase boundary	distinct and sharp interface between parent and product phases	sharp interface between pre-existing and overgrowth phase	compositional diffusion gradients caused by ion exchange in both parent and product phases	distinct and sharp interfaces even at sub-micron scale
Porosity	numerous permeable pores and cracks within product phase	few pores in overgrowth phase; pores exist during rapid growth	few pores within product phase	numerous pores within $Py_{4\text{-}py}$, aggregates of $Mc_{2\text{-}py}$ and $Mc_{3\text{-}py}$; few pores in coarse-grained $Mc_{2\text{-}py}$
Mineral inclusion	numerous mineral inclusions in product phase	existence or absence of inclusions	absence of inclusions	chalcopyrite, galena, and arsenopyrite inclusions within $Py_{4\text{-}py}$; arsenopyrite inclusion within aggregates of $Mc_{2\text{-}py}$ and $Mc_{3\text{-}py}$
Existence of fluid	fluid-involved open system	fluid-involved open system	dry and closed system	episodic infiltration of deep-seated hydrothermal fluids
Temperature	low to high temperature	low to high temperature	high temperature (e.g., 425–500 °C)	low temperature (< 240 °C)
Reaction rate	rapid (e.g., several hours)	rapid (e.g., several hours)	extremely slow (e.g., millions of years)	relative rapid related to hydraulic fracturing

Table 5.2 Summarized LA–ICP–MS analyses of different generations of pyrite and marcasite involved in the pyrite replacement from the Daqiao gold deposit

Iron sulfides	Co	Ni	Cu	Zn	As	Se	Ag	Sb	Te	W	Au	Tl	Pb	Bi
Py_3 (*n* = 49)														
Median	35.6	138.8	4.3	3.0	3115.1	54.4	0.2	10.0	0.2	0.9	0.53	4.4	12.8	0.2
Min	b.d.l.	b.d.l.	b.d.l.	b.d.l.	b.d.l.	b.d.l.	b.d.l.	b.d.l.	b.d.l.	b.d.l.	b.d.l.	b.d.l.	2.9	b.d.l.
Max	1805.7	1679.2	905.3	511.6	87443.9	464.5	52.3	3172.9	18.5	15.4	107.01	227.2	791.1	29.3
$Py_{4\text{-}py}$ (*n* = 33)														
Median	13.0	46.5	53.0	1.2	130.2	36.5	1.3	70.6	0.2	0.1	0.09	1.6	40.4	0.6
Min	b.d.l.	b.d.l.	b.d.l.	b.d.l.	b.d.l.	b.d.l.	b.d.l.	b.d.l.	b.d.l.	b.d.l.	b.d.l.	b.d.l.	2.9	b.d.l.
Max	190.2	3949.7	8730.3	1246.8	8031.4	124.4	78.0	1999.8	20.1	7.4	89.85	238.0	2163.7	166.3
$Mc_{2\text{-}py}$ (*n* = 44)														
Median	0.2	1.3	2.9	7.4	21.4	10.1	1.0	19.1	0.0	8.8	0.08	2.3	1.0	0.0
Min	b.d.l.	b.d.l.	b.d.l.	b.d.l.	b.d.l.	b.d.l.	b.d.l.	b.d.l.	b.d.l.	b.d.l.	b.d.l.	b.d.l.	2.9	b.d.l.
Max	226.3	809.7	250.9	856.7	3028.4	131.3	17.1	514.1	6.6	462.7	5.06	167.3	151.4	1.9
$Mc_{3\text{-}py}$ (*n* = 40)														
Median	1.3	9.7	46.5	3.9	2578.2	142.4	8.9	824.2	0.1	33.2	5.82	104.1	21.4	0.0
Min	b.d.l.	b.d.l.	b.d.l.	b.d.l.	19.4	3.6	b.d.l.	3.2	b.d.l.	b.d.l.	b.d.l.	0.5	2.9	b.d.l.
Max	114.5	872.0	415.2	519.4	12726.5	427.6	815.6	4369.8	9.2	92.7	62.86	1049.6	720.7	6.5

b.d.l.: below detection limit

$Py_{4\text{-}py}$

Based on results of thirty-three LA–ICP–MS spot analysis, trace elements in $Py_{4\text{-}py}$ can be classified into two groups that are enriched and depleted in comparison to Py_3 (Figures. 5.4-5.6). The enriched group consists of Cu, Sb, Ag, Pb, and Bi. The depleted group includes Au (median = 0.09 ppm), As (median = 130 ppm), Te, Se, Zn, Co, Tl, Ni, and W (Figure 5.6a). Some $Py_{4\text{-}py}$ domains show spikes of As, Cu, Sb and Tl in the LA–ICP–MS laser profiles (Figure 5.5c and d).

$Mc_{2\text{-}py}$

Forty-four spot analyses of $Mc_{2\text{-}py}$ reveal that a small number of trace elements are enriched in $Mc_{2\text{-}py}$ relative to Py_3 (Figures. 5.4 and 5.6a). These elements include Sb, Ag, Zn, and W. Concentrations of other trace elements are much lower than those both in Py_3 and $Py_{4\text{-}py}$, notably for Au (median = 0.08 ppm), As (median = 21 ppm), Co, Ni, Pb, and Bi. In the laser profiles, it was difficult to obtain trace element contents of unmixed $Mc_{2\text{-}py}$ or $Mc_{3\text{-}py}$ because the spot size of laser beam was larger relative to the zone width (Figure 5.5c and d).

$Mc_{3\text{-}py}$

The main-ore stage $Mc_{3\text{-}py}$, which occurs in irregular zones with higher average atomic mass than early-ore $Mc_{2\text{-}py}$, shown in brighter BSE images (Figure 5.3l and m) is enriched in a suite of trace elements relative to Py_3, $Py_{4\text{-}py}$ and $Mc_{2\text{-}py}$ (Figures. 5.4 and 5.6a). Based on the results of forty spot analyses, elements enriched in $Mc_{3\text{-}py}$ compared to Py_3 and $Py_{4\text{-}py}$ are Au (median = 5.8 ppm), W, Tl, Ag, Sb, Se, and Zn. Elements depleted in $Mc_{3\text{-}py}$ relative to Py_3 and $Py_{4\text{-}py}$ include Te, Ni, Co and Bi. Although As is depleted in $Mc_{3\text{-}py}$ (median = 2578 ppm ppm) relative to Py_3, it is higher in $Mc_{3\text{-}py}$ than in $Py_{4\text{-}py}$ (Figure 5.6).

The LA–ICP–MS ablation profiles clearly reveal 2–3 distinctive spikes that record zones in the $Mc_{2\text{-}py}$–$Mc_{3\text{-}py}$ aggregates that are enriched in As, Sb, Tl, Cu, and minor Au (marked with red arrows on Figure 5.5c and d). Relative trace element concentrations in the two generations of marcasite ($Mc_{2\text{-}py}$ and $Mc_{3\text{-}py}$) are more similar to each other than they are to Py_3, in spite of higher absolute trace element concentrations in the zones of $Mc_{3\text{-}py}$ (Figure 5.6).

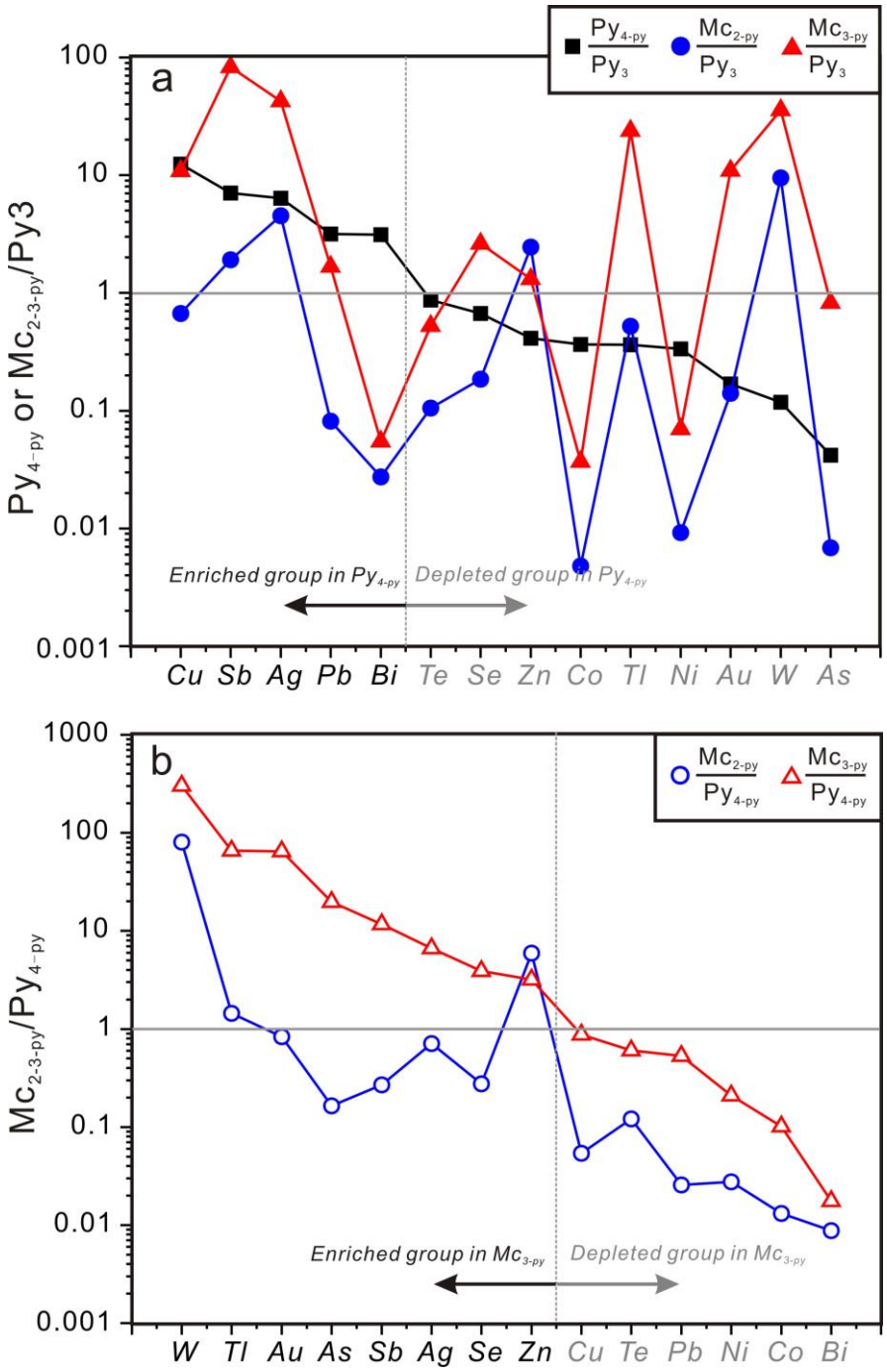

Figure 5.6 Spider diagrams illustrating the gain and loss of trace elements during the Py_3 (a) and $Py_{4\text{-}py}$ (b) replacement processes.

Apy

Fine Apy grains or veinlets mainly occur as 1–10 μm intergrowths with zoned $Mc_{3\text{-}py}$ (Figure 5.3i, j and l). The size of the Apy is smaller than the laser beam, so it was not possible to obtain unmixed analyses of Apy. A small number of SEM-EDS analyses of the Apy grains were obtained (not shown), and these fall on a compositional mixing line between FeS_2 and FeAsS, indicating the analyses are Apy-$Mc_{3\text{-}py}$

mixtures, or that the Apy is depleted in As.

5.4.3. Trace element distribution in sulfides

A typical sulfide texture involving co-existing Py_3, $Py_{4\text{-}py}$ and marcasite was chosen for NanoSIMS mapping (boxed area on Figure 5.7a). The high-resolution NanoSIMS images reveal three chemical microbands in Py_3 (~0.5 μm across; marked with red arrows; Figure 5.7c-g). These bands are of continuous shape and are enriched in Ni, As, and Sb, and to a less extent, Au and Cu compared to the host Py_3. These metal-rich microbands are compositionally consistent with the chemical zoning recorded in the LA–ICP–MS line analyses across Py_3 (Figure 5.5c and d).

The micropores in the $Py_{4\text{-}py}$ and $Mc_{2\text{-}py}$ appear dark in the NanoSIMS elemental maps (Figure 5.7b). Arsenic, Sb, and Au are heterogeneously distributed in porous $Py_{4\text{-}py}$. Cu enrichment occurs as inclusions (0.25–1 μm across; marked with green arrows) in $Py_{4\text{-}py}$ and $Mc_{3\text{-}py}$ (Figure 5.7c). Euhedral or irregular $Mc_{2\text{-}py}$ has lower Cu and Ni concentrations than Py_3 while As, Sb, and Au contents are elevated in $Mc_{2\text{-}py}$ relative to Py_3 though this may be due to some extent to a partial contribution from $Mc_{3\text{-}py}$. The $Mc_{3\text{-}py}$ zones (1–3 μm in thickness) and minor Apy aggregates are characterized by depletion of ^{34}S compared to Py_3, $Py_{4\text{-}py}$, and $Mc_{2\text{-}py}$ (Figure 5.7b). The highest As, Sb, and Au concentrations are associated with irregular finger shaped zones of $Mc_{3\text{-}py}$ (Figure 5.7e-g), which are characterized by a higher average atomic mass than Py_3, $Py_{4\text{-}py}$, and $Mc_{2\text{-}py}$ in the BSE images (Figure 5.7a). There is no Ni enrichment in $Py_{4\text{-}py}$, $Mc_{2\text{-}py}$ or $Mc_{3\text{-}py}$ (Figure 5.7d).

In the NanoSIMS line profile (Figure 5.7h), five zones with elevated Cu, As, Sb and Au ion counts (concentrations) can be identified in Py_3. The $Mc_{3\text{-}py}$ and Apy aggregates also display zoning; three peaks exhibit high concentrations of trace elements compared to other immediately adjacent iron sulfides (Figure 5.7h). The three peaks in $Mc_{3\text{-}py}$ correlate with regions of ^{34}S depletion; however, similar peaks in Py_3 are not associated with sulfur isotopic variations.

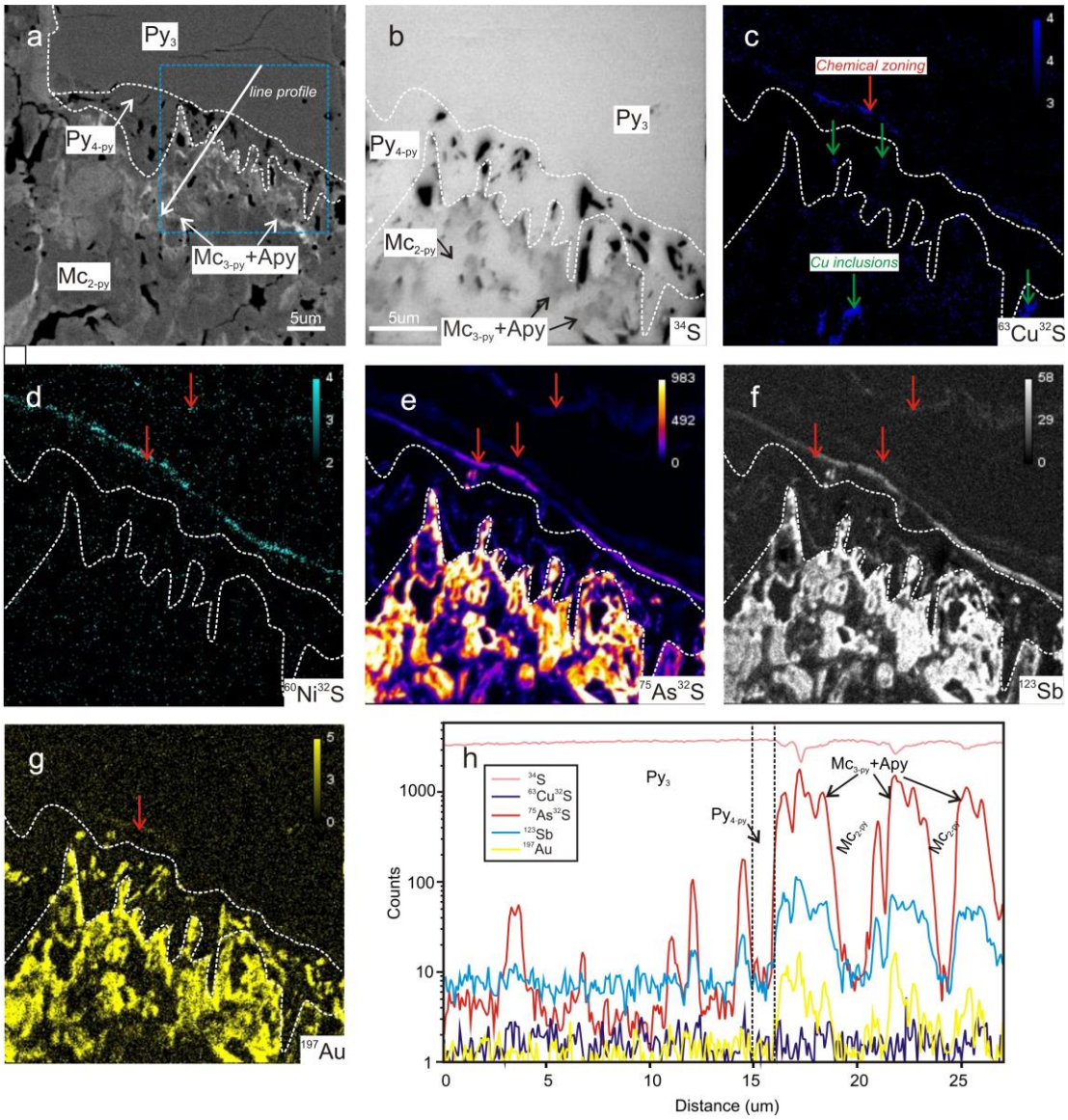

Figure 5.7 NanoSIMS ion maps (b-g) from the boxed area of sulfide aggregate (a) of sulfur (^{34}S), copper ($^{63}Cu^{32}S$), nickel ($^{60}Ni^{32}S$), arsenic ($^{75}As^{32}S$), antimony (^{123}Sb), and gold (^{197}Au) showing the trace element distribution during pyrite replacement, and line profile (h) showing the trace element variation patterns.

5.4.4. Sulfur isotopes

The sulfur isotopic compositions presented herein are from high-resolution, previously unpublished SIMS analyses (Figure 5.8, Table B5.2). The $\delta^{34}S$ values of a total of thirteen analyses of Py_3 vary from +1.9 to +9.0‰, with a mean of +4.6‰ (σ = 1.9); five analyses of $Py_{4\text{-py}}$ vary from +1.7 to +4.3‰, with a mean of +2.9‰ (σ = 1.0); thirteen analyses of $Mc_{2\text{-py}}$ vary from -0.9 to +3.7‰, with a mean of +2.4‰ (σ = 1.2); sixteen analyses of $Mc_{3\text{-py}}$ yield a large range in $\delta^{34}S$ value from -11.4 to

+2.2‰ (mean -1.3‰, σ = 4.4). In contrast, the mean LA-MC-ICP-MS sulfur isotopes of these four types of sulfides (Py_3, $Py_{4\text{-}py}$, $Mc_{2\text{-}py}$, and $Mc_{3\text{-}py}$) are +5.2‰ (s.d. = 2.4, n = 17), +3.4‰ (s.d. = 1.3, n = 11), +5.0‰ (s.d. = 3.9, n = 17), and -9.7‰ (s.d. = 6.2, n = 6), respectively (Figure 5.8, Wu et al., 2018a).

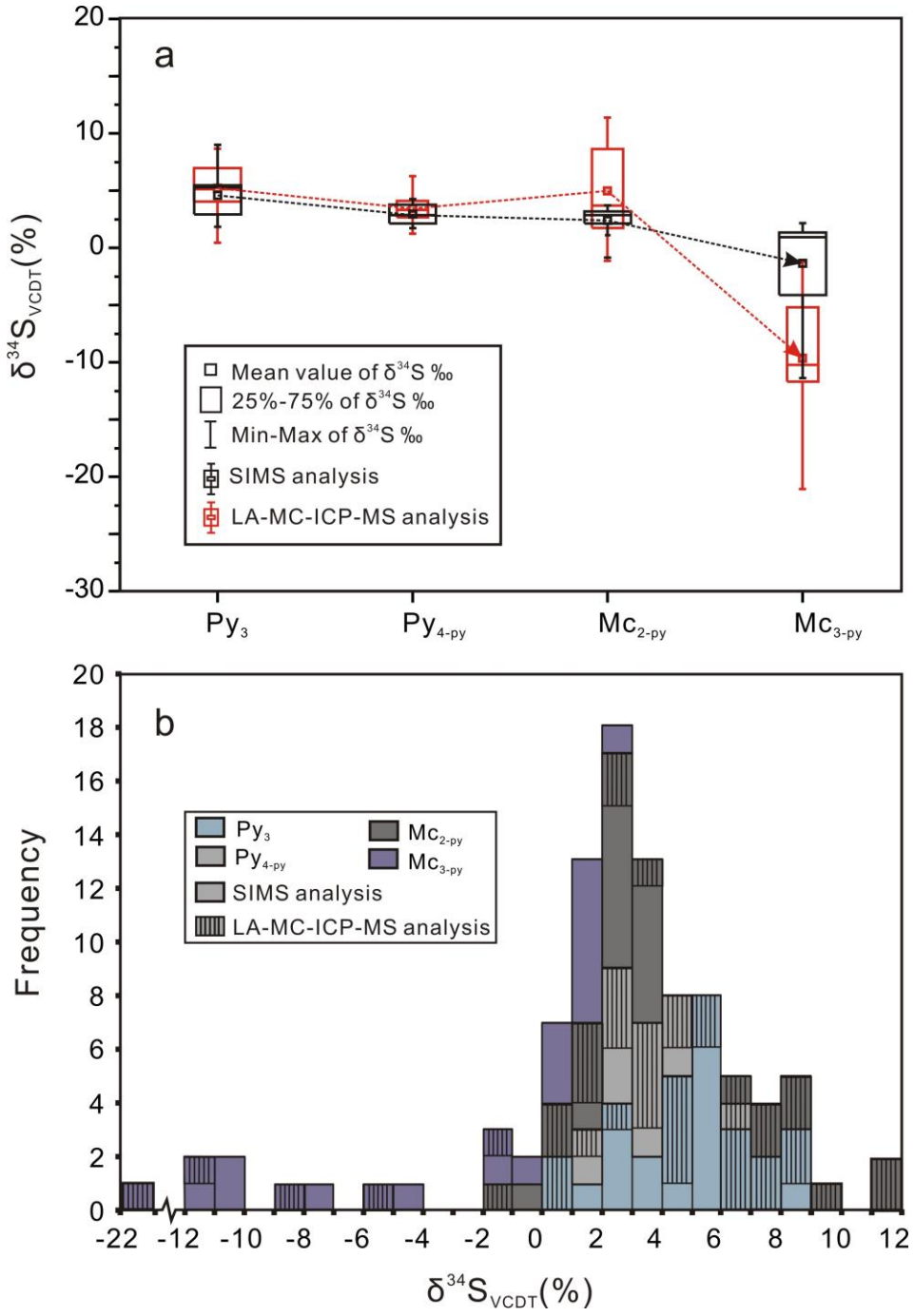

Figure 5.8 Box figure (a) and histogram (b) showing the variation of $\delta^{34}S$ values of different generations of pyrite and marcasite involved in the pyrite replacement.

5.5 DISCUSSION

5.5.1 Textual interpretations

Pyrite replacement by pyrite

Detailed textural observations demonstrate that porous $Py_{4\text{-}py}$, together with chalcopyrite, galena and arsenopyrite inclusions, occurs preferentially along micro-fractures and grain margins of Py_3 (Figure 5.3). The reaction front is sharp and curvilinear at sub-micron resolution of the NanoSIMS mapping and profile (Figure 5.7). These observations are taken as evidence supporting the idea that $Py_{4\text{-}py}$ mainly formed by replacement of Py_3 via a dissolution and reprecipitation mechanism (Table 5.1). Preservation of some aspects of the external morphology of parent Py_3 (Figure 3a-d) implies some degree of a spatial and temporal coupling between the dissolution and reprecipitation (cf. Putnis, 2002, 2009; Altree-Williams et al., 2015). However, it is still possible that some $Py_{4\text{-}py}$ overgrowth may coarsen the external dimension of parent Py_3 that was replaced by $Py_{4\text{-}py}$.

The volume reduction necessary to create the observed porosity in product $Py_{4\text{-}py}$ may be accommodated by some combination of a lower molar volume relative to Py_3, and the partial dissolution of parent Py_3 into the fluid (Walker et al., 1995; Putnis, 2002, 2009; Rubatto et al., 2008). It has been calculated that pyrite containing 3.8 wt% arsenic ($Fe_{32}S_{62}As_2$) has an expansion of 0.83 % in volume relative to pure pyrite as a consequence of the greater length of As-S bonds than S-S bonds (Blanchard et al., 2007). During the replacement of arsenic-rich Py_3 by arsenic-depleted $Py_{4\text{-}py}$ (median 3115 ppm vs. 130 ppm As), the As-induced volume decrease alone cannot explain the 1–10 vol% porosity in $Py_{4\text{-}py}$ (Figure 5.3). Volume reduction during hydrothermal replacement has been suggested to be due to dissolution of parent phase in excess of the product phase precipitated, because of their different solubilities in the interfacial fluids (Putnis, 2002, 2009). However, in this case of pyrite replacement by pyrite, the solubility is not expected to change much.

It has also been suggested that porosity in pyrite from hydrothermal gold deposits is a consequence of rapid crystallization (Simon et al., 1999). Porous pyrite formed via rapid growth is characterized by aggregates of fine grain size microcrystals, several microns across, with the grain size distribution controlled by rapid nucleation relative to crystal growth (Butler and Richard, 2000). Concentrations of Au, As (e.g., up to

2.4 wt% As and 1600 ppm Au; Simon et al., 1999), and other trace elements are high because the extra vacancies and surface defects associated with rapid growth facilitate their incorporation (Reich et al., 2005). Aggregates of porous $Py_{4\text{-}py}$ at Daqiao deposit contains much lower contents of Au, As and other trace metals (130 ppm As and 0.1 ppm Au; Figure 5.4) than Py_3. However, this compositional difference does not eliminate a rapid growth, since trace element concentrations around could be low during the $Py_{4\text{-}py}$ reprecipitation.

Marcasite relationships

Aggregates of $Mc_{2\text{-}py}$ and $Mc_{3\text{-}py}$ commonly occur on the margins of $Py_{4\text{-}py}$ (Figure 5.3e, f, i, k and l), or as euhedral grains containing irregular $Py_{4\text{-}py}$ inclusions (Figure 3g and h). Several lines of textural evidence, including the sharp, planar to curvilinear interface between $Py_{4\text{-}py}$ and $Mc_{2\text{-}py}$ (Figure 5.3e-l), fine pores in $Mc_{2\text{-}py}$ (Figure 5.3e-l), some degree of preservation of $Py_{4\text{-}py}$ external dimension (Figure 5.3g and h), and occurrence of fine-grained Apy inclusions with $Mc_{2\text{-}py}$ and $Mc_{3\text{-}py}$ (Figure 5.3i, j and l), imply that $Mc_{2\text{-}py}$ and $Mc_{3\text{-}py}$ aggregates probably formed by replacement of $Py_{4\text{-}py}$ (Table 5.1). However, during the replacement of $Py_{4\text{-}py}$, cyclic precipitation between $Mc_{2\text{-}py}$ and zoned $Mc_{3\text{-}py}$ (Figure 5.3m) indicates that there may have been switching between the early-ore and main-ore conditions as the ore-forming process progressed.

In some cases, aggregates of fine-grained $Mc_{2\text{-}py}$ crystals and zoned $Mc_{3\text{-}py}$ with little porosity formed directly on $Py_{4\text{-}py}$ margins where this is no sign of dissolution (Figure 5.3l). This texture implies that the marcasite reprecipitation is not tightly coupled with dissolution of $Py_{4\text{-}py}$ (Putnis, 2009; Xia et al., 2009). The degree of coupling between dissolution and precipitation is thought to be controlled by fluid parameters, such as pH, and the degree of supersaturation (Xia et al., 2009; Qian et al., 2011).

Experimental studies have demonstrated that pyrite with fine, homogenous porosity intergrown with marcasite can form via solid-state marcasite transformation in a closed system at temperatures of 425–500 °C (Table 5.1, Fleet, 1970; Murowchick, 1992). However, the observed 1–50 μm pores (1–10 vol%) in $Py_{4\text{-}py}$ are quite different to those in pyrite produced in the experiment. Moreover, it has been

suggested that the rate of solid-state reaction is relatively slow in sulfides even at high temperatures. For example, iron sulfides with peak metamorphic temperature of 500–600 ^{o}C preserve Co and sulfur isotope zoning on the micron scale (Evans et al., 2014). Kinetic studies suggest that a half-life for the solid-state transformation of marcasite to pyrite at 200 °C is 3×10^{6} yr (Lennie and Vaughan, 1992). Precipitation of pyrite and marcasite or their aggregates can occur on timescales of only a few hours under hydrothermal conditions and temperatures to 220 °C (Qian et al., 2011). At Daqiao deposit, conditions were fluid-rich (Wu et al., 2018a) and temperatures are thought to have been low (ca. 100–240 °C; Xu et al., 2015), within the stability field of marcasite (temperature less than 240°C; Murowchick and Barnes, 1986). It is therefore likely that solid-state transformation was not a significant contributor to replacement of pyrite by marcasite.

Coarse-grained $Mc_{2\text{-}py}$ domains also occur perpendicular to aggregates of $Mc_{2\text{-}py}$ and $Mc_{3\text{-}py}$ (Figure 5.3k and l). These $Mc_{2\text{-}py}$ euhedra contain few pores in comparison to those in $Mc_{2\text{-}py}$ inferred to have formed by replacement of porous $Py_{4\text{-}py}$. Cementation of $Mc_{2\text{-}py}$ idiomorphic crystals indicates that marcasite precipitated from fluids as new grains or as overgrowths rather than forming during pyrite replacement (cf. Zhao et al., 2014). In summary, Py_3 was replaced first by porous $Py_{4\text{-}py}$, and the $Py_{4\text{-}py}$ was replaced by a combination of $Mc_{2\text{-}py}$, $Mc_{3\text{-}py}$ and minor Apy, then followed by overgrowth of coarse-grained $Mc_{2\text{-}py}$.

Comparison with pyrite replacements reported in the literature

Replacement of inclusion-free pyrite by porous, inclusion-rich pyrite has been reported from other hydrothermal systems (e.g., Su et al., 2008; Morey et al., 2008; Sung et al., 2009; Pal et al., 2011; Gao et al., 2017; Chen et al., 2018; Li et al., 2018). For example, porous rims of pyrite closely associated with visible gold have been suggested to form via hydrothermal alteration of pre-existing pyrite during increases in temperature and sulfur fugacity during prograde metamorphism (Morey et al., 2008). Porous As-poor pyrite with numerous arsenopyrite inclusions, documented at an Archean orogenic gold deposit, Western Australia, has been proposed to form by partial replacement of As-rich pyrite via fluid-mediated coupled dissolution and reprecipitation (Sung et al., 2009). This replacement of one phase by a porous variant of the same phase has also been observed for other minerals. For instance, the

margins of Ni-bearing arsenopyrite from an Archean orogenic gold deposit have been reported to be hydrothermally replaced by Ni-poor, native Au-bearing rims via dissolution and reprecipitation, with consequent Ni and Au remobilization (LaFlamme et al., 2018). Magnetite is widely hydrothermally replaced by porous, trace element-poor magnetite via the dissolution and reprecipitation (Wen et al., 2017). Magmatic zircon can be also replaced by porous secondary zircon carrying lower concentrations of trace elements than the precursor mineral, with replacement inferred to have occurred via aqueous fluid or melt-mediated coupled dissolution and reprecipitation (Geisler et al., 2007).

Partial dissolution of pyrite, associated with subsequent marcasite precipitation, has been documented in the low-temperature sandstone-hosted uranium deposits, U.S. (Goldhaber et al., 1979; Reynolds et al., 1982). In the global black shale successions ranging in age from Middle Proterozoic to Cretaceous, intermittent marcasite precipitation has also been interpreted to be initiated by oxidation and dissolution of the already existing sedimentary pyrite (Schieber and Riciputi, 2005; Schieber, 2007, 2011).

5.5.2 Trace element remobilization and gold re-enrichment

The LA–ICP–MS and NanoSIMS analyses highlight systematic trace element variations between the different generations of pyrite and marcasite (Figures. 5.4-5.7). In replacement of Py_3 by porous $Py_{4\text{-}py}$ (Figure 5.6a), elements enriched in $Py_{4\text{-}py}$ relative to Py_3 (Cu, Sb, Ag, Pb, and Bi) may be sourced from infiltrating fluids, or from metals hosted in sub-micron inclusions (e.g., chalcopyrite, galena, arsenopyrite) formed during remobilization from Py_3. Existence of these fine mineral inclusions in porous $Py_{4\text{-}py}$ is supported by the spikes of Cu and Sb in LA–ICP–MS laser profiles (Figure 5.5c and d), as well as Cu nano-inclusions in NanoSIMS image (Figure 5.7c). The presence of Cu, Pb, Ag, and Bi-bearing minerals in porous alteration pyrite-arsenopyrite assemblages formed via trace element remobilization and re-enrichment during hydrothermal replacement have been documented in other gold deposits (e.g., Morey et al., 2008; Sung et al., 2009; Cook et al., 2013). In contrast, metals (Te, Se, Zn, Co, Tl, Ni, Au, W, and As; Figure 5.6a) depleted in porous $Py_{4\text{-}py}$ relative to Py_3, commonly exhibit zonation patterns in the parent Py_3 at Daqiao

deposit (Figures. 5.5c, d and 5.7). Similar zonation for Au, As, Co, Ni, and Se in pyrite have also been reported from other hydrothermal gold ores (e.g., Cook et al., 2013; Yan et al., 2018). These metals that are depleted in porous $Py_{4\text{-}py}$ may have been expelled from the system during replacement of Py_3.

The trace element redistribution process during replacement of Py_3 by $Py_{4\text{-}py}$ plus minor inclusions (Ccp, Gn, Apy) may therefore be described by:

$$Py_3 + \text{fluids } (Cu^{2+}, Sb^{-}, Ag^{+}, Pb^{2+}, Bi^{2+})_{(aq)} \rightarrow$$

$$Py_{4\text{-}py} + Ccp + Gn + Apy + \text{fluids } (Te^{-}, Se^{-}, Zn^{2+}, Co^{2+}, Tl^{1+}, Ni^{2+}, Au^{+}, W^{6+}, As^{-})_{(aq)} \quad (1)$$

Few previous studies have documented the compatibility of trace elements in marcasite relative to pyrite, so the processes that controlled trace element incorporation into product marcasite are difficult to determine. However, the solubility of most metals increases as pH decreases so the presence of fluids sufficiently acidic to stabilize marcasite (e.g., pH<2.5 at 220 ^{o}C; Qian et al., 2011) may have led to increased metal mobility and decreased metal compatibility (Reed and Palandri, 2006). Only W is notably enriched in both product $Mc_{2\text{-}py}$ and $Mc_{3\text{-}py}$ compared to the precursor $Py_{4\text{-}py}$. Tungsten is suggested to be transported mainly as carbonate or bicarbonate complexes in carbonic metamorphic fluids (Higgins, 1980), so fluid boiling-related decrease of CO_2 partial pressure could have resulted in W sequestration into marcasite. Other lines of evidence at Daqiao deposit, including the hydrothermally altered in-situ carbonaceous materials in breccia ores, and Au-rich fine-grained pyrite and marcasite characterized by negative $\delta^{34}S$ values hosted in hydrothermal cements, are also consistent with rapid fluid phase separation of a CO_2-bearing fluid phase, triggered by hydraulic fracturing (Wu et al., 2018a).

Despite the likely pH-induced decreased metal compatibility during marcasite precipitation, complex-zoned $Mc_{3\text{-}py}$ is enriched in a suite of trace elements compared to $Py_{4\text{-}py}$ (Figure 5.6b). It has been suggested that metal-rich zones form due to a build-up of high trace element concentrations at local mineral-fluid interfacial layers (Putnis et al., 1995; Putnis and Mauthe, 2001). At the Daqiao deposit, this could manifest as rapid deposition of narrow $Mc_{3\text{-}py}$ zones together with fine-grained arsenopyrite on porous $Py_{4\text{-}py}$ (Figures. 5.3l and 5.7). Precipitation of $Mc_{3\text{-}py}$ could be initiated by a reduction in threshold of the supersaturation of metals

near the interfacial layers triggered by changes in fluid chemistry. Metal enrichment in $Mc_{3\text{-}py}$ relative to $Py_{4\text{-}py}$ (W, Tl, Au, As, Sb, Ag, Se, and Zn; Figure 5.6b) might have been derived to some combination of the $Py_{4\text{-}py}$ dissolution, and metals sourced from infiltrating fluids.

Trace element redistribution during replacement of $Py_{4\text{-}py}$ by $Mc_{2\text{-}py}$, $Mc_{3\text{-}py}$ and minor Apy is described as:

$$Py_{4\text{-}py} + \text{fluids } (W^{6+}, Tl^{1+}, Au^{+}, As^{-}, Sb^{-}, Ag^{+}, Se^{-}, Zn^{2+},)_{(aq)} \rightarrow$$

$$Mc_{2\text{-}py} + Mc_{3\text{-}py} + Apy + \text{fluids } (Cu^{2+}, Te^{-}, Pb^{2+}, Ni^{2+}, Co^{2+}, Bi^{+})_{(aq)} \qquad (2)$$

It is interesting to note that trace elements enriched in $Py_{4\text{-}py}$ commonly occur as an isovalent substitution for Fe^{2+} in pyrite (e.g., Cu and Pb), while those depleted in $Py_{4\text{-}py}$ relative to Py_3 either isovalently substitute for S^{-} (Te, Se, and As; Deditius et al., 2008) or Fe^{2+} with potential As involvement (Co and Ni; Yang and Downs, 2008). Trace elements such as Au, Ag, Tl, and Bi, which show coupled heterovalent substitution for Fe^{2+} with or without As, can display either relative enrichment (Ag and Bi) or depletion (Tl and Au) in $Py_{4\text{-}py}$ compared to Py_3 (Eq. 1 – Figure 5.6a). In contrast, trace elements enriched (e.g., Se, Sb, and As) and depleted (Cu, Pb, Bi, Co, and Ni) in the product zoned $Mc_{3\text{-}py}$ generally isovalently or heterovalently substitute for S^{-} and Fe^{2+} in marcasite, respectively (Eq. 2 – Figure 5.6b).

Little is known about the potential relations between metal redistribution patterns in the replacement pyrite and marcasite and their elemental substitution mechanisms during replacement via dissolution and reprecipitation reactions. It has been suggested that mineral surfaces could become charged during chemical reactions at mineral-solution interfaces (Stumm and Morgan, 1996). To reach electroneutrality between the mineral surface and solution, the charged surfaces attract ions of opposite charge and repels ions of similar charge (Smith, 1999). It is interesting to speculate if, to some extent, metal enrichment generally related to Fe^{2+} and S^{-} substitutions in product pyrite ($Py_{4\text{-}py}$) and marcasite ($Mc_{3\text{-}py}$), respectively, were associated with the different charged reaction interfaces formed during the fluid-mediated replacement process. Changes in surface charge of iron sulfides has been suggested to be related to the changing pH in fluids (Widler and Seward, 2002; Qian et al., 2011).

5.5.3 Drivers for replacement and overgrowth

Pyrite replaced by pyrite

When one phase is replaced by the same phase with a new composition, the substituted solid solutions in the parent phase tend to exsolve to reduce the strain energy, which enhances the surface reactivity and thus the dissolution rate (Geisler et al., 2007). Non-stoichiometric parent phases are likely have higher solubility in fluid than ideal stoichiometric end-member of the daughter phase, which drives dissolution and reprecipitation (Lippmann, 1980; Fougerouse et al., 2016). In addition, it has been proposed that arsenic enrichment in the pyrite lattice can effectively accelerate fluid-mediated pyrite dissolution since the formation of sulfur vacancies preferentially proceeds in the vicinity of arsenic (Blanchard et al., 2007). LA–ICP–MS trace element analysis reveals the much higher contents of As (median 3115 ppm vs. 130 ppm As; Figure 5.4a) plus other solid solutions (Te, Se, Zn, Co, Tl, Ni, Au, W, and As; Figure 5.6a) in parent Py_3 than product $Py_{4\text{-}py}$. These high impurity concentrations provide a driver for replacement of Py_3 by $Py_{4\text{-}py}$ during fluid infiltration.

Pyrite replaced by marcasite

It has been proposed that pyrite replacement textures and subsequent marcasite precipitation in sandstone-hosted uranium deposits and black shales result from oxidation and dissolution of pre-existing pyrite (e.g., Granger and Warren, 1974; Goldhaber et al., 1978, 1979; Reynolds et al., 1982; Schieber and Riciputi, 2005; Schieber, 2007, 2011). These reactions have been suggested to proceed mainly via Eqs. 3 – 6 (Goldhaber et al., 1978; Schieber, 2007):

$$FeS_{2\ (pyrite)} + 3.5\ O_2 + H_2O = Fe^{2+} + 2H^+ + 2SO_4^{2-} \quad (3)$$

$$2FeS_{2\ (pyrite)} + 3.5\ O_2 + 3H_2O = 2FeO\ (OH) + 4H^+ + 4S_2O_3^{2-} \quad (4)$$

$$nH^+ + nS_2O_3^{2-} + 2H_2S_{\ (aq)} = 2H_2S_n + nHSO_3^- \quad (5)$$

$$Fe^{2+} + H_2S_n = FeS_{2\ (marcasite)} + S_{n-2}^0 + 2H^+ \quad (6)$$

Experimental studies have demonstrated that marcasite precipitation is strongly favored over pyrite at $pH<pK_1$ of the aqueous polysulfide species present (e.g., for H_2S_2, $pK_1 = 5$, at 25°C; Murowchick and Barnes, 1986; Schoonen and Barnes, 1991;

Murowchick, 1992; Benning et al., 2000). This pH-dependence is postulated to occur as a consequence of electrostatic interactions between polysulfide species and iron sulfides growth surfaces. Negative ions such as H_2S^- and S^{2-} are strongly attracted to the sites of pyrite growth, while the protonated ends of neutral polysulfide H_2S_2 and H_2S^- favor marcasite (Tossell et al., 1981; Schoonen and Barnes 1991; Murowchick 1992). Polysulfide aqueous species have been suggested to form by partial oxidation of aqueous H_2S by chemically reactive sulfur species electron accepters (e.g., thiosulfate, Eq. 5) resulted from pre-existing pyrite oxidation reaction via Eq. 4 (Goldhaber et al, 1979; Murowchick and Barnes, 1986). The increasing solubility of ferrous iron (Fe^{2+}) derived from partial oxidation of pre-existing pyrite has been suggested to provide another factor favorable for marcasite precipitation (Eq. 6; Granger and Warren, 1974; Goldhaber et al., 1979; Schieber and Riciputi, 2005; Schieber, 2007, 2011).

It has been proposed that formation of marcasite would also occur either at temperatures <220°C and pH<2.5 or where there is a deficiency of S^{2-} under oxic or anaerobic conditions (Qian et al., 2011). At Daqaio, oxidation as a factor facilitating marcasite formation is favored over a deficiency of S^{2-} and other S-bearing species (e.g., polysulfide aqueous species) in the hydrothermal ore fluids, because numerous marcasite veinlets formed, even during the late-ore stage (Figure 5.2f) and the continued formation of sulfides is inconsistent with a deficiency of S-bearing species. Oxidation, on the other hand, is consistent with oxidation inferred from sulfur isotope evidence to have been induced by fluid phase separation during multistage brecciation (Wu et al., 2018a).

Insights from sulfur isotopes

Marcasite deposition as a consequence of oxidation is also consistent with the sulfur isotopic variations observed at Daqiao deposit. A general trend of decreasing $\delta^{34}S$ values obtained by both SIMS and LA-MC-ICP-MS is displayed from Py_3 to $Py_{4\text{-}py}$, and then to $Mc_{2\text{-}py}$ and $Mc_{3\text{-}py}$ (Figure 5.8). The distinct negative $\delta^{34}S$ value of $Mc_{3\text{-}py}$ is also visible in the NanoSIMS profile, where the three $Mc_{3\text{-}py}$ peaks containing high Au and other trace elements are coincident with the positions of ^{34}S depletion (Figure 7h).

Fluid oxidation has been commonly suggested to play a role in gold deposition and negative $\delta^{34}S$ values in sulfides (e.g., Drummond and Ohmoto, 1985; Hodkiewicz et al., 2009; Tang et al., 2013; LaFlamme et al., 2018). Fractionation of heavy ^{34}S into the oxidized sulfur species would lead to ^{34}S depleted H_2S in the residual ore fluid, and consequently pyrite and marcasite precipitated from the fluid post-oxidation would be characterized by decreased $\delta^{34}S$ values relative to sulfides precipitated pre-oxidation (Ohmoto, 1972). In addition, or alternatively, it has been proposed that isotopically light sulfur in marcasite from hydrothermal uranium deposits (-25‰–-40‰) is derived from pre-existing pyrite (>0‰), remobilized via partial oxidation to soluble metastable sulfur oxyanions (Goldhaber et al., 1978; Reynolds et al., 1982).

It is notable that the $\delta^{34}S$ values for pyrite derived from SIMS or LA-MC-ICP-MS analysis are similar (Figure 8; mean +4.6‰ vs. +5.2‰ for Py_3; +2.9‰ vs. +3.4‰ for $Py_{4\text{-}py}$), while those for marcasite, though showing the same trends, are different (+2.4‰ vs. +5.0‰ for $Mc_{2\text{-}py}$; -1.3‰ vs. -9.7‰ for $Mc_{3\text{-}py}$). Matrix effects during SIMS analysis may have contributed to this difference, given that the pyrite standard was applied to correct marcasite data. The crystallographically unmatched standard and analyte could cause mass bias during processes like secondary ion sputtering and ionization (Riciputi et al., 1998). Further work and standard development is needed to better elucidate the matrix effects during SIMS sulfur isotope analysis of marcasite.

Genetic model for observed textures

The textures described here are consistent with the genetic model proposed by Wu et al. (2018a), where the sulfide deposition and dissolution are related to multistage hydraulic fracturing. A pressure-driven genetic model for pyrite replacement at Daqiao deposit is tentatively proposed (Figure 5.9). In the early-ore stage deep-seated fluids discharged from regional thrust faults stalled at the low-permeability Triassic turbidites resulting in sulfide disseminations of Py_3 (Wu et al., 2018a). During deposition of subhedral auriferous Py_3, ore fluids were probably reduced with pH >2.5 (Figure 5.9a; cf. Granger and Warren, 1974; Murowchick and Barnes, 1986; Qian et al., 2011). Temperature is thought to have been between 100°C and 240°C based on microthermometry of fluid inclusions in the ore-related quartz

from breccia ores (Xu et al., 2015).

When fluid pressure exceeds the lithostatic load, accumulating shear stress creates extensive hydraulic fracture permeability (Sibson et al., 1988). Fracturing could have resulted in phase separation and partitioning of reduced H_2S into the vapor phase to produce residual fluids enriched in more oxidized sulfur species (Ohmoto, 1972; Drummond and Ohmoto, 1985).

With the evolution of ore fluids to a more oxidizing condition, pre-existing As-rich Py_3 started to dissolve, with reprecipitation of porous As-poor $Py_{4\text{-}py}$. Some metals transferred from Py_3 into porous $Py_{4\text{-}py}$, others transferred into minor Cu-, Pb-, and As-bearing inclusions, while others were incorporated into metal-rich solutions that migrated within the system on some length scale (Figure 5.9b).

Further oxidation of ore fluids during hydraulic fracturing led to partial dissolution of the product $Py_{4\text{-}py}$ and formation of aqueous polysulfide species and then $Mc_{2\text{-}py}$ reprecipitation, under low pH (<2.5) and high Fe^{2+} solubility conditions (Figure 5.9c). $Mc_{2\text{-}py}$ contains low concentrations of trace elements, plausibly because of high metal solubilities in the low pH environment. Elevated concentrations of metals may have been present in the interfacial solutions, since the presence of small pores and a high proportion of fluids are thought to stabilize metals in solution at concentrations that would be considered metastable in a free fluid (Putnis et al., 1995; Putnis and Mauthe, 2001). Further brecciation and subsequent rapid fluid-pressure fluctuations may have resulted in oxidation and/or an immediate reduction in threshold supersaturation (Putnis et al., 1995). Either of these processes could trigger precipitation of the fine $Mc_{3\text{-}py}$ enriched in gold and other trace elements but depleted in ^{34}S (Figure 5.9c).

The cyclic pressure fluctuations during this stage caused cycling precipitation between $Mc_{2\text{-}py}$ and $Mc_{3\text{-}py}$, leading to the complex-zoned $Mc_{3\text{-}py}$ within $Mc_{2\text{-}py}$ (Figure 5.9c). A similar mechanism has been proposed to explain repeated high-Au negative $\delta^{34}S$ zones within individual pyrite crystals in Porgera porphyry-epithermal gold deposit, Papua New Guinea, which is thought to have formed via episodic rapid pressure release due to fault failure (Peterson and Mavrogenes, 2014).

During wall-rock readjustment after hydraulic fracturing, coarse-grained $Mc_{2\text{-}py}$ euhedra, growing from ore fluids, started to overgrow on the outside of replacement

pyrite and marcasite aggregates (Figure 9d; Sibson, 1987). After the hydrothermal deposition and sealing of the fractures, fluid pressure rebuilds and the hydraulic fracturing cycle repeats.

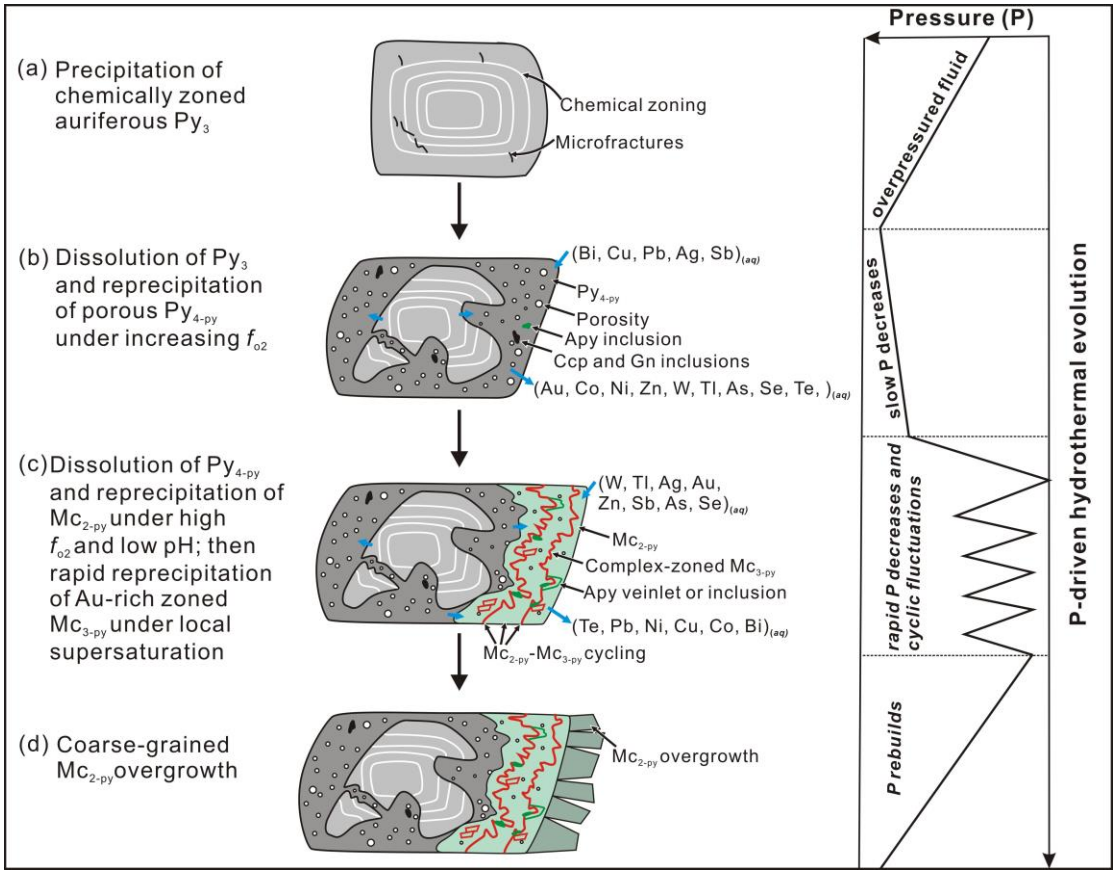

Figure 5.9 Schematic diagram of the pressure-driven two-step replacement process of pyrite, subsequent marcasite overgrowth and associated remobilization of gold and other trace metals at the Daqiao gold deposit. See text for explanations.

5.5.4 Implications for gold redistribution in fault-valve regime

Fluid cycling related to multistage hydraulic fracturing at the Daqiao gold deposit is consistent with cyclic fluid fluctuations triggered by fault-valve behavior as reported in other brittle to ductile hydrothermal systems (e.g., Sibson, 1987; Sibson et al., 1988; Cox, 1995; Robert et al., 1995; Wilkinson and Johnston, 1996). Brittle rheological systems caused by earthquake rupturing and associated zones of brecciation have long been recognized as channels for fluid flow and as sites for high-level (1–2km) hydrothermal systems (Phillips, 1972; Sibson, 1987).

Epizonal orogenic gold mineralization (<6 km) in metamorphic belts, especially

high-grade breccia ore shoots, has been proposed to record a history of incremental extensional opening and hydrothermal recementation (Hagemann et al., 1992; Gebre-Mariam et al., 1995). Mineral deposition in the extensional zones is thought to be triggered by fluid fluctuations and boiling revealed by fluid inclusion microthermometry and critical stress analyses (e.g., Phillips, 1972; Sibson, 1987; Li et al., 2002; Ostapenko and Neroda, 2007). Thermodynamic modelling reveals that removal of H_2S from ore fluids into vapor phase during boiling lowers the total activity of sulfur in ore fluids, which destabilizes gold-bisulphide complexes and leads to gold deposition (Williams-Jones et al., 2009).

However, few previous studies have focused on the sequence of hydrothermal events, sulfide replacement and related metal redistribution in episodically evolving hydrothermal systems. Exceptions include a LA–ICP–MS in-situ sulfur isotope study of ore-related pyrite in dilational structures from orogenic gold deposits, Yilgarn Craton, where negative $\delta^{34}S$ values were suggested to be a result of fluid-pressure fluctuations associated with fault-valve cycling (Hodkiewicz et al., 2009). In a later study, Rottier et al. (2016) proposed that a progressive increase of f_{S2}, f_{O2}, and pH in ore fluids from epithermal systems in Peru, drove replacement of pyrrhotite and arsenopyrite by marcasite and pyrite via a dissolution-reprecipitation mechanism associated with systematic redistribution of trace elements. At the Daqiao deposit, a combination of LA–ICP–MS, SIMS and NanoSIMS analyses record the micron- to nano-scale, complex-zoned redistribution and re-enrichment of gold plus other trace metals during a two-step replacement process related to multistage hydraulic fracturing.

The results emphasize the key role of brittle rheological regimes caused by the fault-valve activity not only in gold deposition, but also in redistribution and re-enrichment of gold and other metals in high-level hydrothermal gold systems worldwide. If, as we suggest, ore fluids in these hydrothermal systems began to partially oxidize during abrupt pressure decreases and fluctuations associated with hydraulic brecciation, pre-existing auriferous pyrite could dissolve and form zoned gold-rich marcasite. Complex zoning in marcasite indicate that this replacement is controlled by episodic processes, plausibly, such as infiltration of hydrothermal fluids in response to pressure variation.

5.6 CONCLUSIONS

Detailed microscopic observations as well as the geochemical data presented in this study indicate that the replacement of auriferous pyrite at the Daqiao epizonal orogenic deposit mainly proceeded via a two-step dissolution and reprecipitation replacement process plus additional marcasite overgrowth.

Results of LA–ICP–MS and NanoSIMS analyses suggest that gold and other trace elements (Te, Se, Zn, Co, Tl, Ni, W, and As) originally incorporated in parent Py_3 are partly expelled and remobilized during replacement by porous $Py_{4\text{-}py}$. Other metals (Cu, Sb, Ag, Pb, and Bi) mainly occurring as mineral inclusions, show enrichment in $Py_{4\text{-}py}$. In the replacement of $Py_{4\text{-}py}$ by aggregates of $Mc_{2\text{-}py}$, $Mc_{3\text{-}py}$ and minor arsenopyrite, $Mc_{2\text{-}py}$ is deficient in metals, while metals (W, Tl, Au, As, Sb, Ag, Se, and Zn) are enriched in zoned $Mc_{3\text{-}py}$.

The textures observed at Daqiao deposit provide a record of evolving f_{O2} and pH in ore fluids. Four steps are proposed for the process of replacement and precipitation of various sulfides and sulfarsenides: (1) Py_3 precipitation; (2) partial dissolution of Py_3 and reprecipitation of $Py_{4\text{-}py}$ with metal redistribution under increasing f_{O2}; (3) partial dissolution of $Py_{4\text{-}py}$ with reprecipitation of metal-poor $Mc_{2\text{-}py}$ and cyclic reprecipitation of metal-rich zoned $Mc_{3\text{-}py}$ plus minor arsenopyrite via a reduction in threshold supersaturation; and (4) overgrowth of $Mc_{2\text{-}py}$.

Similar to findings elsewhere, episodically pressure-driven hydrothermal movement in brittle rheological zones triggered by fault-valve behavior is thought to be critical in the formation of the Daqiao epizonal orogenic gold deposit. This study further quantitatively emphasizes the pressure-driven process plays a key role in the micron- to nano-scale, complex-zoned redistribution and re-enrichment of gold and other metals during the replacement of auriferous pyrite.

5.7 ACKNOWLEDGEMENTS

The authors acknowledge Xiao-Ye Jin and Lei Chen for their help during LA‐ICP‐MS trace element and SIMS sulfur isotope analysis, respectively. The Daqiao

Mining Ltd. and Geological Survey of Gansu Province are also thanked for excellent field assistance. Research work was financially supported by the National Natural Science Foundation of China (grants 41772081, 41325007 and 41072057), the Fundamental Research Funds for the Central Universities, China University of Geosciences, Wuhan (CUGCJ1711), and the GPMR State Key Laboratory (MSFGPMR03). The senior author acknowledges the receipt of Chinese Scholarship Council/Curtin International Postgraduate Research Scholarship. This is contribution 10 from CUG Center for Research in Economic Geology and Exploration Targeting (CREGET). This paper greatly benefited from constructive and thorough reviews from Crystal LaFlamme and an anonymous reviewer. Ours thanks go to editorial suggestions from Marc Norman and Edward M. Ripley.

5.8 REFERENCES

Altree-Williams A., Pring A., Ngothai Y., Brugger J., 2015. Textural and compositional complexities resulting from coupled dissolution-reprecipitation reactions in geomaterials. Earth-Science Reviews 150, 628-651.

Arehart G. B., Eldridge C. S., Chryssoulis S. L., Kesler S. E., 1993. Ion microprobe determination of sulfur isotope variations in iron sulfides from the Post/Betze sediment-hosted disseminated gold deposit, Nevada, USA. Geochimica et Cosmochimica Acta 57, 1505-1519.

Benning L. G., Wilkin R. T., Barnes H. L., 2000. Reaction pathways in the Fe-S system below 100 °C. Chemical Geology 167, 25-51.

Blanchard M., Alfredsson M., Brodholt J., Wright K., Catlow C. R. A., 2007. Arsenic incorporation into FeS_2 pyrite and its influence on dissolution: a DFT study. Geochimica et Cosmochimica Acta71, 624-630.

Brugger J., McFadden A., Lenehan C. E., Etschmann B., Xia F., Zhao J., Pring A., 2010. A novel route for the synthesis of mesoporous and low-thermal stability materials by coupled dissolution-reprecipitation reactions: mimicking hydrothermal mineral formation. Chimia 64, 693-698.

Butler I. B., Rickard D., 2000. Framboidal pyrite formation via the oxidation of iron (II) monosulfide by hydrogen sulfide. Geochimica et Cosmochimica Acta64, 2665-2672.

Chen L., Li X. H., Li J. W., Hofstra A. H., Liu Y., Koenig A. E., 2015. Extreme variation of sulfur isotopic compositions in pyrite from the Qiuling sediment-hosted gold deposit, West Qinling orogen, central China: an in situ SIMS study with implications for the source of sulfur. Mineralium Deposita 50, 643-656.

Chen W. T., Zhou M. F., Li X., Gao J. F., Bao Z., Yuan H., 2018. In situ Pb-Pb isotopic dating of sulfides from hydrothermal deposits: a case study of the Lala Fe-Cu deposit, SW China. Mineralium Deposita https://doi.org/10.1007/s00126-018-0833-1

Cline J. S., 2001. Timing of gold and arsenic sulfide mineral deposition at the Getchell Carlin-type gold deposit, north-central Nevada. Economic Geology 96, 75-89.

Cook N. J., Ciobanu C. L., Mao J. W., 2009. Textural control on gold distribution in As-free pyrite from the Dongping, Huangtuliang and Hougou gold deposits, North China Craton (Hebei Province, China). Chemical Geology 264, 101-121.

Cook N. J., Ciobanu C. L., Meria D., Silcock D., Wade B., 2013. Arsenopyrite-pyrite association in an orogenic gold ore: Tracing mineralization history from textures and trace elements. Economic Geology 108, 1273-1283.

Cox S. F., 1995. Faulting processes at high fluid pressures: an example of fault valve behavior from the Wattle Gully Fault, Victoria, Australia. Journal of Geophysical Research: Solid Earth 100, 12841-12859.

Deditius A. P., Utsunomiya S., Renock D., Ewing R. C., Ramana C. V., Becher U., Kesler S. E., 2008. A proposed new type of arsenian pyrite: Composition, nanostructure and geological significance. Geochimica et Cosmochimica Acta72, 2919-2933.

Dong Y. P, Zhang G. W., Neubauer F., Liu X., Genser J., Hauzenberger C., 2011. Tectonic evolution of the Qinling orogen, China: Review and synthesis. Journal of Asian Earth Sciences 41, 213-237.

Dong Y., Yang Z., Liu X., Sun S., Li W., Cheng, B., Zhang F., Zhang X., He D., Zhang, G., 2016. Mesozoic intracontinental orogeny in the Qinling Mountains, central China. Gondwana Research 30, 144-158.

Drummond S. E., Ohmoto H., 1985. Chemical evolution and mineral deposition in boiling hydrothermal systems. Economic Geology 80, 126-147.

Dubé B., Williamson K., McNicoll V., Malo M., Skulski T., Twomey T., Sanborn-Barrie M., 2004. Timing of gold mineralization at Red Lake, Northwestern Ontario, Canada: New constraints from U-Pb geochronology at the Goldcorp high-grade zone, Red Lake mine, and the Madsen mine. Economic Geology 99, 1611-1641.

Evans K. A., Tomkin A. G., Cliff J., Fiorentini M. L., 2014. Insights into subduction zone sulfur recycling from isotopic analysis of eclogite-hosted sulfides. Chemical Geology 365, 1-19.

Farquhar J., Cliff J., Zerkle A. L., Kamyshny A., Poulton S. W., Claire M., Adams D., Harms B., 2013. Pathways for Neoarchean pyrite formation constrained by mass-independent sulfur isotopes. Proceedings of the National Academy of Sciences 110, 17638-17643.

Fleet M. E., 1970. Structural aspects of the marcasite-pyrite transformation. Can. Mineral. 10, 225-231.

Fleet M. E., Mumin A. H., 1997. Gold-bearing arsenian pyrite and marcasite and arsenopyrite from Carlin Trend gold deposits and laboratory synthesis. American Mineralogist 82, 182-193.

Fougerouse D., Micklethwaite, S., Tomkins A. G., Mei Y., Kilburn M., Guagliardo P., Fisher L. A., Halfpenny A., Gee M., Paterson D., Howard D. L., 2016. Gold remobilisation and formation of high grade ore shoots driven by dissolution-reprecipitation replacement and Ni substitution into auriferous arsenopyrite. Geochimica et Cosmochimica Acta 178, 143-159.

Fougerouse D., Micklethwaite S., Ulrich S., Miller J., Godel B., Adams D. T., McCuaig T. C., 2017. Evidence for two stages of mineralization in West Africa's largest gold deposit: Obuasi, Ghana. Economic Geology 112, 3-22

Franchini M., Mcfarlane C., Maydagán L., Reich M., Lentz D., Meinert L., Bouhier V., 2015. Trace metals in pyrite and marcasite from the Agua Rica porphyry-high sulfidation epithermal deposit, Catamarca, Argentina: Textural features and metal zoning at the porphyry to epithermal transition. Ore Geology Reviews 66, 366-387.

Gao S., Huang F., Gu X., Chen Z., Xing M., Li Y., 2017. Research on the growth orientation of pyrite grains in the colloform textures in Baiyunpu Pb–Zn polymetallic deposit, Hunan, China. Mineralogy and Petrology 111, 69-79.

Gebre-Mariam M., Hagemann S. G., Groves D. I., 1995. A classification scheme for epigenetic Archaean lode-gold deposits. Mineralium Deposita 30, 408-410.

Geisler T., Schaltegger U., Tomaschek F., 2007. Re-equilibration of zircon in aqueous fluids and melts. Elements 3, 43-50.

Goldhaber M. B., Reynolds R. L., Rye R. O., 1978. Origin of a South Texas roll-type deposit; II, Sulfide petrology and sulfur isotope studies. Economic Geology 73,

1690-1705.

Goldhaber M. B. Reynolds R. L., Rye R. O., 1979. Formation and resulfidization of a South Texas roll-type uranium deposit. USGS Open File Report. 79-1651.

Granger H. C., Warren C. G., 1974. Zoning in the altered tongue associated with roll-type uranium deposits, in Formation of uranium ore deposits. In Formation of Uranium Ore Deposits (Chairman R. D. Nininger), I.A.E.A., Proc. Ser., No. STI/PUB/374, pp. 185-200.

Hagemann S. G., Groves D. I., Ridley J. R., Vearncombe J. R., 1992. The Archean lode gold deposits at Wiluna, Western Australia; high-level brittle-style mineralization in a strike-slip regime. Economic Geology 87, 1022-1053.

Harlov D. E., Wirth R., Hetherington C. J., 2011. Fluid-mediated partial alteration in monazite: the role of coupled dissolution-reprecipitation in element redistribution and mass transfer. Contrib. Mineralogy and Petrology 162, 329-348.

Higgins N. C., 1980. Fluid inclusion evidence for the transport of tungsten by carbonate complexes in hydrothermal solutions. Canadian Journal of Earth Sciences 17, 823-830.

Hodkiewicz P. F., Groves D. I., Davidson G. J., Weinberg R.F., Hagemann S.G., 2009. Influence of structural setting on sulphur isotopes in Archean orogenic gold deposits, Eastern Goldfields Province, Yilgarn, Western Australia. Mineralium Deposita. 44, 129-150.

LaFlamme C., Martin L., Jeon H., Reddy S., Selvaraja V., Caruso S., Hao T. B., Roberts M. P., Voute F., Hagemann S., Wacey D., Littman S., Wing B., Fiorentini M., Kilburn M. R., 2016. In situ multiple sulfur isotope analysis by SIMS of pyrrhotite, pentlandite and chalcopyrite to refine magmatic ore genetic models. Chemical Geology 444, 1-15.

LaFlamme C., Sugiono D., Thébaud N., Caruso S., Fiorentini M., Selvaraja V., Jeon H., Voute F. Martin L., 2018. Multiple sulfur isotopes monitor fluid evolution in an orogenic gold deposit. Geochimica et Cosmochimica Acta 222:436-446.

Large R. R., Maslennikon V. V., Robert F., Danyushevsky L. V., Chang Z.S., 2007. Multistage sedimentary and metamorphic origin of pyrite and gold in the giant Sukhoi Log deposit, Lena gold province, Russia. Economic Geology 102, 1233-1267.

Large R. R., Danyushevsky L., Hollit C., Maslennikov V., Meffre S., Gilbert S., Bull S., Scott R., Embsbo P., Thomas H., Singh B., Foster J., 2009. Gold and trace

element zonation in pyrite using a laser imaging technique: Implications for the timing of gold in orogenic and Carlin style sediment-hosted deposits. Economic Geology 104, 635-668.

Lennie A. R., Vaughan D. J., 1992. Kinetics of the marcasite-pyrite transformation: An infrared spectroscopic study. American Mineralogist 77, 1166-1171.

Li J. W., Zhou M. F., Li X. F., Li Z. J., Fu Z. R., 2002. Origin of a large breccia-vein system in the Sanerlin uranium deposit, southern China: a reinterpretation. Mineralium Deposita 37, 213-225.

Lippmann F., 1980. Phase diagrams depicting aqueous solubility of binary mineral systems. Neues Jahrbuch Mineralogische Abhandlungen 139, 1–25.

Liu S. G., Li Z. W., Liu S., Luo Y. H., Xu G. Q., Dai G. H., Gong C. M., Yong Z.Q., 2006. Formation and evolution of Dabashan foreland basin and fold-and-thrust belt. Geological Publishing House, Sichuan, China, pp. 1–248.

Li X. H., Fan H. R., Yang K. F., Hollings P., Liu, X., Hu, F. F., Cai, Y. C., 2018. Pyrite textures and compositions from the Zhuangzi Au deposit, southeastern North China Craton: implication for ore-forming processes. Contributions to Mineralogy and Petrology 173, 73. https://doi.org/10.1007/s00410-018-1501-2

Mao J. W., Qiu Y. M., Goldfarb R. J., Zhang Z. C, Garwin S., Fengshou R., 2002. Geology, distribution, and classification of gold deposits in the western Qinling belt, central China. Mineralium Deposita 37, 352-377.

Meng Q. R., Zhang G. W., 1999. Timing of collision of the North and South China blocks: Controversy and reconciliation. Geology 27, 123-126.

McLoughlin N., Wacey D., Kruber C., Kilburn M. R., Thorseth I. H., Pedersen R. B., 2011. A combined TEM and NanoSIMS study of endolithic microfossils in altered seafloor basalt. Chemical Geology 289, 154-162.

Morey A. A., Tomkins A. G., Bierlein F. P., Weinberg R. F., Davidson G. J., 2008. Bimodal Distribution of Gold in Pyrite and Arsenopyrite: Examples from the Archean Boorara and Bardoc Shear Systems, Yilgarn Craton, Western Australia. Economic Geology 103, 599-614.

Murowchick J. B., Barnes H. L., 1986. Marcasite precipitation from hydrothermal solutions. Geochimica et Cosmochimica Acta 50, 2615-2629.

Murowchick J. B., 1992. Marcasite inversion and the petrographic determination of pyrite ancestry. Economic Geology 87, 1141-1152.

Ohmoto H., 1972. Systematics of sulfur and carbon isotopes in hydrothermal ore deposits

Economic Geology 67, 551-578.

Ostapenko N. S., Neroda O. N., 2007. Fluid pressure and hydraulic fracturing in hydrothermal ore formation at gold deposits. Russian Journal of Pacific Geology 1, 276-289.

Pal D. C., Sarkar S., Mishra B., Sarangi A. K., 2011. Chemical and sulphur isotope compositions of pyrite in the Jaduguda U (-Cu-Fe) deposit, Singhbhum shear zone, eastern India: Implications for sulphide mineralization. Journal of earth system science 120, 475-488.

Pals D. W., Spry P. G., Chryssoulis S., 2003. Invisible gold and tellurium in arsenic-rich pyrite from the Emperor gold deposit, Fiji: implications for gold distribution and deposition. Economic Geology 98, 479-493.

Peterson E. C., Mavrogenes J. A., 2014. Linking high-grade gold mineralisation to earthquake-induced fault-valve processes in the Porgera gold deposit, Papua New Guinea. Geology 42, 383-386.

Phillips W. J., 1972. Hydraulic fracturing and mineralization. J. Geol. Soc. London. 128, 337-59.

Putnis A., Prieto M., Fernandez-Diaz L., 1995. Fluid supersaturation and crystallization in porous media. Geological Magazine 132, 1-13.

Putnis A., Mauthe G., 2001. The effect of pore size on cementation in porous rocks. Geofluids 1, 37-41.

Putnis A., 2002. Mineral replacement reactions: from macroscopic observations to microscopic mechanisms. Geological Magazine 66, 689-708.

Putnis A., 2009. Mineral replacement reactions. Rev. Mineral. Geochem. 70, 87-124.

Qian G., Brugger J., SkinnerW. M., Chen G., Pring A., 2010. An experimental study of the mechanism of the replacement of magnetite by pyrite up to 300 °C. Geochimica et Cosmochimica Acta 74, 5610-5630.

Qian G., Xia F., Brugger J., Skinner W., Bei J., Chen G., Pring A., 2011. Replacement of pyrrhotite by pyrite and marcasite under hydrothermal conditions up to 220 °C: An experimental study of reaction textures and mechanisms. American Mineralogist 96, 1878-1893.

Reed M.H., Palandri J., 2006. Sulfide mineral precipitation from hydrothermal fluids. Reviews in Mineralogy and Geochemistry 61, 609-631.

Reich M., Kesler S. E., Utsunomiya S., Palenik C. S., Chryssoulis S. L., Ewing R. C., 2005. Solubility of gold in arsenian pyrite. Geochimica et Cosmochimica Acta 69,

2781–2796.

Reynolds R. L., Goldhaber M. B., Carpenter D. J., 1982. Biogenic and nonbiogenic ore-forming processes in the South Texas uranium district: Evidence from the Panna Maria deposit. Economic Geology 77, 541-556.

Riciputi L. R., Paterson B. A., Ripperdan R. L., 1998. Measurements of light stable isotope ratios by SIMS: Matrix effects for oxygen, carbon, and sulfur isotopes in minerals. International Journal of Mass Spectrometry 178, 81–112

Robert F., Boullier A. M., Firdaous K., 1995. Gold-quartz veins in metamorphic terranes and their bearing on the role of fluids in faulting. Journal of Geophysical Research: Solid Earth 100, 12861-12879.

Rottier B., Kouzmanov K., Wälle M., Bendezú R., Fontboté L., 2016. Sulfide Replacement Processes Revealed by Textural and LA–ICP–MS Trace Element Analyses: Example from the Early Mineralization Stages at Cerro de Pasco, Peru. Economic Geology 111, 1347-1367.

Rouxel O., Ono S. H., Alt J., Rumble D., Ludden J., 2008. Sulfur isotope evidence for microbial sulfate reduction in altered oceanic basalts at ODP Site 801. Earth and Planetary Science Letters 268, 110–123.

Rubatto D., Müntener O., Barnhoorn A., Gregory C., 2008. Dissolution-reprecipitation of zircon at low-temperature, high-pressure conditions (Lanzo Massif, Italy). American Mineralogist 93, 1519-1529.

Schieber J., Riciputi L., 2005. Pyrite and Marcasite Coated Grains in the Ordovician Winnipeg Formation, Canada: An Intertwined Record of Surface Conditions, Stratigraphic Condensation, Geochemical “Reworking”, and Microbial Activity. J. Sedimentary Research 75, 907-920.

Schieber J., 2007. Oxidation of detrital pyrite as a cause for Marcasite Formation in marine lag deposits from the Devonian of the eastern US. Deep-Sea Res. II Top. Stud. Oceanogr. 54, 1312-1326.

Schieber J., 2011. Marcasite in Black Shales—a Mineral Proxy for Oxygenated Bottom Waters and Intermittent Oxidation of Carbonaceous Muds. Journal of Sedimentary Research 81, 447-458.

Schoonen M. A. A., Barnes H. L., 1991. Reactions forming pyrite and marcasite from solution: II. Via FeS precursor below 100 °C. Geochimica et Cosmochimica Acta 55, 1505-1514.

Selvaraja V., Fiorentini M. L., Jeon H., Savard D. D., LaFlamme C. K., Guagliardo P.,

Caruso S., Bui T. H., 2017. Evidence of local sourcing of sulfur and gold in an Archaean sediment-hosted gold deposit. Ore Geology Reviews 89, 909-930.

Smith K. S., 1999. Metal sorption on mineral surfaces: an overview with examples relating to mineral deposits. Rev. Economic Geology 6, 161-82.

Sibson R. H., 1987. Earthquake rupturing as a mineralizing agent in hydrothermal systems. Geology 15, 701-704.

Sibson R. H. Robert F., Poulsen K. H., 1988. High-angle reverse faults, fluid-pressure cycling, and mesothermal gold-quartz deposits. Geology 16, 551-555.

Simon G., Kesler S. E., Chryssoulis S., 1999. Geochemistry and textures of gold-bearing arsenian pyrite, Twin Creeks, Nevada; implications for deposition of gold in Carlin-type deposits. Economic Geology 94, 405-421.

Stumm W., Morgan J. J., 1996. Aquatic chemistry, third ed. Wiley-Interscience, New York.

Su W., Xia B., Zhang H., Zhang X., Hu R., 2008. Visible gold in arsenian pyrite at the Shuiyindong Carlin-type gold deposit, Guizhou, China: Implications for the environment and processes of ore formation. Ore Geology Reviews 33, 667-679.

Sung Y. H., Brugger J., Ciobanu C. L., Pring A., Skinner W., Nugus M., 2009. Invisible gold in arsenian pyrite and arsenopyrite from a multistage Archaean gold deposit: Sunrise Dam, Eastern Goldfields Province, Western Australia. Mineralium Deposita 44, 765-791.

Tang K. F., Li J. W., Selby D., Zhou M. F., Bi S.J., Deng X. D., 2013. Geology, mineralization, and geochronology of the Qianhe gold deposit, Xiong'ershan area, southern North China Craton. Mineralium Deposita 48, 729-747.

Thomas H. V., Large R. R., Bull S. W., Maslennikov V., Berry R. F., Fraser R., Froud S., Moye R., 2011. Pyrite and Pyrrhotite Textures and Composition in Sediments, Laminated Quartz Veins, and Reefs at Bendigo Gold Mine, Australia: Insights for Ore Genesis. Economic Geology 106, 1-31.

Tomkins A. G., Mavrogenes J. A., 2001. Redistribution of Gold within Arsenopyrite and Löllingite during Pro- and Retrograde Metamorphism: Application to Timing of Mineralization. Economic Geology 96, 525-534.

Tomkins A. G., Pattison D. R. M., Frost B. R., 2007. On the Initiation of Metamorphic Sulfide Anatexis. Journal of Petrology 48, 511-535.

Tossell J. A., Vaughan D. J., Burdett J. K., 1981. Pyrite, marcasite, and arsenopyrite type minerals: crystal chemical and structural principles. Physics and Chemistry of

Minerals 7, 177-184.

Walker F. D. L., Lee M. R., Parsons I., 1995. Micropores and micropermeable texture in alkali feldspars: geochemical and geophysical implications. Mineralogical Magazine =59, 505-534.

Wen G., Li J. W., Hofstra A. H., Koenig A. E., Lowers H. A., Adams, D., 2017. Hydrothermal reequilibration of igneous magnetite in altered granitic plutons and its implications for magnetite classification schemes: Insights from the Handan-Xingtai iron district, North China Craton. Geochimica et Cosmochimica Acta 213, 255-270.

Whitehouse M. J., 2013. Multiple sulfur isotope determination by SIMS: evaluation of reference sulfides for $\Delta^{33}S$ with observations and a case study on the determination of $\Delta^{36}S$. Geostandards and Geoanalytical Research 37, 19-33

Widler A. M., Seward T. M., 2002. The adsorption of gold (I) hydrosulphide complexes by iron sulphide surfaces. Geochimica et Cosmochimica Acta 66, 383-402.

Wilkinson J. J., Johnston J. D., 1996. Pressure fluctuations, phase separation, and gold precipitation during seismic fracture propagation. Geology 24, 395-398.

Williams-Jones A. E., Bowell R. J., Migdisov A. A., 2009. Gold in solution. Elements. 5: 281-287.

Wong K. H., Zhou M. F., Chen W. T., O'Brien H., Lahaye Y., Chan S. L. J., 2017. Constraints of fluid inclusions and in-situ S-Pb isotopic compositions on the origin of the North Kostobe sediment-hosted gold deposit, eastern Kazakhstan. Ore Geology Reviews 81, 256-269.

Wu Y. F., Li J. W., Evans, K., Koeing A. E., Li Z. K., O'Brien H., Lahaye Y., Rempel K., Hu S. Y., Zhang Z. P., Yu J. P., 2018a. Ore-Forming Processes of the Daqiao Epizonal Orogenic Gold Deposit, West Qinling Orogen, China: Constraints from Textures, Trace Elements and Sulfur Isotopes of Pyrite and Marcasite, and Raman Spectroscopy of Carbonaceous Material. Economic Geology 113, 1093-1132.

Wu Y. F., Li J. W., Evans K., Vasconcelos P. M., Thiede, D. S., Fougerouse D., Rempel K., 2018b. Late Jurassic to Early Cretaceous age of the Daqiao gold deposit, West Qinling Orogen, China: Implications for regional metallogeny. Mineralium Deposita 53. https://doi.org/10.1007/s00126-018-0835-z

Xia F., Brugger J., Chen G., Ngothai Y., O'Neill B., Putnis A., Pring A., 2009. Mechanism and kinetics of pseudomorphic mineral replacement reactions: A case study of the replacement of pentlandite by violarite. Geochimica et

Cosmochimica Acta 73, 1945-1969.

Xu L., Wu B. X., Wang Y. L., Wang Z. X., Wang G., Sun Z.P., 2015. Fluid inclusion characteristics and geological significance at Daqiao gold deposit. Journal of Jinlin University 45, 568-569.

Yan J., Hu R., Liu S., Lin Y., Zhang J., Fu S., 2018. NanoSIMS element mapping and sulfur isotope analysis of Au-bearing pyrite from Lannigou Carlin-type Au deposit in SW China: New insights into the origin and evolution of Au-bearing fluids. Ore Geology Reviews 92, 29–41.

Yang H. X., Downs R. T., 2008. Crystal structure of glaucodot, (Co, Fe) AsS, and its relationships to marcasite and arsenopyrite. American Mineralogist 93, 1183-1186.

Zeng Q. T., McCuaig T. C., Tohver E., Bagas L., Lu Y. J., 2014. Episodic Triassic magmatism in the western South Qinling Orogen, central China, and its implications. Geological Journal 49, 402-423.

Zhao J., Brugger J., Chen G., Ngothai Y., Pring, A., 2014. Experimental study of the formation of chalcopyrite and bornite via the sulfidation of hematite: mineral replacements with a large volume increase. American Mineralogist 99, 343-354.

Chapter 6

Synthesis and Conclusions

In this PhD project, I have explored the gold (Au) source and other aspects of Au deportment such as Au transport, precipitation, and remobilization during the formation of the world-class Daqiao orogenic gold deposit in the West Qinling Orogen, China (Figure 6.1). The results show that the Au in orogenic Au deposits in metamorphic belts could be sourced from either metamorphic devolatilization or magmatism, depending to a large extent on the regional geotectonics. Preliminary experimental results suggest that dissolved silica might have an important role in Au transport in hydrothermal fluids. The long-debated question about the formation of Au zoning in arsenian pyrite was addressed via a novel combination of micron- to atomic-scale characterization techniques. Fluid-mediated mineral-scale Au remobilization and re-enrichment formed as a consequence of pressure-driven hydrothermal process have been proposed. This project provides new lines of evidence:

(1) that Au and ore fluids at Daqiao deposit were derived from underlying Paleozoic Ni- and Se-rich carbonaceous sedimentary rocks. Differences in Au source and mineralization styles in the WQO and EQO are likely related to differences in their respective distances from the subduction front of the contemporary Paleo-Pacific plate.

(2) that silica-bearing fluids are capable of stabilizing and transporting dissolved Au by some complexation in hydrothermal Au systems.

(3) that complex gold zoning patterns commonly observed in arsenian pyrite are controlled by both the extrinsic fluctuations in fluid composition and intrinsic crystal-fluid kinetic effects.

(4) that pressure-driven hydrothermal process plays a key role in the redistribution of Au during episodic replacement of pyrite in brittle rheological zones from epizonal orogenic gold systems.

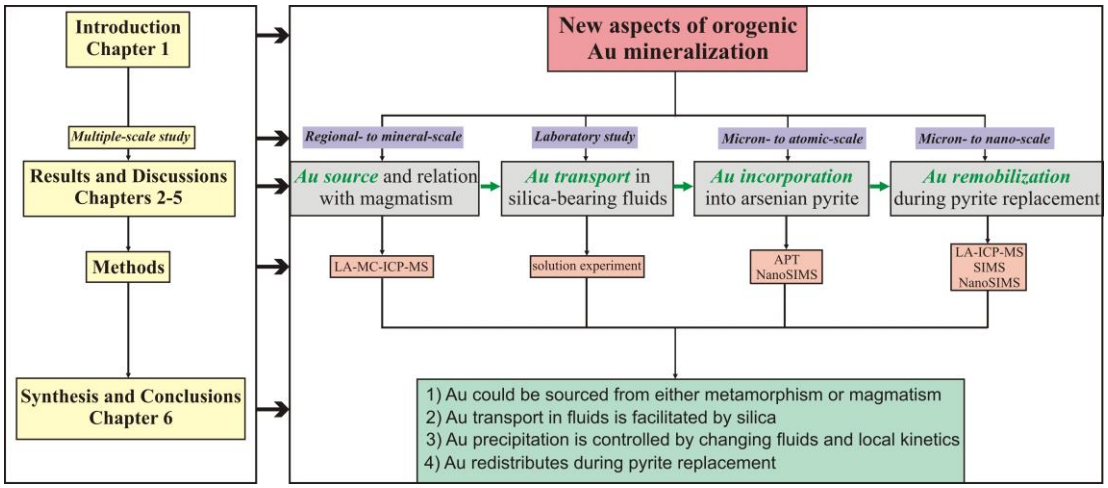

Figure 6.1 A flowchart showing the relationships between each chapter, the structure and main achievements of this thesis.

6.1 Gold source and tectonic driver

Integration of the regional tectonics with previous geochronology suggests that J3–K1 gold deposits in the WQO are a consequence of far-field effects of Mesozoic subduction of the Paleo-Pacific plate beneath the Eurasian continent. J3–K1 changes in plate motion resulted in N-S trending extension and formation of NE-SW and E-W-trending brittle structures that controlled fluid flow and gold deposition. The sources of sulfur and ore fluids in the J3–K1 age Daqiao deposit were produced by metamorphic devolatilization of the underlying Paleozoic trace element-rich sediments, which is different to the Au source for intrusion-related deposits in the EQO. It may be that differences in fluid source and mineralization style of J3–K1 gold deposits in the WQO and EQO are related to differences in their respective distances from the subduction front of the Paleo-Pacific plate, with important implications for the timescales and lateral extent of subduction-related effects on gold mineralization.

6.2 Gold transport in silica-bearing fluids

The new experimental data show that Au concentrations are higher in silica gel solutions than in colloidal silica suspensions at 200°C and water-saturated vapor

pressure. In the acidic silica gel solutions, dissolved Au may be complexed and stabilized as either or both of $AuOH^0$ and $AuH_3SiO_4^0$, while Au may dominantly occur as $AuOH^0$ in the alkaline silica gel suspensions. Gold concentrations in the silica gel solutions are comparable to those in silica -rich geothermal fluids that have been linked with formation of giant Au deposits. The preliminary results suggest that dissolved Au can be stabilized and thus transported in silica-bearing solutions, with broad implications for the formation of intensely silicified low-grade refractory sulfide Au ores in the upper crust.

6.3 Gold incorporation into pyrite

Micron-scale irregular or cyclic gold zoning in pyrite has been commonly interpreted to record fluctuations in hydrothermal fluid composition, however, complex gold zoning patterns observed in the Daqiao arsenian pyrite imply a complicated gold incorporation processes. This chapter characterizes the micron- to nano-scale gold distribution in pyrite with NanoSIMS and APT. Results show that the sharp transition between the μm-scale compositionally distinct core-mantle-rim zones in pyrite formed as a consequence of episodic fluctuations in external fluid composition. However, micron- to atomic-scale distribution and zoning patterns of Au, As, and Cu were controlled by a combination of kinetic effects during pyrite crystallization, including crystal surface structure effects, heteroepitaxial Stranski-Krastanov growth, and diffusion-limited self-organization. Additionally, nano-scale heterogeneities in Au, As, and Cu present as solid solution in pyrite suggest that interpretation of spikes on microbeam-derived depth-concentration profiles as metallic particles could be erroneous.

6.4 Gold remobilization during fluid pressure fluctuations

Detailed microscopic observations as well as the geochemical data presented in this study indicate that replacement of auriferous pyrite at the Daqiao epizonal orogenic deposit proceeded via a two-step dissolution and reprecipitation replacement process plus additional marcasite overgrowth. During the replacement of pyrite, gold and

other trace elements were released from the lattice and precipitated in complex zoned marcasite. The formation of marcasite and a decrease in $\delta^{34}S$ values from parent pyrite to marcasite are consistent with oxidation of ore fluids associated with Au deposition. Similar to findings elsewhere, episodically pressure-driven hydrothermal movement in brittle rheological zones triggered by fault-valve behavior is thought to be critical in the formation of the Daqiao epizonal orogenic gold deposit. This study further emphasizes that pressure-driven processes play a key role in the micron- to nano-scale, complex-zoned redistribution and re-enrichment of gold and other metals during the replacement of auriferous pyrite.

6.5 Limitations and future work

Important scientific questions still need to be answered to further improve understanding of the gold source, transport, deposition, and remobilization during the formation of orogenic gold deposits in the Qinling Orogen. Recommended further work includes:

(1) A more comprehensive process-based study of, and comparison between the Late Jurassic to Early Cretaceous (J3–K1) metamorphism- and magmatism-derived gold mineralization in the Qinling Orogen.

In this study, we have shown that the gold and ore fluids in the J3–K1 age Daqiao deposit in the WQO were produced by metamorphic devolatilization of the underlying Paleozoic trace element-rich sediments, which are unlike the intrusion-related deposits in the EQO. However, more details about ore-forming processes of representative J3–K1gold deposits in the EQO and WQO are needed, for example, the processes of devolatilization and magmatic-hydrothermal evolution responsible for the release of gold and ore fluids.

(2) A better understanding of the regional geotectonic driver for the J3–K1 gold mineralization in the Qinling Orogen.

Though we have tentatively proposed that the differences in source of gold and ore fluids in the EQO and WQO are likely related to differences in their respective

distances from the subduction front of the Paleo-Pacific plate, the specific far-field effects that affected the differential geotectonics in the EQO and WQO remain unknown. Future work could focus on the regional stress fields, in particular, the stress state of structures that control the migration of hydrothermal ore fluids and accommodation of gold ore bodies. These results, when combined with a framework of the previous geotectonic evolution of the Qinling Orogen and East Asia could shed light on the far-field effects of the subduction of the Paleo-Pacific plate.

(3) Further investigations of gold solubility in silica-bearing liquids

The preliminary experiments show a positive correlation between concentrations of dissolved gold and silica in silica gel solutions at 200 °C and saturated vapor pressure. Gold concentrations in silica gel solutions (0.44–7.6 ppb) are comparable to those in silica-rich geothermal fluids that have been linked with formation of giant gold deposits. However, only limited runs were conducted during this PhD project. Thus further investigations of the solubility of gold in silica-bearing liquids over a range of temperatures (150–300°C) and saturated vapor pressures should be performed. In addition, an innovative experimental approach, *in situ* X-Ray absorption spectroscopy (XAS), could be applied to determine the speciation of silica-gold complexes in fluids.

(4) Experimental study on the oxidation of auriferous pyrite and gold redistribution

This study has suggested that auriferous arsenian pyrite could be gradually replaced by later generations of pyrite and marcasite during pressure-driven fluid oxidation triggered by hydraulic fracturing. Gold and other trace elements were liberated from the lattice of parent pyrite and reprecipitated in finely zoned marcasite during the complex replacement processes. However, no previous experimental studies have focused on the fluid-mediated replacement of pyrite by marcasite in oxidized fluid conditions. Future experimental studies on the oxidation of auriferous arsenian pyrite could be conducted to better constrain the role of changing fluid conditions during the replacement process, such as redox state and pH, and the exchange of trace metals between pyrite and surrounding fluids.

Bibliography

A

Allègre, C.J., Provost, A., Jaupart, C., 1981. Oscillatory zoning. a pathological case of crystal growth. Nature, v. 294, p. 223-228.

Altree-Williams A., Pring A., Ngothai Y., Brugger J., 2015. Textural and compositional complexities resulting from coupled dissolution-reprecipitation reactions in geomaterials. Earth-Science Reviews 150, 628-651.

Arehart, G. B., Chryssoulis, S. L., Kesler, S. E., 1993. Gold and arsenic in iron sulfides from sediment-hosted disseminated gold deposits; implications for depositional processes. Economic geology 88, 171–185.

B

Barker, S., Hickey, K., Cline, J., Dipple, G., Kilburn, M., Vaughan, J., Longo, A., 2009. Uncloaking invisible Au: use of nanoSIMS to evaluate Au, trace elements and sulfur isotopes in pyrite from Carlin-type Au deposits. Economic Geology 104, 897–904.

Belousov, I., Large, R.R., Meffre, S., Danyushevsky, L.V., Steadman, J., Beardsmore, T., 2016. Pyrite compositions from VHMS and orogenic Au deposits in the Yilgarn Craton, Western Australia: Implications for gold and copper exploration. Ore Geology Reviews 79, 474-499.

Benning, L.G., Seward, T.M., 1996. Hydrosulphide complexing of Au (I) in hydrothermal solutions from 150–400°C and 500–1500 bar. Geochimica et Cosmochimica Acta 60, 1849-1871.

Benning L. G., Wilkin R. T., Barnes H. L., 2000. Reaction pathways in the Fe-S system below 100 °C. Chemical Geology 167, 25-51.

Blanchard M., Alfredsson M., Brodholt J., Wright K., Catlow C. R. A., 2007. Arsenic incorporation into FeS_2 pyrite and its influence on dissolution: a DFT study. Geochimica et Cosmochimica Acta71, 624-630.

Bi, S.H., Li, Z.K., Tang, K.F., Gao, K., 2016. LA–ICP–MS in situ trace element analysis of pyrite from Dongtongyu gold deposit and its metallogenic significance. Earth Science 41, 1121-1140.

Bowell, R.J., Baumann, M., Gingrich, M., Tretbar, D., Perkins, W.F., Fisher, P. C.,

1999. The occurrence of gold at the Getchell mine, Nevada. Journal of Geochemical Exploration 67, 127-143.

Brill, B.A., 1989. Trace-element contents and partitioning of elements in ore minerals from the CSA Cu-Pb-Zn deposit, Australia, and implications for ore genesis. The Canadian Mineralogist 27, 263-274.

Brugger J., McFadden A., Lenehan C. E., Etschmann B., Xia F., Zhao J., Pring A., 2010. A novel route for the synthesis of mesoporous and low-thermal stability materials by coupled dissolution-reprecipitation reactions: mimicking hydrothermal mineral formation. Chimia 64, 693-698.

Butler I. B., Rickard D., 2000. Framboidal pyrite formation via the oxidation of iron (II) monosulfide by hydrogen sulfide. Geochimica et Cosmochimica Acta64, 2665-2672.

C

Chen L., Li X. H., Li J. W., Hofstra A. H., Liu Y., Koenig A. E., 2015. Extreme variation of sulfur isotopic compositions in pyrite from the Qiuling sediment-hosted gold deposit, West Qinling orogen, central China: an in situ SIMS study with implications for the source of sulfur. Mineralium Deposita 50, 643-656.

Chen W. T., Zhou M. F., Li X., Gao J. F., Bao Z., Yuan H., 2018. In situ Pb-Pb isotopic dating of sulfides from hydrothermal deposits: a case study of the Lala Fe-Cu deposit, SW China. Mineralium Deposita https://doi.org/10.1007/s00126-018-0833-1

Chen, Y., 1994. Sources of ore-forming materials in the Liba gold deposit, west Qinling orogen. Northwestern Geology 15, 5-9.

Chen, Y.J., Zhang, J., Zhang, F.X., Franco, P., Li, C., 2004. Carlin and Carlin-like gold deposits in the Western Qinling Mountains and their metallogenic time, tectonic setting and model. Geological Review 50, 134-152.

Chen, Y.J., Santosh, M., 2014. Triassic tectonics and mineral systems in the Qinling Orogen, central China: Geological Journal 49, 338–358.

Choi, S.G., Kwon, S.T., Ree, J.H., So, C.S., Pak, S.J., 2005. Origin of Mesozoic gold mineralization in South Korea. The Island Arc 14, 102-114.

Chouinard, A., Paquette, J., Williams-Jones, A.E., 2005. Crystallographic controls on trace-element incorporation in auriferous pyrite from the Pascua epithermal high-sulfidation deposit, Chile-Argentina. The Canadian Mineralogist 43, 951-963.

Cline J. S., 2001. Timing of gold and arsenic sulfide mineral deposition at the Getchell Carlin-type gold deposit, north-central Nevada. Economic Geology 96, 75-89.

Cline, J.S., Hofstra, A.A., 2000. Ore-fluid evolution at the Getchell Carlin-type gold deposit, Nevada, USA. European Journal of Mineralogy 12, 195–212.

Cook, N.J., Ciobanu, C.L., Mao, J., 2009. Textural control on gold distribution in As-free pyrite from the Dongping, Huangtuliang and Hougou gold deposits, North China Craton (Hebei Province, China). Chemical Geology 264, 101-121.

Cook, N. J., Ciobanu, C. L., Meria, D., Silcock, D., Wade, B., 2013. Arsenopyrite-pyrite association in an orogenic gold ore: Tracing mineralization history from textures and trace elements. Economic Geology 108, 1273–1283.

Cox S. F., 1995. Faulting processes at high fluid pressures: an example of fault valve behavior from the Wattle Gully Fault, Victoria, Australia. Journal of Geophysical Research: Solid Earth 100, 12841-12859.

Crede, L.S., Liu, W., Evans, K.A., Rempel, K.U., Testemale, D., Brugger, J., 2019, Crude oils as ore fluids: An experimental in-situ XAS study of gold partitioning between brine and organic fluid from 25 to 250° C. Geochimica et Cosmochimica Acta 244, 352-365.

D

Deditius A. P., Utsunomiya S., Renock D., Ewing R. C., Ramana C. V., Becher U., Kesler S. E., 2008. A proposed new type of arsenian pyrite: Composition, nanostructure and geological significance. Geochimica et Cosmochimica Acta72, 2919-2933.

Deditius, A.P., Utsunomiya, S., Ewing, R.C., Chryssoulis, S.L., Venter, D., Kesler, S.E., 2009. Decoupled geochemical behavior of As and Cu in hydrothermal systems. Geology 37, 707–710.

Diener, A., Neumann, T., 2010. Synthesis and incorporation of selenide in pyrite and mackinawite. Radiochimica Acta 99, 791-798.

Dong, G., Morrison, G., Jaireth, S., 1995. Quartz textures in epithermal veins, Queensland: classification, origin and implication. Economic Geology 90, 1841-1856.

Dong, Y.P., Zhang, G.W., Neubauer, F., Liu, X.M., Genser, J., Hauzenberger, C., 2011. Tectonic evolution of the Qinling orogen, China: Review and synthesis. Journal of Asian Earth Sciences 41, 213–237.

Dong, Y.P., Liu, X.M., Neubauer, F., Zhang, G.W., Tao, N., Zhang, Y.G., Zhang, X.N., Li, W., 2013. Timing of Paleozoic amalgamation between the North China and South China Blocks: Evidence from detrital zircon U-Pb ages. Tectonophysics 586, 173–191.

Dong, Y.P., Santosh, M., 2016, Tectonic architecture and multiple orogeny of the Qinling orogenic belt, central China. Gondwana Research 29, 1–40.

Dong Y., Yang Z., Liu X., Sun S., Li W., Cheng, B., Zhang F., Zhang X., He D., Zhang, G., 2016. Mesozoic intracontinental orogeny in the Qinling Mountains, central China. Gondwana Research 30, 144-158.

Dowty, E., 1976. Crystal structure and crystal growth: II. Sector zoning in minerals. American Mineralogist 61, 460-469.

Drummond S. E., Ohmoto H., 1985. Chemical evolution and mineral deposition in boiling hydrothermal systems. Economic Geology 80, 126-147.

Dubé B., Williamson K., McNicoll V., Malo M., Skulski T., Twomey T., Sanborn-Barrie M., 2004. Timing of gold mineralization at Red Lake, Northwestern Ontario, Canada: New constraints from U-Pb geochronology at the Goldcorp high-grade zone, Red Lake mine, and the Madsen mine. Economic Geology 99, 1611-1641.

E

Evans K. A., Tomkin A. G., Cliff J., Fiorentini M. L., 2014. Insights into subduction zone sulfur recycling from isotopic analysis of eclogite-hosted sulfides. Chemical Geology 365, 1-19.

F

Fan, H.R., Zhai, M.G., Xie, Y.H., Yang, J.H., 2003. Ore-forming fluids associated with granite-hosted gold mineralization at the Sanshandao deposit, Jiaodong gold province, China. Mineralium Deposita 38, 739-50.

Fan, H.R., Hu, F.F., Wilde, S.A., Yang, K.F., Jin, C.W., 2011. The Qiyugou gold-bearing breccia pipes, Xiong'ershan region, central China: fluid inclusion and stable-isotope evidence for an origin from magmatic fluids. International Geology Review 53, 25-45.

Fan, W., Wang, S., Tian, Y., Chen, Z.X., 2001. Complexation of Si in hydrothermal systems. Chinese Journal of Geochemistry 20, 201-209.

Farquhar J., Cliff J., Zerkle A. L., Kamyshny A., Poulton S. W., Claire M., Adams D., Harms B., 2013. Pathways for Neoarchean pyrite formation constrained by mass-independent sulfur isotopes. Proceedings of the National Academy of Sciences 110, 17638-17643.

Faure, G., 1986. Principles of Isotope Geology, 2nd edition. John Wiley and Sons, New York, 1779 pp.

Ferry J. M., 1981. Petrology of graphitic sulfide-rich schists from south-central Maine: an example of desulfidation during regional prograde metamorphism. American Mineralogist 66, 908–931.

Fleet M. E., 1970. Structural aspects of the marcasite-pyrite transformation. Can. Mineral. 10, 225-231.

Fleet M. E., MacLean P. J., and Barbier J., 1989. Oscillatory-zoned As-bearing pyrite from strata-bound and stratiform gold deposits; an indicator of ore fluid evolution. Econ. Geol. Monog 6, 356–362.

Fleet, M. E., Mumin, A. H., 1997. Gold-bearing arsenian pyrite and marcasite and arsenopyrite from Carlin Trend gold deposits and laboratory synthesis. American Mineralogist 82, 182-193.

Fougerouse, D., Reddy, S.M., Saxey, D.W., Rickard, W.D., Van, Riessen. A., and Micklethwaite, S., 2016. Nanoscale Au clusters in arsenopyrite controlled by growth rate not concentration: Evidence from atom probe microscopy. American Mineralogist 101, 1916–1919.

Fougerouse D., Micklethwaite S., Ulrich S., Miller J., Godel B., Adams D. T., McCuaig T. C., 2017. Evidence for two stages of mineralization in West Africa's largest gold deposit: Obuasi, Ghana. Economic Geology 112, 3-22

Fougerouse, D., Reddy, S.M., Kirkland, C.L., Saxey, D.W., Rickard, W.D., Hough,

R.M., 2019. Time-resolved, defect-hosted, trace element mobility in deformed Witwatersrand pyrite. Geoscience Frontiers 10, 55–63.

Fournier, R.O., Rowe, J. J., 1977, The solubility of amorphous silica in water at high temperatures and pressures. American. Mineralogist 62, 1052-1056.

Fournier, R.O., 1985, The behavior of silica in hydrothermal solutions, in Berger, B.R., and Bethke, P.M., eds., Geology and Geochemistry of Epithermal Systems: Reviews in Economic Geology 2, 45-62.

Fowler, A., Prokoph, A., Stern, R., Dupuis, C., 2002. Organization of oscillatory zoning in zircon: analysis, scaling, geochemistry, model of a zircon from Kipawa, Quebec, Canada. Geochimica et Cosmochimica Acta 66, 311-328.

Franchini, M., McFarlane, C., Maydagán, L., Reich, M., Lentz, D. R., Meinert, L., Bouhier, V., 2015. Trace metals in pyrite and marcasite from the Agua Rica porphyry-high sulfidation epithermal deposit, Catamarca, Argentina: Textural features and metal zoning at the porphyry to epithermal transition. Ore Geology Reviews, 66, 366–387.

Frank M.R., Candela P.A., Piccoli P.M., Glascock M.D., 2002. Gold solubility, speciation and partitioning as a function of HCl in the brine-silicate, melt-metallic gold system at 800°C and 100 MPa. Geochimica et Cosmochimica Acta 66, 3719-3732.

Frondel, C., 1938. Stability of colloidal gold under hydrothermal conditions. Economic Geology 33, 1-20.

G

Gansu Geological Survey, 2011. Verification report of reserve resource at Daqiao gold deposit, Xihe County, Gansu Province, unpublished report (in Chinese).

Gao S., Huang F., Gu X., Chen Z., Xing M., Li Y., 2017. Research on the growth orientation of pyrite grains in the colloform textures in Baiyunpu Pb–Zn polymetallic deposit, Hunan, China. Mineralogy and Petrology 111, 69-79.

Gebre-Mariam M., Hagemann S. G., Groves D. I., 1995. A classification scheme for epigenetic Archaean lode-gold deposits. Mineralium Deposita 30, 408-410.

Genna, D., Gaboury, D., 2015. Deciphering the hydrothermal evolution of a VMS system by LA–ICP–MS using trace elements in pyrite: An example from the Bracemac-McLeod deposits, Abitibi, Canada, and implications for

exploration. Economic Geology 110, 2087-2108.

Geisler T., Schaltegger U., Tomaschek F., 2007. Re-equilibration of zircon in aqueous fluids and melts. Elements 3, 43-50.

Gilbert, S.E., Danyushevsky, L.V., Rodemann, T., Shimizu, N., Gurenko, A., Meffre, S., Thomas, H., Large, R.R., Death, D., 2014. Optimisation of laser parameters for the analysis of sulphur isotopes in sulphide minerals by laser ablation ICP-MS. Journal of Analytical Atomic Spectrometry 29, 1042-1051.

Gaboury, D., 2013. Does gold in orogenic deposits come from pyrite in deeply buried carbon-rich sediments?: Insight from volatiles in fluid inclusions. Geology 41, 1207-1210.

Gammons C. H. Williams-Jones A. E., 1995. The solubility of Au-Ag alloy AgCl in HCl/NaCl solutions at 300°C: New data on the stability of Au (I) chloride complexes in hydrothermal solutions. Geochimica et Cosmochimica Acta 59, 3453-3468.

Goldfarb, R.J., Snee, L.W., Miller, L.D., Newberry, R.J., 1991. Rapid dewatering of the crust deduced from ages of mesothermal gold deposits. Nature 354, 296-298.

Goldfarb, R.J., Phillips, G.N., Nokleberg,W.J., 1998. Tectonic setting of synorogenic gold deposits of the Pacific Rim. Ore Geology Reviews 13, 185-218.

Goldfarb, R.J., Groves, D.I., Gardoll, S., 2001. Orogenic gold and geologic time: a global synthesis. Ore Geology Reviews 18, 1-75.

Goldfarb, R.J., Baker, T., Dubé, B., Groves, D.I., Hart, C.J.R., Gosselin, P., 2005. Distribution, character, and genesis of gold deposits in metamorphic terranes. Economic Geology 100th Anniversary, 407-450.

Goldfarb, R.J., Hart, C., Davis, G., Groves, D., 2007. East Asian gold: Deciphering the anomaly of Phanerozoic gold in precambrian cratons. Economic Geology 102, 341-345.

Goldfarb, R.J., Taylor, R.D., Collins, G.S., Goryachev, N.A., Orlandini, O.F., 2014. Phanerozoic continental growth and gold metallogeny of Asia. Gondwana Research 25, 48-102.

Goldfarb, R.J., Santosh, M., 2014. The dilemma of the Jiaodong gold deposits: are they unique? Geoscience Frontiers 5, 139-153.

Goldfarb, R.J., Groves, D.I., 2015. Orogenic gold: common or evolving fluid and metal sources through time. Lithos 233, 2-26.

Goldhaber M. B., Reynolds R. L., Rye R. O., 1978. Origin of a South Texas roll-type deposit; II, Sulfide petrology and sulfur isotope studies. Economic Geology 73, 1690-1705.

Goldhaber M. B. Reynolds R. L., Rye R. O., 1979. Formation and resulfidization of a South Texas roll-type uranium deposit. USGS Open File Report. 79-1651.

Gong, Y.J., 2014. The study on the tectonic-fluid system and metallogeni mechanism of Shuangwang gold deposit in Shaanxi Province. Ph.D. thesis, China University of Geosciences (Wuhan), 101p.

Granger H. C., Warren C. G., 1974. Zoning in the altered tongue associated with roll-type uranium deposits, in Formation of uranium ore deposits. In Formation of Uranium Ore Deposits (Chairman R. D. Nininger), I.A.E.A., Proc. Ser., No. STI/PUB/374, pp. 185-200.

Gregory, D., Meffre, S., Large, R., 2014. Comparison of metal enrichment in pyrite framboids from a metal-enriched and metal-poor estuary. American Mineralogist 99, 633-644.

Gregory, D.D., Large, R.R., Halpin, J.A., Baturina, E.L., Lyons, T.W., Wu, S., Danyushevsky, L., Sack, P., Chappaz, A., Maslennikov, V.V., Bull, S.W., 2015. Trace element content of sedimentary pyrite in black shales. Economic Geology 110, 1389-1410.

Groves, D.I., Phillips, G.N., Ho, S.E., Houstoun, S.M., Standing, C.A., 1987. Craton-scale distribution of Archaean greenstone gold deposits: predictive capacity of the metamorphic model. Economic Geology 82, 2045-2058.

Groves, D.I., 1993. The crustal continuum model for late-Archaean lode-gold deposits of the Yilgarn Block, Western Australia. Mineralium Deposita 28, 366-374.

Groves, D. I., Ridley, J. R., Bloem, E. M. J., Gebre-Mariam, M., Hagemann, S. G., Hronsky, J. M. A., McCuaig, T. C., 1995. Lode-gold deposits of the Yilgarn block: products of Late Archaean crustal-scale overpressured hydrothermal systems. Geological Society, London, Special Publications 95, 155-172.

Groves, D.I., Goldfarb, R.J., Gebre-Mariam, M., Hagemann, S.G., Robert, F., 1998. Orogenic gold deposits: a proposed classifi cation in the context of their crustal distribution and relationship to other gold deposit types. Ore Geology Reviews 13, 7-27.

Groves, D.I., Goldfarb, R.J., Knox-Robinson, C.M., Ojala, J., Gardoll, S., Yun, G.Y.,

Holyland, P., 2000. Late-kinematic timing of orogenic gold deposits and significance for computer- based exploration techniques with emphasis on the Yilgarn Block, Western Australia. Ore Geology Reviews 17, 1-38.

Groves, D. I., Goldfarb, R. J., Robert, F., Hart, C. J., 2003. Gold deposits in metamorphic belts: overview of current understanding, outstanding problems, future research, and exploration significance. Economic geology 98, 1-29.

Groves, D.I., Santosh, M., 2015. The giant Jiaodong gold province: the key to a unified model for orogenic gold deposits. Geoscience Frontiers 7, 409-2417.

Groves, D. I., Goldfarb, R. J., Santosh, M., 2016. The conjunction of factors that lead to formation of giant gold provinces and deposits in non-arc settings. Geoscience Frontiers 7, 303-314.

Groves, D. I., Santosh, M., Goldfarb, R. J., Zhang, L., 2019. Structural geometry of orogenic gold deposits: Implications for exploration of world-class and giant deposits. Geoscience Frontiers 9, 1163-1177.

H

Hagemann S. G., Groves D. I., Ridley J. R., Vearncombe J. R., 1992. The Archean lode gold deposits at Wiluna, Western Australia; high-level brittle-style mineralization in a strike-slip regime. Economic Geology 87, 1022-1053.

Hannington, M., Hardardóttir, V., Garbe-Schönberg, D., Brown, K.L., 2016. Gold enrichment in active geothermal systems by accumulating colloidal suspensions. Nature Geoscience 9, 299-302

Harlov D. E., Wirth R., Hetherington C. J., 2011. Fluid-mediated partial alteration in monazite: the role of coupled dissolution-reprecipitation in element redistribution and mass transfer. Contrib. Mineralogy and Petrology 162, 329-348.

Herrington, R.J., Wilkinson, J.J., 1993. Colloidal gold and silica in mesothermal vein systems. Geology 21, 539-542.

Higgins N. C., 1980. Fluid inclusion evidence for the transport of tungsten by carbonate complexes in hydrothermal solutions. Canadian Journal of Earth Sciences 17, 823-830.

Hodkiewicz, P.F., Groves, D.I., Davidson, G.J., Weinberg, R.F., Hagemann, S.G., 2009. Influence of structural setting on sulphur isotopes in Archean orogenic

gold deposits, Eastern Goldfields Province, Yilgarn, Western Australia. Mineralium Deposita 44, 129-150.

Hough, R.M., Noble, R.R.P., Reich, M., 2011. Natural gold nanoparticles. Ore Geology Reviews, 42, 55-61.

Hu, Q.Q., 2015. The mineralization features, mechanism and metallogenic regularity of the Fengtai Pb-Zn polymetallic ore cluster in West Qinling, China (in Chinese). Ph.D. thesis, Chinese Academy of Geological Sciences, 150 pp.

Hua, R.M., Chen, P.R., Zhang, W.L., Yao, J.M., Lin, J.F., Zhang, Z.S., Gu, S.Y., Liu, X.D., Qi, H.W., 2005. Metallogenesis related to Mesozoic granitoids in the Nanling Range, South China and their geodynamic settings. Acta Geologica Sinica 79, 810-820.

Huang, W.K., Gan, X.P., Shan, Z.X., Chen, L.X., Liu, Y., 1996. A study of petrology and metallognetic epoch of gold in Jianchaling deposit, Shaanxi Province. Geochimica 25, 150-156.

Huston, D.L., Sie, S.H., Suter, G.F., Cooke, D.R., Both, R.A., 1995. Trace elements in sulfide minerals from eastern Australian volcanic-hosted massive sulfide deposits; Part I, Proton microprobe analyses of pyrite, chalcopyrite, and sphalerite, and Part II, Selenium levels in pyrite; comparison with delta ^{34}S values and implications for the source of sulfur in volcanogenic hydrothermal systems. Economic Geology 90, 1167-1196.

I

Iler, R.K., 1979, The chemistry of silica: New York, John Wiley & Sons, 866 p.

J

K

Kaiser, N., 2002. Review of the fundamentals of thin-film growth. Applied optics 41, 3053-3060.

Keith, M., Smith, D.J., Jenkin, G.R., Holwell, D.A., Dye, M.D., 2018. A review of Te and Se systematics in hydrothermal pyrite from precious metal deposits: insights into ore-forming processes. Ore Geology Reviews 96, 269-282.

Kerrich, R., 1991. Mesothermal gold deposits: a critique of genetic hypotheses. In: Robert, F., Sheahan, P.A., Green, S.B. (Eds.), Greenstone Gold and Crustal Evolution: Geological Association of Canada, NUNA Conference Volume, pp. 13-31.

Kerrich, R., Cassidy, K. F., 1994. Temporal relationships of lode gold mineralization to accretion, magmatism, metamorphism and deformation—Archean to present: A review. Ore Geology Reviews 9, 263-310.

Kooi, E., 1966, The surface charge in oxidized silicon. The Surface Properties of Oxidized Silicon. Springer, Berlin, Heidelberg, 114-132.

Koppers, A.A.P., Staudigel, H., Duncan, R.A., 2003. High-resolution $^{40}Ar/^{39}Ar$ dating of the oldest oceanic basement basalts in the western Pacific basin. Geochemistry, Geophysics, Geosystems 4, 8914.

L

LaFlamme C., Martin L., Jeon H., Reddy S., Selvaraja V., Caruso S., Hao T. B., Roberts M. P., Voute F., Hagemann S., Wacey D., Littman S., Wing B., Fiorentini M., Kilburn M. R., 2016. In situ multiple sulfur isotope analysis by SIMS of pyrrhotite, pentlandite and chalcopyrite to refine magmatic ore genetic models. Chemical Geology 444, 1-15.

LaFlamme C., Sugiono D., Thébaud N., Caruso S., Fiorentini M., Selvaraja V., Jeon H., Voute F. Martin L., 2018. Multiple sulfur isotopes monitor fluid evolution in an orogenic gold deposit. Geochimica et Cosmochimica Acta 222:436-446.

Lan, T.G., Fan, H.R., Santosh, M., Hu, F.F., Yang, K.F., Yang, Y.H., Liu, Y., 2011. Geochemistry and Sr-Nd-Pb-Hf isotopes of the Mesozoic Dadian alkaline intrusive complex in the Sulu orogenic belt, eastern China: Implications for crust–mantle interaction. Chemical Geology 285, 97-114.

Large R. R., Maslennikon V. V., Robert F., Danyushevsky L. V., Chang Z.S., 2007. Multistage sedimentary and metamorphic origin of pyrite and gold in the giant Sukhoi Log deposit, Lena gold province, Russia. Economic Geology 102, 1233-1267.

Large, R.R., Danyushevsky, L., Hollit, C., Maslennikov, V., Meffre, S., Gilbert, S., Bull, S., Scott, R., Emsbo, P., Thomas, H., Singh, B., Foster, J., 2009. Gold and trace element zonation in pyrite using a laser imaging technique:

Implications for the timing of gold in orogenic and carlin-style sedimenthosted deposits: Economic Geology and the Bulletin of the Society of Economic Geologists 104, 635-668.

Large, R.R., Bull, S.W., and Maslennikov, V., 2011. A carbonaceous sedimentary source-rock model for Carlin-type and orogenic gold deposits: Economic Geology and the Bulletin of the Society of Economic Geologists 106, 331-358.

Large, R.R., Halpin, J.A., Danyushevsky, L.V., Maslennikov, V.V., Bull, S.W., Long, J.A., Gregory, D.D., Lounejeva, E., Lyons, T.W., Sack, P.J., McGoldrick, P.J., Calver, C.R., 2014. Trace element content of sedimentary pyrite as a new proxy for deep-time ocean-atmosphere evolution. Earth and Planetary Science Letters 389, 209-220.

Large, R.R., Gregory, D.D., Steadman, J.A., Tomkins, A.G., Lounejeva, E., Danyushevsky, L.V., Halpin, J.A., Maslennikov, V.V., Sack, P.J., Mukherjee, I., Berry, R., Hickman, A., 2015. Gold in the oceans through time. Earth and Planetary Science Letters 428, 139-150.

Lennie A. R., Vaughan D. J., 1992. Kinetics of the marcasite-pyrite transformation: An infrared spectroscopic study. American Mineralogist 77, 1166-1171.

Li, F.D., Zou, X.H., Gao, J.P., Lu, Y., Zhang, H.Y., 2001. On the rapid-positioning and prediction for micro dissemination type (sedimentary rock host) gold deposit (ore bodies), Ma'anqiao. Northwestern Geology 34, 27-63.

Li, J.W., Bi, S.J., Selby, D., Chen, L., Vasconcelos, P., Thiede, D., Zhou, M.F., Zhao, X.F., Li, Z.K., Qiu, H.N., 2012b. Giant Mesozoic gold provinces related to the destruction of the North China craton. Earth and Planetary Science Letters 349, 26-37.

Li, J.W., Li, Z.K., Zhou, M.F., Chen, L., Bi, S.J., Deng, X.D., Qiu, H.N., Cohen, B., Zhao, X.F., 2012a. The Early Cretaceous Yangzhaiyu lode gold deposit, North China Craton: a link between craton reactivation and gold veining. Economic Geology 107, 43-79.

Li, J.W., Vasconcelos, P.M., Zhang, J., Zhou, M.F., Zhang, X.J., Yang, F.H., 2003. $^{40}Ar/^{39}Ar$ constraints on a temporal link between gold mineralization, magmatism, and continental margin transtension in the Jiaodong gold province, eastern China. The Journal of geology 111, 741-751.

Li, J.W., Vasconcelos, P.M., Zhou, M.F., Zhao, X.F., Ma, C.Q., 2006.

Geochronology of the Pengjiakuang and Rushan gold deposits, eastern Jiaodong gold province, northeastern China: implications for regional mineralization and geodynamic setting. Economic Geology 101, 1023-1038

Li J. W., Zhou M. F., Li X. F., Li Z. J., Fu Z. R., 2002. Origin of a large breccia-vein system in the Sanerlin uranium deposit, southern China: a reinterpretation. Mineralium Deposita 37, 213-225.

Li, J.Y., Wang, Z.Q., Zhao, M., 1999. $^{40}Ar/^{39}Ar$ thermochronological constraints on the timing of collisional orogeny in the Mian-Lue collision belt, southern Qinling Mountains. Acta Geologica Sinica 73, 208-215.

Lippmann F., 1980. Phase diagrams depicting aqueous solubility of binary mineral systems. Neues Jahrbuch Mineralogische Abhandlungen 139, 1–25.

Liu S. G., Li Z. W., Liu S., Luo Y. H., Xu G. Q., Dai G. H., Gong C. M., Yong Z.Q., 2006. Formation and evolution of Dabashan foreland basin and fold-and-thrust belt. Geological Publishing House, Sichuan, China, pp. 1–248.

Li, S.G., Sun, W.D., Zhang, G.W., 1996. Chronology and geochemistry of metavolcanic rocks from Heigouxia valley in Mian-Lue tectonic belt, South Qinling: evidence for a Paleozoic oceanic basin and its close time. Science in China (Series D) 39, 300-310.

Li X. H., Fan H. R., Yang K. F., Hollings P., Liu, X., Hu, F. F., Cai, Y. C., 2018. Pyrite textures and compositions from the Zhuangzi Au deposit, southeastern North China Craton: implication for ore-forming processes. Contributions to Mineralogy and Petrology 173, 73. https://doi.org/10.1007/s00410-018-1501-2

Lin, Z.W., Zhou, Y.Z., Qin, Y., Yue, S.W., 2017. Fuchsite $^{40}Ar/^{39}Ar$ geochronology of the Huachanggou gold Deposit and its tectonic implications. Geotectonica et Metallogenia 41, 315-327 (in Chinese with English abs.)

Liu, J.J., Zheng, M.H., 1993. La'erma Se-Cu-U-Ni-Mo-PGE-Au deposit of submarine exhalative genesis in La'erma. Journal of Precious Metallic Geology 2, 100-103.

Liu, J.J., Zheng, M.H, Liu, J.M., Su, W.C., 2000. Geochemistry of the La'erma and Qiongmo Au-Se deposits in the western Qinling Mountains, China. Ore Geology Reviews 17, 91-111.

Liu, J.J., Dai, H.Z., Zhai, D.G., Wang, J.P., Wang, Y.H., Yang, L.B., Mao, G.J., Liu,

X.H., Liao, Y.F., Yu, C., Li, Q.Z., 2015. Geological and geochemical characteristics and formation mechanisms of the Zhaishang Carlin-like type gold deposit, western Qinling Mountains, China. Ore Geology Reviews 64, 273-98.

Liu, W., Etschmann, B., Testemale, D., Hazemann, J. L., Rempel, K., Müller, H., Brugger, J., 2014, Gold transport in hydrothermal fluids: Competition among the Cl^-, Br^-, HS^- and $NH_{3\ (aq)}$ ligands. Chemical Geology, 376, 11-19.

Liu, X.L., Wang, Y.T., Hu, Q.Q., Wei, R., Wang, R.T., Wen, S.W., Chen, M.S., Yang, G.H., 2014. Sm-Nd isotopic dating of carbonate minerals from the Chaima gold deposit in the Fengxian-Taibai ore concentration area, Shaanxi Province and its implications. Acta Petrologica Sinica 30: 271-280 (in Chinese with English abs.)

Liu, Y.H., Li, Z., Zhou, S., Han, Y.X., Li, H., Li, X., Zhou, S.F., 2015. Geological characteristics, ore-forming ages and geological significance of Donggou-Jinlongshan gold deposit, South Qinling belt. Earth Science Frontiers 22, 1-13.

Liu, Y., Han, Y., Wei, J., Teng, F., Tian, R., Gao, Z., 2018. Geological and geochemical characteristics and prospecting potential of the Daqiao hot spring-type gold deposit in the west Qinling Orogen. Geological Journal 53, 136-146.

Loftus-Hills, G., Solomon, M., 1967. Cobalt, nickel and selenium in sulphides as indicators of ore genesis. Mineralium Deposita 2, 228-242.

Loucks, R. R., Mavrogenes, J. A., 1999. Gold solubility in supercritical hydrothermal brines measured in synthetic fluid inclusions. Science 284, 2159-2163.

Longerich, H.P., Jackson, S.E., Günther, D., 1996. Laser ablation inductively coupled plasma mass spectrometric transient signal data acqusition and analyte concentration calculation. Journal of Analytical Atomic Spectroscopy 11, 899-904.

Lu, Y.M., Li, H.G., Chen, Y.G., Zhang, G.L., 2006. $^{40}Ar/^{39}Ar$ dating of alteration minerals from Zhaishang gold deposit in Minxian County, Gansu Province, and its geologic significance. Mineral Deposits 25, 590-597.

Lubben, J.D., Cline, J.S., Barker, S.L., 2012. Ore fluid properties and sources from quartz-associated gold at the Betze-Post Carlin-type gold deposit, Nevada, United States. Economic Geology 107, 1351-1385.

M

Mao, J.W., Qiu, Y.M., Goldfarb, R.J., Zhang, Z.C, Garwin, S., Fengshou, R., 2002. Geology, distribution, and classification of gold deposits in the western Qinling belt, central China. Mineralium Deposita 37, 352-377.

Mao, J.W., Xie, G.Q., Zhang, Z.H., Li, X.F., Wang, Y.T., Zhang, C.Q., Li, Y.F., 2005. Mesozoic large-scale metallogenic pulses in North China and corresponding geodynamic settings. Acta Petrologica Sinca 21, 169-188.

Mao, J.W., Wang, Y.T., Lehmann, B., Yu, J.J., Du, A.D., Mei, Y.X., Li, Y.F., Zang, W.S., Stein, H.J., Zhou, T.F., 2006. Molybdenite Re-Os and albite $^{40}Ar/^{39}Ar$ dating of Cu-Au-Mo and magnetite porphyry systems in the Yangtze River valley and metallogenic implications. Ore Geology Review 29, 307-324.

Mao, J.W., Xie, G.Q., Bierlein, F., Qu, W.J., Du, A.D., Ye, H.S., Pirajno, F., Li, H.M., Guo, B.J., Li, Y.F., Yang, Z.Q., 2008. Tectonic implications from Re-Os dating of Mesozoic molybdenum deposits in the East Qinling-Dabie orogenic belt. Geochimica et Cosmochimica Acta 72, 4607-4626.

Mao, J.W., Xie, G.Q., Pirajno, F., Ye, H.S., Wang, Y.B., Li, Y.F., Xiang, J.F., Zhao, H.J., 2010. Late Jurassic-Early Cretaceous granitoid magmatism in Eastern Qinling, central-eastern China: SHRIMP zircon U-Pb ages and tectonic implications. Australian Journal of Earth Sciences 57, 51-78.

Mattauer, M., Matte, P., Malavieille, J., Tapponnier, P., Maluski, H., Qin, X.Z., Lun, L.Y., Qin, T. Y., 1985. Tectonics of Qinling Belt: Build-up and evolution of Eastern Asia. Nature 317, 496-500.

Meng, Q.R., Zhang, G.W., 1999. Timing of collision of the North and South China blocks: Controversy and reconciliation. Geology 27, 123-126.

McLoughlin N., Wacey D., Kruber C., Kilburn M. R., Thorseth I. H., Pedersen R. B., 2011. A combined TEM and NanoSIMS study of endolithic microfossils in altered seafloor basalt. Chemical Geology 289, 154-162.

Mikucki, E. J., 1998. Hydrothermal transport and depositional processes in Archean lode-gold systems: A review. Ore geology reviews 13, 307-321.

Mitchell, K., Mason, P.R., Van Cappellen, P., Johnson, T.M., Gill, B.C., Owens, J.D., Diaz, J., Ingall, E.D., Reichart, G.J., Lyons, T.W., 2012. Selenium as paleo-oceanographic proxy: A first assessment. Geochimica et Cosmochimica

Acta 89, 302-317.

Mo, Y.W., Savage, D.E., Swartzentruber, B.S., Lagally, M.G., 1990. Kinetic pathway in Stranski-Krastanov growth of Ge on Si (001). Physical Review Letters 65, 1020-1023.

Molnar, P., Tapponnier, P., 1975. Cenozoic tectonics of Asia: effects of a continental collision. Science 189, 419-426.

Morey, A. A., Tomkins, A. G., Bierlein, F. P., Weinberg, R. F., Davidson, G. J., 2008. Bimodal distribution of gold in pyrite and arsenopyrite: Examples from the Archean Boorara and Bardoc shear systems, Yilgarn craton, Western Australia. Economic Geology 103, 599-614.

Müller, W., Shelley, M., Miller, P., Broudec, S., 2009. Initial performance metrics of a new custom-designed ArF excimer LA-ICPMS system coupled to a two-volume laser-ablation cell. Journal of Analytical Atomic Spectrometry 24, 209-214.

Murowchick, J. B., Barnes, H. L., 1986. Marcasite precipitation from hydrothermal solutions. Geochimica et Cosmochimica Acta 50, 2615-2629.

Murowchick, J. B., 1992. Marcasite inversion and the petrographic determination of pyrite ancestry. Economic Geology 87, 1141-1152.

N

Nie, F.J., Jiang, S.H., Zhao,Y.M., 2001. Lead and sulfur isotope study of the Wenyu and Dongchuang quartz vein-type gold deposits in the Xiaoqinling area, Henan and Shaanxi Province, central China. Mineral.Deposita 20, 163-173.

Niu, B.G., He, Z.J., Song, B., Ren, J.S., 2003. SHRIMP dating of the Zhangjiakou volcanic series and its significance. Geological Bulletin of China 22, 140-141.

O

Ohmoto H., 1972. Systematics of sulfur and carbon isotopes in hydrothermal ore deposits Economic Geology 67, 551-578.

Ostapenko N. S., Neroda O. N., 2007. Fluid pressure and hydraulic fracturing in hydrothermal ore formation at gold deposits. Russian Journal of Pacific Geology 1, 276-289.

P

Palenik, C.S., Utsunomiya, S., Reich, M., Kesler, S.E., Wang, L., Ewing, R.C., 2004. "Invisible" Au revealed: Direct imaging of Au nanoparticles in a Carlin-type deposit. American Mineralogist 89, 1359-1366.

Pals, D. W., Spry, P. G., Chryssoulis, S., 2003. Invisible gold and tellurium in arsenic-rich pyrite from the Emperor gold deposit, Fiji: implications for gold distribution and deposition. Economic Geology 98, 479-493.

Peterson E. C., Mavrogenes J. A., 2014. Linking high-grade gold mineralisation to earthquake-induced fault-valve processes in the Porgera gold deposit, Papua New Guinea. Geology 42, 383-386.

Phillips, G. N., Groves, D. I., 1983. The nature of Archaean gold-bearing fluids as deduced from gold deposits of Western Australia. Journal of the Geological Society of Australia 30, 25-39.

Phillips, G.N., Australian and global setting for gold in 2013, in Proceedings World Gold 2013, Brisbane, Australia, 26-29 September, 2013. The Australian Institute of Mining and Metallurgy, 15-21.

Phillips, G.N., Evans, K.A., 2004. Role of CO_2 in the formation of gold deposits. Nature 429, 860-863.

Phillips, G.N., Powell, R., 2009. Formation of gold deposits: Review and evaluation of the continuum model. Earth-Science Reviews 94, 1-21.

Phillips, G.N., Powell, R., 2010. Formation of gold deposits: A metamorphic devolatilization model: Journal of Metamorphic Geology 28, 689-718.

Phillips W. J., 1972. Hydraulic fracturing and mineralization. J. Geol. Soc. London. 128, 337-59.

Plümper, O., Botan, A., Los, C., Liu, Y., Malthe-Sørenssen, A., Jamtveit, B., 2017. Fluid-driven metamorphism of the continental crust governed by nanoscale fluid flow. Nature geoscience 10, 685-690.

Pitcairn, I.K., Teagle, D.A.H., Craw, D., Olivo, G.R., Kerrich, R., Brewer, T.S., 2006. Sources of metals and fluids in orogenic gold deposits: Insights from the Otago and Alpine Schists, New Zealand. Economic Geology and the Bulletin of the Society of Economic Geologists 101, 1525-1546.

Powell, R., Will, T.M., Phillips, G.N., 1991. Metamorphism in Archaean greenstone

belts: Calculated fluid compositions and implications for gold mineralization. Journal of Metamorphic Geology 9, 141-150.

Prokofiev V. Y., Kamenetsky V. S., Selektor S. L., Rodemann T., Kovalenker V. A., Vatsadze S. Z., 2017. First direct evidence for natural occurrence of colloidal silica in chalcedony-hosted vacuoles and implications for ore-forming processes. Geology 45, 71-74.

Putnis, A., Fernandez-Diaz, L., Prieto M., 1992. Experimentally produced oscillatory zoning in the (Ba, Sr) SO_4 solid solution. Nature 358, 743-745.

Putnis A., Prieto M., Fernandez-Diaz L., 1995. Fluid supersaturation and crystallization in porous media. Geological Magazine 132, 1-13.

Putnis A., Mauthe G., 2001. The effect of pore size on cementation in porous rocks. Geofluids 1, 37 Putnis A., 2002. Mineral replacement reactions: from macroscopic observations to microscopic mechanisms. Geological Magazine 66, 689-708.

Putnis A., 2009. Mineral replacement reactions. Rev. Mineral. Geochem. 70, 87-124.

Q

Qi, J.Z., Yuan, S.S., Li, L., Sun, B., Guo, J.H., Li, Z.H., Fan, Y.X., Liu, W., Gao, Q.B., 2003. Geological features and ore-controlling factors of the Yangshan superlarge gold deposit, Gansu province, China. Geological Review 49, 85-92.

Qi, J.Z., Yang, G.C., Li, L., Fan, Y.X., Liu, W., 2006. Isotope geochemistry, chronology and genesis of the Yangshan gold deposit, Gansu. Geology in China 33, 1345-1353.

Qian G., Brugger J., SkinnerW. M., Chen G., Pring A., 2010. An experimental study of the mechanism of the replacement of magnetite by pyrite up to 300 °C. Geochimica et Cosmochimica Acta 74, 5610-5630.

Qian G., Xia F., Brugger J., Skinner W., Bei J., Chen G., Pring A., 2011. Replacement of pyrrhotite by pyrite and marcasite under hydrothermal conditions up to 220 °C: An experimental study of reaction textures and mechanisms. American Mineralogist 96, 1878-1893.

Qiu, Y.M., Groves, D.I., McNaughton, N.J., Wang, L.G., Zhou, T.H., 2002. Nature, age, and tectonic setting of granitoid-hosted, orogenic gold deposits of the

Jiaodong Peninsula, eastern North China craton, China. Mineralium Deposita 37, 283-305.

R

Ratschbacher, L., Hacker, B.R., Calvert, A., Webb, L.E., Grimmer, J.C., McWilliams, M.O., Hu, J., 2003. Tectonics of the Qinling (Central China): tectonostratigraphy, geochronology, and deformation history. Tectonophysics 366, 1-53.

Reed M.H., Palandri J., 2006. Sulfide mineral precipitation from hydrothermal fluids. Reviews in Mineralogy and Geochemistry 61, 609-631.

Ren, J.S., Chen, T.Y., Niu, B.G., 1992. Tectonic evolution of the continental lithosphere of the East China and adjacent area and relevant mineralization. Science Press, Beijing, 230 pp.

Reich, M., Kesler, S.E., Utsunomiya, S., Palenik, C.S., Chryssoulis, S.L., Ewing, R.C., 2005, Solubility of Au in arsenian pyrite. Geochimica et Cosmochimica Acta 69, 2781-2796.

Reynolds R. L., Goldhaber M. B., Carpenter D. J., 1982. Biogenic and nonbiogenic ore-forming processes in the South Texas uranium district: Evidence from the Panna Maria deposit. Economic Geology 77, 541-556.

Riciputi L. R., Paterson B. A., Ripperdan R. L., 1998. Measurements of light stable isotope ratios by SIMS: Matrix effects for oxygen, carbon, and sulfur isotopes in minerals. International Journal of Mass Spectrometry 178, 81–112

Ridley, J.R., Diamond, L.W., 2000. Fluid chemistry of orogenic lode gold deposits and implications for genetic models. Reviews in Economic Geology 13, 146-162.

Robert F., Boullier A. M., Firdaous K., 1995. Gold-quartz veins in metamorphic terranes and their bearing on the role of fluids in faulting. Journal of Geophysical Research: Solid Earth 100, 12861-12879.

Rottier, B., Kouzmanov, K., Wälle, M., Bendezú, R., Fontboté, L., 2016. Sulfide replacement processes revealed by textural and LA–ICP–MS trace element analyses: example from the early mineralization stages at Cerro de Pasco, Peru. Economic Geology 111, 1347-1367.

Rouxel O., Ono S. H., Alt J., Rumble D., Ludden J., 2008. Sulfur isotope evidence

for microbial sulfate reduction in altered oceanic basalts at ODP Site 801. Earth and Planetary Science Letters 268, 110–123.

Rubatto D., Müntener O., Barnhoorn A., Gregory C., 2008. Dissolution-reprecipitation of zircon at low-temperature, high-pressure conditions (Lanzo Massif, Italy). American Mineralogist 93, 1519-1529.

S

Saunders, J.A., 1990. Colloidal transport of gold and silica in epithermal precious-metal systems: Evidence from the Sleeper deposit, Nevada. Geology 18, 757-760.

Saunders, J.A., 1994. Silica and gold textures in bonanza ores of the Sleeper Deposit, Humboldt County, Nevada; evidence for colloids and implications for epithermal ore-forming processes. Economic Geology 89, 628-638.

Saunders, J.A., Schoenly, P.A., 1995. Boiling, colloid nucleation and aggregation, and the genesis of bonanza Au-Ag ores of the Sleeper deposit, Nevada. Mineralium Deposita 30, 199-210.

Schieber J., 2007. Oxidation of detrital pyrite as a cause for Marcasite Formation in marine lag deposits from the Devonian of the eastern US. Deep-Sea Res. II Top. Stud. Oceanogr. 54, 1312-1326.

Schieber J., 2011. Marcasite in Black Shales—a Mineral Proxy for Oxygenated Bottom Waters and Intermittent Oxidation of Carbonaceous Muds. Journal of Sedimentary Research 81, 447-458.

Schoonen M. A. A., Barnes H. L., 1991. Reactions forming pyrite and marcasite from solution: II. Via FeS precursor below 100 °C. Geochimica et Cosmochimica Acta 55, 1505-1514.

Selvaraja V., Fiorentini M. L., Jeon H., Savard D. D., LaFlamme C. K., Guagliardo P., Caruso S., Bui T. H., 2017. Evidence of local sourcing of sulfur and gold in an Archaean sediment-hosted gold deposit. Ore Geology Reviews 89, 909-930.

Seward, T. M., 1973. Thio complexes of gold and the transport of gold in hydrothermal ore solutions. Geochimica et Cosmochimica Acta 37, 379-399.

Shan, L., Zhang, D.M., Pang, Y.C., Liu, J.J., Zhang, W.Y., Zhao, M.M., Zhang, Z.P., 2016. Late Triassic magmatic activity in the Daqiao gold deposit of West

Qinling belt: Zircon U-Pb chronology and Lu-Hf isotope evidence. Geological Bulletin of China 35, 2045-2057.

Sherlock, R.L., Lehrman, N.J., 1995. Occurrences of dendritic gold at the McLaughlin Mine hot-spring gold deposit. Mineralium Deposita 30, 323-327.

Shenberger, D.M., Barnes, H.L., 1989. Solubility of gold in aqueous sulphide solutions from 150 to 350 °C. Geochimica et Cosmochimica Acta 53, 269-278.

Shi, Z.L., Liu, J.X., Fan, S.C., 1989. Geological characteristics and genesis of Shuangwang gold deposit, Shaanxi province. Science and Technology Publishing House of Shaanxi, Xi'an, 98pp.

Shore, M., Fowler, A.D., 1996. Oscillatory zoning in minerals: a common phenomenon. The Canadian Mineralogist 34, 1111-1126.

Sibson R. H., 1987. Earthquake rupturing as a mineralizing agent in hydrothermal systems. Geology 15, 701-704.

Sibson R. H. Robert F., Poulsen K. H., 1988. High-angle reverse faults, fluid-pressure cycling, and mesothermal gold-quartz deposits. Geology 16, 551-555.

Simmons, S.F., Brown, K.L., 2006. Gold in magmatic hydrothermal solutions and the rapid formation of a giant ore deposit. Science 314, 288-291.

Simmons, S.F., Brown, K.L., 2007. The flux of gold and related metals through a volcanic arc, Taupo Volcanic Zone, New Zealand. Geology 35, 1099-1102.

Simon G., Kesler S. E., Chryssoulis S., 1999. Geochemistry and textures of gold-bearing arsenian pyrite, Twin Creeks, Nevada; implications for deposition of gold in Carlin-type deposits. Economic Geology 94, 405-421.

Smith K. S., 1999. Metal sorption on mineral surfaces: an overview with examples relating to mineral deposits. Rev. Economic Geology 6, 161-82.

Stefánsson, A., Seward T. M., 2003a. The hydrolysis of gold (I) in aqueous solutions to 600°C and 1500 bar. Geochimica et Cosmochimica Acta 67, 1677-1688.

Stefánsson, A., Seward T.M., 2003b. The stability of chloridogold (I) complexes in aqueous solutions from 300 to 600°C and from 500 to 1800 bar. Geochimica et Cosmochimica Acta 67, 4459-4576.

Stefánsson, A., Seward T M., 2004. Gold (I) complexing in aqueous sulphide solutions to 500°C at 500 bar. Geochimica et Cosmochimica Acta 68, 4121-4143.

Stumm W., Morgan J. J., 1996. Aquatic chemistry, third ed. Wiley-Interscience, New York.

Su W., Xia B., Zhang H., Zhang X., Hu R., 2008. Visible gold in arsenian pyrite at the Shuiyindong Carlin-type gold deposit, Guizhou, China: Implications for the environment and processes of ore formation. Ore Geology Reviews 33, 667-679.

Sun, W.D., Li, S.G., Chen, Y.D., Li, Y.J., 2002. Timing of synorogenic granitoids in the South Qinling, central China: Constraints on the evolution of the Qinling-Dabie orogenic belt. Journal of Geology 110, 457-468.

Sun, W.D., Ding, X., Hu, Y.H., Li, X.H., 2007. The golden transformation of the Cretaceous plate subduction in the west Pacific. Earth and Planetary Science Letters 262, 533-542.

Sun, W.D., Ling, M.X., Yang, X.Y., Fan, W.M., Ding, X., Liang, H.Y., 2010. Ridge subduction and porphyry copper-gold mineralization: An overview. Science China Earth Sciences 53, 475-84.

Sun, W.D., Li, S., Yang, X.Y., Ling, M.X., Ding, X., Duan, L.A., Zhan, M.Z., Zhang, H., Fan, W.M., 2013. Large-scale gold mineralization in eastern China induced by an Early Cretaceous clockwise change in Pacific plate motions. International Geology Review 55, 311-21.

Sung Y. H., Brugger J., Ciobanu C. L., Pring A., Skinner W., Nugus M., 2009. Invisible gold in arsenian pyrite and arsenopyrite from a multistage Archaean gold deposit: Sunrise Dam, Eastern Goldfields Province, Western Australia. Mineralium Deposita 44, 765-791.

T

Tan, G.Y., 1992. Geological character of Pingding As-Au deposit and its metallogenic mechanism. Acta Geologica Gansu 1, 48-54.

Tan, J., Wei, J., Audétat, A., Pettke, T., 2012. Source of metals in the Guocheng gold deposit, Jiaodong Peninsula, North China Craton: link to early Cretaceous mafic magmatism originating from Paleoproterozoic metasomatized lithospheric mantle. Ore Geology Reviews 48, 70-87.

Tang K. F., Li J. W., Selby D., Zhou M. F., Bi S.J., Deng X. D., 2013. Geology, mineralization, and geochronology of the Qianhe gold deposit, Xiong'ershan

area, southern North China Craton. Mineralium Deposita 48, 729-747.

Tapponnier, P., Molnar, P., 1979. Active faulting and Cenozoic tectonics of the Tien Shan, Mongolia, and Baykal regions. Journal of Geophysical Research: Solid Earth 84, 3425-3459.

Tardani, D., Reich, M., Deditius, A.P., Chryssoulis, S., Sánchez-Alfaro, P., Wrage, J., Roberts, M.P., 2017. Copper-arsenic decoupling in an active geothermal system: A link between pyrite and fluid composition. Geochimica et Cosmochimica Acta 204, 179-204.

Thomas, H.V., Large, R.E., Bull, S.W., Maslennikov, V., Berry, R.F., Fraser, R., Froud, S., Moye, R., 2011. Pyrite and pyrrhotite textures and composition in sediments, laminated quartz veins, and reefs at Bendigo gold mine, Australia: Insights for ore genesis. Economic Geology 106, 1-31.

Tomkins A. G., Mavrogenes J. A., 2001. Redistribution of Gold within Arsenopyrite and Löllingite during Pro- and Retrograde Metamorphism: Application to Timing of Mineralization. Economic Geology 96, 525-534.

Tomkins A. G., Pattison D. R. M., Frost B. R., 2007. On the Initiation of Metamorphic Sulfide Anatexis. Journal of Petrology 48, 511-535.

Tomkins, A.G. Grundy, C., 2009. Upper temperature limits of orogenic gold deposit formation: constraints from the granulite-hosted Griffin's Find Deposit, Yilgarn Craton. Economic Geology 104, 669-685.

Tomkins, A.G., 2010. Windows of metamorphic sulfur liberation in the crust: Implications for gold deposit genesis. Geochimica et Cosmochimica Acta 74, 3246-3259.

Tomkins, A. G., 2013. On the source of orogenic gold. Geology 41, 1255-1256.

Tomkins, A.G., 2013b. A biogeochemical influence on the secular distribution of orogenic gold. Economic Geology and the Bulletin of the Society of Economic Geologists 108, 193-197.

Tomkins, A.G., Grundy, C., 2009. Upper Temperature Limits of Orogenic Gold Deposit Formation: Constraints from the Granulite-Hosted Griffin's Find Deposit, Yilgarn Craton: Economic Geology and the Bulletin of the Society of Economic Geologists 104, 669-685.

Tossell J. A., Vaughan D. J., Burdett J. K., 1981. Pyrite, marcasite, and arsenopyrite type minerals: crystal chemical and structural principles. Physics and Chemistry of Minerals 7, 177-184.

Tu, H.K., 2008. Discovery and application of the Qinling Se deposit with its forming mechanism research. Mineral Resources and Geology 22, 27-32.

U

V

W

Walker F. D. L., Lee M. R., Parsons I., 1995. Micropores and micropermeable texture in alkali feldspars: geochemical and geophysical implications. Mineralogical Magazine =59, 505-534.

Wang, L.S., 2009. Study on the metallogenic regularity and geological-geochemistry for black rock series and related typical deposits in Qinling Mountains, Shaanxi. Ph.D. thesis, Northwest University, 165 pp.

Wang, Y., Xu, H., Merino, E., Konishi, H., 2009. Generation of banded iron formations by internal dynamics and leaching of oceanic crust. Nature Geoscience 2, 781-784.

Wang, Y.T., Li, X., Wang, R.T., Liu, X.L., Hu, Q.Q., Li, J.H., 2014. Evidence of Ar-Ar age for the metallogenic epoch of Simaoling gold deposit in Fengxian-Taibai ore cluster of Shaanxi. Journal of Earth Science and Environment 36, 61-72.

Watson, E.B., 2004. A conceptual model for near–surface kinetic controls on the trace-element and stable isotope composition of abiogenic calcite crystals1. Geochimica et Cosmochimica Acta 68, 1473-1488.

Wen G., Li J. W., Hofstra A. H., Koenig A. E., Lowers H. A., Adams, D., 2017. Hydrothermal reequilibration of igneous magnetite in altered granitic plutons and its implications for magnetite classification schemes: Insights from the Handan-Xingtai iron district, North China Craton. Geochimica et Cosmochimica Acta 213, 255-270.

Whitehouse M. J., 2013. Multiple sulfur isotope determination by SIMS: evaluation of reference sulfides for $\Delta^{33}S$ with observations and a case study on the determination of $\Delta^{36}S$. Geostandards and Geoanalytical Research 37, 19-33

Widler A. M., Seward T. M., 2002. The adsorption of gold (I) hydrosulphide

complexes by iron sulphide surfaces. Geochimica et Cosmochimica Acta 66, 383-402.

Wilkinson, J.J. Nolan, J. Rankin, A.H., 1996. Silicothermal fluid: A novel medium for mass transport in the lithosphere: Geology, v. 24, p. 1059-1062.

Williams-Jones, A.E., Bowell, R.J., Migdisov, A.A., 2009. Gold in solution. Elements 5, 281-287.

Wilson, S.A., Ridley, W.I. Koenig, A.E., 2002. Development of sulfide calibration standards for the laser ablation inductively coupled plasma mass spectrometry technique. Journal of Analytical Atomic Spectroscopy 17, 406-409.

Wong, K.H., Zhou, M.F., Chen, W.T., O'Brien, H., Lahaye, Y., Chan, S.L.J., 2017. Constraints of fluid inclusions and in-situ S-Pb isotopic compositions on the origin of the North Kostobe sediment-hosted gold deposit, eastern Kazakhstan. Ore Geology Reviews 81, 256-269.

Wood, S.A., Mountain, B.W., Pan, P., 1992, The aqueous geochemistry of platinum, palladium and gold: recent experimental constraints and a re-evaluation of theoretical predictions. The Canadian Mineralogist, 30, 955-982.

Wu Y.F., Li J.W., Evans K., Koenig A.E., Li Z.K., O'Brien H., Lahaye Y., Rempel K., Hu S.Y., Zhang Z.P., and Yu J.P., 2018a. Ore-Forming Processes of the Daqiao Epizonal Orogenic Gold Deposit, West Qinling Orogen, China: Constraints from Textures, Trace Elements, and Sulfur Isotopes of Pyrite and Marcasite, and Raman Spectroscopy of Carbonaceous Material. Economic Geology 113, 1093-1132.

Wu Y.F., Li J.W., Evans K., Vasconcelos P.M., Thiede D.S., Fougerouse D., and Rempel K., 2018b. Late Jurassic to Early Cretaceous age of the Daqiao gold deposit, West Qinling Orogen, China: implications for regional metallogeny. Mineralium Deposita, doi: 10.1007/s00126-018-0835-z.

X

Xia F., Brugger J., Chen G., Ngothai Y., O'Neill B., Putnis A., Pring A., 2009. Mechanism and kinetics of pseudomorphic mineral replacement reactions: A case study of the replacement of pentlandite by violarite. Geochimica et Cosmochimica Acta 73, 1945-1969.

Xie, G.Q., Mao, J.W., Wang, R.T., Meng, D.M., Sun, J., Dai, J.Z., Ren, T., Li, J.B.,

Zhao, H.J., 2017. Origin of the Lengshuigou porphyry-skarn Cu deposit in the Zha-Shan district, South Qinling, central China, and implications for differences between porphyry Cu and Mo deposits. Mineralium Deposita 52, 621-639.

Xu, L., Wu, B.X., Wang, Y.L., Wang, Z.X., Wang, G., and Sun, Z.P., 2015. Fluid inclusion characteristics and geological significance at Daqiao gold deposit. Journal of Jinlin University 45, 568-569.

Y

Yan, J., Hu, R., Liu, S., Lin, Y., Zhang, J., Fu, S., 2018. NanoSIMS element mapping and sulfur isotope analysis of Au-bearing pyrite from Lannigou Carlin-type Au deposit in SW China: New insights into the origin and evolution of Au-bearing fluids. Ore Geology Reviews 92, 29-41.

Yang, C.H., Wei, C.J., Zhang, S.G., Li, H.M., Wan, Y.S., Li, R.S., 1999. U-Pb zircon dating of granulite facies rocks from the Foping area in the southern Qinling mountains. Geological Review 45, 173-179.

Yang H. X., Downs R. T., 2008. Crystal structure of glaucodot, (Co, Fe) AsS, and its relationships to marcasite and arsenopyrite. American Mineralogist 93, 1183-1186.

You, G.J., Zhang, Z.P., 2009. Geological characteristics of Daqiao gold deposit in Gansu province and its significance in prospecting for gold deposit. Gansu Geology 18, 1-8.

Z

Zeng, Q.T., McCuaig, T.C., Hart, C.J.R., Jourdan, F., Muhling, J., Bagas, L., 2012. Structural and geochronological studies on the Liba goldfield of the West Qinling Orogen, Central China. Mineralium Deposita 47, 799-819.

Zeng, Q.T, Mccuaig, T.C., Tohver, E., Bagas, L., Lu, Y.J., 2014. Episodic Triassic magmatism in the western South Qinling Orogen, central China, and its implications. Geological Journal 49, 402-423.

Zeng, Y.S. Wang, F.Z., Ai, R.Y., 1997. Solubility of gold in the SiO_2-NaCl-H_2O system at 300°C and50 MPa. Science in China Series D: Earth Sciences 40, 485-490.

Zhai, Y., Deng, J., 1996. Outline of the mineral resources of China and their tectonic setting. Australian Journal of Earth Sciences 43, 673-685.

Zhang, G.W., Zhang, Z.Q., Dong, Y.P., 1995. Nature of main tectono-lithostratigraphic units of the Qinling Orogen: implications for the tectonic evolution. Acta Petrologica Sinica 11, 101-114.

Zhang, G.W., Meng, Q.G., Yu, Z.P., Sun, Y., Zhou, D.W., Guo, A.L., 1996. Orogenesis and dynamics of the Qinling orogen. Science in China Series D: Earth Sciences (English Edition) 39, 225-234.

Zhang, G.W., Zhang, B.R., Yuan, X.C., Xiao, Q.H., 2001. Qinling orogenic belt and continental dynamics. Science Press, Beijing, 855 pp (in Chinese).

Zhang, J., 2016. Study of mineralization process and mechanism in Baguamiao super large gold deposit, Fengtai ore region, Shaanxi, China. Ph.D. thesis, Chinese Academy of Geological Sciences, 200 pp.

Zhang, J., Li, L., Gilbert, S., Liu, J.J., Shi, W.S., 2014. LA–ICP–MS and EPMA studies on the Fe-S-As minerals from the Jinlongshan gold deposit, Qinling Orogen, China: implications for ore-forming processes. Geological Journal. 49, 482-500.

Zhang, Z.P, Wu, Y.F, Li, J.W., 2018. Characteristics and Genesis of the silicified breccias in the Daqiao gold deposit, West Qinling Orogen: Geological Science and Technology Information 37, 79-88.

Zhang, Z.Q., Zhang, G.W., Tang, S.H., Wang, J.H., Xu, J.F., Yang, Y.C., 2002. Age of Anzishan granulites in the Mianxian-Lueyang suture zone of Qinling orogen: with a discussion of the timing of final assembly of Yangtze and north China craton blocks. Chinese Science Bulletin 47, 1925-1929.

Zhao J., Brugger J., Chen G., Ngothai Y., Pring, A., 2014. Experimental study of the formation of chalcopyrite and bornite via the sulfidation of hematite: mineral replacements with a large volume increase. American Mineralogist 99, 343-354.

Zhou, T.H., Goldfarb, R.J., and Phillips, N.G., 2002. Tectonics and distribution of gold deposits in China - an overview. Mineralium Deposita 37, 249-282.

Appendix A [1]GSA Data Repository

Gold, arsenic, and copper zoning in pyrite: a record of fluid chemistry and growth kinetics

Ya-Fei Wu, Denis Fougerouse, Katy Evans, Steven M. Reddy, David W. Saxey, Paul Guagliardo, Jian-Wei Li

A1. List of supplementary figures and tables

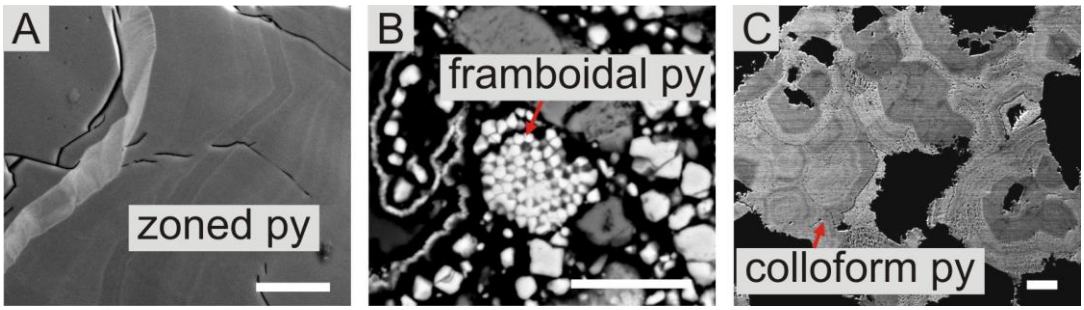

Figure 4.DR1. Zoned (A), framboidal (B), and colloform (C) pyrite in the hydrothermal cements of Daqiao breccia ores. Py–Pyrite. Scale bar is 10 μm

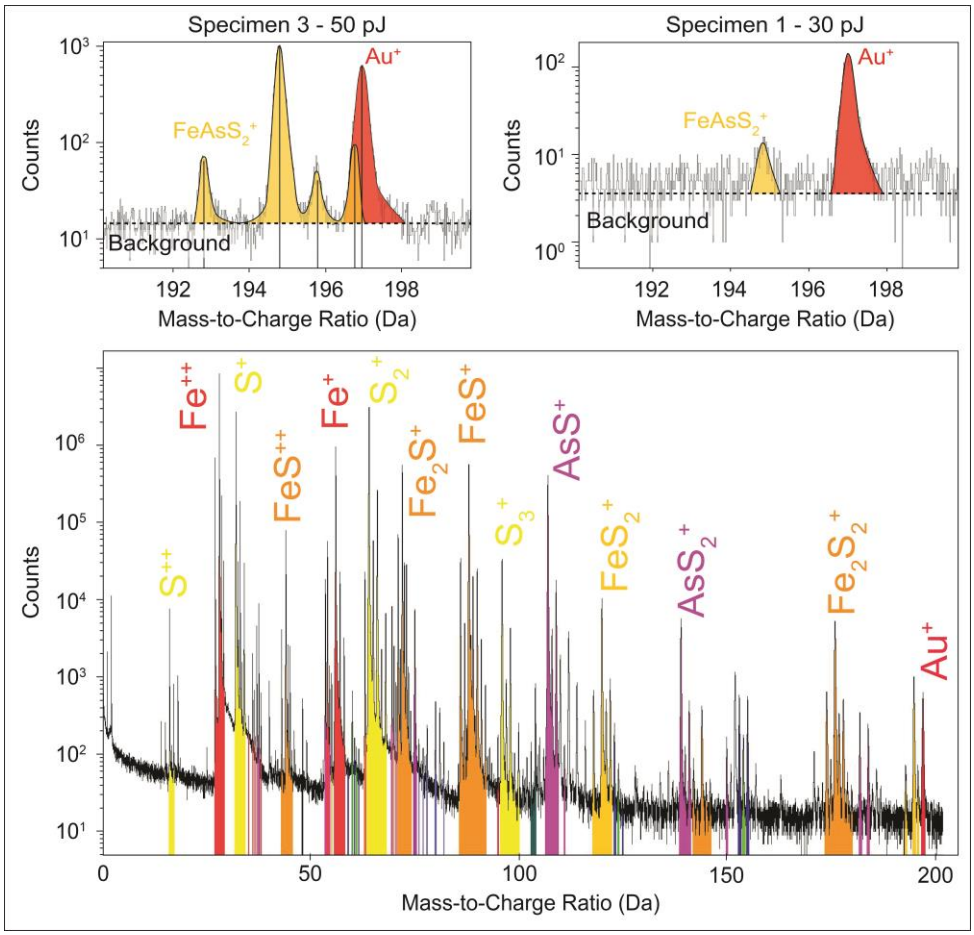

Figure 4.DR2. Atom probe mass spectrum. Peaks are color-coded by atomic or molecular species.

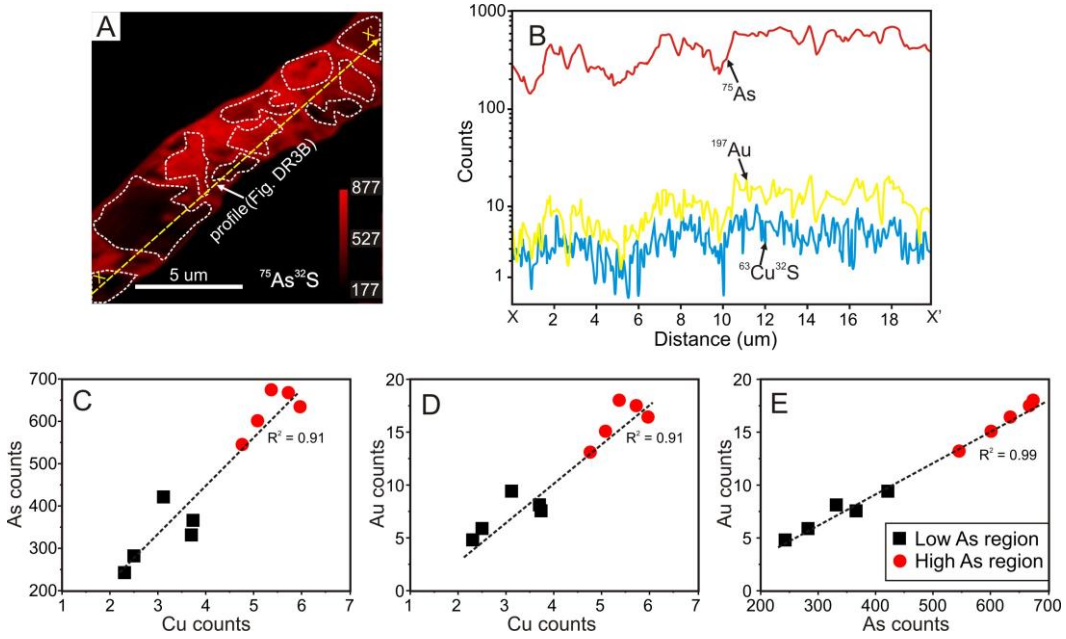

Figure 4.DR3. Line profile (B) and diagrams of mean elemental counts (C-E) for different regions on NanoSIMS arsenic ($^{75}As^{32}S$) map (A) showing the correlations between Cu, As, and Au

A2. Analytical methods

A2.1 NanoSIMS analysis

NanoSIMS analysis was performed on polished epoxy mounts at the Centre for Microscopy, Characterisation and Analysis (CMCA) at the University of Western Australia (UWA), using a CAMECA NanoSIMS 50L optimized as described by Wu et al. (2019). A Cs^+ ion source with a spot size of approximately 50 nm was employed. Multiple electron multipliers record ion counts from the same sputtered sample volume at seven masses simultaneously.

Each region of interest was pre-sputtered using a beam current of 250 pA, to remove surface contaminants and implant Cs^+ ions into the sample matrix to achieve a steady state of secondary ion emission. Negative secondary ions of interest ($^{63}Cu^{32}S^-$, $^{75}As^{32}S^{--}$, and $^{197}Au^-$) were then sputtered from the sample surface using a beam current of ~2.5 pA. The electron gun was used for charge compensation because the samples were predominantly composed of insulating materials. Analysis areas ranged in size from 15×15 to 40×40 μm^2, the image sizes were 256×256 to 512×512 pixels, and the dwell times were 40–160 ms per pixel. NanoSIMS images were processed using ImageJ. The ion intensity of each trace element provides a simple, semi-quantitative expression of localized trace element enrichment.

Appendix

Table 4.DR1. Analysis and reconstruction parameters for atom probe data following recommendation of Blum et al. (2018)

Specimen/data Set	Specimen 1	Specimen 2	Specimen 3
Instrument model	LEAP 4000X HR		
Instrument settings			
Laser wavelength (nm)	355	355	355
Laser pulse energy (pJ)	30	40	50
Pulse frequency (kHz)	125	125	125
Evaporation control	Detection rate	Detection rate	Detection rate
Target detection rate (ions/pulse)	0.01	0.01	0.01
Nominal flight path (mm)	382	382	382
Set point temperature (K)	50	50	50
Chamber pressure (Torr)	$1.3x10^{-10}$	$1.3x10^{-10}$	$1.2x10^{-10}$
Data summary			
LAS root version	15.41.342l	15.41.342l	15.41.342l
CAMECAROOT version	18.44.416	18.44.416	18.44.416
Analysis software	IVAS 3.8	IVAS 3.8	IVAS 3.8
Total ions:	12,417,315	10,490,929	76,251,106
Single	56.4%	60.2%	62.6%
Multiple	42.6%	38.8%	36.7%
Partial	1.1%	1.0%	0.7%
Reconstructed ions:	11,813,609	9,216,276	72,600,477
Ranged	98.3%	98.9%	99.1%
Unranged	1.7%	1.1%	0.9%
Volt./bowl corr. peak (Da)	16	16	16
Mass calib. (peaks/interp.)	5/Lin.	4/Lin.	5/Lin.
†(M/ΔM) for $^{32}S^{++}$	666.6	707.1	822.8
††($M/\Delta M_{10}$)	296.6	333.3	405.4
time independent background (ppm/ns)	2.5	2.1	1.8
Reconstruction			
Final specimen state	Fractured	Fractured	Fractured
Pre-/post-analysis imaging	SEM/n.a.	SEM/n.a.	SEM/n.a.
Radius evolution model	"voltage"	"voltage"	"voltage"
Field factor (k)	3.3	3.3	3.3
Image compression factor	1.65	1.65	1.65
Assumed e-field (V/nm)	33	33	33
Detector efficiency	36%	36%	36%
Avg. atomic volume (nm^3)	0.0108	0.0108	0.0108
$V_{initial}$ (V)	2,474	3,566	3,048

†ΔM is full width at half maximum.
††ΔM_{10} is full width at tenth maximum.

Table 4.DR2. Arsenic, Au, and Cu compositions of three atom probe specimens from the Daqiao Au-rich zoned pyrite

Specimen no.	Arsenic (As) regions	As (at. %)	Au (appm)	Cu (appm)
Specimen 1	Homogeneous As	4.30 ± 0.01	131 ± 3	1028 ± 8
Specimen 2	High-As region	4.28 ± 0.01	164 ± 5	1189 ± 14
	Low-As region	2.11 ± 0.01	71 ± 3	640 ± 10
Specimen 3	High-As region	4.35 ± 0.01	118 ± 6	1087 ± 17
	Low-As region	2.22 ± 0.01	54 ± 4	713 ± 14
Mean		3.45 ± 1.05	108 ± 40	931 ± 216

A2.2 Atom probe analysis

Three atom probe needle-shaped specimens (inset of Figure 4.2A) from the zoned pyrite were prepared and analyzed at the Advanced Resource Characterization Facility at Curtin University. The specimens were prepared using a Tescan Lyra3 Focused Ion Beam Scanning Electron Microscope (FIB-SEM) with a Ga^+ ion source, employing standard lift-out techniques (Thompson et al., 2007). A Cameca LEAP 4000X HR in laser assisted mode was employed for analysis. Approximately 10 to 76 million ions (Table DR1) were collected from each specimen at an evaporation rate of 0.01 ions/pulse, a UV laser (λ = 355 nm) pulse energy of 30 to 50 pJ, and a pulse rate of 125 kHz, at a base temperature of 50 K. Peaks were identified and ranged using the Cameca IVAS 3.8 processing software (Figure 4.DR2). Compositions of specific domains were isolated by volumes defined by concentration isosurfaces (Hellman et al., 2000). The background noise, mass peak overlaps and detector saturation are assessed from the data sets themselves, with uncertainties typically comparable to those arising from the counting statistics for each atomic species. Minor overlapping of Au^+ by $FeAsS_2^+$ (e.g., $^{56}Fe^{75}As^{32}S^{34}S^+$) in specimen 3 (Figure 4.DR2) has been corrected via the percentage calculation and deduction of this part of $FeAsS_2^+$ molecule following the peak decomposition method (Sha et al., 1992; Dmitrieva et al., 2011). APT offers a novel method that allows atom-resolution quantitative three-dimensional elemental mapping of ion distributions down to 10 appm (atomic parts per million) concentrations (Kelly and Larson, 2012).

A3. References cited

Blum, T.B., Darling, J.R., Kelly, T.F., Larson, D.J., Moser, D.E., Perez-Huerta, A., Prosa, T.J., Reddy, S.M., Reinhard, D.A., and Saxey, D.W., 2018, Best practices for reporting atom probe analysis of geological materials: Microstructural Geochronology: Planetary Records Down to Atom Scale, v. 232, p. 369–373.

Dmitrieva, O., Choi, P., Gerstl, S., Ponge, D., and Raabe, D., 2011, Pulsed-laser atom probe studies of a precipitation hardened maraging TRIP steel: Ultramicroscopy, v. 111, p. 623–627.

Hellman, O.C., Vandenbroucke, J.A., Rüsing, J., Isheim, D., and Seidman, D.N., 2000, Analysis of three-dimensional atom-probe data by the proximity histogram: Microscopy and Microanalysis, v. 6, p. 437–444.

Kelly, T.F., and Larson, D.J., 2012, Atom probe tomography 2012: Annual Review of Materials Research, v. 42, p. 1–31.

Sha, W., Chang, L., Smith, G., Cheng, L., and Mittemeijer, E., 1992, Some aspects of atom-probe analysis of Fe-C and Fe-N systems: Surface Science, v. 266, p. 416–423.

Thompson, K., Lawrence, D., Larson, D., Olson, J., Kelly, T., and Gorman, B., 2007, In situ site-specific specimen preparation for atom probe tomography: Ultramicroscopy, v. 107, p. 131–139.

Wu, Y.F., Evans, K., Li, J.W., Fougerouse, D., Large, R.R., and Guagliardo, P., 2019, Metal remobilization and ore-fluid perturbation during episodic replacement of auriferous pyrite from an epizonal orogenic gold deposit: Geochimica et Cosmochimica Acta, v. 245, p. 98–117.

Appendix B Supplementary Material

Metal remobilization and ore-fluid perturbation during episodic replacement of auriferous pyrite from an epizonal orogenic gold deposit

Ya-Fei Wu, Katy Evans, Jian-Wei Li, Denis Fougerouse, Ross R. Large, Paul Guagliardo

METHODS

SEM and EMP

The instrumentation employed was a Quanta 450 field emission scanning electron microscope (SEM) equipped with a SDD Inca X-Max 50 at the State Key Laboratory of Geological Processes and Mineral Resources (GPMR), China University of Geosciences, Wuhan. An accelerating voltage of 10–15 kV and a working distance of ~10 mm were used.

Major elements in sulfides used for calibration of the LA–ICP–MS analyses were performed using a JEOL JXA-8230 electron microprobe (EMP) at the Center for Material Research and Analysis, Wuhan University of Technology, China. The operating conditions consisted of an acceleration voltage of 25 kV, a probe current of 20 nA, and a beam diameter of 1–5 μm.

LA–ICP–MS multi-element analysis of sulfides

These data were acquired when the sample was moving at a constant rate of 3 μm/s under a fixed beam. Ablated material was transported to the detector in pure He gas. Data reduction was undertaken using Fe as the internal standard (Longerich et al., 1996). An in-house Li borate fused glass of a pyrite and/or sphalerite mixture was used as the primary calibration standard, which was analyzed twice every one and a half hours to account for instrument drift. Mass-spectrometer drift was <5% between each standard measurement. After in-situ analyses, all laser pits were imaged by SEM to check the accuracy of ion beam placement, and data from pits containing a mixture of minerals, large cracks, or large cavities were rejected.

NanoSIMS multi-element imaging of sulfides

Multiple electron multipliers record ion counts from the same sputtered sample volume at seven masses simultaneously. Each region of interest was pre-sputtered using a beam current of 250 pA, to remove surface contaminants and implant Cs^+ ions into the sample matrix to achieve a steady state of secondary ion emission. The electron gun was used for charge compensation because the samples were predominantly composed of insulating materials (McLoughlin et al., 2011). Analysis areas ranged in size from 25×25 to 40×40 μm^2, the image sizes were 256×256 to 512×512 pixels, and the dwell times were 40–160 ms per pixel.

NanoSIMS images were processed using ImageJ (http://rsbweb.nih.gov/ij/). The colour scales on the NanoSIMS maps refer to the intensity of the ion yield (i.e. total ion counts per pixel obtained during the dwell time on that pixel) with brighter colours representing higher counts. This ion intensity of each trace element provides a simple, semi-quantitative expression of localized trace element enrichment. Measurements are not quantitative because appropriate standards were not incorporated into the analysis.

SIMS sulfur isotope analysis

The instrument was operated in multicollector mode using three off-axis Faraday cups. The high mass resolution power (MRP) of 2400 was employed to have flat top peaks on all the masses. Each analysis takes about 4.5 min, consisting of 30 s pre-sputtering, 60 s of automated centering of secondary ions, and 160 s integrating S isotope signals. Every 6 pyrite and marcasite analyses were bracketed by 3 Sonora pyrite analyses, which were used as running standards for the S isotope analysis. The Balmat pyrite standard of was analyzed several times during each of two sessions, bracketing analyses of pyrite with unknown isotopic composition. The analyses of the Balmat pyrite standard were used specifically to yield a realistic estimate of external reproducibility on $\delta^{34}S_{VCDT}$ of ±0.12‰ and $\delta^{33}S_{VCDT}$ of ± 0.16‰ (2σ, Chen et al., 2015).

REFERENCES

Chen L., Li X. H., Li J. W., Hofstra A. H., Liu Y., Koenig A. E., 2015. Extreme

variation of sulfur isotopic compositions in pyrite from the Qiuling sediment-hosted gold deposit, West Qinling orogen, central China: an in situ SIMS study with implications for the source of sulfur. *Mineralium Deposita* 50, 643-656.

Longerich H. P., Jackson S. E., Günther D., 1996. Laser Ablation Inductively Coupled Plasma Mass Spectrometric Transient Signal Data Acqusition and Analyte Concentration Calculation. *J. Anal. At. Spectrom*. 11, 899-904.

Table B5.1 LA–ICP–MS analyses of different generations of pyrite and marcasite involved in the pyrite replacement from the Daqiao gold deposit

Sample no.	Analysis no.	Iron Sulfides	Co	Ni	Cu	Zn	As	Se	Ag	Sb	Te	W	Au	Tl	Pb	Bi
DQ391-1	DQ391-1		13.82	273.92	4.27	0.67	3133.08	78.99	0.06	4.65	0.19	0.01	0.02	0.07	7.79	0.63
DQ391-2	DQ391-2		93.64	150.49	32.39	6.03	5729.82	70.28	0.21	42.80	0.04	0.04	0.06	1.06	54.32	0.66
DQ447-1	DQ447-1		1.19	12.74	103.83	6.26	21746.89	283.64	4.74	126.27	0.00	0.93	10.05	2.38	18.67	0.00
DQ447-2	DQ447-2		5.28	138.83	72.46	3.00	5026.65	50.27	10.15	463.18	0.28	5.22	3.16	31.28	74.69	0.05
DQ462-1	DQ462-1		15.17	610.84	5.79	0.46	6516.35	1.66	0.11	6.93	0.15	2.52	0.17	0.01	6.60	0.29
DQ462-2	DQ462-2		258.02	1225.82	99.13	1.66	9392.46	2.58	4.78	67.72	0.90	0.17	1.28	0.22	45.02	0.27
DQ445-1	DQ445-1		52.26	261.61	54.85	14.62	1816.96	52.50	16.51	709.33	0.00	1.75	10.90	130.88	34.44	0.10
DQ-107-3	DQ-107-3		0.55	8.64	29.54	45.23	2010.46	1.53	12.26	67.59	0.00	2.84	0.42	28.06	2.59	0.02
DQ-282-1	DQ-282-1		55.91	102.28	11.80	0.73	225.38	42.10	0.24	4.54	0.23	0.00	0.14	0.03	20.08	7.12
DQ-291-2	DQ-291-2	Py_3	7.23	54.87	342.49	1.15	4812.63	54.37	18.17	190.31	0.11	0.80	10.93	12.22	41.00	0.60
DQ-291-5	DQ-291-5		12.43	26.63	195.29	1.82	3317.96	33.93	19.67	311.23	0.10	0.40	5.21	24.85	73.26	0.31
DQ-383-1	DQ-383-1		970.49	392.25	0.24	0.26	1637.62	77.07	0.07	0.82	0.00	0.03	0.04	0.04	1.46	0.29
DQ-288-1	DQ-288-1		82.12	542.62	113.66	12.26	4215.92	71.85	13.33	596.29	1.87	1.20	4.95	40.76	63.44	4.24
DQ-288-2	DQ-288-2		91.71	448.34	513.18	36.41	10967.87	126.98	52.30	3172.87	4.04	2.67	33.66	164.63	569.17	19.53
DQ-379-3	DQ-379-3		144.84	543.93	0.29	0.20	2565.18	31.31	0.03	0.73	0.18	0.03	0.00	0.00	1.30	1.09
DQ-379-6	DQ-379-6		78.10	379.20	282.76	3.32	3143.03	13.94	7.51	190.74	7.05	0.15	2.32	19.31	178.00	29.27
DQ-379-7	DQ-379-7		74.25	1248.61	905.31	62.21	3827.86	20.95	3.96	68.64	3.08	0.37	0.30	13.86	10.87	11.83
DQ-395-1	DQ-395-1		90.72	326.78	18.01	7.48	1472.57	6.48	0.21	44.53	0.19	8.73	0.01	4.36	791.14	5.22
DQ-477-1	DQ-477-1		0.91	23.86	98.45	1.27	22624.49	458.31	3.59	30.53	6.03	0.01	2.99	1.93	37.65	0.02

Sample no.	Analysis no.	Iron Sulfides	Co	Ni	Cu	Zn	As	Se	Ag	Sb	Te	W	Au	Tl	Pb	Bi
DQ-477-2	DQ-477-2	Py3	160.49	649.19	98.77	1.23	13345.52	464.46	6.38	120.69	8.34	1.35	1.67	0.46	203.38	0.40
DQ-477-3	DQ-477-3		3.37	123.42	88.52	1.90	16560.87	437.39	6.73	96.55	5.31	12.70	2.46	1.55	65.31	0.07
DQ-198-1	DQ-198-1		4.79	153.74	346.96	4.71	5584.95	139.46	1.59	503.80	0.06	9.79	16.13	29.73	41.15	0.21
DQ-198-7	DQ-198-7		35.55	137.14	682.38	4.31	7613.33	122.05	28.73	1944.06	0.06	1.07	107.01	227.24	77.82	0.17
DQ403-1	DQ403-1	$Py_{4\text{-}py}$	3.79	46.45	13.95	62.12	43.79	3.66	0.05	342.66	0	0	0.42	1.58	6.41	0
DQ429-2	DQ429-2		22.16	138.49	57.5	0.47	2.13	27.34	1.57	206.54	0.3	0.02	0.07	1.41	511.58	1.79
DQ445-2	DQ445-2		55.76	213.94	53.06	9.31	489.15	11.63	4.77	99.46	0.04	4.91	0.9	10.3	237.58	1.43
DQ445-3	DQ445-3		45.81	337.63	98.21	3.36	365.51	3.19	8.34	126.99	0.34	0.14	0.26	7.39	317.18	4.47
DQ-282-2	DQ-282-2		13.71	62.87	1.5	0.38	57.7	61.9	0.04	0.14	0.37	0	0.01	0.01	0.81	0.6
DQ-291-4	DQ-291-4		8.29	33.95	183.61	1.41	2642.29	52.93	20.86	473.36	0	6.2	2.91	30.33	77.74	0.67
DQ-383-2	DQ-383-2		1.93	137.9	53.27	1.88	71.36	3.99	1.34	70.56	0	0.51	0.12	11.82	70.18	0.57
DQ-263-1-1	DQ-263-1-1		173.92	362.17	9.08	0.12	0.32	34.04	0.89	46.19	1.15	0	0.08	0.02	177.76	4.15
DQ-263-1-2	DQ-263-1-2		77.51	300.39	118.67	1.07	13.04	37.08	9.32	1126.52	2.24	0	1.56	0.12	2163.71	166.32
DQ-263-2-3	DQ-263-2-3		145.27	3949.73	8730.3	20.25	2.53	37.24	40.03	6.66	0	0.01	0.09	0.05	189.01	3.48
DQ-263-2-4	DQ-263-2-4		0.17	2.35	5.14	0.07	0	35.88	0.36	0.05	0.12	0	0	0	7.42	0.39
DQ-355-1	DQ-355-1		4.13	8.01	10.14	0.85	662.86	50.3	0.18	9.77	0	0.19	0.01	0	49.03	0.35
DQ-355-2	DQ-355-2		0.29	3.79	36.98	77.64	838.79	25.88	0.29	38.33	0.21	0.25	0.01	0.01	151.2	1.4
DQ-198-6	DQ-198-6		85.03	269.03	536.5	5.15	6901.95	102.13	22.49	1999.77	0.01	3.59	89.85	237.96	156.82	0.23
DQ382-1	DQ382-1		94.81	111.14	35.84	0.37	4416.88	59.77	0.7	97.31	20.08	0.08	0.4	4.79	75.57	77.78
DQ382-2	DQ382-2		76.88	281.83	94.8	0.99	1063.69	47.1	2	90.21	0.96	1.02	0.23	3.9	14.13	3.53

Sample no.	Analysis no.	Iron Sulfides	Co	Ni	Cu	Zn	As	Se	Ag	Sb	Te	W	Au	Tl	Pb	Bi
DQ403-2	DQ403-2	$Mc_{2\text{-}py}$	1.58	25.95	5.8	230.94	0.16	3.48	0.04	18.98	0	0	0	0.24	0.86	0
DQ429-1	DQ429-1		1.1	28	25.72	2.11	38.37	8.03	0.26	3.04	0.04	3.7	0.1	33.47	0.6	0
DQ462-3	DQ462-3		50.56	157.41	156.29	101.79	524.79	2.13	14.3	272.52	0.05	462.72	0.01	11.69	151.43	0.02
DQ-107-2	DQ-107-2		0.04	1.06	12.45	29.84	1701.41	2.96	8.53	42.76	0	0.31	0.23	49.36	1.5	0.01
DQ-395-2	DQ-395-2		0.22	0.37	30.07	5.25	273.27	2.67	0.07	97.74	-0.05	25.78	0.11	28.84	19.9	0.05
DQ-198-9	DQ-198-9		0.39	1.5	20.42	8.59	2393.31	131.29	1.35	131.92	0.16	83.28	5.06	9.62	8.52	0.08
DQ-208-1	DQ-208-1		0	1.06	5.11	45.49	253	5.93	16.05	362.55	0	12.81	0.23	4.13	1.03	0
DQ-208-5	DQ-208-5		0	0.03	0.59	28.98	169.59	55.48	3.3	455.01	0	36.69	0.12	72.8	0.54	0
DQ-208-7	DQ-208-7		0.02	0.62	3.02	1.02	8.38	1.54	17.14	11.77	0	0.25	0.08	3.47	0.26	0
DQ-209-2	DQ-209-2		0.12	0.04	0.26	17.16	132.45	83.68	4.47	514.05	0.08	10.75	0.12	55.22	1.86	0
DQ-209-3	DQ-209-3		0	0	0.26	6.12	137.68	20.19	5.59	31.53	0	7.15	0.07	5.62	0.79	0.01
DQ-209-4	DQ-209-4		0.01	0	1.66	2.41	357.02	12.09	4.65	118.87	0	10.52	0.71	44.57	3.96	0
DQ-379-1	DQ-379-1		203.25	596.71	9.36	0.16	2176.12	20.69	0.86	19.34	0.23	0	0.09	4.32	11.13	1.9
DQ-379-2	DQ-379-2		226.32	809.66	4.15	0.44	3028.36	28.75	0.85	12.15	0.19	0.03	0.11	1.28	15.17	1.45
DQ-107-1	DQ-107-1	$Mc_{3\text{-}py}$	1.55	15.18	42.48	36.28	1758.77	3.58	19.97	49.73	0.1	10.38	0.89	33.53	7.36	0.19
DQ-282-3	DQ-282-3		0	7.07	367.64	2.69	2437.23	149.9	9	1550.65	0.55	45.55	0.76	131.23	28.7	0.02
DQ-291-3	DQ-291-3		13.2	180.75	86.65	2.06	4625.02	37.09	29	868.37	0.49	33.19	10.87	54.66	197.2	6.51
DQ-291-1	DQ-291-1		1.22	67.46	112.43	2.26	4749.37	96.33	29.12	1097.33	0.17	44.49	7.79	55.91	104.53	1.13
DQ-383-3	DQ-383-3		0.11	94.26	244.08	0.99	3240.15	60.72	1.28	500.18	0.28	18.69	2.29	74.14	33.91	0.1
DQ-379-4	DQ-379-4		108.27	172.8	415.16	3.18	5009.62	36.02	18.95	511.5	1.19	3.52	8.46	155.61	11.03	1.89
DQ-379-5	DQ-379-5		2.67	436.92	148.13	2.49	2728.77	18.53	20.48	387.49	0.49	3.29	6.11	100.41	52.27	2.25
DQ-198-2	DQ-198-2		2.11	60.22	300.88	2.48	12726.47	301.58	4.98	1389.27	0.01	5.6	52.61	123.55	43.51	0.25
DQ-198-3	DQ-198-3		1.44	68.41	290.61	2.2	10708.14	241.6	2.87	852.11	0	17.25	62.86	62.47	23.74	0.16
DQ-198-4	DQ-198-4		1.54	53.2	160.02	3.94	12217.57	305.05	7.16	1610.6	0.06	35.97	48.47	106.05	39.51	0.36

Sample no.	Analysis no.	Iron Sulfides	Co	Ni	Cu	Zn	As	Se	Ag	Sb	Te	W	Au	Tl	Pb	Bi
DQ-198-5	DQ-198-5		3.35	78.79	144.74	3.55	10934.02	275.2	7.51	1640.6	0.01	70.96	40.81	102.19	45.99	0.34
DQ-198-8	DQ-198-8		114.49	871.95	216.53	19.32	7870.94	109.09	8.82	2174.47	0.33	32.76	44.89	86.41	389.78	1.62
DQ-198-10	DQ-198-10		1.31	4.31	34.43	11.02	3866.47	118.71	1.58	213.79	0	92.68	10.55	15.19	22.78	0.15
DQ-198-11	DQ-198-11		1.05	3.4	46.69	6.88	5711.13	310.1	2.61	415.07	0	38.61	13.06	25.44	42.17	0.19
DQ-208-2	DQ-208-2	Mc3-py	0.08	0.35	27.95	28.16	2719.1	108.5	577.13	4369.77	0.18	51.7	7.96	902.78	4.76	0.02
DQ-208-3	DQ-208-3		0.02	0.89	38.49	15.73	7836.08	216.18	549.59	3085.07	0	28.72	45.05	786.7	2.47	0
DQ-208-4	DQ-208-4		0.05	0.62	46.25	107.25	6736.69	142.36	815.6	4225.72	0.04	46.52	50.68	1049.59	4.51	0
DQ-208-6	DQ-208-6		0.09	9.6	49.3	28.79	7690.66	427.63	617.36	3461.39	0.1	63.73	22.48	868.16	13.65	0.02
DQ-209-1	DQ-209-1		0.48	5.89	37.35	21.49	6279.67	189.09	409.88	1945.33	0	3.89	32.23	442.71	35.95	0.03

Appendix

Table B5.2 SIMS in situ sulfur isotope compositions of different generations of pyrite and marcasite involved in the pyrite replacement from the Daqiao gold deposit

Analysis no.	Iron Sulfides	$\delta^{34}S‰_{VCDT}$	2s
DQ198-1		2.9	0.02
DQ198-7		2.5	0.02
DQ291-1		4.1	0.02
DQ291-3		4.0	0.03
DQ383-1		1.9	0.02
DQ379-5		2.3	0.02
DQ395-2	Py_3	9.0	0.03
DQ477-1		5.3	0.02
DQ477-2		5.5	0.02
DQ477-3		5.3	0.02
DQ477-4		5.3	0.03
DQ477-5		6.0	0.03
DQ477-6		5.5	0.03
DQ198-6		4.3	0.02
DQ291-4		1.7	0.02
DQ383-2	$Py_{4\text{-}py}$	2.1	0.02
DQ383-3		2.9	0.02
DQ379-2		3.8	0.02
DQ198-8		1.1	0.02
DQ198-10		3.2	0.02
DQ208-1		3.0	0.03
DQ208-2		3.7	0.03
DQ208-3		2.3	0.01
DQ208-6		2.9	0.03
DQ291-5	$Mc_{2\text{-}py}$	2.1	0.03
DQ291-6		3.3	0.02
DQ383-4		2.9	0.02
DQ379-1		2.3	0.02
DQ379-3		3.2	0.03
DQ379-6		2.1	0.02
DQ395-1		-0.9	0.05
DQ198-2		1.3	0.03
DQ198-3		-1.6	0.04
DQ198-4		0.9	0.03
DQ198-5		1.2	0.02
DQ198-9		2.2	0.02
DQ198-11		1.4	0.02
DQ198-12		1.4	0.02
DQ198-13	$Mc_{3\text{-}py}$	1.5	0.02
DQ198-14		1.0	0.03
DQ208-4		2.0	0.02
DQ208-5		-4.1	0.05
DQ208-8		-8.0	0.09
DQ208-7		-11.4	0.14
DQ291-2		0.9	0.02
DQ379-4		-10.0	0.02
DQ379-7		-0.1	0.08

Appendix C Statements of contribution by others

To Whom It May Concern,

I, Yafei Wu, contributed to all aspects of research including, but not limited to, sample collection, processing and analysis, data processing, and manuscript preparation to the publication entitled:

Manuscript 1:

Wu Y.F., Li J.W., Evans K., Fougerouse D., and Rempel K., 2019, Source and possible tectonic driver for Jurassic–Cretaceous gold deposits in the West Qinling Orogen, China. *Geoscience Frontiers*, 10 (1): 107–117 (Impact factor 4.256).

Manuscript 2:

Wu Y.F., Fougerouse D., Evans K., Reddy S.M., David W.S., Paul G., and Li J.W., 2019, Gold, arsenic, and copper zoning in pyrite: a record of fluid chemistry and growth kinetics. *Geology*, 47 (7): 641–644 (Impact factor 5.451).

Manuscript 3:

Wu Y.F., Evans K., Li J.W., Fougerouse D., Large R.R., and Guagliardo P., 2019, Metal remobilization and ore-fluid perturbation during episodic replacement of auriferous pyrite from an epizonal orogenic gold deposit. *Geochimica et Cosmochimica Acta*, 245 (15): 98–117 (Impact factor 4.609).

Yafei Wu

Date 08/05/2019

A realistic breakdown of contribution by co-authors is as follows:

Manuscript 1:

Author	Yafei Wu	Jian-Wei Li	Katy Evans	Denis Fougerouse	Kirsten Rempel
Percentage	72%	8%	10%	5%	5%

Manuscript 2:

Author	Yafei Wu	Denis Fougerouse	Katy Evans	Steven M. Reddy	David W. Saxey	Paul Guagliardo	Jian-Wei Li
Percentage	68%	13%	11%	3%	1%	1%	3%

Manuscript 3:

Author	Yafei Wu	Katy Evans	Jian-Wei Li	Denis Fougerouse	Ross R. Large	Paul Guagliardo
Percentage	70%	15%	7%	6%	1%	1%

I, as one of the co-authors, endorse that this level of contribution by the candidate indicated above is appropriate.

Name	**Signature**
Katy Evans	
Jian-Wei Li	
Denis Fougerouse	
Kirsten Rempel	
Steven M. Reddy	
David W. Saxey	
Paul Guagliardo	
Ross R. Large	

Appendix D Permission of copyright from third parties

The following is the rights granted by Elsevier and GeoScienceWorld to the publications that form **Chapter 2, Chapter 4** and **Chapter 5** of this thesis, to allow the reproduction of the full article in a thesis.

COPYRIGHT 1

This paper “Wu Y.F., Li J.W., Evans K., Fougerouse D., and Rempel K., 2019, Source and possible tectonic driver for Jurassic–Cretaceous gold deposits in the West Qinling Orogen, China. *Geoscience Frontiers*, 10 (1): 107–117” is published as an open access article under a Creative Commons Attribution-Non Commercial-No Derives (CC BY-NC-ND) and can be reproduced with no copyright infringements as a part of this thesis. Further details can be found at https://creativecommons.org/licenses/by-nc-nd/4.0/

COPYRIGHT 2

Geology

Order detail ID: 71905541
Order License Id: 4593930600193

ISSN: 1943-2682
Publication Type: e-Journal
Volume:
Issue:
Start page:
Publisher: Geological Society of America
Author/Editor: Geological Society of America

Permission Status: Granted

Permission type: Republish or display content
Type of use: Republish in a thesis/dissertation

Hide details

Requestor type	Author of requested content
Format	Print, Electronic
Portion	chapter/article
The requesting person/organization	Yafei Wu
Title or numeric reference of the portion (s)	Gold, arsenic, and copper zoning in pyrite: A record of fluid chemistry and growth kinetics; whole content
Title of the article or chapter the portion is from	Gold, arsenic, and copper zoning in pyrite: A record of fluid chemistry and growth kinetics
Editor of portion(s)	Dennis Brown
Author of portion(s)	Yafei Wu ; Denis Fougerouse ; Katy Evans ; Steven M. Reddy ; David W. Saxey ; Paul Guagliardo ; Jian-Wei Li
Volume of serial or monograph	https://doi.org/10.1130/G46114.1
Page range of portion	
Publication date of portion	May 02, 2019
Rights for	Main product
Duration of use	Life of current edition
Creation of copies for the disabled	no
With minor editing privileges	no
For distribution to	Worldwide
In the following language(s)	Original language of publication
With incidental promotional use	no
Lifetime unit quantity of new product	Up to 499
Title	Mr.
Institution name	Curtin University
Expected presentation date	Jun 2019

Note: This item will be invoiced or charged separately through CCC's **RightsLink** service. More info **$ 0.00**

COPYRIGHT 3

Please note that, as the author of this Elsevier article, you retain the right to include it in a thesis or dissertation, provided it is not published commercially. Permission is not required, but please ensure that you reference the journal as the original source. For more information on this and on your other retained rights, please visit: https://www.elsevier.com/about/our-business/policies/copyright#Author-rights